Formability of Polymer-coated Metals

Author:
Wolfram REINHARDT
MEng

Supervisors:
Dr. William HARRISON
Dr. Robert DONE
Dr. Martin WATSON
Mark GREENFIELD
Dr. Blanca PASCUAL

A thesis submitted to Swansea University in fulfilment of the requirements for the degree of Doctor of Engineering

SWANSEA UNIVERSITY
May 19, 2021

This work is funded by the European Social Fund (ESF) through the European Union's Convergence programme administered by the Welsh Government.

Abstract

Wolfram REINHARDT

Formability of Polymer-coated Metals

This project was undertaken to explore the viability of manufacturing polymer-coated cans using current drawing-wall-ironing methods, and centres around exploring polymer-coated alternatives to lacquered food and beverage cans. A full process FEA model was developed in Abaqus, and a polymer coating characterisation was attempted via tensile and compressive tests of available PET. As an alternative, the polymer was modelled as a force/over-closure contact definition in finite element analysis models, using force data derived from existing polymer data. The contact definition demonstrated an effective alternative to modelling a finite element meshed polymer layer but needed optimising to match physical results. A tensile test machine rig was designed and manufactured capable of ironing strip metal specimens for otherwise unavailable ironing metrology. The rig was calibrated using uncoated steel, then used to gain data on force and resulting geometry for polymer coated steel during and after ironing. Rig data was used in a finite element analysis automated feedback loop to optimise the force/over-closure and friction coefficients for the contact definition. Finally, a full-process drawing-wall-ironing simulation on polymer coated steel was implemented in a design of experiments study, which mapped the previously unexplored design space. The most significant parameters in resulting can geometry were the percentage of redraw and ironing during the respective forming phases, as well as the redraw radius. Decreasing the diameter of both redraw and ironing tooling rings resulted in a longer and thinner can, as did decreasing the redraw radius. Whilst not an exhaustive study, the project ultimately demonstrated the viability of modelling polymer-coatings using contact definitions in finite element analysis and paves the way for further study into the polymer-coated steel can.

Declaration of Authorship

I, Wolfram REINHARDT, declare that this thesis titled, "Formability of Polymer-coated Metals" and the work presented in it are my own. I confirm that:

- This work was done wholly or mainly while in candidature for a research degree at this University.
- Where any part of this thesis has previously been submitted for a degree or any other qualification at this University or any other institution, this has been clearly stated.
- Where I have consulted the published work of others, this is always clearly attributed.
- Where I have quoted from the work of others, the source is always given. With the exception of such quotations, this thesis is entirely my own work.
- I have acknowledged all main sources of help.
- Where the thesis is based on work done by myself jointly with others, I have made clear exactly what was done by others and what I have contributed myself.

Signed:

Date:

Acknowledgements

- My sincerest thanks go to my academic supervisor Dr Will Harrison, who has been an irreplaceable font of knowledge and experience throughout the project. Without his advice and guidance, I would scarcely have navigated the full potential of the project.
- I would like to express my deepest gratitude to Dr Martin Watson, Mark Greenfield, Dr Robert Done, Dr Blanca Pascual, Dr Alejandro Graner Solana, Keith Vincent, and all the others at Crown who have been a tremendous help guiding me through the complex models, processes, and data involved in can-making.
- Further thanks to my institution Swansea University, the M2A admin team, and the lab and workshop teams who made this project possible.
- Finally, thank you to my partner Anastasia Paramore, for supporting me in all ways throughout the project.

Contents

List of Figures

List of Tables

Glossary

anisotropy Anisotropy (contrary to Isotropy) describes a material which applies different material behaviours in different directions. 17

axisymmetric Axisymmetric models convey a specified 1 radian slice of a cylindrical 3D model: the variables of which are applied per radian and calculated as though it were part of a perfectly rotationally-symmetrical 3D geometry. 24

bench-top Bench-top simply describes any apparatus used on a work surface, as opposed to free standing equipment. Generally portable, or requiring no professional installation. 90

blanks Blanks is a general term used to refer to the piece of metal which is initially cut for further manufacturing processes. In the case of DWI, a blank is a specifically sized disk, punched out before DWI processing. 5

bodymaker The term bodymaker refers to the general processing machinery required to manufacture the bulk body of a can. In the case of three-piece cans these processes include rolling and welding the seam. When referring to a two-piece can, a bodymaker is the machinery combining a high-speed punch and ring-dies which embodies the DWI process. 5

carbon footprint Carbon footprint is a colloquial term used to quantify and compare the amount of carbon dioxide produced by a company, or particular process. In some cases the term is used to refer to the general environmental cost. 1

continuum element Continuum elements are hexahedrons which contain nodes at each corner, and interpolation points throughout the element. These deformable elements are generally used in a wide variery of FEA applications, and carry engineering variables - configurable using complex material models. 21

discretisation Discretisation is the term for the process by which continious sufaces or functions are broken up into discrete parts. In FEA discretisation concerns the processing of surfaces or volumes into mesh. 109

earing Earing is a metal forming defect characterised by a variation in height of the final product. Usually earing is caused by anisotropic properties in the raw material. 8

encastre The encastre boundary condition defines a zero or fixed movement for every available degree of freedom. 61

equiaxed grains Equiaxed grains are simply grains which have axes of similar (or identical) measurement. 19

extensometers Extensometers are devices used to measure extension or changes in dimensions of a specimen. Usually in metallurgy these will be of a similar construction to strain gauges, but can often be as simple as a needle and measuring stick separately affixed to a specimen. 15

grain boundaries Grain boundary describes the interface between metallic grains, inevitably grains are misaligned at grain boundaries, causing different properties between grains compared to within grains. 19

grains Grains in metal are singular crystals made of an uninterupted crystalline lattice of atoms. 19

ingot is the general term to describe a piece of metal which has been made into a large block, primarily for storage, transport and further processing. 18

input file An input file (or input deck) is the text file which Abaqus solvers use to read the information and data pertaining to the generation of an FEA simulation. 68

isomers Isomers are chemical compounds with identical formula but differing molecular arrangement (and thus differing mechanical properties). 30

load cells Load cells are metrology equipment used to measure a force across the loading direction. These can function in a number of ways, often using similar technology to a strain gauge. 93

parameterising Parameterising an input file describes the process of cross-referencing certain dimensional values with a versatile parameter format. Parameterised input files allow changes to be made to the model using third party software, or simply by changing simple values which derive many others. 68

pugh matrix A Pugh matrix is a decision tool used to organise a disciplined consensus based on the total score of various weighted criteria. Ideas or designs are ranked according to suitability in categories or specification, and each said category is given a weight. The product of the weight and rank contributes to the score. 93

restart simulations Restart simulations are FEA simulations which import a mesh geometry from a previous simulation, keeping all associated engineering data within the meshed material. 52

rosette strain gauge A rosette strain guage setup describes an arrangement of strain gauges at angles to one another in order to measure different directions or multi-axial strain. 14

shell element Shell elements are two-dimensional elements often used model a zero-thickness geometry, though can be used with extra interpolation points to model thin materials. 21

shims Shims are simply arbitrary pieces of material used to fill gaps or slightly increase dimensions. Shims can be measured in thickness, or randomly installed until requirements are met. 113

simulation driven design Simulation driven design is a design process by which failure modes, excess and unsuitable material or design aspects are identified by simulating the duty conditions of a design in a finite element analysis. Usually done in an iterative approach, simulating again after each issue is satisfied. 13

snagging Snaggin describes a problem with elemental distortion, which occurs when contact is defined between two surfaces, and the nodes forming them are caught upon one another (usually due to a large element size). Once a node has snagged, it will continue to drag the rest of the surface along with it. 50

springback Springback refers to the period of relaxation between forming processes after tooling forces are removed. 38

steady state Steady state systems have reached a point of equilibrium, and engineering behaviour does not change during the steady-state. 65

strain gauge A strain guage is a tool used for measuring strain changes in a material, usually constructed from wire or foil on a flexible backing. When force is applied in any direction, the resistance of the conducting material changes, which can be measured when passing a current through. 13

stress concentrators Stress concentrators are generally referring to any feature in a material or design which creates areas of concentrated stress. Some typical examples would be notches, holes, or cracks. 14

surface to surface contact Surface to surface is a computational contact method where surfaces (that being the interlinking segments between nodes) are used as the basis of contact to other surfaces. This method generally provides cleaner contact for moving surfaces, but ignored node penetration - which can lead to snagging issues if mesh is too coarse. 26

tear-off A tear-off is a failure mode during can manufacturing where a can literally tears during forming, usually around the circumference of the can. Tear-offs are usually caused by deviation in materials, or excessive buildup of stress during processing. 10

three-piece can Three-piece can refers to a can design utilising a rolled and welded construction, with separately manufactured caps and bases. These cans are generally bulkier and heavier than their two-piece counterparts. *A typical "Baked beans" can is a prime example.* 5

trailing edge In canmaking, a trailing edge is the edge furthest from the tooling when ironing occurs. For this thesis it refers to the top edge of the can (the end where a can is typically opened). 54

transition fit Transition fit describes a compromise between clearance and interference fits. Accurate placement is necessary but clearance or tolerance is permissable. A transition fit does not require force to fit. 115

two-piece can Two piece can refers to a can design manufactured via the Drawing and Wall Ironing method, creating only a cup and and a cap. These cans are generally much lighter than their three-piece counterparts, as a result of smaller wall thicknesses. *A typical "Coca Cola" can is a prime example* . 6

Ultimate tensile strength Ultimate tensile strength is the maximum tensile stress before which catastrophic failure occurs in a material (see ultimate tensile stress). 61

worm Trails Worm trails are Ironing defects characterised by a gouged silhouette along the ironing direction. Worm Trails are caused by trapped particulate preventing ironing between the blank and the tooling. 10

Acronyms

CAE Computer Aided Engineering - generally referring to Abaqus in this thesis. 38

DIC Digital Image Correlation. 15

DOF Degree Of Freedom. 22

DWI Drawing and Wall Ironing. 6

FEA Finite Element Analysis. 13

FMEA Failure Mode and Effect Analysis. 99

GUI Graphical User Interface. 68

List of Equations

Chapter 1

Introduction

1.1 Motivation for the project

This project *Formability of polymer-coated metals* undertaken with Crown Packaging PLC. (Crown), explores prospective alterations to the current drawing/wall-ironing (DWI) processes presently used in the construction of two-piece cans. Currently, the process chain used for a majority of two-piece cans involves several post-processes to clean, lacquer or otherwise protect both the interior and exterior of the product - ensuring food safety standards or optimal printing surfaces are achieved. These post-processes are an expensive addition to the manufacturing process and mark a reasonable target for improvement.

By removing the in-house post-processes used in the two-piece can, and transferring them to the substrate manufacturing facilities, Crown hopes to reduce the overall cost and environmental footprint of two-piece cans.

Metal sheet is manufactured at a mass scale, and the protective layer can be more easily laminated on during this process of rolling and coiling, compared to applying a protective layer after the metal production. In this way the costs of purchasing pre-coated metal promises to be more economical than spraying and curing the coating on each formed can, and produces fewer exhaust chemicals and grey water. In this sense the project improves overall sustainability without simply shifting the cost or carbon footprint somewhere else.

Feeding a pre-coated substrate through the existing DWI machinery (bodymaker) prompts a new set of challenges to investigate. A polymer coating alters variables such as friction and wall thickness, whilst potentially adding new defects and failure modes relating to the polymer itself, or a new complex compound-stiffness value for the can. Since DWI is a high-strain-rate, high-deformation

process, it is difficult to monitor engineering variables physically; and thus a simulation-driven design is more feasible when exploring the effects of the new substrate on the tooling (and vice versa).

Using both finite element analysis and physical testing, this project seeks to map out some of the uncharted territory involved in performing the DWI processes on polymer-coated substrates, and gain a better understanding of the interactions between major variables.

1.1.1 Overview of the work involved

Chapter **2** of the thesis begins with a literature review of existing can-making processes and industry, as well as exploring the types of metals widely used in cans. The literature review examines methods used to test and model the process, as well as establishing basic concepts discussed in the project.

The workflow then progresses in chapter **3** to demonstrate and explore the capability of finite element analysis modelling the complex DWI process for two-piece beverage and food cans, using scripting capabilities to generate the finite element analysis (FEA) models required, and explores the major FEA methods suitable to the research.

Some material characterisation is pursued in the beginning of **4** , but ultimately the available testing apparatus and methods proved unsuitable for precise material metrology, and so the work was put aside in favour of a different modelling approach. Instead, the bulk of the chapter explores the potential methods of modelling the contact between polymer film and metal, and details the limitations involved in current methods.

Chapter **5** follows the design, manufacture and testing of a custom bench top ironing-rig, for use in a screw-driven tensile testing machine. This rig produces slow-speed strip ironing in an open, observable apparatus which can be disassembled to allow specimen retrieval mid-ironing. The rig is used in the project to verify FEA models for both the polymer-coated material, and the DWI process itself.

Chapter **6** follows by revisiting the polymer-coated material model, and explores a novel method of simulating polymer-coated steel using a force/overclosure contact model in FEA, as opposed to meshing a polymer layer with finite elements. The FEA and ironing rig data are used in an optimisation process

to finely tune the polymer definition.

Chapter **7** details the results of a design of elements (DoE) study using the assembled FEA model for a polymer-coated food can, and explores the relationships between various parameters and their interactions during the DWI process. Two FEA DoEs are included, as well as a limited physical study from Crown.

Finally chapter **8** covers the conclusive summary of the project, and investigates the avenues of research which have been opened up by this work.

Chapter 2

Literature Review

2.1 Introduction

This project is scoped around improving the current manufacturing processes of metal cans in both steel and aluminium at Crown Packaging. Though the project will focus on the process behind two-piece cans, this review serves as a complementary background knowledge to the metal packaging industry, and covers all appropriate topics surrounding the processes used in package-manufacturing. The project itself is an investigation into the feasibility and capability of utilising a pre-coated sheet of laminated metal in the body-making process of cans, which would otherwise be coated in post-processing. As such, this review will cover characteristic behaviours of materials such as anisotropy and its effects on forming processes, as well as typical current production processes and proposed alterations in the processing chain. Whilst some material data is featured during this review, it is intended as a comparative reference to the materials which may be used in the project, and not a characterisation of materials exclusive to the can-making process or this project.

2.2 The metal packaging industry

Metal food and beverage containers are made using a variety of different methods, however the overall production line is generally similar. The main steps in creating a food or beverage can are to create the body, top and bottom, and finally an exterior coating for food-safety and decoration. Two methods have dominated can-making in recent years; cans can either be two or three-piece and this determines by which method they will be created [1].

2.2.1 Three piece cans

The three-piece can [2] is a design utilising three individual pieces of metal for the body, top and base of the can. These cans are most commonly used in the food industry, and often feature structurally ribbed surfaces which serve to both increase rigidity, as well as provide a structure that is able to withstand the pressure variations experienced during the sterilising stage.

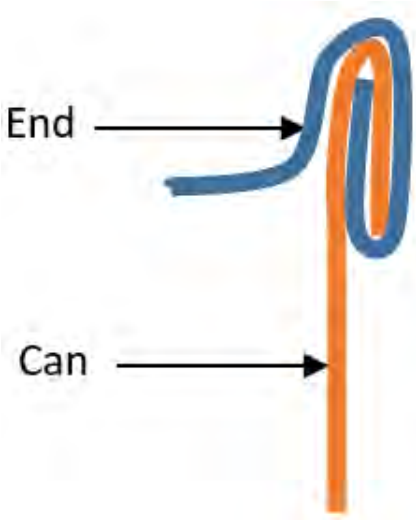

FIGURE 2.1: Double seaming.

Initially, the three-piece can starts off as a sheet of metal (often steel) cut from much larger reels. The metals used in this packaging process are coated during manufacture, to protect product contents from the metal wall (and vice versa). Foods stored within metal cans often contain high levels of acidity or alkalinity, and can corrode the metal of the can wall during sterilisation or storage if not properly protected. Protective layers can be either metallic or non-metallic. Non-metallic coatings usually take the form of a liquid lacquer which can be sprayed or rolled onto the formed sheet [3], (however a polymer coating can also be used), whereas metallic layers are usually seen in the form of non-reactive tinplate coatings [4]: which are either hot-dipped or galvanised onto the steel [5].

The processed sheet is then cut into blanks which are used in the bodymaker (the main tooling operations for creating the can). The blanks are shaped in a rolling process to create a cylindrical shell with the desired wall thickness of the can. Figure 2.2 demonstrates the process wherein the blank sheet becomes the cylindrical body [6].

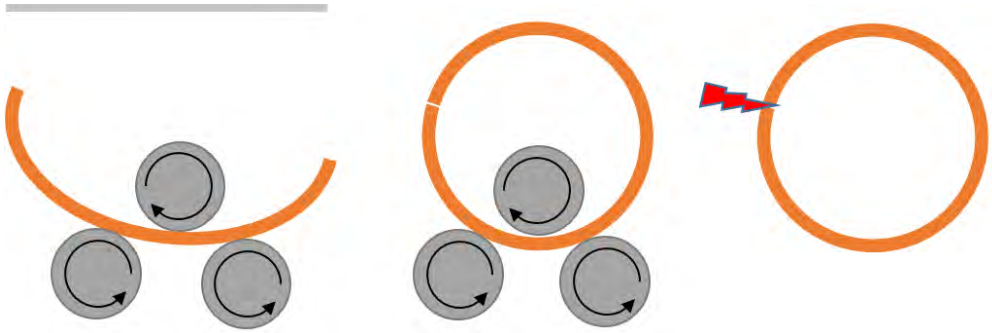

FIGURE 2.2: Three piece can rolling and welding depiction.

After rolling, the blank is sealed along its seam, usually via welding but sometimes using an adhesive, solder or cement to adhere the two edges. Structural ribs and aesthetic features can be added at this stage in order to customise the shape of the can for purpose. Finally a flange is formed on both ends of the body for use in the double seaming process illustrated in Figure 2.1, and the base of the can attached. A food-safe sealant is applied to the base during this process to ensure a hermetic seal. At this point, if a non-metallic coating is used, a final layer of spray-coated protection is applied to the inside of the can, and a baking procedure ensures full curing of the coating. The can is tested for leakage and then packed into its appropriate pallet. The 3 piece can (complete with base), is illustrated in Figure 2.7. 3 piece cans are normally seamed with one end, and then stored and shipped off to the appropriate food manufacturer, where they are filled with their contents and sealed on-site. An air pressure test is often undertaken to ensure that the seal has not been compromised at any point before shipping for retail.

2.2.2 Two piece cans

The second method of production produces a two-piece can. A two-piece can is created using an entirely different process, and utilises a series or combination of drawing, redrawing and wall ironing (DWI) metal forming processes[7]. Two piece cans similarly begin as a large coil of metal, but are then punched out into circular disks of metal (also referred to as *blanks*) and punched into cylindrical cups in the same motion (Figure 2.3).

The cups are then sent via a conveyor system to a bodymaker, where the redrawing process occurs and wall-ironing process occurs. During redrawing, the can diameter is reduced to approximately the final size, but wall thickness

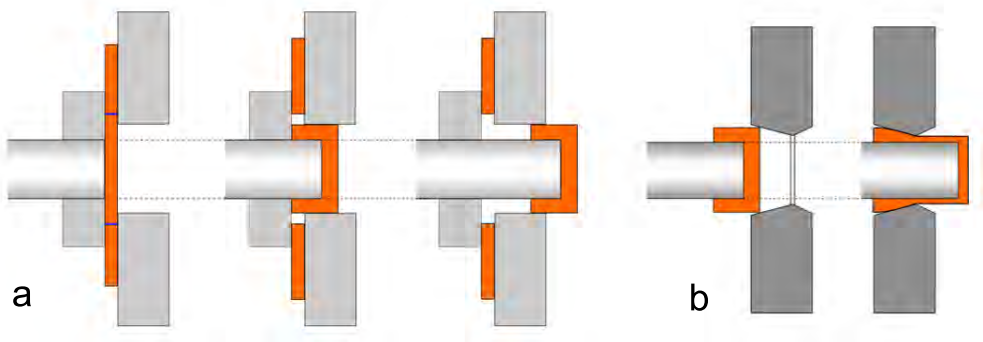

FIGURE 2.3: Depiction of a DWI process (the orientation is usually depicted vertically).

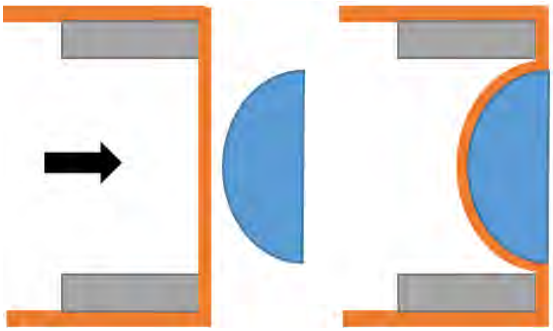

FIGURE 2.4: Depiction of a Doming process (the orientation is usually depicted vertically).

remains largely the same. Ironing involves forcing the can through a series of ring-shaped dies, reducing thickness dramatically and increasing the height of the can. Figure 2.3 shows a single step in the wall ironing process, but often multiple ironing rings are often utilised in order to reduce the per-step deformation. Between 5 and 6 cans can be manufactured per second in a single bodymaker. Ironing rings are designed to create a smooth finish on the surface of the can, and are thus kept at a regulated temperature using cooling and lubricant streams. Whilst the metal experiences dramatic adiabatic heating as a result of the deformation occurring, the process is still considered cold [8]. As such, the piece experiences the usual advantages (increased yield stress with increased strain), but also the various unwanted deformations and failures (due to uneven stress concentrations) [9], commonly associated with cold-forming processes.

After wall ironing, the base of the can is forced onto a dome. This process is done by allowing the hollow DWI punch to continue along its trajectory, forcing the can over a dome-shaped die, creating the structural dome at the base of the can. (Figure 2.4) The dome shape is inherently strong in its ability to resist

the internal pressure of carbonated liquid. Anisotropy in the mechanical properties of sheet metal, the deformation during drawing and wall ironing is not constant in all directions. As a result, the can will exhibit earing: regions where wall heights deviate from the average [10][11][12]. These *ears* must be trimmed to give uniform wall height. Due to the different requirements for food and beverage containers, the post-bodymaking processes differ. All cans must undergo a cleaning process to remove any residue or precipitate from the previous tooling processes. When the surface is completely clean, a similar printing process as before is undertaken using rollers illustrated in Figure 2.5 to print the desired design and subsequently varnish the can to preserve the print.

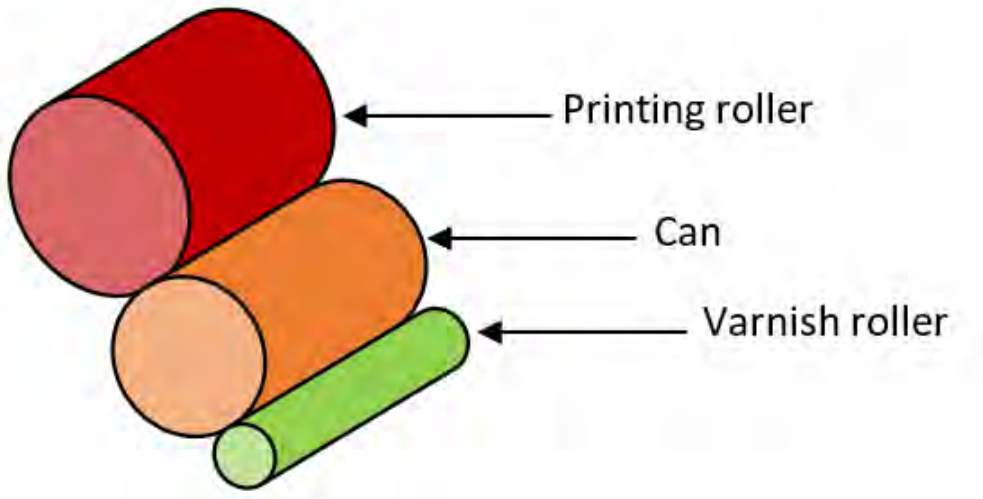

FIGURE 2.5: Depiction of a printing process.

After varnishing, the cans undergo an intense baking process to dry and set the lithography. Directly after this process, a probe is inserted into the can and the inside sprayed with a protective lacquer. As in three-piece construction the coating prevents contamination as well as reaction between the contents and the container. After spraying the can is baked once again in an oven, where the protective coating cures completely, bonding to the interior metal [13].

Beverage cans are then necked to reduce the diameter of the aperture. This is done by forcing the coated cans through a series of necking dies, which gradually reduce the diameter of the top of the cans, whilst retaining the shape of the remaining body. Finally, the necked cans are then flanged and packaged into large pallets which are then stored or shipped to their customers. As before, the cans are only fully sealed once filled.

FIGURE 2.6: Two-piece can design [14]

FIGURE 2.7: Three-piece can design [15]

2.2.3 Major differences between manufacturing routes

There are various differences between a three and two-piece construction can, and it is difficult to quantify whether or not one is preferable in an overall sense that covers technical, commercial, and environmental factors. Three-piece cans are generally stronger structurally, as the steel wall thickness used is far larger than the aluminium wall thickness often used in two-piece constructions. Three-piece cans undergo a far less dramatic deformation during forming, and appropriately hold less residual stress, whereas two-piece cans undergo extreme deformation at very high strain rates and thus suffer from residual stress build-up [16]. This residual stress and associated work-hardening explains why two piece cans are made with much greater force. Financially, the cost difference between the two methods is difficult to assess. Steel can be more expensive than Aluminium, and more difficult to form, which is why DWI processes tend to (but in no way exclusively, as this project demonstrates) use aluminium, and the steel cans tend to favour the simpler roll/welding process. Much higher forces are required to perform the DWI process on steel blanks, which can significantly increase the production costs of can-making, compared to using Aluminium. Whilst Aluminium is currently cheaper to buy as raw material, the tooling and machinery required to setup a DWI processing line is far more expensive than the roll/welding seen in three-piece cans. DWI processes are associated with an increased capital investment, but can produce cans at a much faster rate [17]. Subsequently, more packaging firms are investing in DWI and Steel is becoming more common in two-piece cans [18].

2.3 Gaps in research and market niche

Capital investments are not the only difficulty involved with a DWI process and two-piece cans. The extensive array of complex processing machinery required comes with a substantial requirement for both power and money, and serves as the most obvious target for improvement. Due to the high strain rates which are experienced by the blank during wall ironing, the tooling punch requires considerable force, speed and energy to ensure that the cupped blank is correctly ironed. The punch needs enough kinetic energy, hardness, and geometric accuracy to ensure that it repeats the same cycle on each can and doesnt compromise even the smallest tolerance in accuracy. Since the wall thickness of the final product can be as low as 100 microns [19], a small deviation in can quality could result in failure of the can during forming, known as a tear-off. Once the DWI process has been completed, the necessary lacquer must be applied in a separate step and baked to cure. This is undertaken in a separate machine, which yields its own power, chemical and water requirement.

Power requirements are not the sole potential improvement in the two-piece production line however, as arguably the largest ecological input from the two-piece system stems from the cleaning of the cans between processes. Due to the aforementioned fine tolerances required in DWI, any sediment or contamination on the tooling can create various defects: such as trapped particulate propagating a silhouette during drawing (colloquially known as worm Trails). This kind of defect occurs as a result of the metal blank being ironed between surfaces which are no longer smooth, due to a trapped contaminant [20]. An unclean blank or residual contaminants can also prevent full adhesion between the fully formed metal can and the protective non-reaction layer of lacquer which is sprayed on during the final post-processing steps. Failure of the polymer to bond results in a container which is unfit for food or beverage use (in the case of two-piece cans, beverage). Various other defects and failures can occur for similar reasons; as such it is important to rinse the metal and tooling between each process [19], which often requires the use of hazardous chemicals.

2.3.1 Project scope

Crown have identified these issues as a significant opportunity to reduce the carbon footprint and ecological impact of their two-piece can production. Many of the complexities involving the two-piece can processing system revolve around

the requirement for food-safe coatings and recent concerns about Bisphenol A, Chromium VI, and other commonly used volatile organic compounds (VOCs). Crown have decided to investigate the possibility of utilising a pre-coated sheet of metal in the DWI process. Polymer coatings act as protection against contaminants, and eliminate the post-processing involved with spraying on and curing a protective coating. Removing these issues, as well as an entire post-processing section would result in a significant decrease to the environmental impact of creating two-piece cans. This implementation sees dramatically decreased water and power requirements and no foreseeable negative effect on the functionality or recyclability of the finished can, however the process is not yet fully understood. Modelling provides engineers with this improved understanding of the process, and helps to reduce failures during manufacture.

Conceptually, the introduction of pre-coated polymer sheet metal holds many benefits over the existing processes. By purchasing pre-coated sheet the process of coating, rinsing, and baking would be shifted up the manufacturing line and become a task for the metal suppliers and not the packaging plant. Whilst this is expected to drive the price up for the metal sheet, the cost is potentially cheaper than the cost of spray-coating each individual can in a production line. Metal manufacturers are much better equipped to mass-laminate the metal coils without incurring significant cost disadvantage. In a process similar to that displayed in Figure 2.8, the sheet metal can be coated after exiting the initial rolling stage, enabling the polymer lamination before the sheet is even coiled into the packaged state used for DWI. PET is featured in this example, but not exclusively in the industry. Similarly, cooling processes can be air cooling or liquid cooling baths.

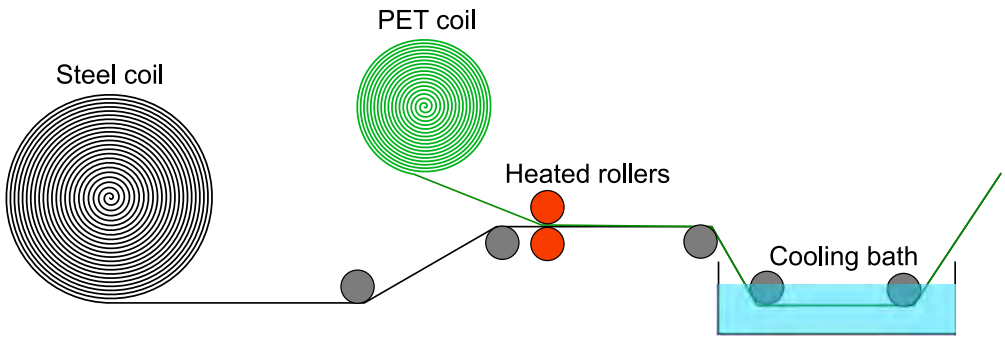

FIGURE 2.8: Depiction of the process by which steel is laminated with a food-safe polymer coating.

Figure 2.9 and Figure 2.10 demonstrate the positive differences between the

current system and the proposed improvements. Inwards-facing arrows indicate materials consumed in the process, and outwards-facing arrows indicate by-products produced. Post-processing cannot be eliminated due to quality control systems, but a significant portion can be reduced. Crowns bodymaking machinery are capable of outputting up to 6 cans per second. With the elimination of processes relating to coating, rinsing, and curing, the cost and ecological footprint of each individual can will be driven down by an according factor.

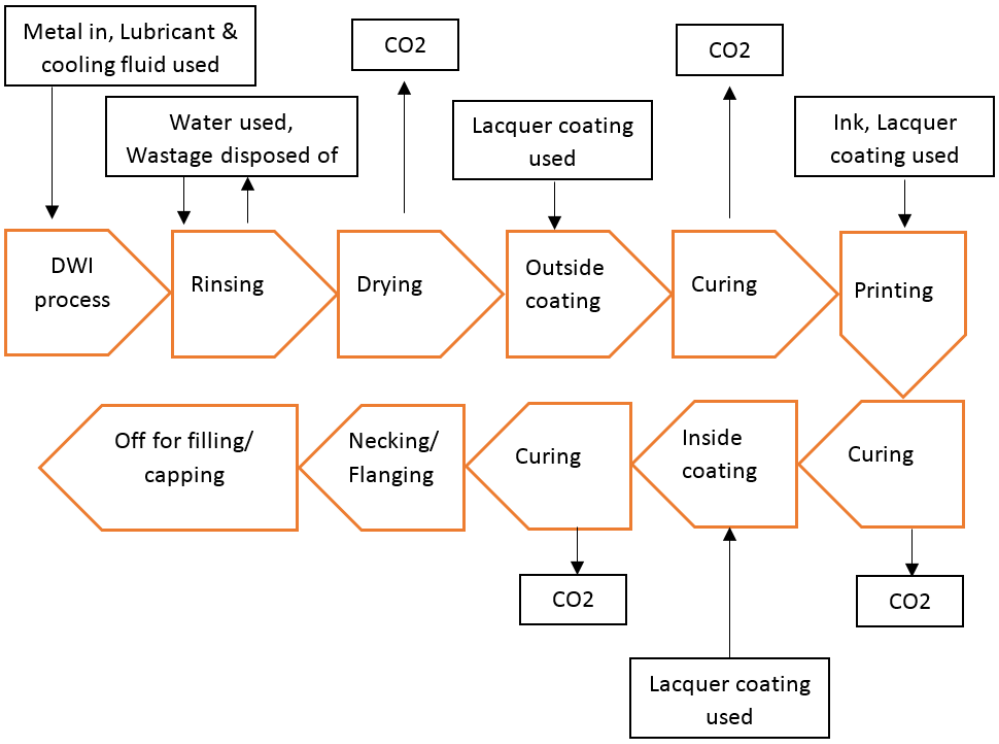

FIGURE 2.9: Flow chart of conventional two-piece can manufacture process.

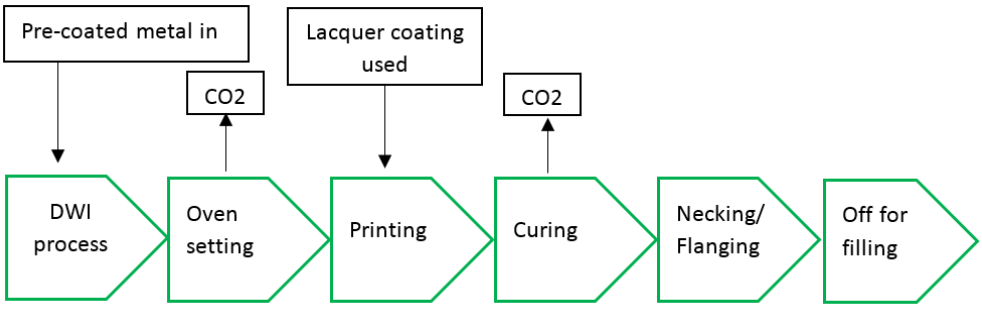

FIGURE 2.10: Flow chart of pre-laminated two-piece can manufacture process.

2.3.2 The application of Finite element Analysis in the project

In the past, the most effective way to investigate a proposed change in tooling or machinery was to physically introduce the change in a pilot manufacturing

line, and monitor the output of the physical product. Many industries still perform the majority of their testing in this way. Software utilising FEA has grown more popular as computational technology has increased, and the advantages of a computer simulated model have become increasingly apparent. Whilst the advantages of a physical test trial are undeniable for physical observation, an FEA solution consumes no raw materials and requires only program or coding changes to explore alternative tooling and process parameters. A model can be constructed in various manners and parameterised in such a way that a full factorial of production trials with various tooling, speeds and forces can be represented and input using a series of text files. These text files can then be run as a FEA simulation at any point and changes in parameters can be done readily. Additionally, an FEA simulation poses no danger to operators and can be left unmanned and unobserved safely. This advanced process allows a simulation driven design where any design decision is made with a clear knowledge and understanding of how it will impact product performance. This makes FEA very advantageous to this project, being in essence a very experimental investigation, and instead of having to build separate experimental processing rigs for each trial where a major factor is changed (e.g. Ironing ring diameter), a separate simulation can be adapted, taking no more than a few minutes to adjust such a parameter.

Advantages of FEA

Convenience aside, some of the major advantages to utilising an FEA approach lie in the ability to visualise, illustrate, and probe results. FEA simulations are not limited to measuring resulting geometry, they are just as capable simulating internal stresses, strains, deformations, reaction forces and almost any engineering concept which may be applicable to the simulation. Conventionally, when physically testing a specimen there are a variety of methods in which a variable like strain may be recorded or monitored. A strain gauge (depicted in Figure 2.11 is the most common method of monitoring engineering strain. Strain gauges are parallel arrangements of wire, with an insulated backing. Electrical current is passed through the wire and the conductivity recorded. When adhered to a specimen subject to a force, the strain gauge stretches or deforms with the specimen and the resulting change in conductivity is recorded and processed as a measure of strain.

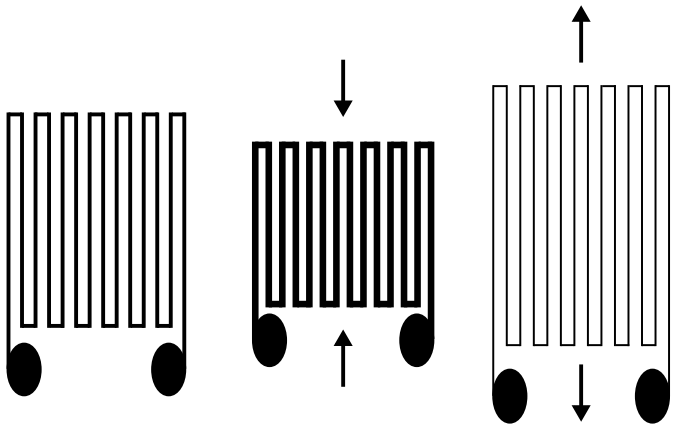

FIGURE 2.11: Depiction of a strain gauge at rest, compressed, and in tension.

Strain gauges are reliable when working in one direction. If strain needs to be measured in multiple directions, a rosette strain gauge (pictured in Figure 2.12) may be used to better capture multiple strain directions. A Rosette arrangement of strain gauges, all linked via the same computing or data-logging system, allows the metrology of surface strain in multiple different angles. Calculations can be done to derive the triaxial components of strain in the material [21]. The negative aspects of using a strain gauge are the limitations associated with surface adhesion. It is very challenging to use a strain gauge to determine strain within the cross-section of a specimen. If stress concentrators exist within the specimen, a strain gauge will not be able to identify them, as the gauge works only on surface deflection. An equal problem with strain gauges resides in the physicality of the gauge itself. It is extremely difficult to apply a strain gauge into environments such as a bodymaker. Naturally, any product present between the punch and wall ironing rings could be destroyed, or otherwise negatively impact the behaviour of the process and the can (see Figure 2.13). Any data gathered would be useless and the final product largely unusable.

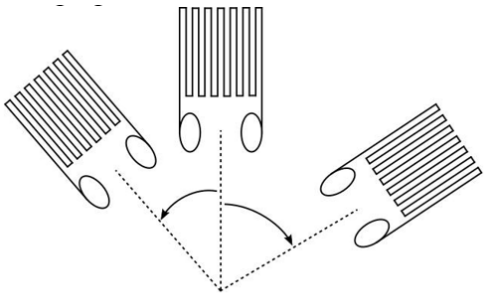

FIGURE 2.12: Depiction of a rosette strain gauge arrangement. Angles are chosen at time of fixture but typically 45 degree increments are used

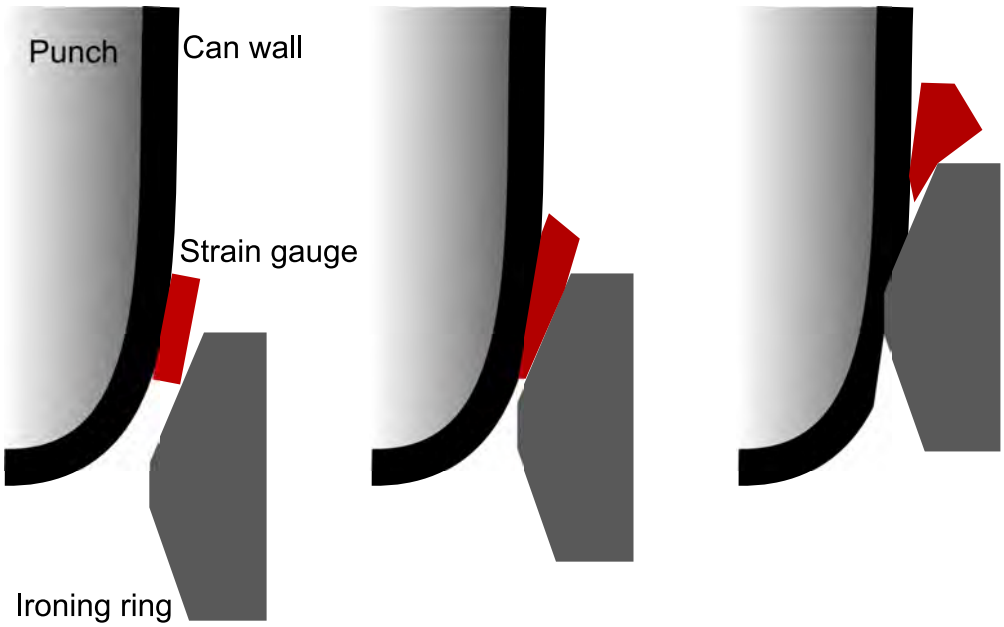

FIGURE 2.13: Issues using strain gauges with drawing and ironing processes

Strain gauges are not the only equipment with limitations to consider. Any physical piece of apparatus will require attachment to the system in some way. As mentioned, this attachment becomes an issue when attempting annular processes such as wall ironing. In this sense very little recording equipment is suitable for the task of directly monitoring a can bodymaking process. Generally, the most fundamental issues with physical testing revolve around the inability (or limited ability) to accurately measure engineering variables across a test specimen. This issue is not necessarily centred around the cross-sectional area (which cannot be seen), many problems arise when attempting to measure surface interactions such as displacement. Extensometers, whilst simple and often effective, run into issues when performing on specimens which are of a particularly small size or flexible structure. An alternative approach uses DIC [22] to monitor the movement of a speckled pattern which has been marked on the surface of the specimen. Even such advanced technology can fall into error however, as the process is limited by calibration and preparation.

FEA Functionality

FEA utilises a mesh of *finite elements* constructed from grids of nodes [23]. Complex calculations can be performed on each element by interpolating and integrating between these nodes, constructing a larger picture of the required model. An example of a mesh can be seen in Figure 2.14. An FEA uses these

elements to create a mesh for any deformable body, and can apply material behaviour such as density or stiffness. Abaqus utilises a Newton-Raphson method [24], [25] to integrate the approximate curvature of any model input. This effect is hugely advantageous, as it allows the simulation to model and record the engineering variables in places which cannot be reached or interacted with in the real world. The result of this is the ability to measure variables such as the reactionary hoop force within a wall ironing ring, or the strain experienced on a cross-section of a can wall. Any data calculated can be retrieved from any part of the meshed model, allowing the inspection of failure modes such as wrinkling and crack propagation. The different values for engineering variables can be visualised in a meaningful and easily interpreted manner during each time step of the simulation. This allows the identification of not only the failures experienced, but also onset and propagation of these failures. Using this information it is easier identified which variables require change as well as when in the process the change should be introduced. Figure 2.14 demonstrates the application of the finite element method on a drawn blank. The stress distribution is allowed to spread through the elements using integration points between nodes. This is effectively similar to simply using more nodes, but is less computationally expensive. FEA has been utilised for an expansive variety of applications and the canmaking industry is no exception. Various processes from cupping to curing are commonly modelled using FEA when a stochastic approach is required, or specific data is required about the deformation or stress/strain data during the process [26][27][28]. Canmaking specifically poses an extra set of challenges, as the high-speed forming processes undertaken during bodymaking produce large-scale permanent deformation throughout the can. The magnitude of both speed and deformation provide further challenges for metrology using physical experimental research, and thus the industry benefits even more so from the modelling approach.

2.3.3 Anisotropy in metals

Isotropy is the property of a material to be directionally independent - applying the same material behaviour in all directions. Conversely, anisotropy describes a material which behaves different depending on the direction of manipulation. A number of factors are responsible for anisotropy in different materials, however in the situation of sheet metal (as used in a standard DWI process),

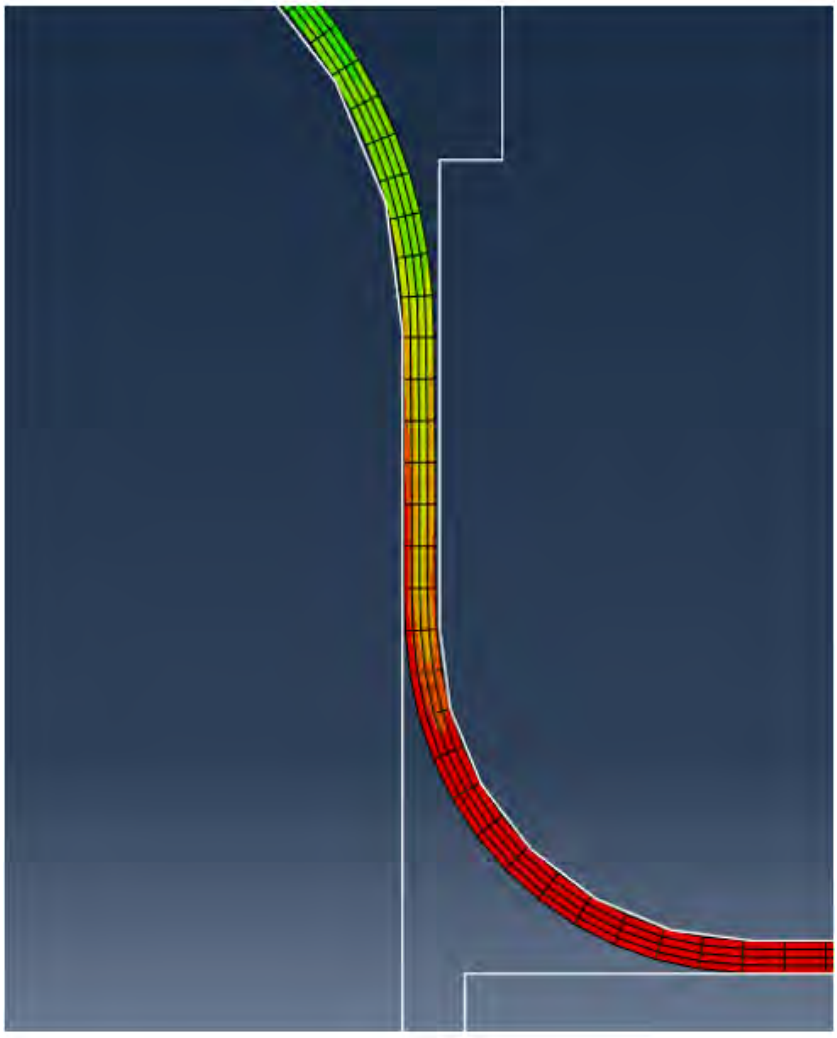

FIGURE 2.14: Abaqus simulation of axisymmetric drawing model after 0.025 seconds. The colours indicate the stress distribution across the blank.

the main contributing factor is the oriented grain structure of the metals during the rolling processes of sheet metal manufacture[29]. Notably in hot rolling processes, the high energy state during deformation drives nucleation of new low-energy grains, which is responsible for fewer defects in the metal compared to cold rolling[30]. A metallic *grain structure* describes the separate entities of nucleation caused by the solidification of a liquid metal. To fully understand the characteristics of certain grains and their corresponding effects, it is necessary to look further back in the journey of the metal which will be used in the DWI process. The flow diagram in Figure 2.15 demonstrates the journey of a standard rolled coil of metal.

During *Melting*, a combination of desired metals and additives are heated in a crucible until they become one molten alloy. This molten alloy is then cast

FIGURE 2.15: Demonstration of the process by which a metal sheet is manufactured from a slab [31]

into a movable chunk of metal known as an ingot, or in the rolling industry a slab. These slabs are then dipped into a vat containing a cocktail of chemicals and acids, which cleans the surface of any unwanted oxidation or particulate . At this point in the metals journey, these slabs can be shipped off to different manufacturing firms: who can tool-forge, heat, or melt them according to their own requirements. If metal sheet is required however, the slab is often moved along the metal processing facility to be rolled between a series of large cylindrical rollers, which slowly decrease the thickness and increase the length. This process can be done hot or cold depending on the characteristics desired, and can include any number of pickling stages for surfacing effects. A hot rolled sheet allows grains to shift and reform, as the rolling occurs above recrystallisation temperature. This minimises residual stress but also minimises any work-hardening. Conversely, cold rolling forces the existing grains to elongate and dislocate as they are force through the rollers, which increases grain length and work-hardening effects. In the can-making situation, the metal is cold rolled and work-hardened: giving a harder metal as a result [32]. Figure 2.16 depicts the (exaggerated) effects on grain structure when comparing hot and cold rolling. The effects of this work-hardening can be significantly reduced by undertaking an annealing process after the cold-rolling has occurred. Annealing is treatment which involves heating the worked metal up beyond recrystallisation temperature (usually beyond 600 °C) and maintaining this temperature for a period of time, before employing various methods of cooling. This process allows recovery recrystallisation to occur - suppressing the dislocations which are responsible for the hardening [33].

2.3.4 Grain formation and relevance

Taking a more detailed look at the process allows a better understanding of anisotropy. During the initial pouring stage, as the molten metal hits the ingot mould and begins to solidify, nuclei of dendritic growths appear along surface of metal as it contacts the (much colder) mould [35]. As the molten liquid

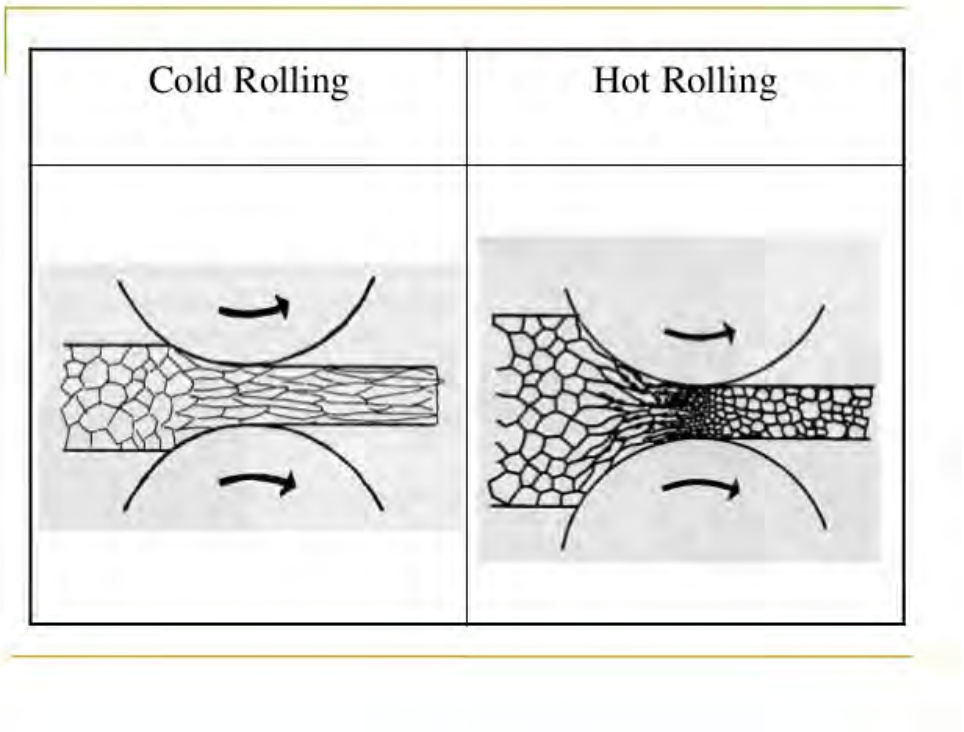

FIGURE 2.16: Depiction of hot and cold rolling processes. Note the differences in grain structure by the end of the process. [34].

loses its bulk energy (to the mould or the ambient atmosphere) these nuclei propagate and grow into small pockets of solid metal known as grains. As the metal cools completely, these grains eventually meet one another and form grain boundaries at the connection interface. Due to the nature of the molecular bonds the metal within the grain is far mechanically stronger than the grain boundary itself, and subsequently causes a fault line along each boundary [36]. Depending on the alignment and distribution, grains can dramatically alter the mechanical properties of a metal. Generally, at lower temperatures there is little difference in strength between the area of a grain and its boundary, however at higher temperatures (similar to ones experienced as a result of high strain rates), the differences in strength become far more apparent: as grain boundaries demonstrate a far inferior strength [37].

Rolling the metal ingot creates elongated grains in the metal sheet as any equiaxed grains are flattened and stretched during the process [38]. At higher temperatures, grains are stronger and better resist fracture within their own area than along their boundaries, therefore a grid of long, thin grains will perform far better when force is applied parallel to their length, but far worse when applied

perpendicular [39]. At lower temperatures the the yield properties and elongation are slightly different. This is an important characteristic to consider when cold-forming the metal further or generating heat.

The DWI process is advantageous when processing metals which have undergone heavy grain transformation. Since the punch applies a force normal to the plane of the rolled sheet (and not specifically perpendicular to the elongated grain boundaries), there is a minimised focus of stress in any particular direction. Instead, the deformation occurs universally and radially around the punch, ensuring that no particular direction of grains is more heavily stressed, beyond any inherent weakness along a grain boundary. Figure 2.17 illustrates the universal punching effect upon grain structures.

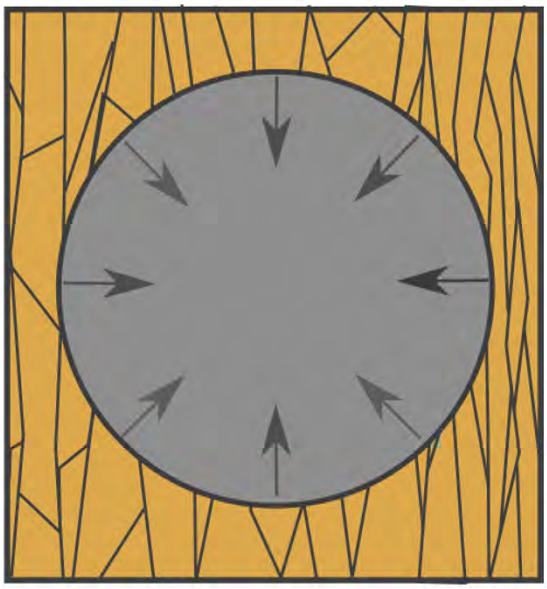

FIGURE 2.17: Illustration of a typical rolled grain structure and the direction of punching force disrupting the metal

2.4 Application of Finite Element Analysis

The FEA approach is capable of simulating a vast amount of different problems and arrangements, limited only by the availability of data and method when constructing the model. During the models creation, a number of decisions have to be undertaken in order to refine exactly the kind of simulative output desired. These choices include the number of dimensions and the element types, which will be discussed later on in this chapter. This project focuses

on the application of commercial available FEA software *Abaqus*, though most FEA software are based on the same underlying principles.

2.4.1 Element Family

Elements in Abaqus belong to a *family* which indicates the approximate behaviour and characteristics of the element. Each of these families holds unique advantages and disadvantages during simulation; these can manifest in the form of computational time or computation accuracy. It is important to choose the correct element when modelling a simulation, as failing to do so may result in skewed results, massive error, or at the worst majorly increased time taken to simulate. Some of the most commonly used elements are illustrated in Figure 2.18. The first letter (or letters) featured in an elements name are indicative of the element family to which it belongs. For example, an *S4R* element indicates a shell element, *CAX4R* indicates a continuum element [24]. Only a handful of element types are applicable to each individual modelling solution. For the DWI model used in this course, a handful of elements are major applicants Continuum, Shell, Rigid and Connector elements, which can again be seen in Figure 2.18.

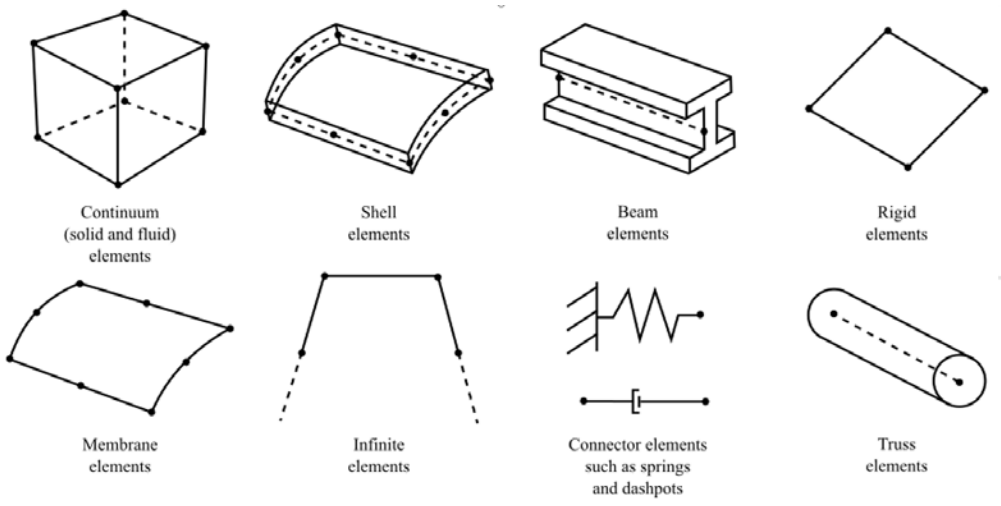

FIGURE 2.18: Element families used in abaqus [24]

Continuum elements are tetrahedrons or hexahedrons which contain nodes at each corner, and interpolation points often throughout the element (explained later). Continuum elements are easily the most versatile of the group, as they can be assigned to almost any geometry in any model. They are generally the most computationally expensive elements of each order, using the most nodes

and integration points, and are thus often substituted for less expensive elements when possible. Continuum elements are not always more expensive than other elements however, as there are many permutations of continuum element and the number of nodes depends on many factors such as quadratic or linear intergration approach. Continuum elements come in various varieties, including elements with reduced integration and anti-hourglassing characteristics [40]. Continuum elements can only translate in the three axes, and cannot rotate.

Shell elements are similar to continuum elements in their application, except that a shell element generally models a small-thickness geometry. This means that shell elements are extremely applicable for applications loading in one or two planes, but unsuitable for most applications requiring compression or extension through the thickness of the element. Many shell elements house integration points throughout a virtual thickness of the shell. These are more applicable to compression and extension along the thickness, but not as much as continuum elements. Shell elements are much cheaper computationally as they are 2 dimensional elements in 3 dimensional space; this makes them preferable substitutes whenever the thickness loading can be ignored [41]. Shell elements can translate in all three axis, and also rotate in all three rotationally axes.

Rigid elements do not perform the same functions as deformable elements in FEA. A rigid element can be used as a contact surface but suffers from no deformation or engineering strain in any plane or direction. Instead rigid elements are used to simulate surfaces or geometries which have an effectively infinite hardness and strength when compared to the deformable geometry - or where the deformation behaviour of a part is irrelevant. In this project rigid elements are used to simulate tooling and die surfaces minute degradation during duty cycles is negligible during each simulation and can thus be safely omitted.

Finally, connector elements are used to simulate a spring, dashpot, or generally any other inclusion used for damping or suspending. Connector elements are mostly used for applications where connectors exist in the real model, however they can be utilised as gap-fillers to ensure that stiffness matrices are balanced in certain models and prevent large-scale deformations which can impede the simulation. Springs and dashpots use a characteristic stiffness constant instead of material behaviour models, and can act and move along any axis specified.

2.4.2 Degrees of freedom (DOFs)

The DOF which an element can experience are a major variable used in Abaqus calculations. DOFs are experienced by the element at each node (as follows with all engineering variables). During stress/displacement simulation, the DOFs are experienced as translations and rotations about the principle axes, and during heat transfer simulations they are experienced as temperatures [24].

2.4.3 Nodes and order of interpolation

As mentioned previously, elements themselves do not technically exist as computational geometric identities. Instead these elements are representing a series of nodal points (nodes) and the interpolated lines between them (*sides*), depending on the element type [42]. This means that only the nodes of the elements themselves measure any displacements and at any other point in the element, Abaqus will calculate the variables by interpolating these nodal displacements [24]. An order of interpolation is determined by the number of nodes in the element; elements of only a few nodes (usually located at corners) utilise linear interpolation between the straight lines and are thus referred to as first order elements. Second order elements utilise additional nodes spanning along their midpoints or sides and calculate using quadratic interpolation. The number of elements used are clearly identified in the element name: usually the final number indicates the number of nodes in each element. [43].

2.4.4 Integration points

Though interpolation calculates the behaviour throughout each side or length of an element, it does not accommodate for the volume directly between all nodes. Instead Abaqus utilises numerical methods to integrate any specified variables throughout the volume of each element. This calculative approach allows complete customisation in material behaviour. Using Gaussian quadrature [44] for most elements, Abaqus is able to determine the response at each and every integration point in an element (the number of which differs between elements). Continuum elements can utilise full or reduced integration procedures which significantly affects both the accuracy and computational time for a given problem. Figure 2.19 demonstrates how elements are named according to their properties.

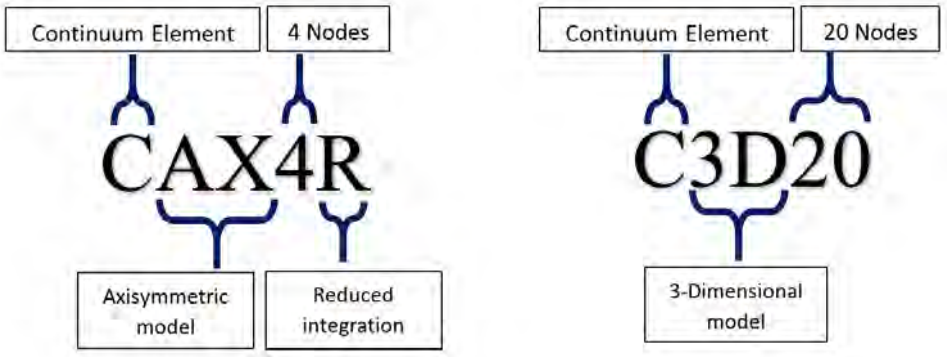

FIGURE 2.19: A breakdown of the notation used for Abaqus elements

2.4.5 Modelling formats

Abaqus can model a problem in many formats, most simply separated into the number of dimensions modelled. 1D, 2D, 3D, and axisymmetric (or 2½D) are the major dissections for a model format (and corresponding element types) in Abaqus. These dimensional models alter the available degrees of freedom for a model, and where symmetry exists in a model certain DOFs may be ignored. A 1 dimensional model will have degrees of freedom only in the plane specified (usually X or Y), a 2 dimensional model will have both X and Y translations and rotations, and a fully 3 dimensional model will allow translation and rotation in all X, Y, and Z axes. Axisymmetric modelling proposes a slightly different solution, and is unique in its application. An axisymmetric model conveys a specified slice of an annular 3D model: the variables of which are applied per radian and calculated as though it were a 1 radian slice of a perfectly rotationally-symmetrical 3D geometry [45]. This makes axisymmetric geometries suitable only for applications where the original model has rotational symmetry. Figure 2.20 and 2.21 demonstrate the differences between a 3D and axisymmetric model. Both model types have applications for the DWI process; being a rotationally symmetric process. Whilst axisymmetric modelling is a an order of magnitude computationally cheaper and faster than 3D modelling, the latter is necessary to accurately consider variations in behaviour around the central axis of the metal annulus, and its appropriate responses during processing. 3D modelling of some kind can never be neglected completely if directional effects need to be considered.

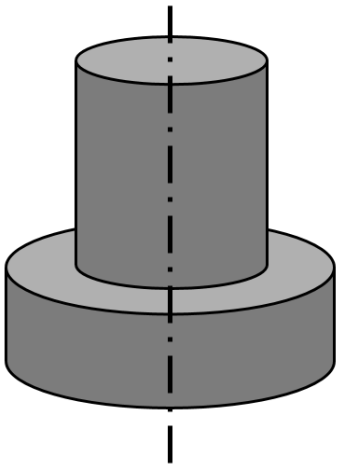

FIGURE 2.20: Example of a 3D model with an axis of rotational symmetry (or centreline) displayed in the centre

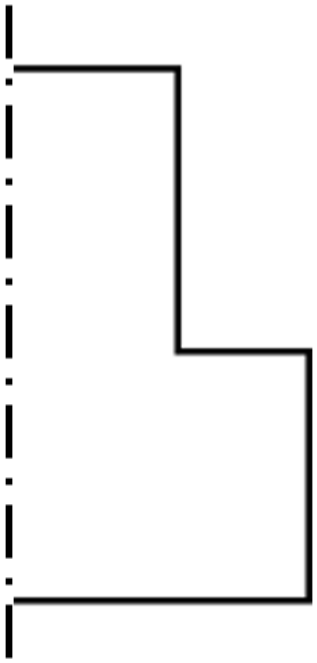

FIGURE 2.21: Example of an axisymmetric model. The centreline can be seen on the right, demonstrating the *slice* effect

2.4.6 Standard and Explicit time integration solvers

Modelling with Abaqus concerns two major distinctions for the solver; models can either be solved in *Standard* (also known as Implicit), or *Explicit* (also known as Dynamic explicit). The primary difference between the two solvers is how and when the Jacobian stiffness matrices of the model are executed and solved. For *standard* simulations the equations are solved for each time step and must iterate to equilibrium before the step progresses for this reason Abaqus standard tends to be more precise, but cannot adequately handle excessively non-linear geometry, rapid strain-rates, or dynamic movement. In *explicit* simulations, the equations are solved based on the history of the previous time step, and are solved without iteration. This enables the solvers to better assess rapidly-changing geometries, but does so at the expense of accuracy: explicit simulations can often diverge from the actual solution, and two identical simulations can calculate differing results. Implicit solvers are thus considered unconditionally stable whilst explicit solvers are dependent on a sufficiently small time step to minimise the risk of divergence from previous time steps. Minimising the time step can result in large numbers of attempts between particularly difficult solution steps: causing the dramatically increased time requirement for

explicit solvers [46]. Implicit simulation is always preferred for slow or static loading, but explicit is better suited for the rapid forming processes found in DWI, assuming the time step can be small enough. Explicit simulations also account for inertia and mass inputs, and so explicit is necessary to model resonance or vibration in a system.

2.4.7 Contact Modelling

Abaqus models contact in one of two fundamental methods:

Node-to-surface contact discretisation.

In node-to-surface contact, each node on the *slave* surfaces interacts with a projected surface on the opposing *master* surface. Each contact moment involves a single slave node and multiple master nodes in the proximity, through which values of exact contact are interpolated. Slave nodes cannot penetrate the master surface, however the master surface may penetrate the slave surface. Node to surface contact is necessary for modelling sharp surface interaction such as penetration, since the penetrating nodes are calculated alone. Figure 2.22 shows the node-to-surface contact method and resulting penetration during different meshes.

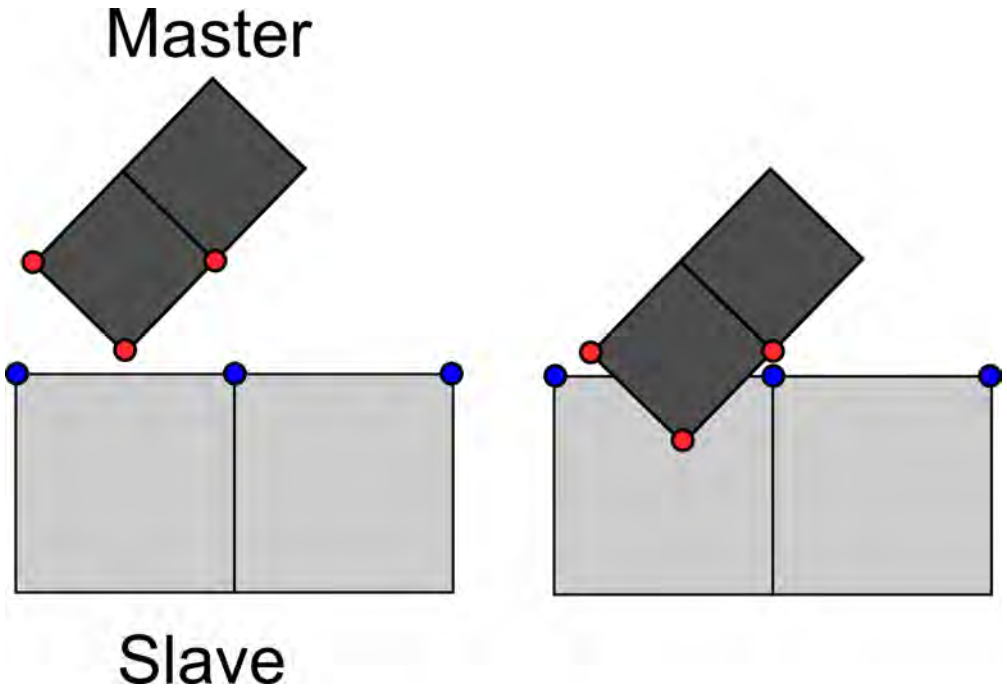

FIGURE 2.22: Node to surface contact, demonstrating penetration of the slave surface by the master surface.

Surface-to-surface contact discretisation.

In *surface to surface contact* contact, the slave and master surfaces are considered in the same format. Contact moments consider individual slave nodes, but in addition also consider adjacent slave nodes for an average calculation of contact. Some penetration is possible at individual nodes, but large penetrations of master into slave surfaces do not occur. Surface-to-surface contact is more accurate when surfaces geometry is well represented, and is less sensitive to master/slave designation[47]. Figure 2.23 shows the surface-to-surface contact method and resulting lack of penetration.

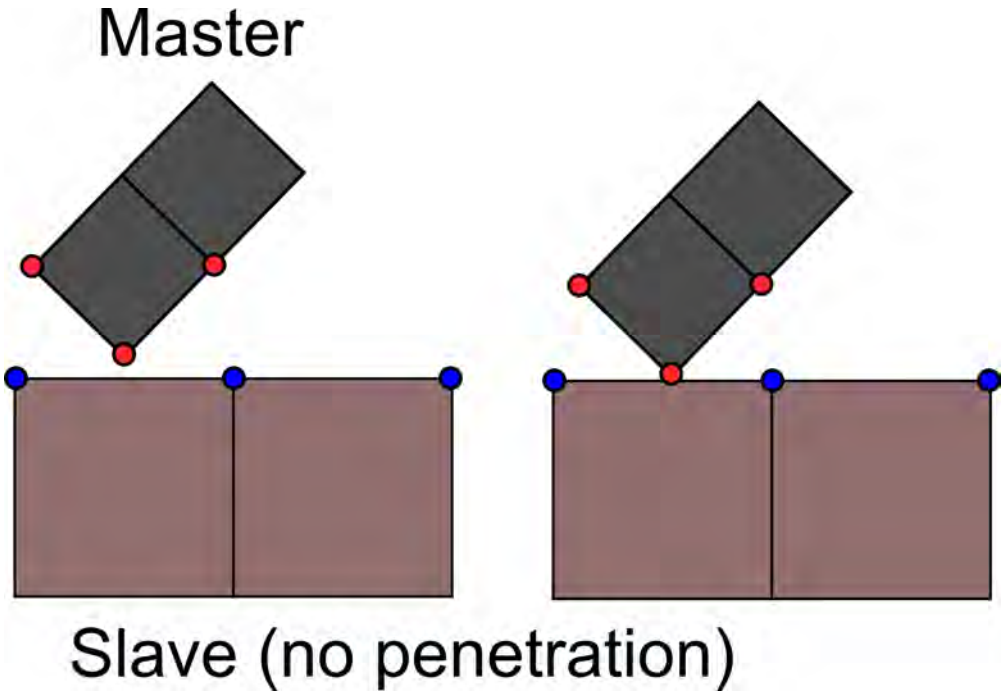

FIGURE 2.23: Surface to surface contact, showing no penetration between master and slave surfaces, due to average contact calculations between surrounding nodes.

Contact can be tracked in either*finite-sliding* or *small-sliding* approaches. Finite-sliding allows contact sliding, rotation, and separation. Small-sliding assumes that movement between surfaces is minimal, but is computationally faster.

In addition, there is also two difference enforcements of contact to choose from when simulation in explicit solvers: *kinematic* or *penalty* contact enforcements. Kinematic or *hard contact* is a method which advances the kinematic state of the model into conditions calculated pre-time-step, and then calculates the penetration and movement of surfaces for a given time increment (without altering the stable time increment). Opposing forces are derived to ensure no penetration between surfaces and applied to each necessary surface. For this reason kinematic contact can be faster, but once the time step has completed and the correct

kinematic state is achieved, it is possible for some penetration to occur due to differences between the predicted effect and analysed effect. Kinematic contact conserves momentum during contact by absorbing energy upon impact. For this reason it is not preferable when contact forces and effects are being measured.

Penalty contact enforces fewer contact constraints on the model, but instead enforces a penalty stiffness to the contacting surfaces, with an automatically calculated spring constant. This spring effect allows the conservation of energy during contact, but can influence the stable time increment, slowing down the computational step. Due to the ability of penalty contact to conserve impact energy, it is preferable when modelling rigid surfaces [48].

For this project, all explicit simulations will be modelling surface-to-surface, finite-sliding contact using penalty enforcement to account for the high-speed impact between tooling dies and the can during forming.

2.4.8 Layer Modelling

One of the most unique aspects of this project is the intent to model the fully bonded pre-laminated metal sheet during the DWI and full forming processes. Whilst usually a complicated task, Abaqus is able to model full bonded contact between two materials in a multitude of different methods.

Modelling a blank with the final resulting thickness of a pre-laminated piece allows a partition to be created along the known thickness of the polymer layer away from the geometric surface. This partition allows multiple sections to be assigned throughout the single model geometry, and as such multiple material properties to be applied [49]. This means that Abaqus will model a single piece as though it were constructed from multiple pieces with shared nodes (each with their corresponding mechanical or thermal properties), joined at the partition line. The issue with this method is the inability to specify a contact bond behaviour. Abaqus will model this solution as though the two sections are inseparable which makes the solution suitable for problems investigating different deformation or strain experiences during the process, but unsuitable for any application demonstrating delamination between the polymer coating and the metal substrate, or *peel-off* as a primary failure mode.

Additionally Abaqus can utilise a contact interaction for which a specific pair of surfaces can be assigned a specific behaviour. This method is extremely useful for the lamination application; contact strength can be modelled in such a way that the resulting solution will accurately portray any delamination or cracking suffered as a result of the DWI process [50]. This function is extremely useful for later investigative models, however it is once again computationally expensive, so partition methods are usually more suitable.

Investigating contact modelling using the most effective and appropriate methods is a major part of this project. Since the unique hook is the layering of polymer coating, it is important that this layer can be adequately modelled in a realistic and meaningful way which will enable an accurate representation of the real-world processing. It is likely that various mechanical tests will need to be undertaken in order to completely validate any contact models, along with the failure modes which flag up as problematic during simulation. Discrepancy between simulative and testing behaviour highlight a need for more refined simulations.

2.4.9 Limitations of FEA

Finite element analysis is not without limitations. An FEA model relies on empirical data in order to be able to accurately reflect a process or material. Any material used in an FEA simulation must be characterised according to the simulation parameters. For example if damage is to be modelled, a damage criterion must be numerically specified with accurate data. FEA is not an exhaustive approach to process investigation, and to have confidence in modelling results some kind of validation must be performed which demonstrates a favourable comparison between the simulation results and real experimental or trial results. Validation is often done on simple models in order to verify individual methods against appropriate specimen testing, and then more complex models can combine verified methods without the requirement for complex validation.

2.4.10 Isight and automation

Simulia Isight is a software automation package which allows various cross-disciplinary models and applications to work together in a single process. During this project, Isight is frequently used as a means of optimising Abaqus models via a method of measuring model outputs in order to inspire future model

inputs, in a loop of FEA runs. As an optimiser, Isight effectively substitutes results from an FEA run into a feedback loop of generated input files, in order to slowly converge results towards a desired point.

Isight is also capable of creating a Design of Experiments (DoE) study, mapping out an unknown design space using a variety of numerical methods. Creating a table of unique values for multiple independent variables in the FEA run, the DoE can be used to efficiently cover a large array of unknown parameter combinations. Ultimately these results can be used in a response surface method calculation, which allows accurate prediction regarding the relationships between independent and dependent variables, as well as interactions between multiple independent variables. This method is also utilised in this thesis.

2.5 Material data and properties

The two main materials used in food and beverage can production are Steel and Aluminium. The project will be focusing on TH330 steel and a range of 5000 series Aluminium: both materials which see global use in can body-making. Both Aluminium and Steel have isomers with a face-centred cubic (FCC) allotropic forms, whereas Steel also has Isomers with a body-centred cubic (BCC) allotropic form, and subsequently higher strength properties. Figures 2.24 and Figure 2.25, picture the differences in structure between the BCC and FCC forms.

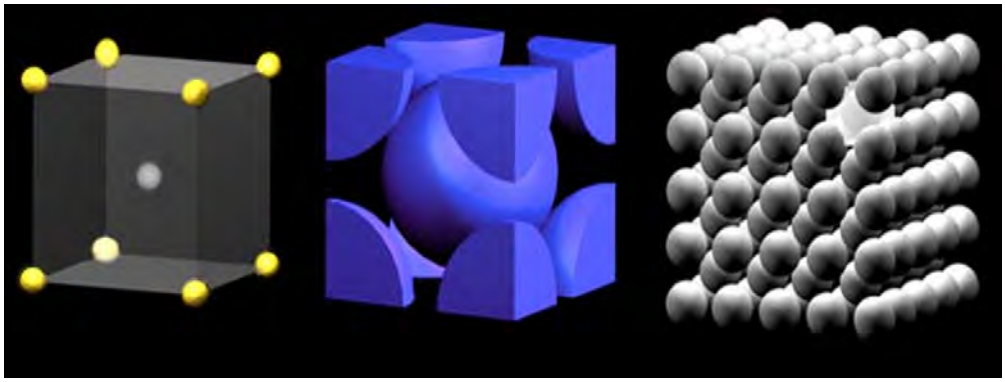

FIGURE 2.24: Example of a body centre cubic allotropic form [51].

Steel metallurgy is more complex than aluminium, and exists in many forms

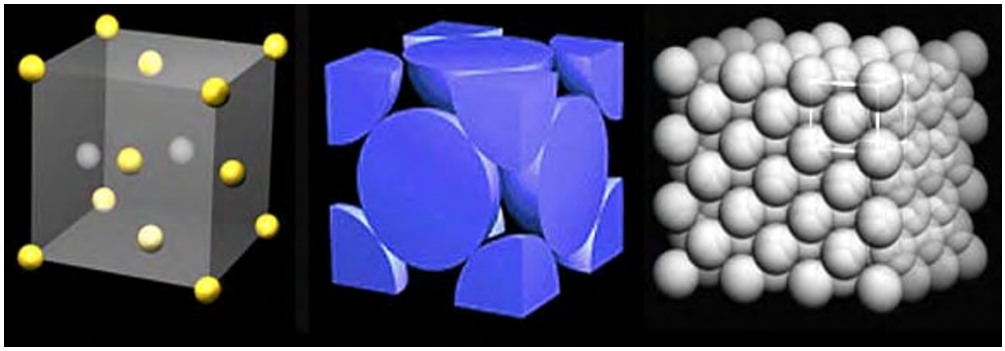

FIGURE 2.25: Example of a face centre cubic allotropic form [51].

depending on how the steel was quenched during manufacture and the inclusion fraction of carbon. There are three individual phases of steel - cementite, austenite, ferrite. Martensite, whilst not a phase, is noted as a specific microstructure within the ferritic phase. The phases of steel and their dependency on temperature and carbon inclusion can be seen in figure 2.26. Low-carbon steels like TH330 are characterised by martensitic inclusions in a ferritic matrix: which provide a combination of ductility and strength due to a high rate of work-hardening during initial plastic deformation [52], making it a very suitable material for the DWI manufacturing process.

Both of the materials which stand to see use in the project are processed by cold-rolling ingots into coils. This cold rolling, as discussed previously, allows for a work-hardened material. This characteristic is extremely useful for use in metal packaging, as it allows for a tougher and stronger material despite an extremely thin wall thickness application [32]. Figures 2.27 through 2.29 graphically illustrate the mechanical behaviour of alloys Steel TH330, and Aluminium AA5352.

Steel suffers less directional effects than aluminium, and the stress/strain curves are more closely clustered than in the aluminium. The difference in stress between orientations (the point at which the lines visibly split) begins far earlier in the steel, at around 0.025% plastic strain, and this difference remains constant for the rest of the curve. Aluminium on the other hand, begins to split at around 0.01% strain, and this difference slowly increases as the strain progresses. From this data anisotropic behaviour is far more prevalent in aluminium at higher plastic strains, and less so for steel. The maximum difference in proof stress between orientations at 25% proof stress is approximately 22MPa for AA5352, and 10MPa for TH330. Given the cylindrical nature of the DWI process, there is no use in orientating the blank with or against the rolling direction, as forming will occur both with and against the elongated grains. For this reason, the data

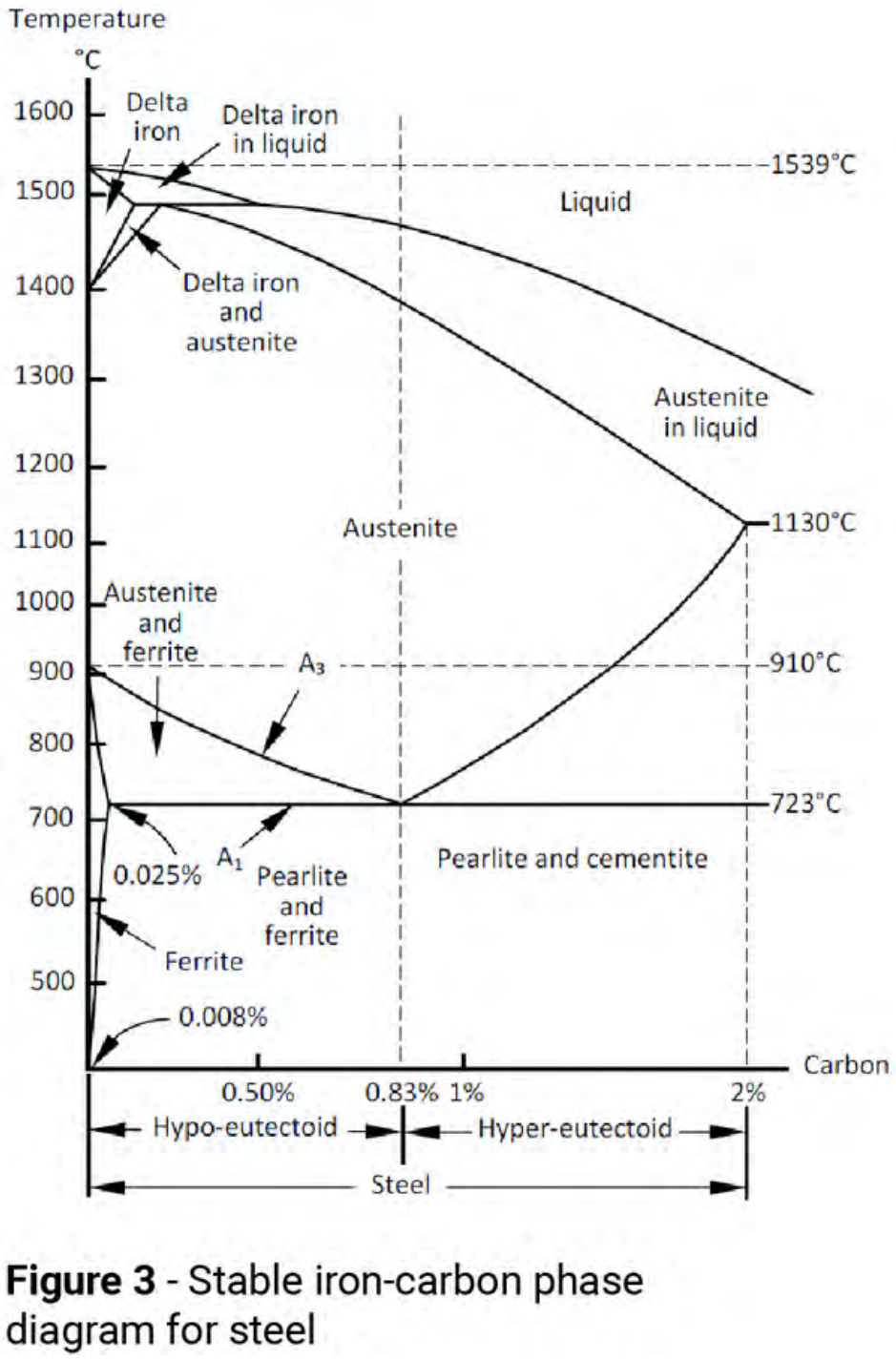

FIGURE 2.26: Stable iron-carbon phase diagram for steel [53].

demonstrates an advantage of using steel compared to Aluminium.

The mechanical behaviour of polymers are much different than metals. Unlike the ionic lattice strucutre of metals, polymers are structured by long molecular chains, held together with Van der Waals forces. This structure is not as strong

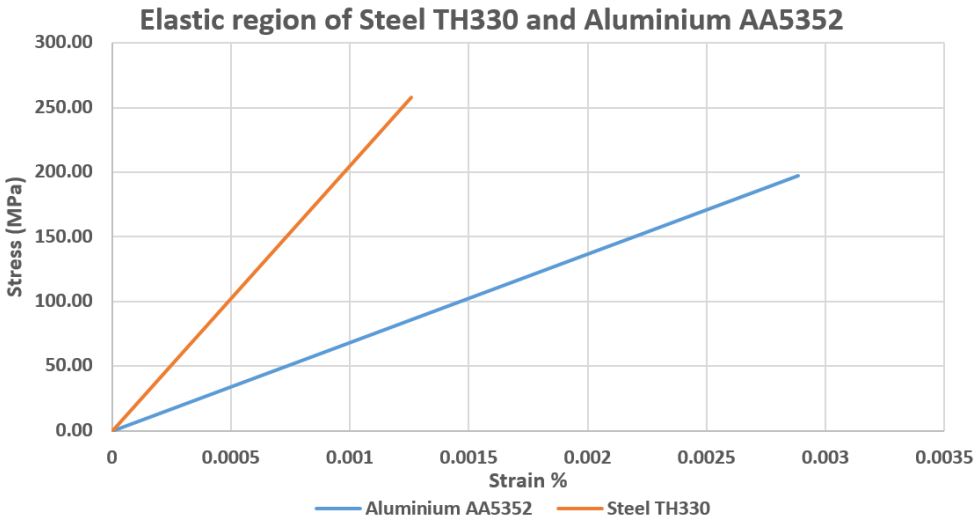

FIGURE 2.27: Graphical comparison between average stress and strains in the elastic region, for various orientations of TH330 Steel and AA5352 Aluminium found in figure 2.28 and 2.29

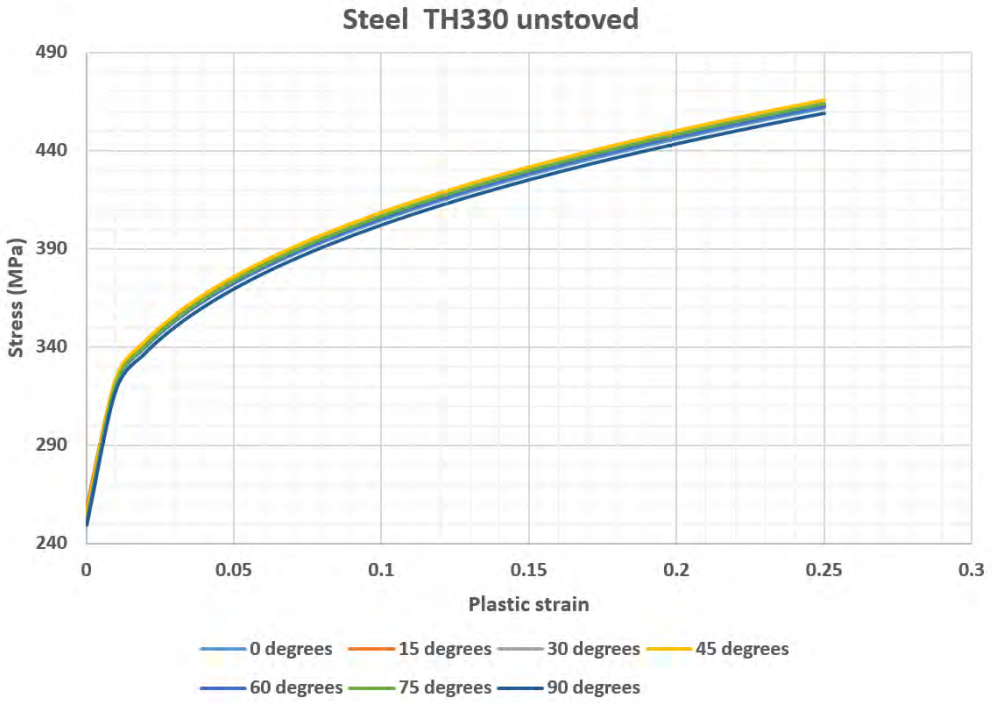

FIGURE 2.28: Stress and plastic strain data for unstoved TH330 Steel after yielding. [54]

as the ionic lattice, but strengthens during the sliding dislocation and interlocking of the long polymer chains, and can experience a much higher degree of strain before fracture.

PET is a semi-crystalline polymer with notable stiffness and strength, owing to the presence of a large aromatic ring in its repeating molecular construction[56].

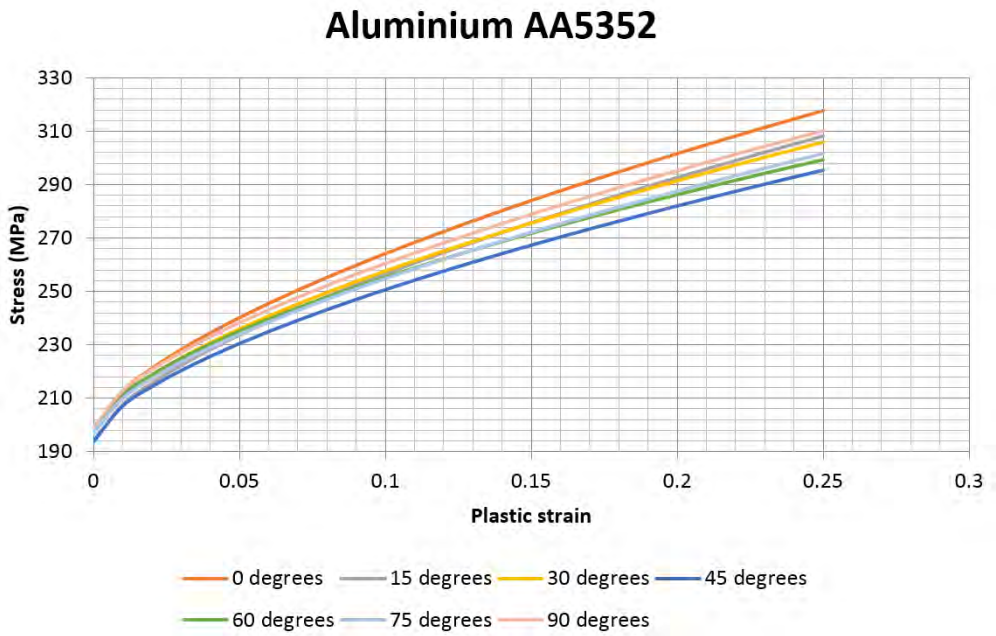

FIGURE 2.29: Stress and plastic strain data for AA5352 Aluminium after yielding. [54]

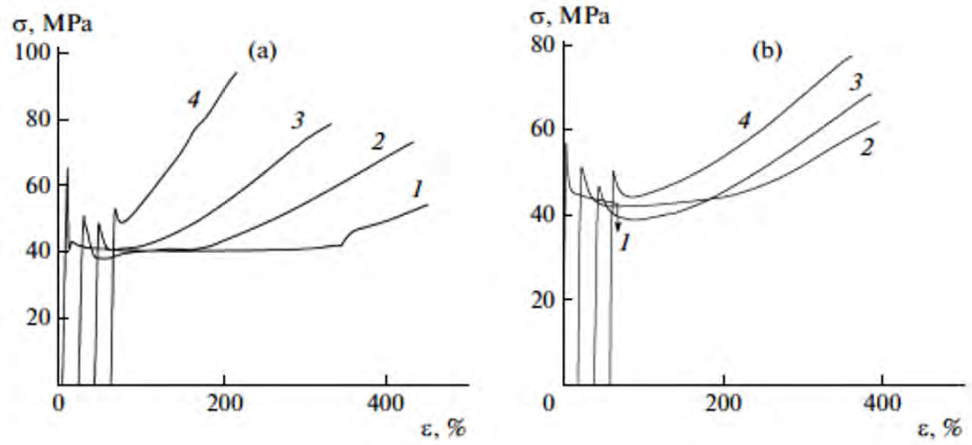

FIGURE 2.30: *Engineering stress/strain diagrams. (a) PET-1: (1) Unrolled sample and (2-4) samples with rolling ratios of (2) 1.23, (3) 1.38, (4) 2. (b) PET-2: (1) unrolled sample and (2-4) samples with rolling ratios of (2) 1.2, (3) 1.38, (4) 1.5. Curves 2-4 are shifted by 20, 20, 60% along the deformation axis for clarity.* (sic) [55]

During drawing or rolling processes the long polymer chains are stretched and aligned which further increases these properties. The PET stress/strain response seen in figure 2.30 demonstrates a typical response following a distinctive yield stress, followed by strain softening (the dip in the curve) and strain hardening which notable increases at larger strains [57]. This effect is not seen in the metals, which follow a simpler elastic/plastic yielding response.

Figure 2.30 demonstrates a significantly reduced resistance to deformation when

comparing a PET film with the two sheet alloys. Steel for example, requires around 450MPa of force to produce 0.25% plastic strain. However, some variants of the PET film required only 100MPa to produce 400% strain, but did not fracture at this strain. Equally, the yielding stress on some PET films occurred at approximately 10% strain, whereas steel and aluminium yield at 0.0012 and 0.0028 respectively. This comparison demonstrates the higher extend of deformation which polymers can experience.

2.5.1 Conclusions

This literature review has highlighted some of the challenges of introducing polymer-coated metal into the two-piece can-making process, and shed light on the industrial and metallurgic background associated with the project. It was drawn attention to the important of material selection, as well as the fundamental differences involved between processing aluminium and steel. The review has demonstrated the utility and value of FEA as tool to hypothesise and validate physical experimentation. The remainder of this thesis will explore the major steps of work responsible for completing this investigation.

Chapter 3

Modelling the Ironing Process

3.1 Introduction

This chapter begins the main bulk of the project by introducing the concept of modelling the main bodymaking process using finite element methods. The aims of this facet of the work are mainly to investigate the different approaches to modelling in general, and determining the suitability of each particular method for modelling a can in a DWI process. By the end of this chapter the work will have outlined the differences between modelling the Aluminium beverage can and Steel food can bodymaking processes, as well as discussed the use of various user interface tools for use in setting up or automating the execution of said models. Finally the different types of solver will be investigated, with the intention to find the most advantageous modelling approach for the high-speed, multi-tooled DWI process and additionally highlighted the challenges involved.

3.2 Aluminium Beverage Can Modelling

3.2.1 Modelling the DWI process

The DWI process proves challenging when gathering engineering characteristic data. Whilst it is possible to measure certain geometric or visual variables on a formed can, the measuring of engineering variables such as stress and plastic equivalent strain is far more difficult. Aggressive ironing reductions between two tooling surfaces combined with a closed annular tooling construction render a cross-section view impossible in physical machinery. This issue highlights

the advantages of FEA mentioned in chapter 2, and justify the use of computational models for metrology when physical tests are unsuitable. For this reason this project focuses on FEA simulations as a primary research mode, but features experimental testing to validate and verify models at various stages.

Models were initially built in Abaqus CAE, a commercially available FEA preprocessor. Levels of complexity were added until a full can model had been made. The earliest models served only as points of reference between the project's work and Crown's existing data about the process. It was important to certify that the simulations would yield realistic results before moving ahead with the more advanced and computationally expensive models mapping more uncertain territory.

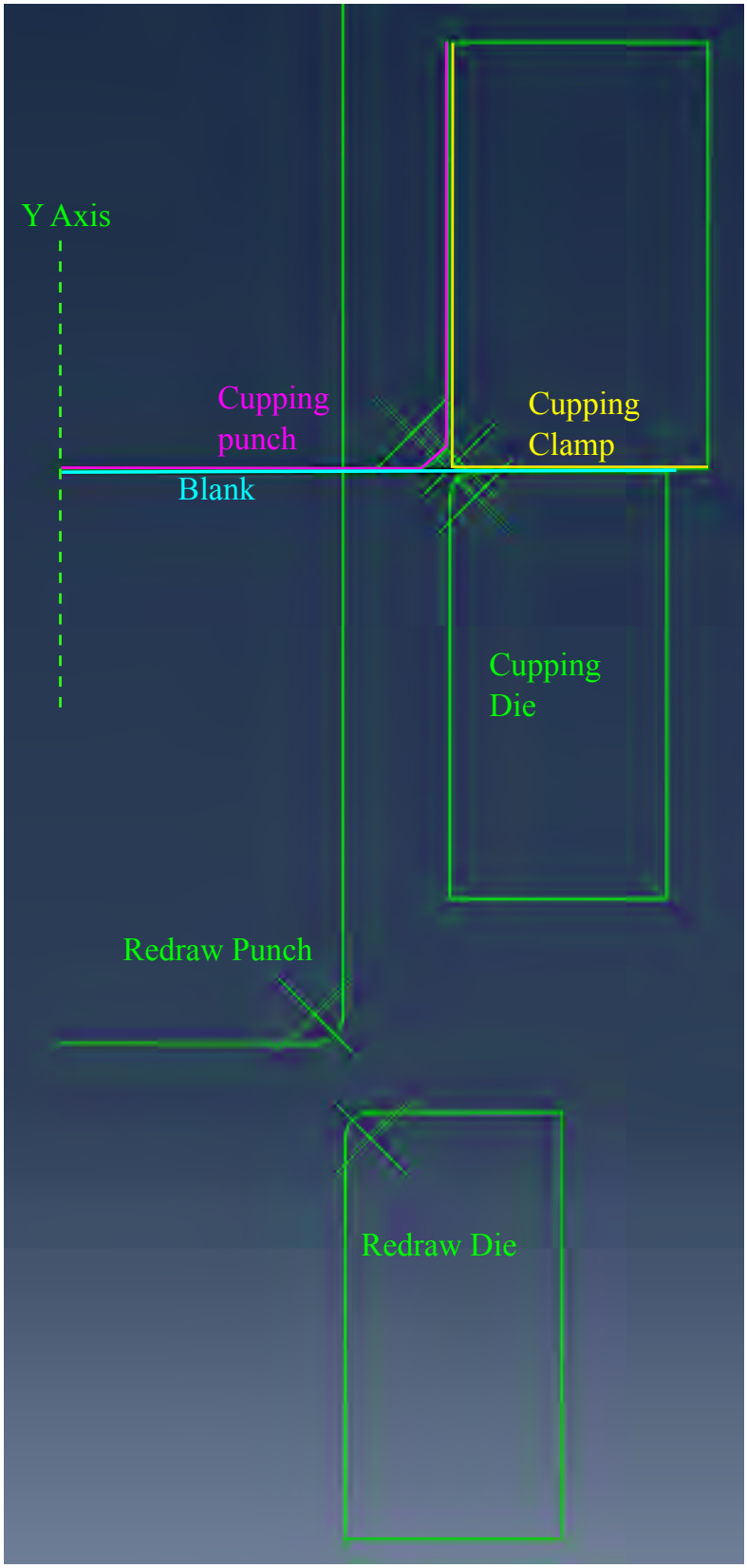

FIGURE 3.1: Axisymmetric view of the cupping and redraw processes modelled in Abaqus.

Figure 3.1 demonstrates the layout of the first milestone simulation achieved, a $330ml$ $65mm$ diameter European beverage can model. The geometry modelled the cupping/drawing and redrawing process, but did so as though operated by a single machine. In reality, these two stages are performed in different machines, and the cupped blanks appropriately experience a period of stress relaxation (or springback) between the two processes. At the beginning of the modelling stage it was more important to observe and test the behaviour of elements during simulation, so the process was kept simplistic. For the beginning a simple aluminium material was generated with properties visible in table 3.1 and Figure 3.2, and applied to the entire mesh via a tabulated plastic deformation model in Abaqus.

The tooling was modelled as analytical rigid surfaces in CAE. Modelling tooling as rigid is appropriate when variables experienced by the tooling are considered negligible compared to the deformable mesh (data concerning forces acting upon the tool is still gathered for a rigid surface). The blank was meshed with CAX4R axisymmetric continuum elements in a dynamic simulation. Due to the symmetrical nature of the can, the advantages in computational time make modelling in axisymmetric preferable in this scenario.

TABLE 3.1: Material properties for simple aluminium model.

Density ($kgmm^{-3}$)	Young's Modulus (MPa)))	Poisson's Ratio
0.0027	70000	0.3

Figure 3.3 depicts the Von Mises stress distribution across the blank after the first stage of cupping is complete. The cupping die can be observed on the left, and the cup rests upon the redraw die; the punch has been hidden from view. The bands of increased stress were consistent with similarly simulated data from Crown, and the elements across the thickness kept similar aspect ratios during ironing. This favourable comparison indicated that there would be no issue continuing with the modelling approach and thus could progress to the full DWI process model.

A full DWI model was the next major milestone in the project, though still functioning primarily as an indicator of forward progression rather than yielding workable data. The model was simulated using dynamic explicit time integration, with arbitrary clamping loads of $1kN$ to secure the blank during cupping,

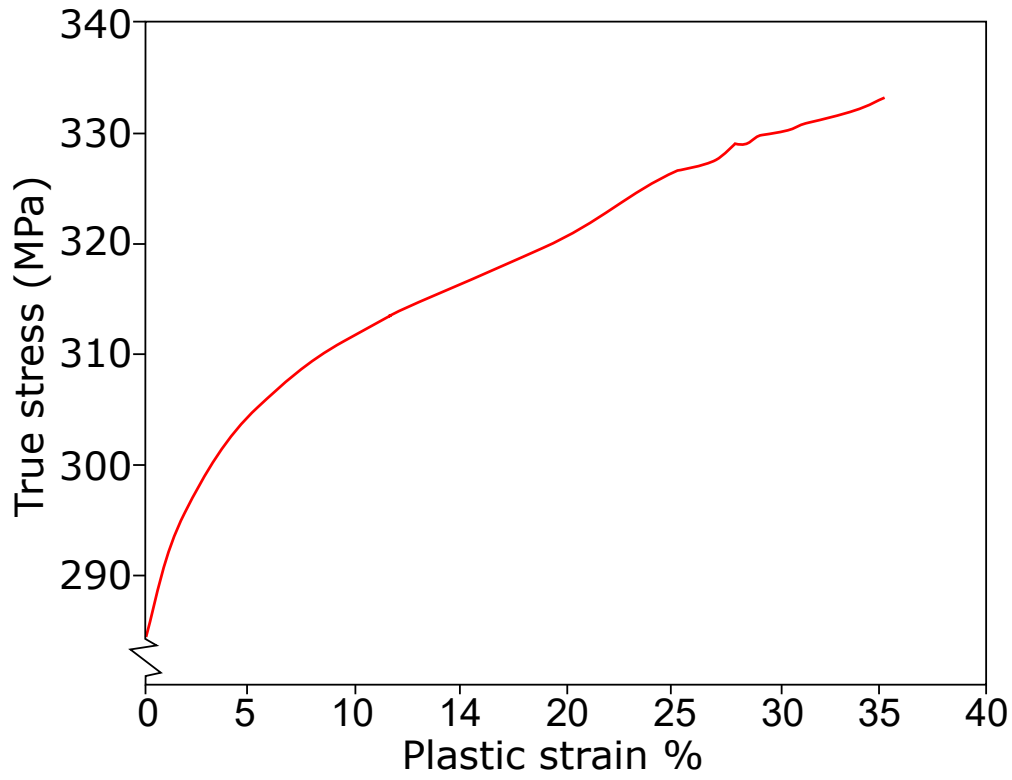

FIGURE 3.2: Graph displaying true stress vs plastic strain for test model aluminium AA 5352 series [58].

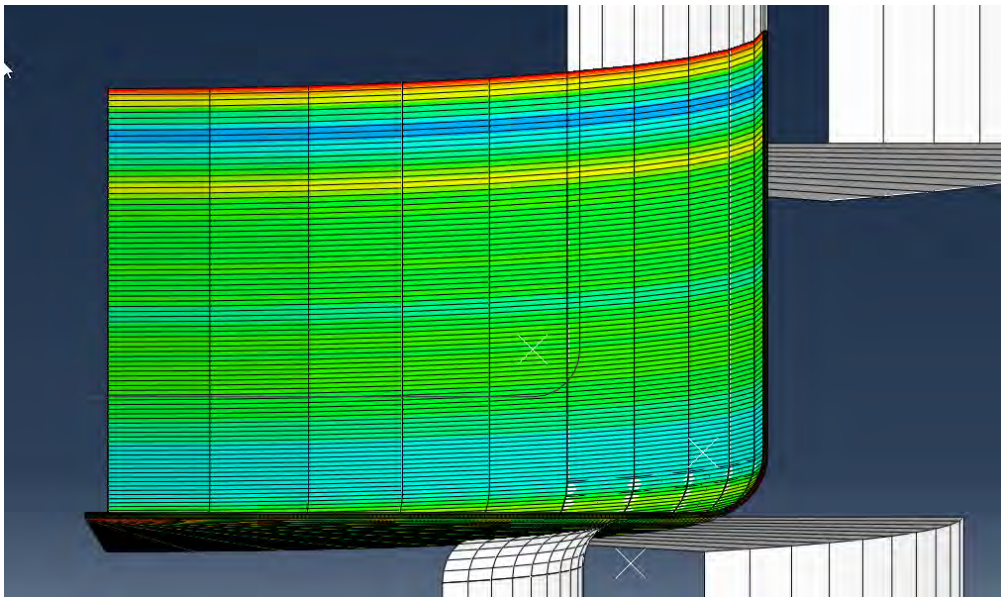

FIGURE 3.3: Diagram illustrating the Von Mises stress distribution of an AA5352 blank after cupping.

and a friction coefficient of 0.1 (both industry recommendation). The geometry was kept as simplistic as possible to reduce computational load: fillets were used to round off corners, and tooling complexity was compressed to simple curves. The models naturally kept distances and thicknesses within realistic

tolerances to ensure that the transition to more advanced models was minimal. Figures 3.4 and 3.5 illustrate the process of the full DWI (Legend is identical for both Figures) . The images have been clipped to highlight the aspect ratio and certain tooling has been minimised in the viewport to allow for better observation of the blank. The progressive equivalent plastic strain distribution demonstrates that the ironing is interacting in a realistic and desired manner: illustrating a work-hardening behaviour which was expected during ironing. The change in aspect ratio similarly demonstrates the correct material behaviour during ironing (namely a decrease in wall thickness and an increase in length [59],[60]). It is worth noting at this point in the simulation progress, that no damage criterion was specified in Abaqus, and so the metal could experience conditions beyond failure, and so failure can only be predicted by evaluation of numerical stress and plastic strain distributions.

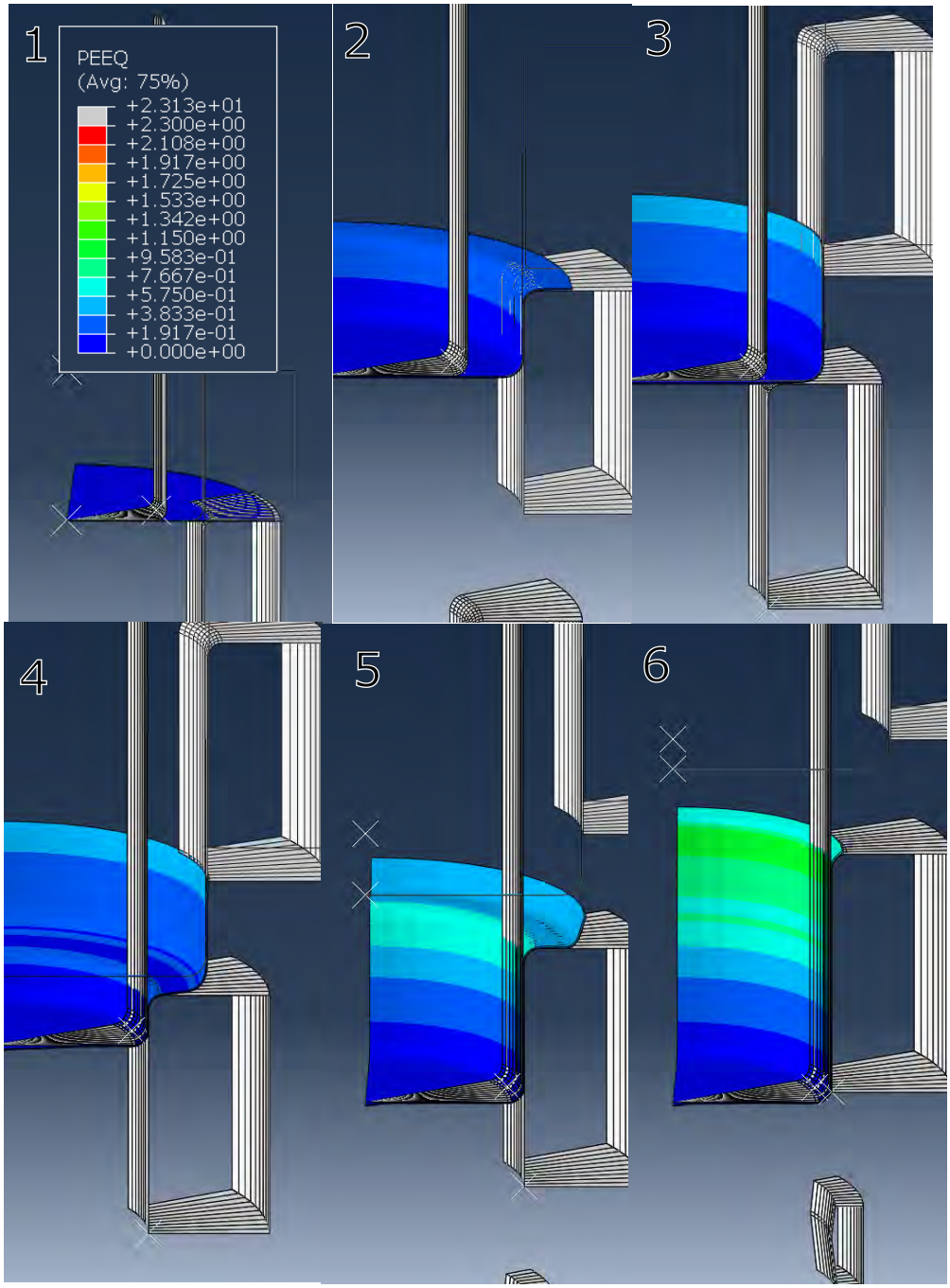

FIGURE 3.4: Progressive stills from the full DWI process performed on an all-aluminium substrate. Stages 1-6.

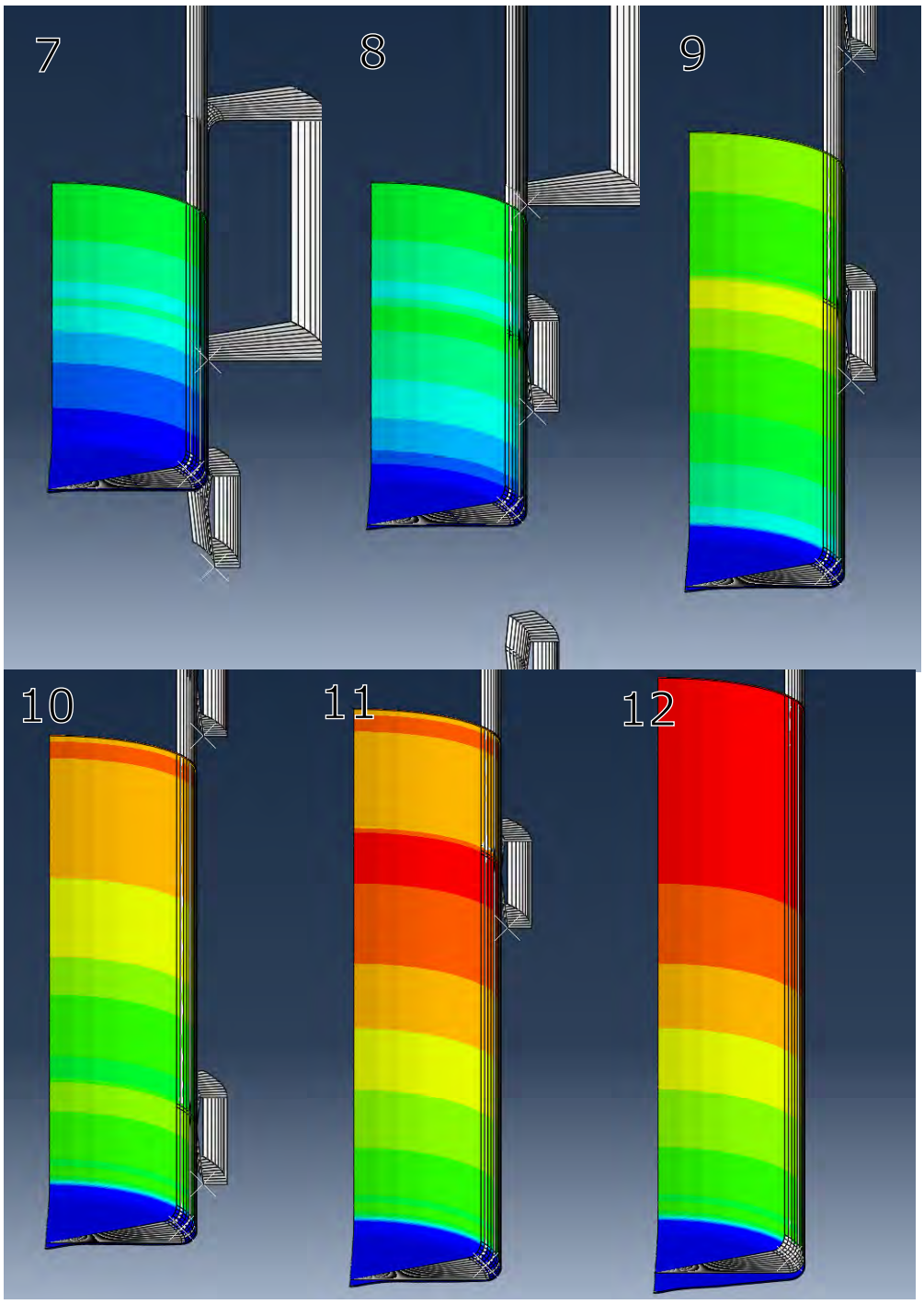

FIGURE 3.5: Further Progressive stills from the full DWI process performed on an all-aluminium substrate. Stages 7-12.

3.2.2 Mesh sensitivity study

Once the full DWI model was working as intended, a mesh sensitivity study was imperative to determine the effect on mesh density on results data. Although the data collected is not usable as process results, the mesh sensitivity study is a good indicator of the scope of mesh which will be required to maintain an accurate result throughout changing variables in future DWI simulations. For this reason it is likely that once reliable material data and more accurate geometry is implemented, the mesh sensitivity data collected will serve as a reasonable starting point for a future study. The mesh sensitivity was undertaken on the same blank model as previously seen in figures 3.4 and 3.5 The density variables are listed in Table 3.2 (where 4, 6, 8 are the elements along the width, and 125, 250, 500 along the length). Although some mesh densities result in the same total number of elements, it is important to understand that the differences in mesh geometry mark these as fundamentally different mesh densities, and one should expect different results from each.

x	4	6	8
125	500	750	1000
250	1000	1500	2000
500	2000	3000	4000

TABLE 3.2: Mesh sensitivity study mesh densities for the aluminium beverage can DWI model.

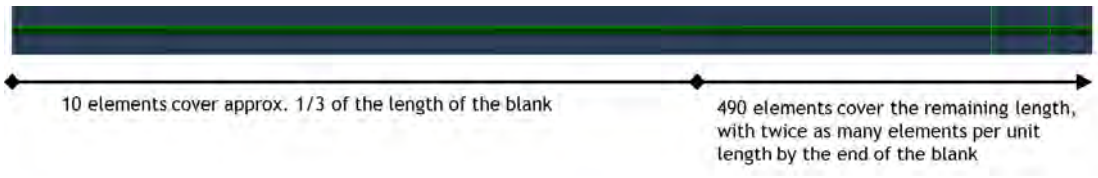

FIGURE 3.6: Diagram showing the biased mesh distribution during the mesh sensitivity study on all-aluminium DWI.

The computational time taken to complete a simulation is governed by the the stable time increment: which is itself affected by various factors including the size of the element, number of elements experiencing contact with other surfaces [61], and the differences in density between all materials used. Finding an appropriate mesh density is an important task to ensure that the models can run as fast as possible whilst keeping maximum accuracy. For this reason, the majority of the blank which did not experience ironing was meshed using larger elements, as the results for this region can be largely ignored. Figure 3.6 demonstrates the distribution of elements along the blank. A 2:1 ratio bias was used to ensure that the area experiencing the maximum deformation (namely the trailing edge of the blank) was meshed as densely as possible whilst reducing mesh in unimportant regions. The bias towards the trailing edge of the blank was a decision supported by the nature of the ironing process. Since the substrate is undergoing plastic deformation during the entire process [62], and the leading edge of the can is essentially pinned to the punch - clamped between the punch and the ironing rings in each phase (see Figure 3.7), the ultimate direction in which the plastic deformation travels is away from the punch end and towards the trailing edge. Generally speaking the deformation at the cut edge of the blank is far higher than at the centre.

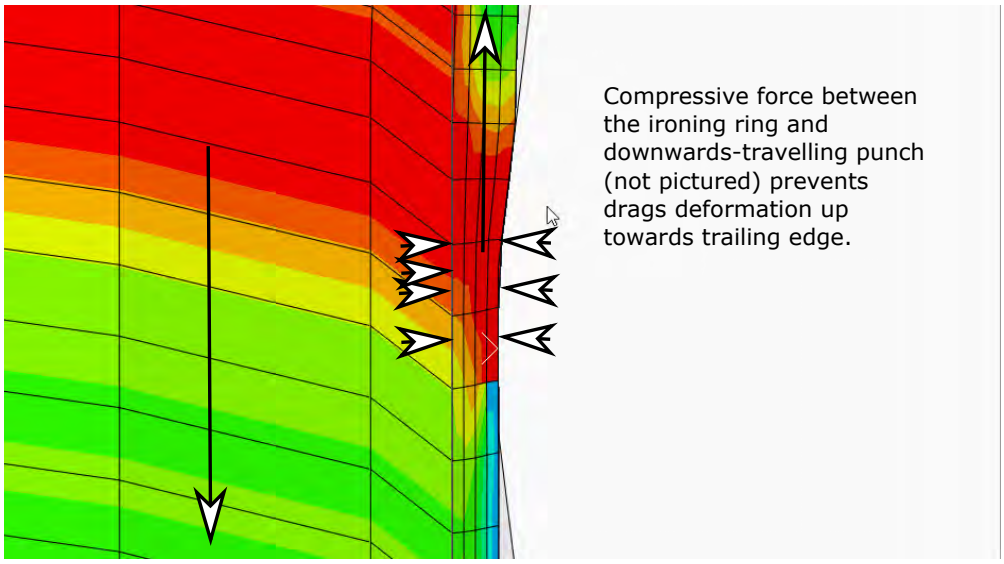

FIGURE 3.7: Diagram showing the pinching stresses between the punch and the ironing ring (causing deformation to occur in an upwards direction).

Figures 3.8 and 3.9 demonstrates the distribution of plastic strain and Von Mises stress after the final ironing process has completed. It is clearly illustrated that plastic strain increases from the leading to trailing edges of the can, and the Von

Mises distribution shows a maximum at the trailing edge (the last place ironing occurred) at the process moment pictured. Though it may seem important to finely mesh every moment of contact during ironing, the process actually becomes steady state after contact forces equalise, and the engineering variables experienced will be largely the same throughout the ironing stage (from contact to release) [63].

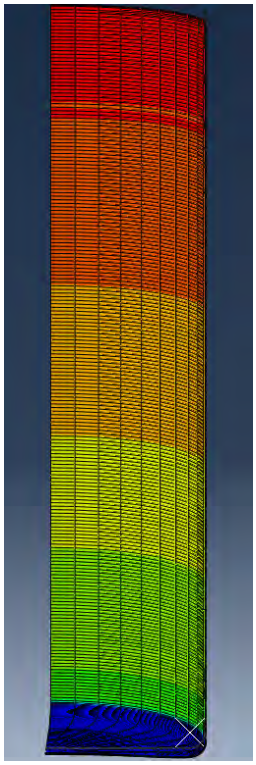

FIGURE 3.8: Diagram showing the plastic strain distribution of the fully ironed blank.

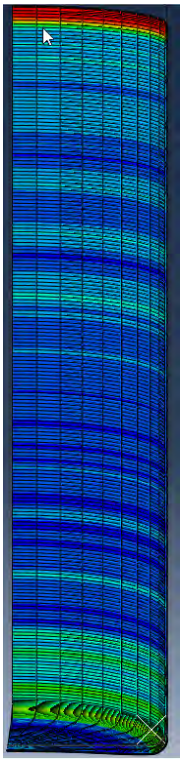

FIGURE 3.9: Diagram showing the Von Mises distribution of the fully ironed blank.

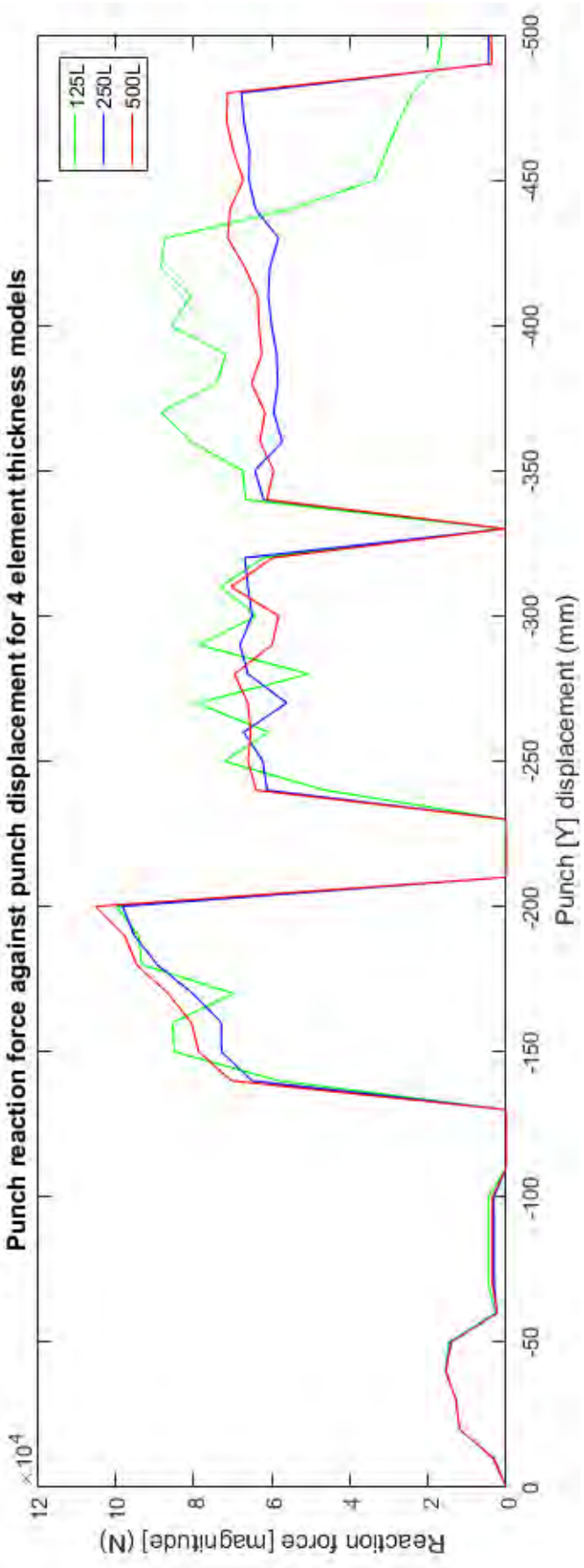

FIGURE 3.10: Mesh sensitivity results for the full aluminium DWI models using 4 elements across each layer thickness.

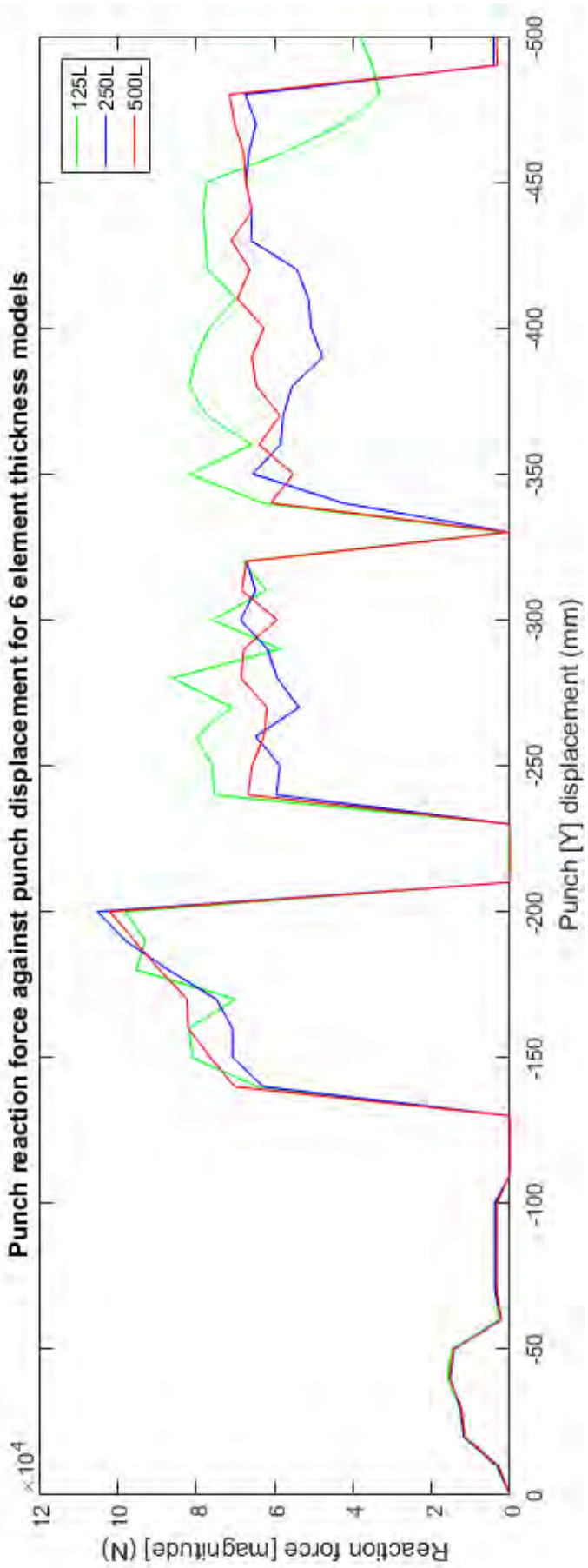

FIGURE 3.11: Mesh sensitivity results for the full aluminium DWI models using 6 elements across each layer thickness.

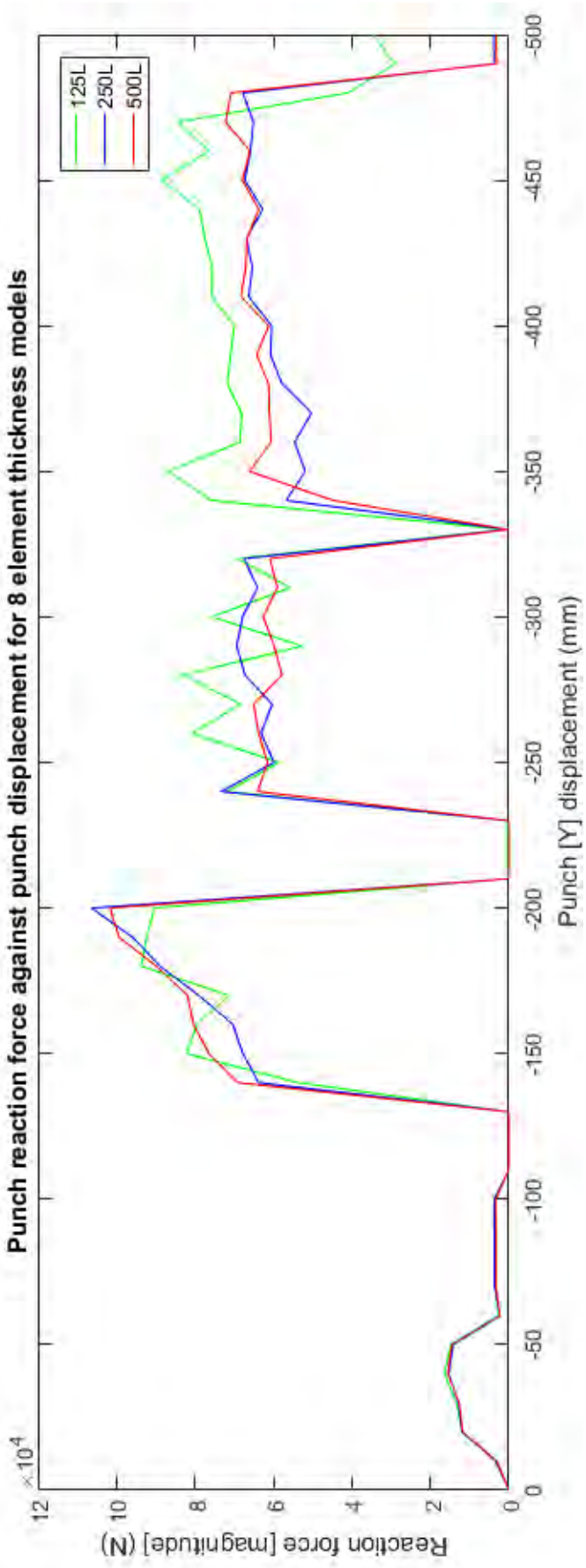

FIGURE 3.12: Mesh sensitivity results for the full aluminium DWI models using 8 elements across each layer thickness.

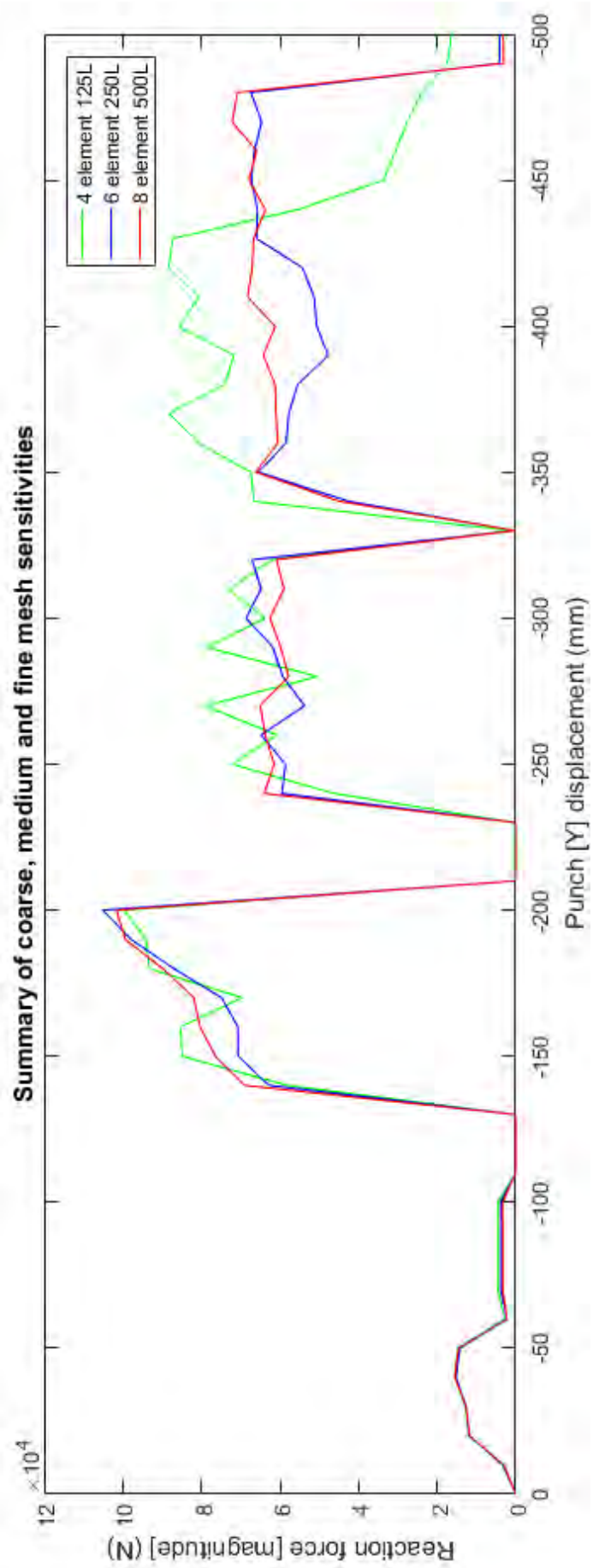

FIGURE 3.13: Summary results for the Coarse, Medium and Fine meshes taken from the results of Figures 3.10, 3.11, 3.12.

A mesh sensitivity study was undertaken by applying three element thickness densities (4, 6, 8) across three length densities (125, 250, 500) and simulating all nine meshes on otherwise identical DWI beverage setups. Figures 3.10 through 3.12 illustrate the results of the mesh sensitivity study. Data was probed from the single node upon which all forces and variables experienced by the ironing punch are projected throughout each simulation, so the forces are comparable. The shape of the graph depicts the Redraw-Ironing process, and from left to right the spikes in reaction force illustrate the four contacts: the redrawing die is contacted at around -10mm displacement (the punch travels along a negative Y axis in the simulation), and initial contact with the three ironing rings occurs at approximately -130mm, -230mm, and -330mm respectively. Since the punch was modelled to be travelling at a fixed speed throughout the simulation, the displacement data can also be used to demonstrate the proportional lengths of time during which the ironing occurred at each ring by observing the rise and fall of force data at these locations.

All simulations demonstrate visible fluctuations in reaction force during the steady-state ironing stages. This behaviour is difficult to quantify, but it is possible that oscillations due to friction are being accounted for, since the simulation runs in explicit (which models inertia and thus vibration). Since methods using dynamic explicit time integration model vibration, and standard implicit methods do not [64], an implicit study would clarify these queries. Ideally a physical study would put the investigation to rest, however no such metrology equipment was available which could measure vibration during the ironing process.

Beyond the question of oscillations, the graphs still provide useful data regarding the effects of the mesh density on ironing results. In all nine simulations the mesh of 125 length experiences far higher nominal reaction forces during the second and third stages of ironing, showing an increase compared to the 250 and 500 length experiments in every element thickness. This indicates that 125 elements in length is clearly too few, as meaningful differences in results are occurring. The same conclusion cannot be drawn between 250 and 500 lengths as the oscillation obscures any differences in reaction force. Similarly in all three graphs the reaction force of the 125-length does not settle back towards zero, despite all experiencing ironing for the same time/displacement. This may indicate a snagging or hyper-deformation behaviour [65] of the elements - which can negatively affect the forces applied to the punch. For these reasons it can

generally be considered that 125 elements in length is too few for this type of geometry.

Figure 3.13 compares the evolution of reaction forces from 3 summary densities: 4 thickness: 125 length, 6 thickness: 250 length, and 8 thickness: 500 length. This serves as a generic *coarse*, *medium*, and *fine* mesh plot, and provides a visual representation of the differences between these milestone densities. From this graph, the disqualification of the 125 length meshes can be observed, however the remaining two curves are very similar. The *fine* mesh reads higher reaction forces than the *medium* throughout the initial ironing stage, but this is not the case during the second ironing stage: where the *medium* curve reads higher peaks than the *fine*. This discrepancy highlights the need to later investigate the oscillation behaviour in the simulations.

3.2.3 Restart Analyses

Modelling the entire DWI process requires a complex simulation with multiple forming steps: demanding a proportional computational time if no accuracy-affecting debugging short-cuts (such as mass-scaling) [66] are used. For this reason progressing forward with simulations and the requirement of a trial-and-error debugging approach raises a concern with computational time. Each different iteration only changed perhaps a single variable, such as a clearance or geometry of one piece of tooling, but required an entirely new simulation to be completed. Often the results gathered were right at the end of the ironing process, or were focused on an interaction in the very late stages of the process. One solution would appear to be simply simulating the latter half of the process: selecting a point before which data did not change and simulating from there onwards. However, the nature of drawing and ironing is such that the extreme plastic deformation [62] combined with a non-heated pressing process [67] creates a resulting residual stress distribution [16] and work hardening which cannot be easily implemented into a material definition.

Using restart analyses allows the reduction of run times by using a previous simulations output as the starting data for a new simulation with identical meshed geometry. In this way, a cupped blank can be imported as an engineered part as opposed to a fresh CAD part, or a can can be imported into a different simulation after partial ironing. Figure 3.14 demonstrate the differences in stress distribution when modelling a curved cup from the beginning

of the redraw stage against Figures 3.15 and 3.16, which show the stress and PEEQ distributions of a restart-imported cup. A restart analysis is far superior to importing a "deformed" CAD part as engineering properties from a previous process like work-hardening[68], residual stress, and plastic strain are all retained in the model. Equally, a restart analysis is generally superior to a full simulation when the previous forming process and geometry is not being altered between runs.

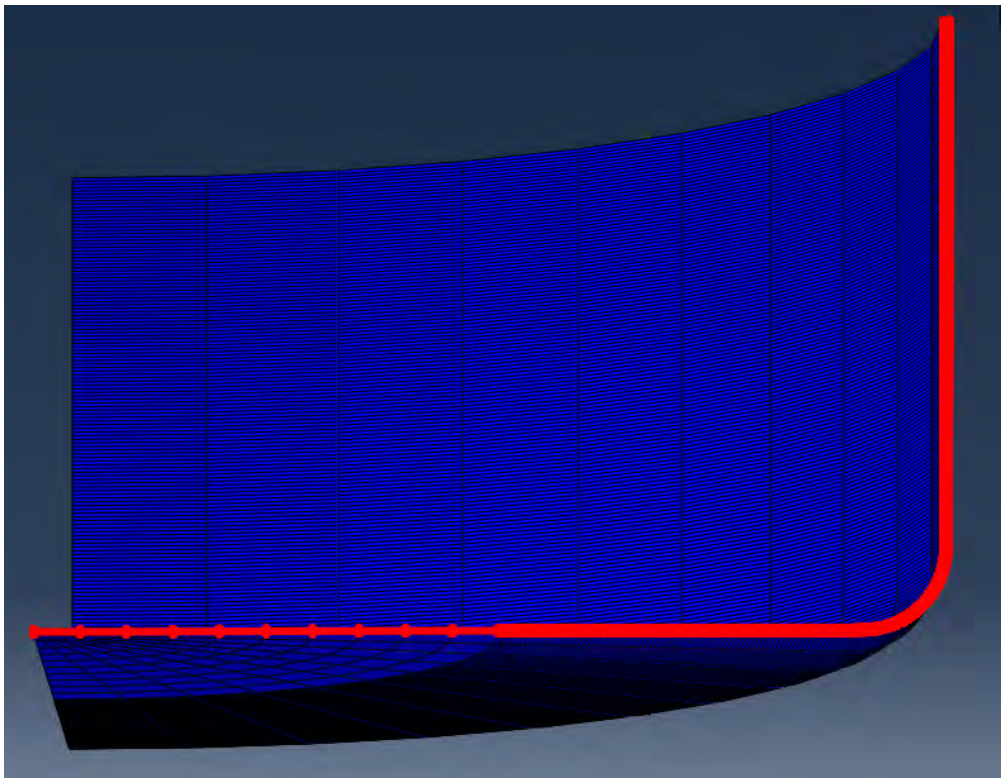

FIGURE 3.14: Stress and PEEQ overlay distribution of a 'fresh' modelled cup (Both Stress and PEEQ are at 0).

Figures 3.14 through 3.16 demonstrate the need to preserve the material state obtained during all stages of the DWI model in order to preserve the overall material data of the model. Omitting any step of simulation in an attempt to cut computational time down would simply render any results inaccurate - as the corresponding chunk of engineering variables associated with the process would be similarly omitted. This issue can be solved using *restart simulations* formats. Restart simulations allow the resumption of completed or partially-completed simulations, continued in a further process [69]. A model can be partially completed, and then imported to a Restart simulation - which subsequently imports all of the material data and engineering properties of the geometry at a specified step, allowing the remaining processes to be simulated. To

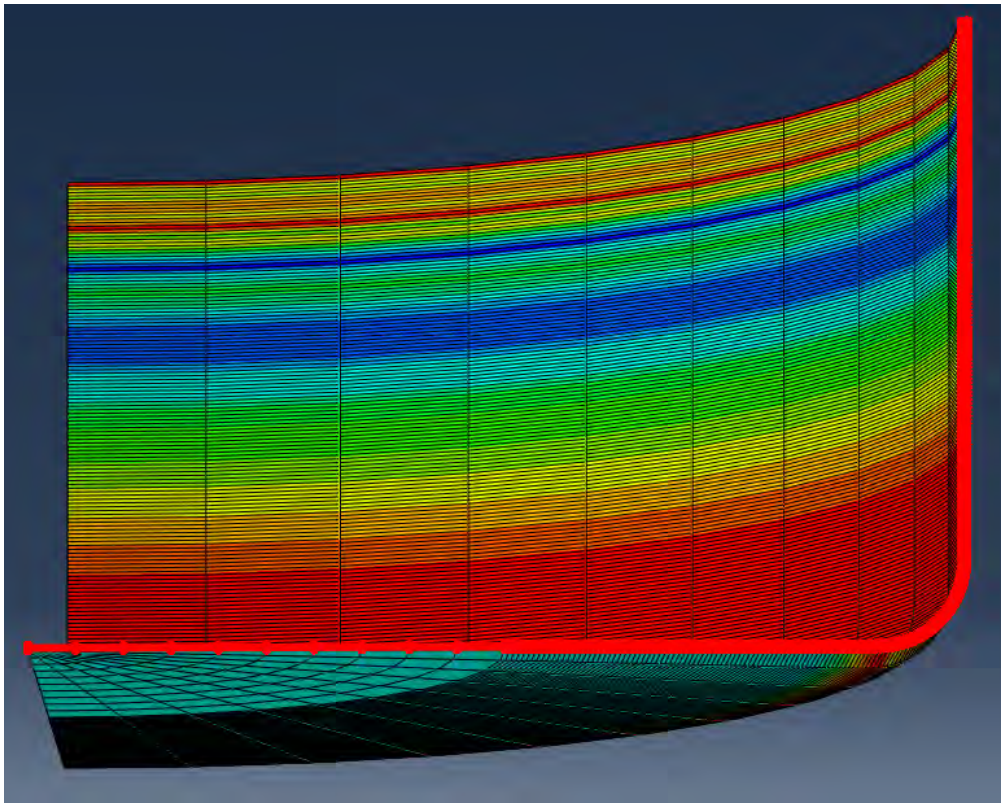

FIGURE 3.15: Stress distribution of a simulated 'cupped' cup from a restart analysis.

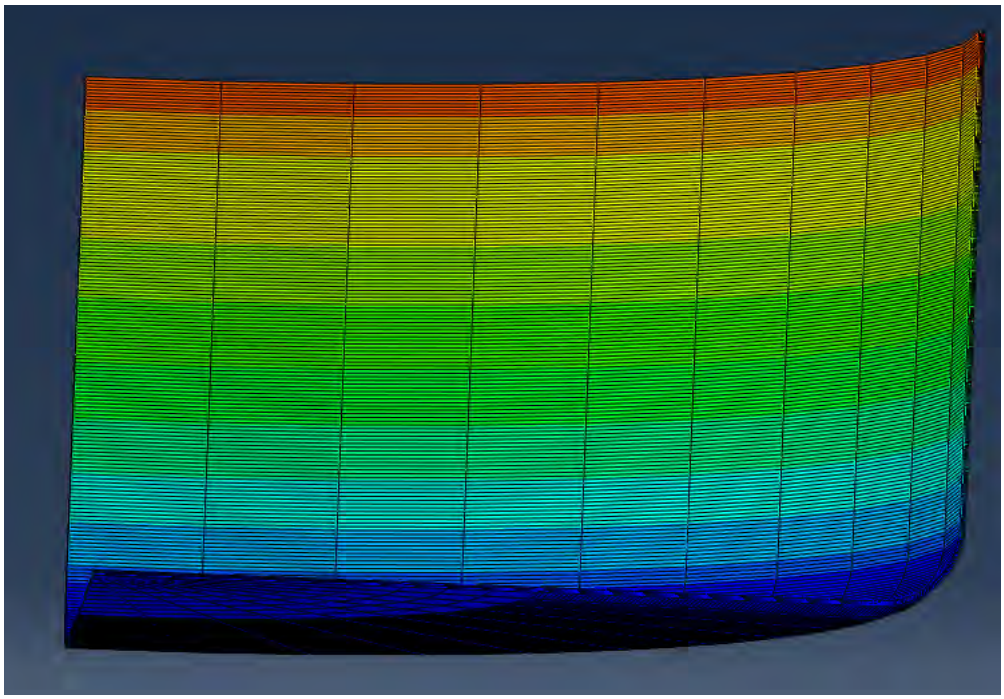

FIGURE 3.16: PEEQ distribution of a simulated 'cupped' cup from the same restart analysis.

better illustrate this idea, Figure 3.17 demonstrates the very beginning of a simulation (where step time = 0). The material state data including Plastic strain,

stress, etc has been imported to the unsolved model. Restart simulations prove a useful tool in this project, as the method allows various changes to the ironing parameters without necessarily having to re-run the cupping process (which would otherwise remain unchanged). In this sense computational time can be cut down somewhat without diminishing any results whatsoever. Restart files are limited however, in the sense that imported geometry cannot change - so a bodymaking ironing process could not be restarted using a different mesh to the one used for cupping.

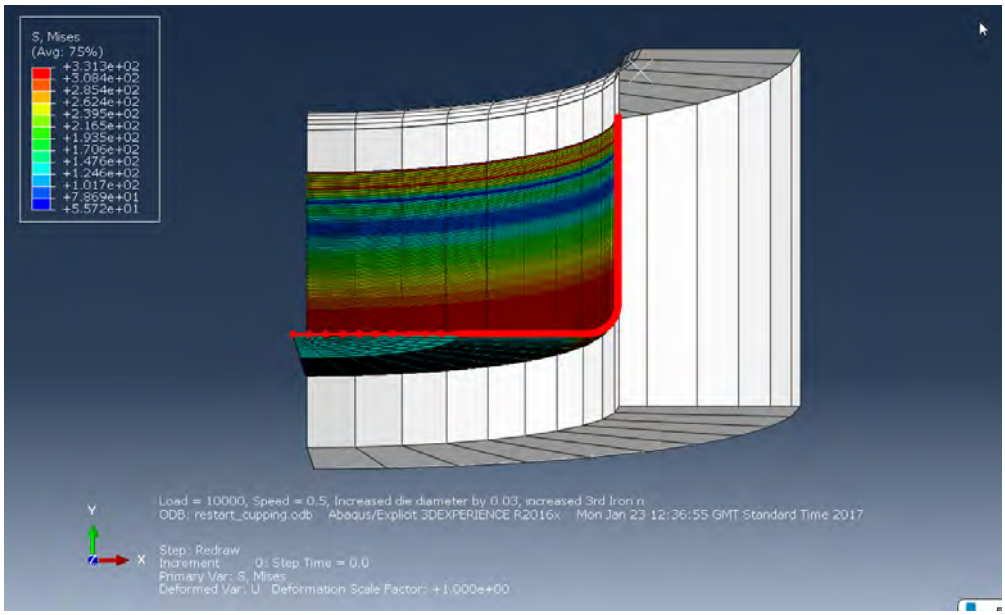

FIGURE 3.17: Diagram of Abaqus CAE interface from a restarted file, demonstrating the saved data at a zero step time: before any simulation has been undertaken.

3.2.4 Updating geometry

An issue was identified with deformation occurring in the final ironing stage of the model, towards the tip of the trailing edge. Figure 3.18 exhibits the issue. The problem concerned a skewed deformation in the final elements, possibly caused by snagging, or an excessive ironing ratio. Behaviour highlighted in figure 3.18 demonstrates penetration between the blank elements and the punch - despite specifying a surface-to-surface contact pair which bars this interaction. Whilst surface-to-surface contact generally tries to solve contact with no penetration when an element deforms dramatically enough to stretch or push nodes through the tooling geometry, contact becomes difficult to solve and penetration is often the result. The deformation of the trailing elements into long thin triangles may indicate a general pinching phenomenon occurring during the

final ironing moments, as it is expected that all elements react largely the same during deformation. These issues mean that any results taken from those elements or nodes may be compromised - as they are acting unlike any relevant material.

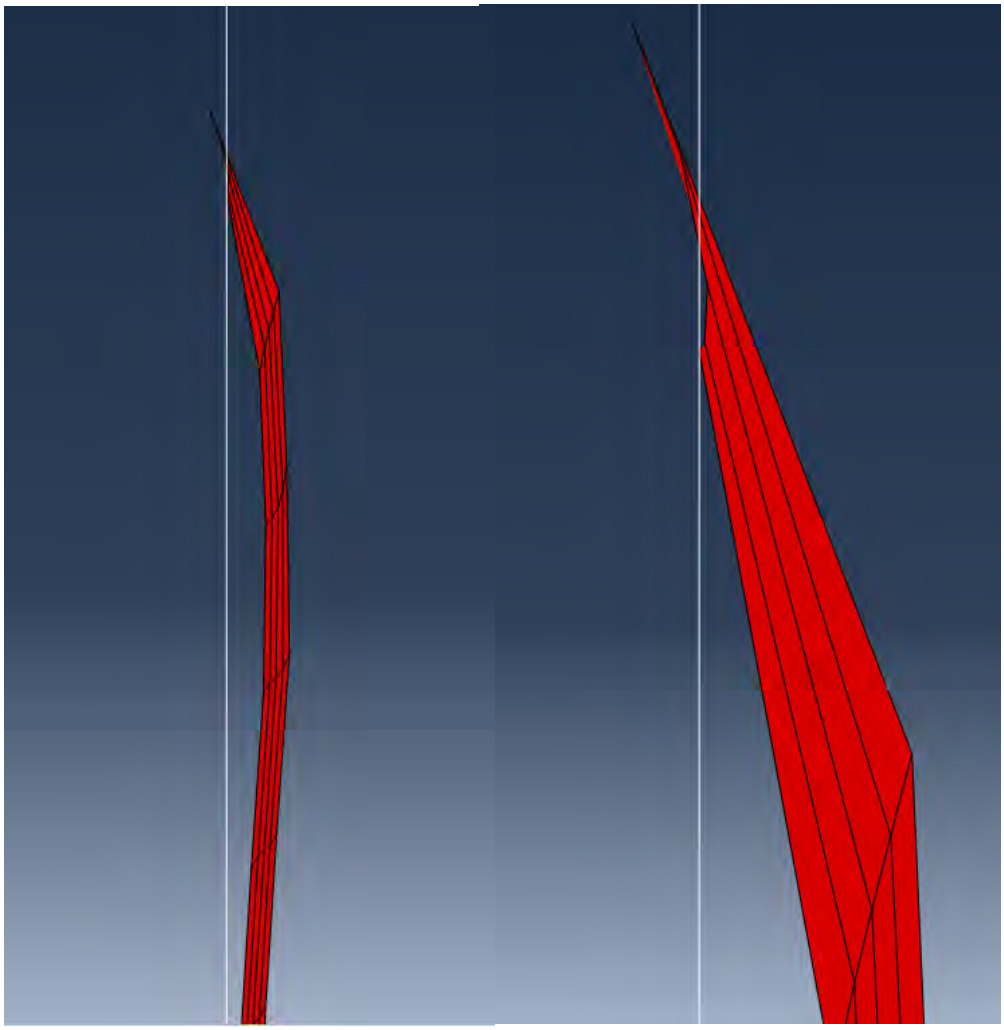

FIGURE 3.18: Diagram showing two close-up views of the trailing edge after excessive and unwanted deformation patterns.

After some investigation it was discovered that the cause behind this deformation problem was likely the geometry of the ironing punch. At this point in the project the models were accurately representing most clearances and thicknesses of tooling and substrate, but the punch geometry was still modelled as a very basic curve. In reality the ironing punch geometry is much more complex, and the reasons behind this complexity play a part in the reduction of stress and strains towards the trailing edge. Figure 3.19 demonstrates the differences in geometry between the old punch (left) and the newly updated punch geometry (right).

FIGURE 3.19: Diagram showing the differences in geometry between the simplified punch model (left) and the updated model (right). The red line indicates the path of the blank during processing.

Though not pictured, the geometry along the length of the punch is also altered. Originally a directly straight line was used to model the contacting side for simplicity, however the industrial punch geometry features a series of shorter straight edges, conjoined via tangential intersections of varying radii. This feature allows the punch to slowly reduce in diameter as the length progresses, which allows the clearance between punch and ironing die to proportionally decrease as ironing progresses. Figure 3.20 represents the changing Equivalent plastic strain experienced by 1 element at the tip of the trailing edge, on the side meeting the ironing ring. Figure 3.20 clearly demonstrates similar plastic strain, until the final ironing stage where the advanced punch geometry shows significantly reduced plastic strain. This difference in forming is an intentional step to aid the necking process: which cans undergo after DWI to obtain their final shape. Excess material must be left at the cut edge to prevent failure during necking [70]. The simplified punch was creating ironing conditions unlike those experienced by the blank during a comparable bodymaking process. Figure 3.21 similarly reinforces the theory, and demonstrates an identically scaled stress distribution of the old and new punch geometries effect on the trailing edge of the blank. The model featuring newer punch geometry demonstrates lower peak stress and lower stress concentration around the tip of the trailing edge (peak stress is red) accounting for the section left for necking. Retrospectively, whilst the simple punch geometry was unlikely to ever yield a realistic can, it was not a certainty that the alternative would lead to model failure. This

information confirms that any DWI process simulation (diagnostic or otherwise) needs to feature the full tooling geometry or risk model failure.

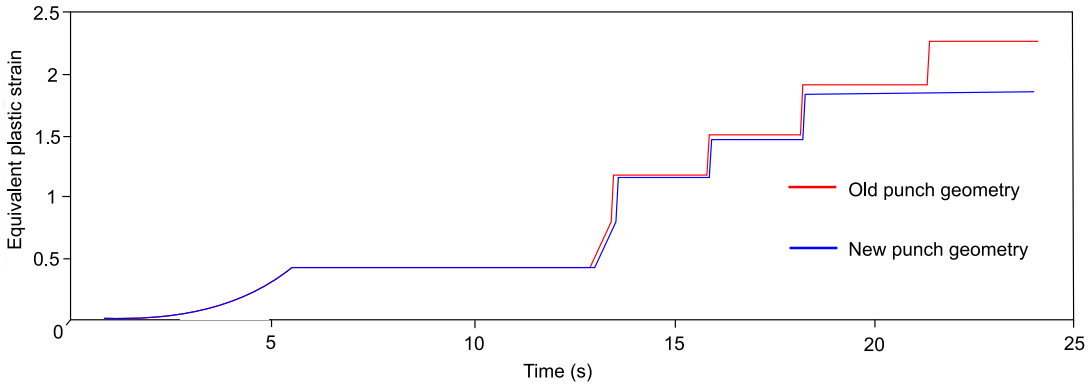

FIGURE 3.20: Graphical representation of the time-derived plastic equivalent strain experienced by the final element contacting ironing dies on the trailing edge.

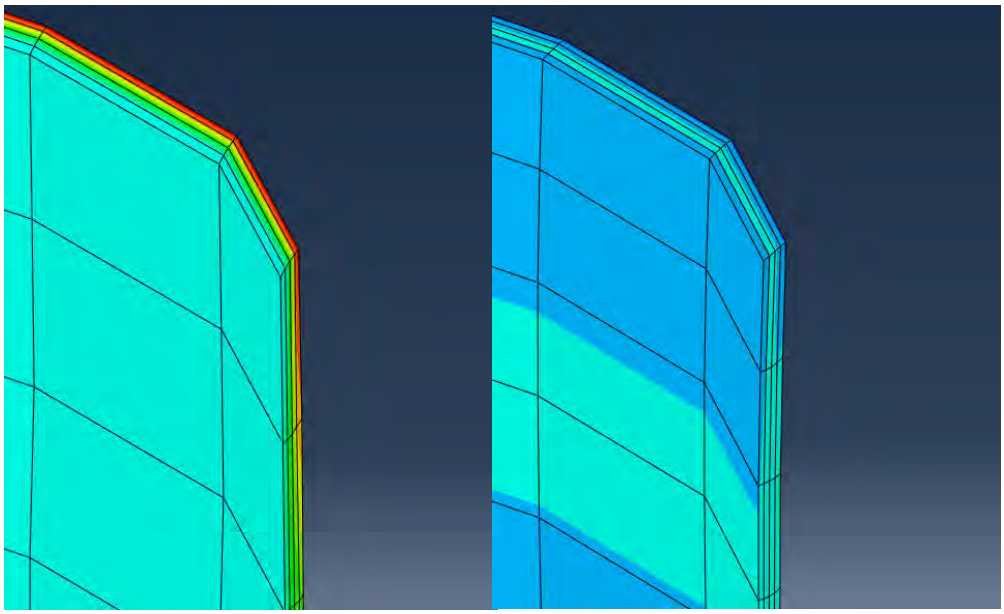

FIGURE 3.21: Comparison of the Von Mises distribution at the trailing edge of a blank, when using the old (left) and new (right) punch geometry.

Figures 3.20 and 3.21 demonstrate both stress and plastic equivalent strain of the problematic trailing edge are dramatically reduced by switching to the more complex punch geometry. Moving forward this serves as a reasonable basis of understanding the relevance and importance of including all tooling geometry, else loads and deformations could be incorrectly calculated.

3.2.5 Simulating coated substrates

Among many methods of modelling a multi-material model, the simplest at this time was to simply apply different material properties to separate partitioned geometry in the model. This strategy did not account for an interface layer between the two materials, and would thus not allow for modelling of a de-lamination fault, however discussions opted to focus progression on strain data throughout the metal, so a bond interface was assumed negligible at this time. The only data obtainable for rolled PET was a full stress/strain graph (Figure 3.22): in order to obtain the plastic strain values equation (3.1) was utilised. If de-laminaton failure modes were considered important, an alternative approach would be using a **TIE* or other interaction to join separate meshed entities. In this situation however, a bond interface would first need to be characterised for numerical input.

$$\varepsilon_{plastic} = \varepsilon - \sigma_{elastic} \therefore \varepsilon_{plastic} = \varepsilon - \frac{\sigma}{E} \tag{3.1}$$

These plastic strain values were then plotted against stress in Microsoft Excel, where the data was smoothing using a *line of best fit* tool with a sixth order polynomial in order to match the curve. Once these polynomial equations had been obtained they were then used to generate standardised stress/plastic strain values in a format suitable for a plastic behaviour model in Abaqus. Equations (3.2), (3.3), and (3.4) demonstrates the equation for $0.25mm/s$, $0.025mm/s$, and $0.0025mm/s$ respectively). The results of the reduced plastic strain data along with these lines-of-best-fit can be seen in Figure 3.23. The lines-of-best-fit were automatically generated by excel to match the data as closely as possible.

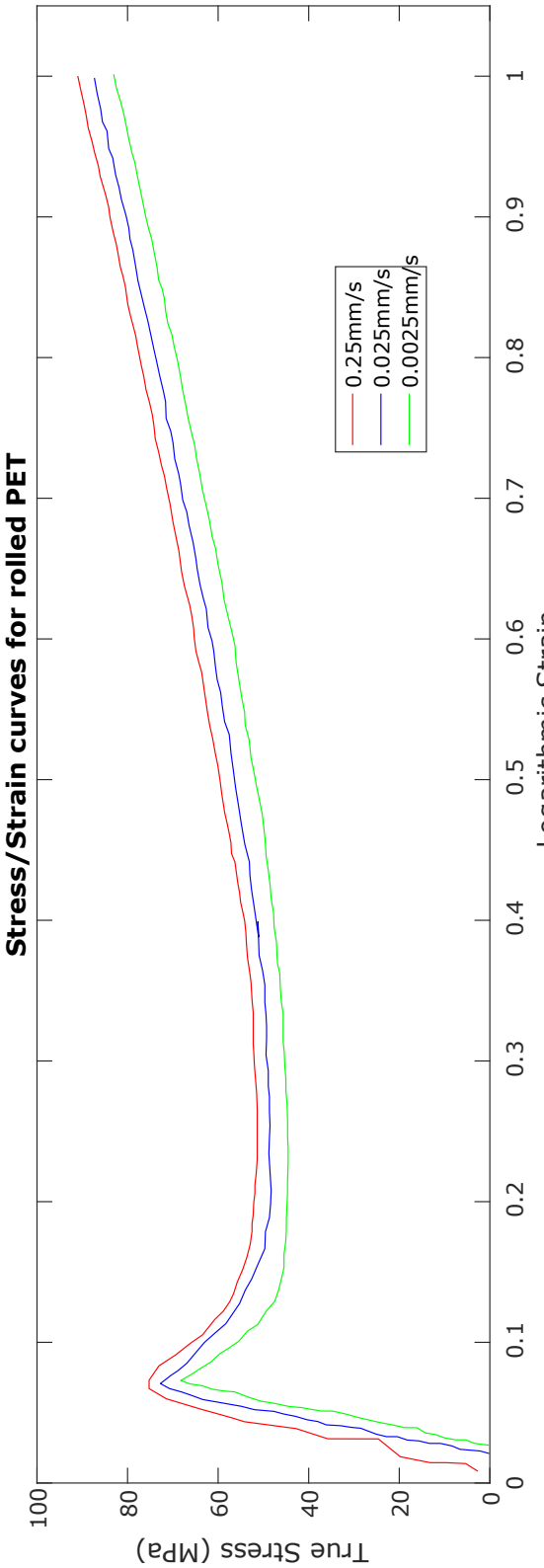

FIGURE 3.22: Graph showing the stress/strain data for rolled PET at various strain-rates [71].

$$y = 2046x^6 - 6447.3x^5 + 8182.2x^4 - 5402.5x^3 + 2023.8x^2 - 372.95x + 76.609 \tag{3.2}$$

$$y = 1776x^6 - 5744.9x^5 + 7481.3x^4 - 5058.1x^3 + 1934.9x^2 - 363.38x + 73.573 \tag{3.3}$$

$$y = 3522.2x^6 - 10844.3x^5 + 13133x^4 - 7976.6x^3 + 2613.9x^2 - 415.4x + 68.681 \tag{3.4}$$

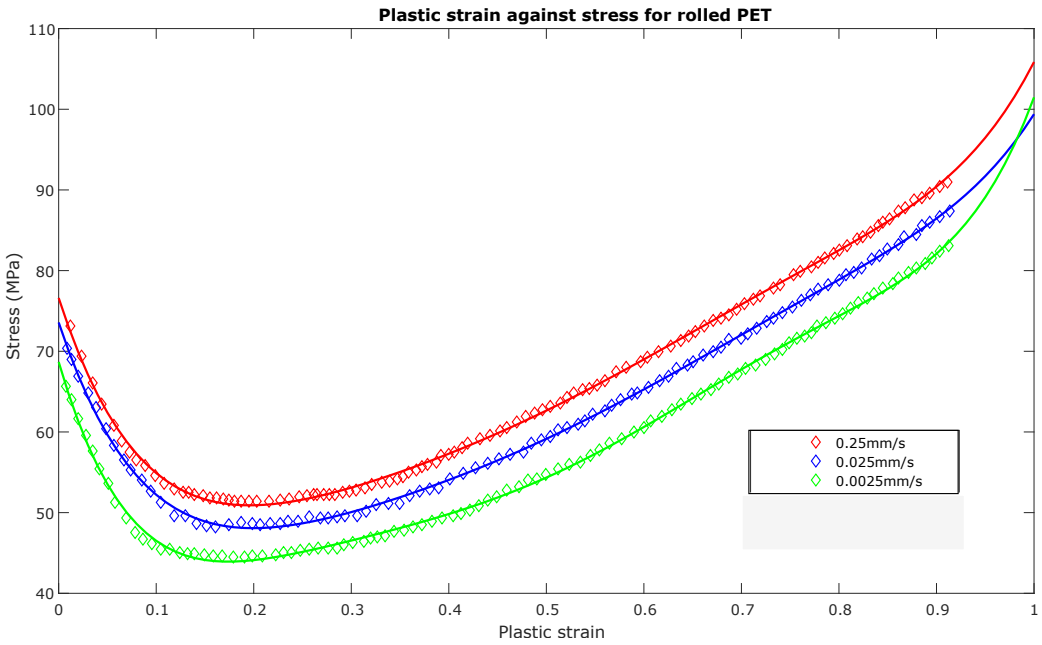

FIGURE 3.23: Graph showing the stress / Plastic strain data for rolled PET at various strain-rates, along with curves of best fit [71].

By implementing this material data into an Abaqus simulation, the model became much more reflective of a multi-material substrate. However figure 3.23 demonstrates a fundamental difference in PET material behaviour as rate of deformation is increased. The maximum rate of deformation tested in the experiments from which the data was derived was limited to $0.25mm/s$. This is

approximately four orders of magnitude away from the experienced strain rate during ironing ($2500 - 3000 mm/s$). Since the PET data displays a clear change in behaviour with an increasing strain rate in orders of magnitude, extrapolation would suggest that the behaviour changes even further: however there is no data to suggest the degree of this change. For this reason the PET simulations were postponed until further data could be gathered to support the interpolation.

3.3 Steel food can modelling

At this point the project gained access to a pilot bodymaking line for steel food cans at Crown's research facility. Discussion tended towards shifting the project from the aluminium beverage can to the steel food can, for a chance to better validate the computational modelling using physical trials. Though both two-piece cans and made with the same processes, food cans differ somewhat, as the extent of ironing is less severe (a necessary step to account for the stiffer material behaviour of steel [72]). The existing work on aluminium cans still serves as a fine basis of understanding the DWI process - which does not differ significantly except for the omission of two tooling rings when it comes to food can processing. The project was able to maintain speed and momentum despite changing directions.

Figure 3.24 demonstrates the stress/strain curve of the steel substrate sourced. It is clear from the data that the forming steel is very different compared to aluminium: having higher yield stresses, Ultimate tensile strength, different elongation behaviour, and different work-hardening effects . It is this difference in behaviour which demands the alternate tooling system seen in the food can processing line.

3.3.1 Modelling ironing in food cans

The process of ironing steel is far more sensitive in terms of severity and associated failure [73]. For this reason the redirection of the project began by studying an isolated ironing process on solid steel substrates to recalibrate the ironing modelling methods. Initially, the model featured a straight, rectangular section of steel blank, suspended by an *encastre* boundary condition along the top edge. The punch and ironing die then move downwards using a displacement

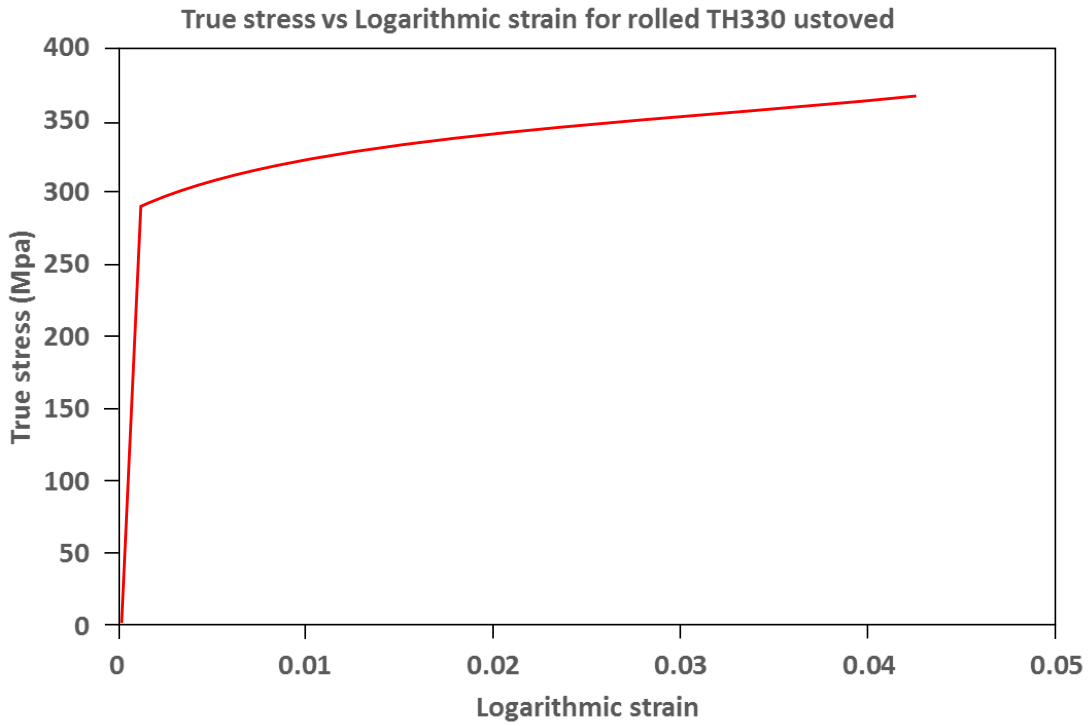

FIGURE 3.24: Graphical stress/strain data for steel TH330 unstoved [58].

boundary condition, ironing the steel between them. Contact between tooling and blank was defined using a surface-to-surface, finite sliding definition, and the elements used were 2D plane strain elements. Figure 3.25 demonstrates the process and the associated Von Mises distribution. It can be seen during the final stages that residual pinching is occurring at the top of the blank (in this case the leading edge). This is a convergence issue with the start of ironing: as the square blank edge meets the ironing die. This geometry is not accurate to a bodymaker, as the edge meeting the die would ordinarily be curved around the punch, and thus reduces the impact at the tooling interface. Modelling towards a more curved geometry was the natural progression to eliminate these discrepancies. Figure 3.26 shows the difference made by switching this geometry. It is clear that the curved edging makes a fundamental difference to the stress distribution of the blank. Initially this simulation was intended to model the most simplistic approach possible whilst maintaining relevance in its results. With enough length behind the point of contact, it was assumed that any inaccuracies associated with the square contact method would smooth out with the length. These iterations have proved that some curvature must be included in all future models, as the meeting between blank and ironing is a sensitive part of the process.

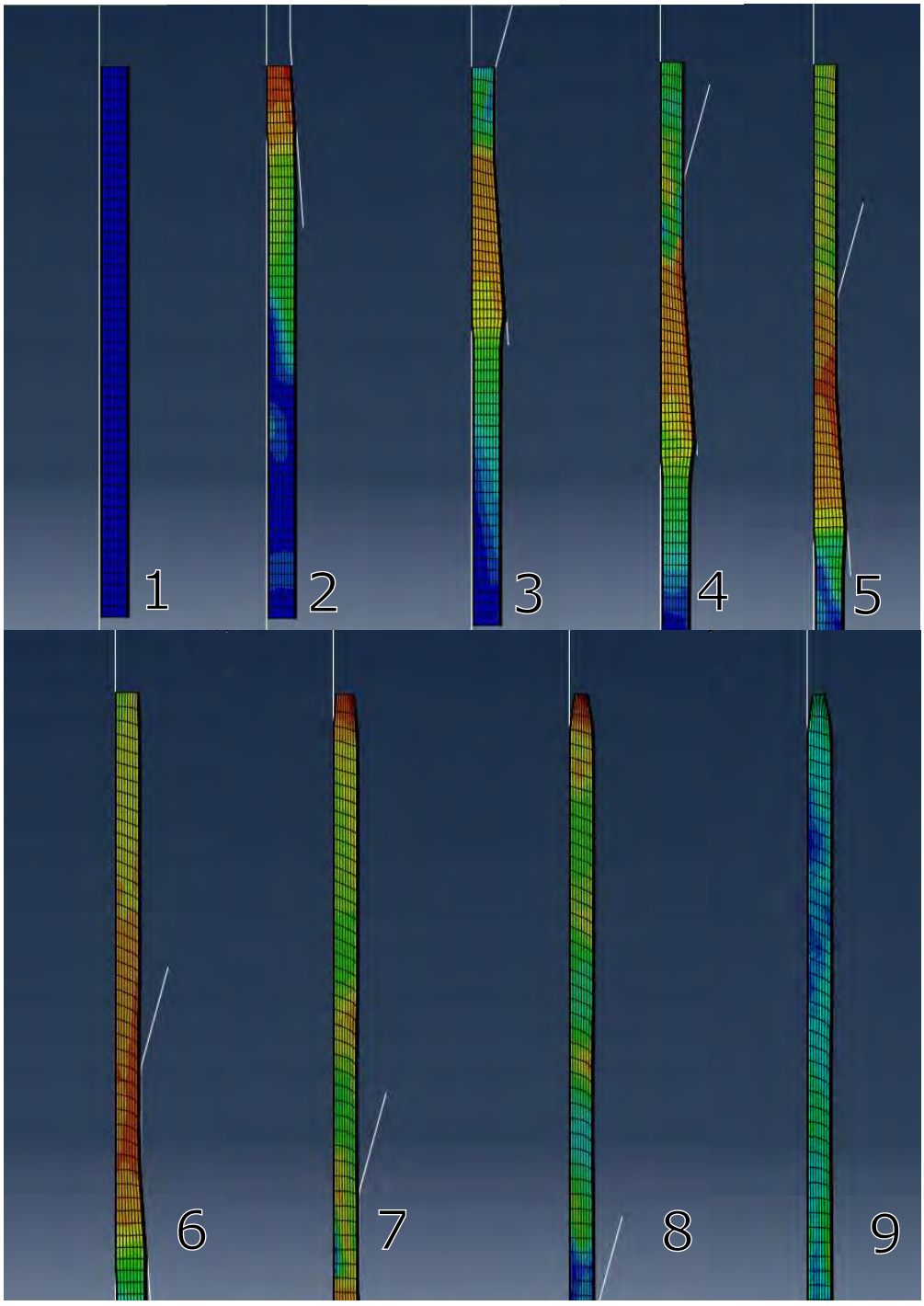

FIGURE 3.25: Evolution of σ_{vm} in the steel ironing model.

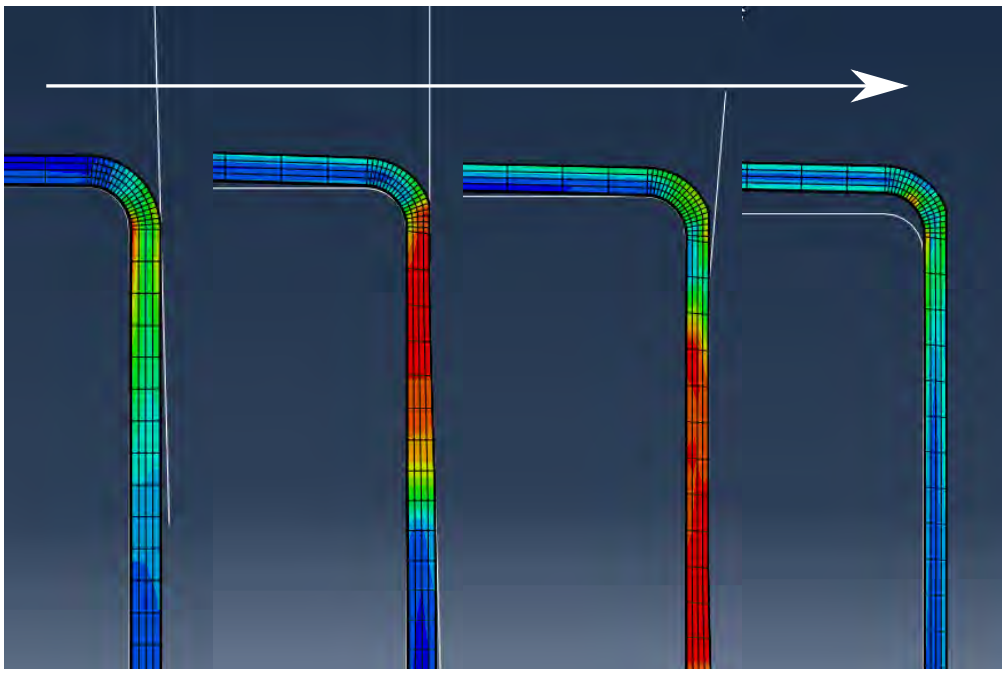

FIGURE 3.26: Evolution of σ_{vm} in the steel ironing model at the simple curved edge.

At this point in the project, it was decided to reintroduce a polymer material to the coating of the model. Despite the lack of material data for relevant strain rates, applying the material gives rise to a much more realistic computational time: simulating multiple materials with vastly different densities slows down simulation substantially [61]. Since the partitions had already been created, the only step required was to apply the material properties to the section.

3.3.2 Optimising mesh geometry

Once these models had been debugged and were working correctly, the next step was to reduce the computational time. The models were taking between 2 and 5 hours to run depending on mesh density, with the finest meshes taking even longer. As gathered from previous studies in this project: the optimal mesh density across the different thicknesses is likely above 5, or perhaps even above 8 elements thick if material behaviour metrology is important. These numbers interacting with the necessity for small aspect ratios elements during ironing (to prevent snagging/elemental distortion as before) gives rise to extremely fine mesh densities and a large number of total elements. These ironing simulations were intended to rapidly model a small part of the DWI process, so keeping computational time to a minimum required an optimisation of mesh geometry.

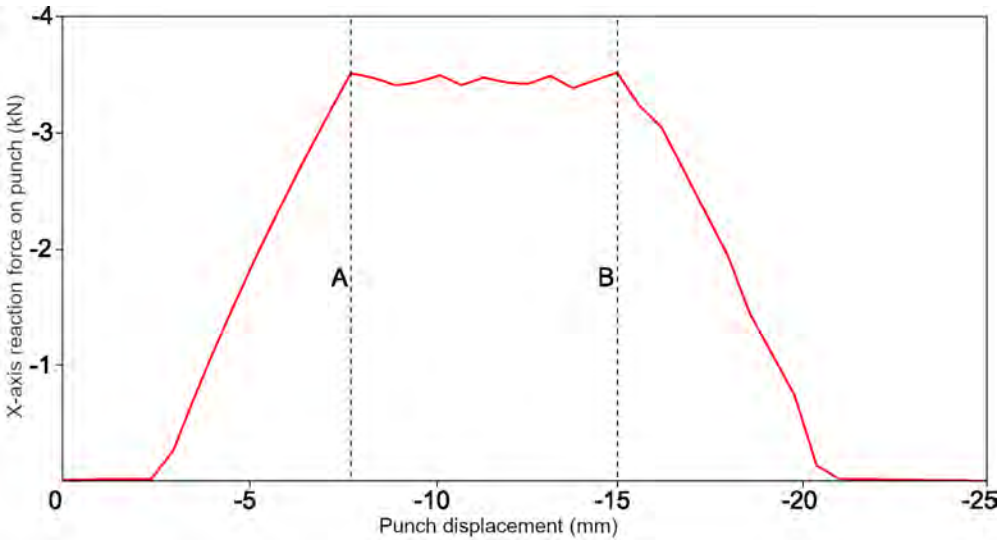

FIGURE 3.27: Graph showing reaction force acting upon punch against the displacement of the punch for the simple ironed steel model.

The first thing to focus on during the optimisation was elemental density across the length of the blank. Figure 3.27 demonstrates the reaction force experienced by the punch during a single phase of ironing. Between points A and B, the ironing reaction force is largely the same. This indicates that ironing has reached a steady state operation, and subsequently results will not change dramatically from one point to another [63]. For this reason the blank can be optimised such that ironing is only steady-state for a small moment in time: as all further ironing will give approximately similar results.

Since it is seen that prolonged ironing causes reaction forces to reach steady state, computational time can be reduced by reducing the area of the blank undergoing ironing. The speed of the punch should be kept the same to account for proper strain-rate data, so the entire blank must be shortened, or a smaller area meshed as finely. The polymer coating need only cover the area of fine mesh for the same reason. The optimisation of the mesh across the blank was undertaken on a largely trial-and-error basis, as the scale of the work did not justify a prolonged DoE optimisation.

Figure 3.28 illustrates the differences in mesh density along the length of the blank. Enlarged sections demonstrate the step-down geometry implemented, focusing closer on the mesh itself. The mesh features the same number of elements across each thickness of each material (in this case only 4 elements across each thickness), and a varying number of elements across the length

depending on which part of the geometry is experiencing contact. It is necessary to keep some material either side of the important results-yielding section to ensure that deformation effects are fully considered. Section A shows the step-down along the top edge; the curvature meeting the ironing ring and surrounding area is finely meshed to preserve accuracy. The rest of the blank to the left is meshed far more densely, with a 2:1 bias towards the curved edge. Section C demonstrates the same behaviour at the bottom edge of the blank. In both cases the polymer ends abruptly, without waste sections: as the residual stress stored in the order of $10\mu m$ rolled PET film is plays an insignificant role in altering the steel [74]. Section B and C demonstrate the main meshing area, which holds a consistent mesh density along its length and width. In this case the mesh is quite coarse, but in other models this area alone changes in density whilst the other areas remain the same.

This optimised mesh geometry approximately halved the computational time and results were identical. For this reason the simulations all utilise this mesh geometry moving forward.

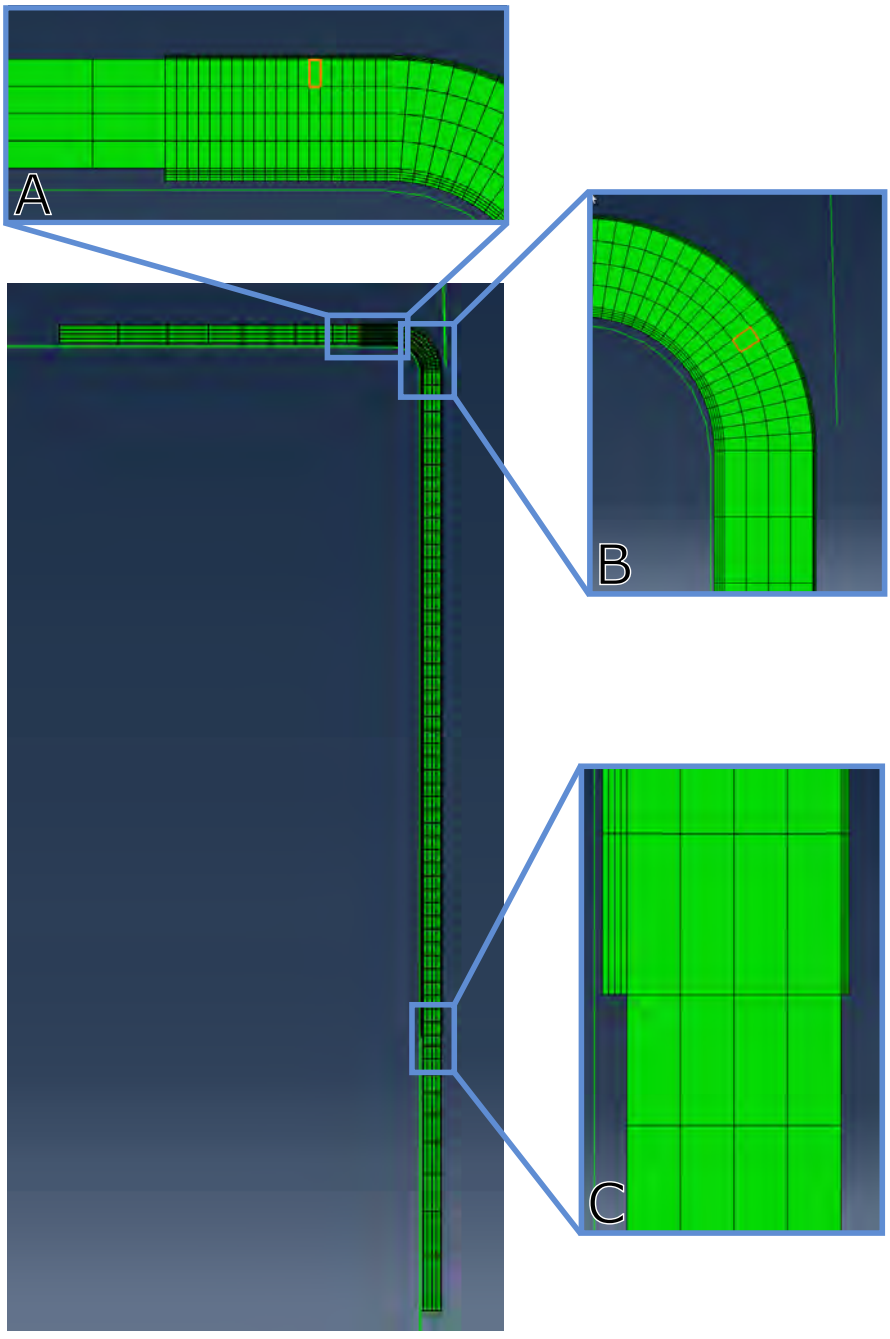

FIGURE 3.28: Diagram demonstrating the optimised mesh of the steel/polymer ironing model.

3.4 Using Input files and script

The CAE interface is not the only way to prepare Abaqus simulations. An alternative method is to use a text-based input file, which relays all necessary information for model generation and execution to the Abaqus solver via a command line. In CAE, a force or boundary condition might be specified in using a GUI: filling out appropriate boxes in sequence and clicking generated geometry to select surfaces. Using input files on the other hand, the same force or boundary condition may be specified using lines of code such as:

```
*BOUNDARY,OP=NEW,TYPE=VELOCITY
PUNCH,2,2,-0.5
```

To specify a velocity acting upon the *Punch* set of elements (or nodes), in the 2nd degree of freedom, with a magnitude of 0.5. Naturally this approach only works well when built up from the bottom. Nodes, elements, surfaces, sets, etc., must first be generated and named before any behaviour can be projected upon them. The approach is more time-consuming than using CAE, but allows for a clearer view and understanding of the simulation data. Input files also allow for some behaviour which cannot be specified in the CAE interface.

3.4.1 Parameterising

A main advantage of input files is the ease of parameterising for fully customisable variables without changing any code or doing any extra legwork. Using the keyword:

```
*PARAMETER
```

allows the specification of any parameter used at any point in the text file. For example, the following code plots a 2 by 3 rectangle *A,B,C,D* (which is then illustrated in figure 3.29) . By specifying the width and height of the shape, and the coordinates for the first node, all subsequent nodes can be plotted via derived parameters. In this sense the width, height, and position have been parameterised. The coordinates of A, and position of the rectangle can be easily changed without altering the shape or size.

```
*PARAMETER
WIDTH = 2
HEIGHT= 3
AX=1
AY=0
BX=AX+WIDTH
BY=AY
CX=BX
CY=BY+HEIGHT
DX=AX
DY=CY
```

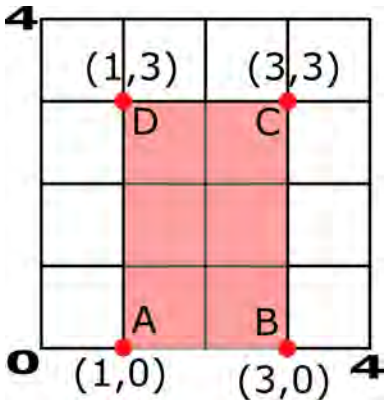

FIGURE 3.29: Demonstration of the plotted parameterised X and Y coordinates for rectangle *A,B,C,D*.

All geometry and simulation data can be parameterised, meaning angles, widths, and material properties can be easily exchanged. There is no limit to the extent of parameterisation in an input file, and parameters can be derived from other parameters. Software such as *Simulia Isight* can be used in this manner to read parameterised input decks and draw these parameters into a design interface where various studies can be undertaken on the input file to explore and analyse the effects of changing parameters in an optimisation or design of experiments. This approach will be useful later in the project to allow parameter studies and Design Of Experiments studies to be run.

3.4.2 Calling *include files

As with any coding method, input text files can be an unlimited number of lines depending on complexity of model geometry and setup, which makes file navigation and alteration difficult. To solve this problem, *Include* commands can be used to compartmentalise different parts of code into specific *.sets* files. A master file can be created which calls in all necessary data from other .sets files. The example below demonstrates a command file calling in all necessary data for materials, tooling and blank geometry.

```
*Include, input=PARAMETERS.sets
*Include, input=Tooling_ring.sets
*Include, input=Tooling_punch_curved.sets
*Include, input=Blank_curve_8x100_optimised.sets
*Include, input=TH330.sets
*Include, input=PETimp.sets
```

From this point on, only contact pairing, interactions and Step data need be specified in the master file. In point of fact, all of those could be called in from separate .sets files too if necessary. In this particular case, this kind of method reduced the master input file by almost 1200 lines.

Using *Include files, a combination of CAE and input files can be utilised for the most efficient model setup. CAE is preferential if complex and extensive geometry like the ironing punch is being used. CAE's GUI is a far easier environment for the generation of complex shapes, as the user can use shape and dimensioning to draw these models in a 2D or 3D plane. Trying to manually code the coordinates of a complex 2D shape or 3D shape would be incredibly challenging, so CAE holds that advantage in geometry generation. CAE can generate an input file from all specified model data - which can subsequently be changed to a *.sets* file, and drawn in with an **Include* command. In this way, the simplicity and transparency of input files can be kept whilst ensuring complex geometry is properly and easily generated by CAE.

3.5 Implicit vs explicit time integration

Once the modelling method had been streamlined it was decided that the differences in modelling between implicit and explicit processes should be investigated. As explained in Chapter 2, Implicit results do not consider inertia and appropriate mass properties, so an implicit method could lose out on a reasonable level of accuracy compared to explicit during high speed ironing - where inertial effects are more prevalent [75]. A study was undertaken running both explicit and implicit models for the previously seen curved blank geometry at punch speeds of 3m/s, with element densities listed in table 3.3. Bold numbers across the top and left side signify number of elements across the thickness and length respectively. The corresponding cells demonstrate the total number of elements for that combination.

TABLE 3.3: Mesh sensitivity study mesh densities for the implicit vs explicit investigation.

×	**4 thickness**	**6 thickness**	**8 thickness**
100 length	400 total	6000 total	800 total

The results of the study are demonstrated in figures 3.30, 3.31, and 3.32. Figure 3.33 has been included for simpler comparison, but some lines overlap between runs. The explicit simulation running for the 6x100 combination repeatedly failed due to snagging, but has been plotted incompletely for the sake of clarity. The implicit simulation for 6x100 still demonstrates a clear shape correlation with the other implicit models. Increasing the elements across the thickness seems to alter the overall reaction force to closer match the explicit models (though the absence of data for 6x100 challenges that assumption). The densest element combination on 8x100 shows the closest relationship between implicit and explicit, whereas the data for 4x100 varies substantially after the ironing is finished at around $-20mm$ displacement. This points towards the notion that increasing the element density reduces the difference in results between using implicit and explicit. This may prove for higher speed models as Implicit runs in a fraction of the time compared to explicit [76]. In this case switching from explicit to implicit methods reduced run times from approximately four hours, to 30 minutes on the 8x100 model. Figure 3.33 has been included for simpler comparison.

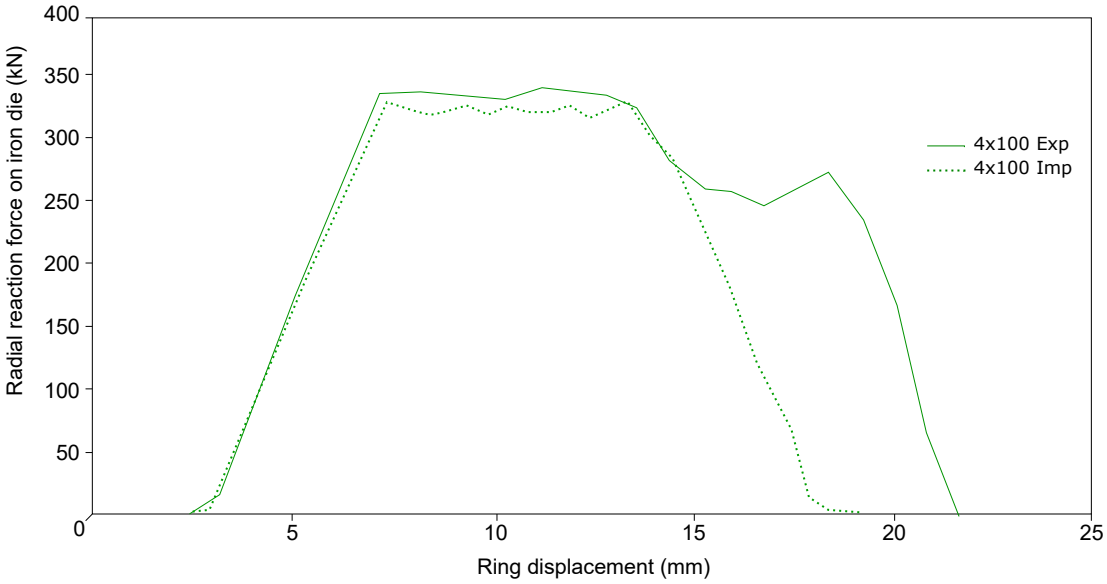

FIGURE 3.30: Graph of radial reaction force against ring displacement featuring implicit and explicit model data for the 4x100 mesh.

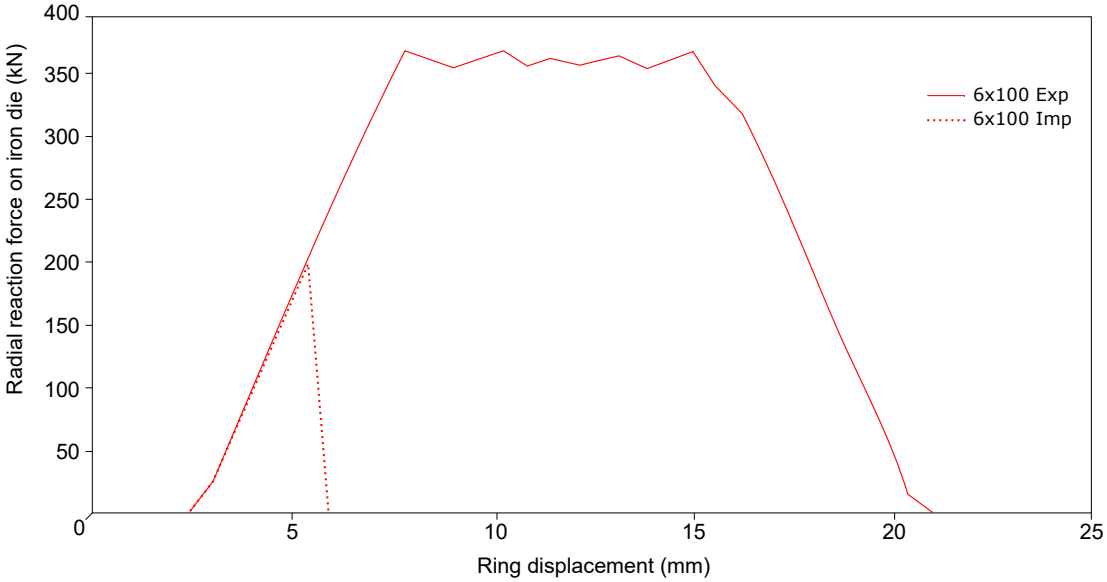

FIGURE 3.31: Graph of radial reaction force against ring displacement featuring implicit and explicit model data for the 6x100 mesh.

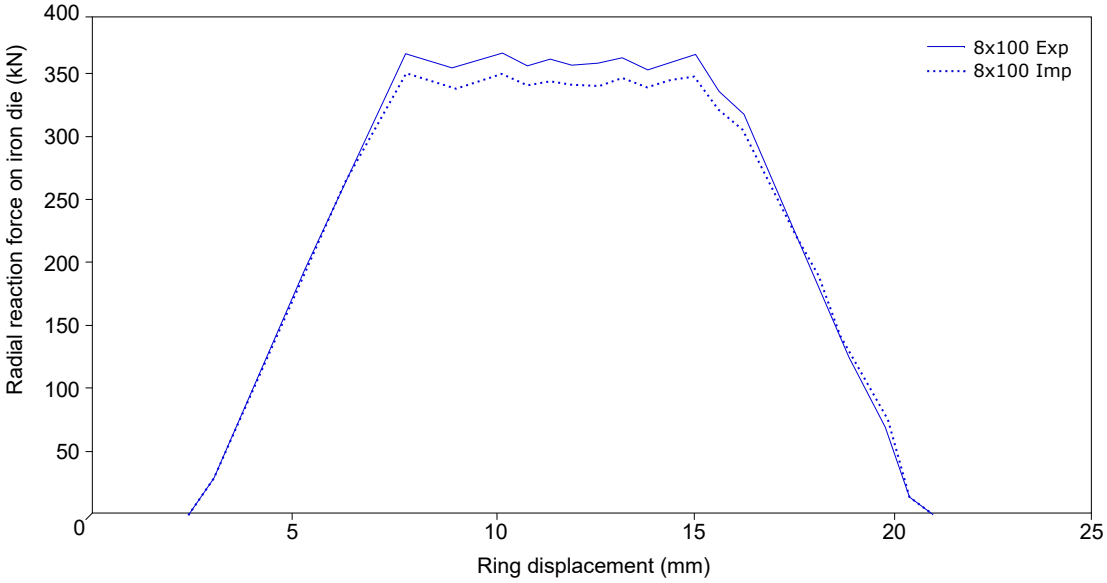

FIGURE 3.32: Graph of radial reaction force against ring displacement featuring implicit and explicit model data for the 8x100 mesh.

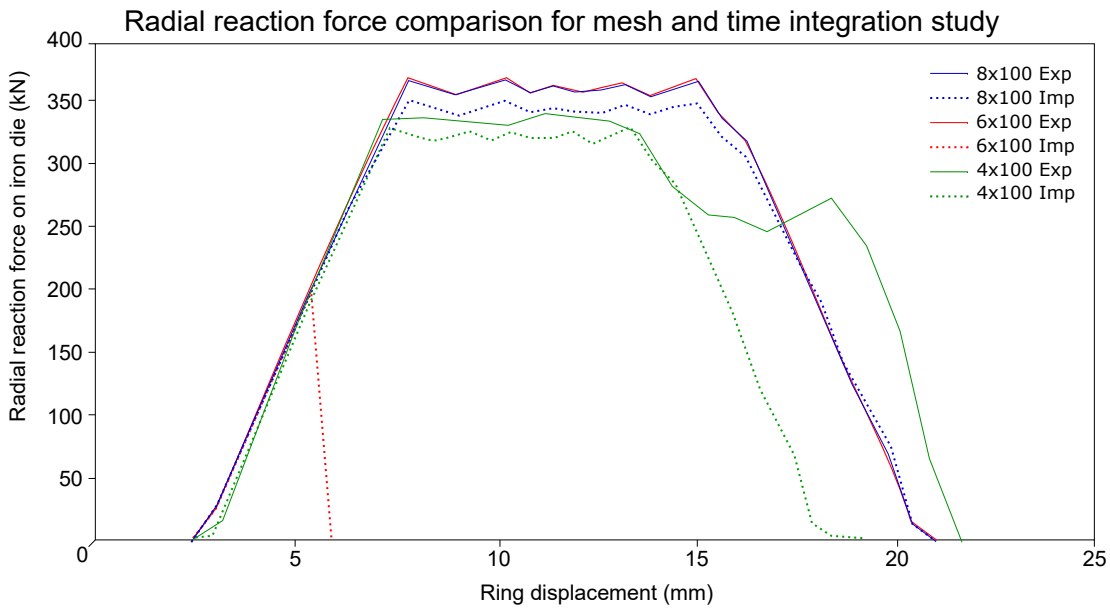

FIGURE 3.33: Graph of all radial reaction forces plotted for comparison.

Finally, these results answer the earlier query regarding the vibratory/oscillatory behaviour experienced during the ironing stage. Since vibration is a product of mass and inertia of the specimen [77], it is not accounted for in the implicit models[78]. Regardless, this oscillation in the reaction force is still present in the implicit simulations, implying that the oscillatory behaviour seen in all models so far is not a product of simulated vibrations/waves, and is instead something altogether different, such as a mesh stepping. This may prove to be an area of investigation as the project progresses.

3.5.1 Conclusions

The work in this chapter has reached a decisive conclusion about the modelling methods and approaches best suited to the DWI process. Investigating the mesh sensitivity has highlighted the requirement to keep the metallic element count as high as possible throughout the ironed sections, whilst minimising element count in less deformed areas in order to minimise computational time. The use of restart analyses will be critical in the DoE studies involved later in the project, as the fixed tooling sections of the process can be bypassed with each subsequent run. The difficulty modelling multi-layered substrate highlights the need for further investigation into modelling specifically polymer-coated metal blanks, and will be addressed with detail in chapter 4. Finally the differences between the implicit and explicit solvers demonstrate positive and

negative attributes associated with each. The two solvers will be used throughout the project: using explicit when strain-rate and process speed is a significant factor, and using implicit when computational speed is imperative whilst process speed is not.

Chapter 4

Modelling the polymer film

4.1 Introduction

Having gained a fundamental understanding and knowledge towards the key mechanisms involved in modelling the DWI process in Abaqus, the focus shifted towards the complicated and inconsistent behaviour encountered when modelling the polymer-coated metal. This branch of the project pursued the polymer specifically: first attempting to characterise the material using experimental procedures with tensile testing machinery, and then progressing to modelling the polymer using different approaches in Abaqus to best capture the effects of a polymer-coated metal. By the end of this chapter, a preferred method of modelling the polymer-coated material will have been established, and this method will be verified using experimental trials in chapter 5.

4.2 Characterising the material

4.2.1 Tensile testing the polymer-coated steel

The characterisation of the coated steel via tensile testing was attempted at various stages throughout the project. Unfortunately, the lack of friction between tooling clamps and the polymer coating resulted in consistent testing failure - as slipping occurred before significant yielding. Various tooling clamps were utilised in addition to a slot-in set of draw-beads, but fundamentally the clamping force provided by the hand-operable specimen clamps was insufficient. Mechanical or chemical removal of the polymer layer could have changed the material properties or compromised the specimen, and bolted specimens were unable to be obtained, so the project moved past the material tensile tests and

focused on the characterisation granted by a bespoke ironing rig, detailed later in chapter 5.

4.2.2 Compression testing the polymer-coated steel

Due to the microstructure (chain molecules) of polymers, they behave differently in tension and compression. Characterising the tensile properties of such a material was outside of the scope of research for this project due to the specialist apparatus required to tensile test at such small loads. In an attempt to quantify the compressive properties of the PET layers, a compression test was undertaken using a tensile testing machine. The apparatus was set up to sandwich a stack of 10, 5, and 2 polymer-coated steel disks between compression plates. The machine measures force and displacement of the compression punch, and so using the equations 4.2 and 5.10 (given a known area and specimen length) those metrics were derived into a stress and strain plot.

The expectation is that a stress and strain plot characterises the material - not simply the application of it. In this case it is expected that every stack of coated disks would produce the same (or similar) stress/strain plot - even though the force/displacement plots would differ significantly. Instead, the results clearly seen in figure 4.1 demonstrate quite a significant difference between each curve.

TABLE 4.1: Gradients (2 decimal places) of PET-stack compression stress/strain curves.

Stack	Gradient
2	8.48
5	18.71
10	34.89
20	125.19

To clarify these results, further study was undertaken at Crown on a different machine. The resulting data points towards the unsuitability of compression equipment for such high loads and such small specimen thickness. It's likely that the *stress/strain* curves seen are not representing the PET nor steel at all, but are instead demonstrating the compliance in the load cell of the compression machine.This is supported by the fact that Crown's machine follows the trend that increasing stack size increases the gradient of the *stress/strain* curves (which again, should be unaffected by volume); but begins the steep gradient far sooner than the other tests. This indicates that the compliance on the University apparatus was substantially different to the compliance on Crown's

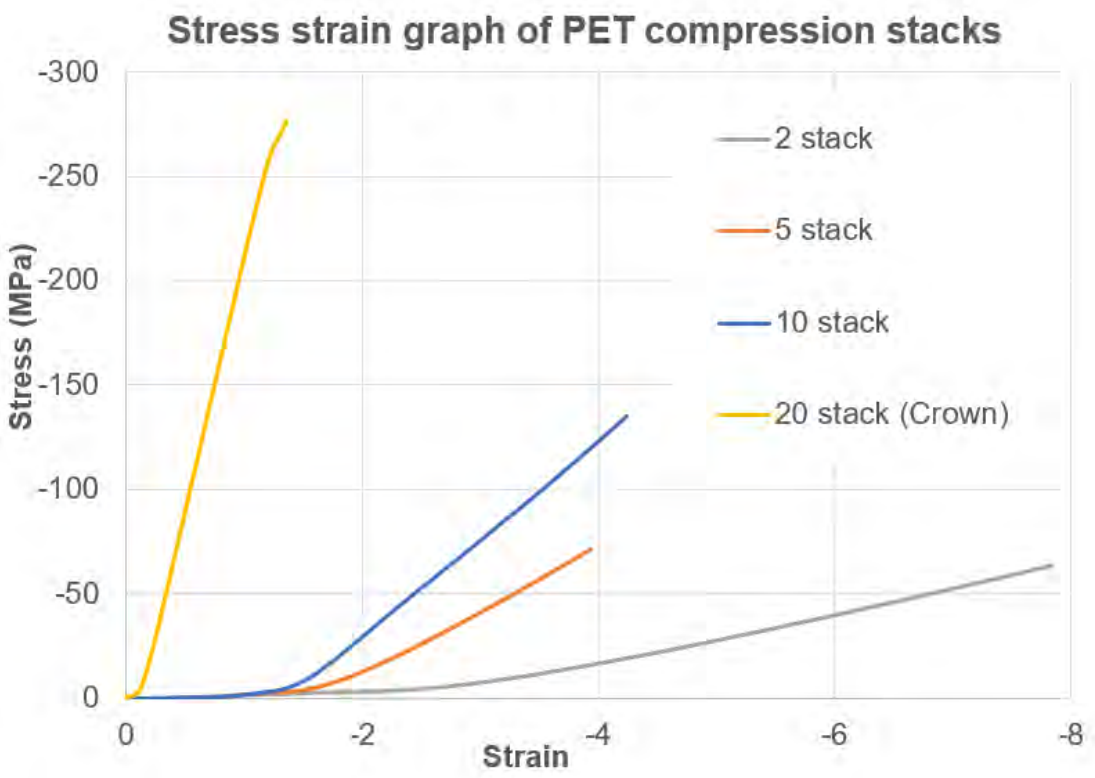

FIGURE 4.1: Stress/strain curves for various stacks of 14.4mm diameter PET-coated steel disks during compression. Derived from force/displacement data from the data-logger attached to the load cell.

machine - since the other three tests follow the slow gradient increase despite the change in stack size. These results are interesting, but do not provide clarification for any of the scientifically-grounded expectations of the materials. Fundamentally the material characteristic of PET coatings itself is not a primary subject of this research, and so this work instead serves as a reasonable point to abandon the simple characterisation of the PET itself, and instead focus on a numerical representation which best matches the testing outputs.

4.3 Modelling contact

The simulation of the entire DWI process for laminated metal is a computationally heavy demand, so a primary objective in the project is to reduce computational time in whatever way possible. FEA calculates a stable time increment per element, and the minimum time increment for all elements is what drives the computational time. Time increment is calculated on a number of factors including element size, aspect ratio, and material properties. As a result, simulating three layers comprised of 2 different materials an order of magnitude

apart in thickness and several orders of magnitude apart in tensile strength, yield stress, and density is always going to see higher run times than a simulation of just metal [79]. This situation pinpoints an area for improvement in the simulation process.

A simulation was constructed in Abaqus CAE to explore the detail and characteristics necessary when modelling the laminated metal. A 2D plane strain construction was chosen in order to represent a finite area of material during a single ironing phase without complicating the model or adding further load. The model used tooling geometry from a standard industrial setup, and dimensions of stocked PET-coated steel. Tooling was generated from rigid analytic surfaces and the blank partitioned into three material layers, meshed appropriately. The construction of the tooling model and blank can be seen in Figure 4.2. CPE4R elements were used for all the meshing to best demonstrate a thin slice of material, and each layer of polymer had the same mesh density. Shell elements were briefly investigated for the layering technique, but since there was no way to understand what relevance the interaction between metal and polymer strain distributions would be, continuum elements were elected to maximise potential for data. Metal mesh was much coarser since the focus of study was primarily the lesser-studied polymer and any potential associated engineering data. These layers were made up using TH330 Steel in the centre flanked by polyethylene terephthalate (PET) material definitions. The bend seen in the blank geometry was included as a solution to the interfacing problem between a straight-cornered surface and an angled die. The shape of the curve approximately follows the punch, but extends only minimally past the point of first contact: in order to minimise computational load.

The movement of the system was modelled by moving the die in a vertical (Y axis) positive displacement. X and Z degrees of freedom were fixed for the die, whereas all degrees of freedom for the punch and the lower edge of the blank were fixed. Arrows representing fixed boundary conditions can be seen in Figure 4. During the CAE modelling phase, numbers such as displacement magnitude and step time were arbitrarily set to 1, and later overwritten in the input file for a simpler approach to altering variables. For this step, interactions were created between the rigid bodies and the deformable blank using a penalty contact [80] method with finite sliding and an industry-standard friction property of 0.1. Material data for the TH330 was taken from an existing benchmark [58]

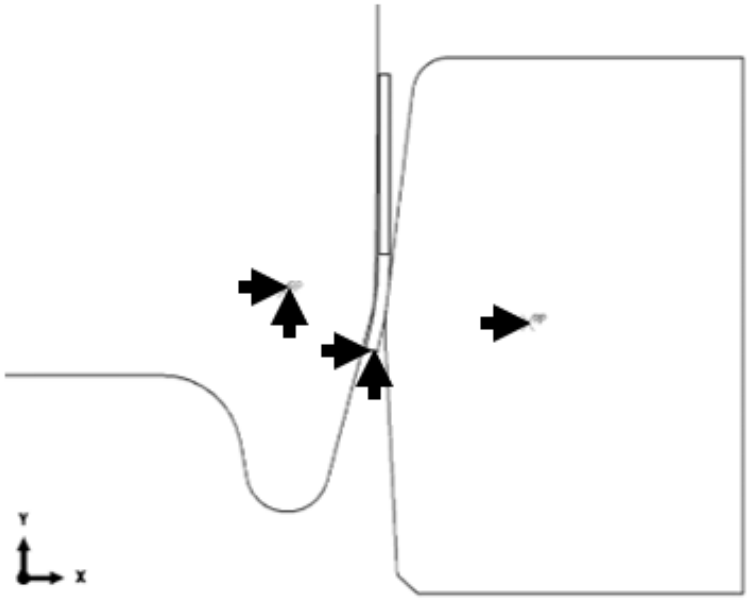

FIGURE 4.2: 2D basic strip model outline with visualised boundary conditions.

and input as density, elastic, and plastic definitions using a Johnson-Cook formula for plastic deformation. PET data was taken from *Van der Aa's* tensile testing work [71] and input as plastic using tabular data. At this point it is important to note that the accuracy of the PET characteristic model is not the focus of this paper. Instead this work focuses on the comparison between different ways to model a laminate and thus any data could be used assuming it is used consistently throughout.

4.3.1 Modelling PET-coated steel using mesh in Dynamic explicit

The direct method for a laminated metal model would be approached by meshing all three layers of material separately [81] but keeping geometry attached. This allows identification and metrology of any movement or engineering variables occurring throughout the polymer and steel layers but does not necessitate a contact interaction between the layers. The primary directive in this section was to find out the necessary element count to properly conserve material data during simulation. Generally, Crown simulate using between 4 and 8 elements throughout the thickness of the material (the X axis in Figure 4), and any number of elements throughout the length (Y axis) depending on necessity. Elements do play a part in increasing computational load, so the target is to achieve mesh independence using the fewest (or largest) elements possible[82].

As a standard, 100 elements were used throughout the length of the blank, split into 50 throughout the curved section and 50 throughout the straight section. This number was kept constant throughout the study and at no point showed signs of snagging or otherwise interfering with data. Dynamic-Explicit simulations were run with 1, 2, 4, and 8 elements through the thickness of the polymer layers, and 3 elements through the metal thickness. The results can be seen in figures 4.3 and 4.4, as well as table 4.2.

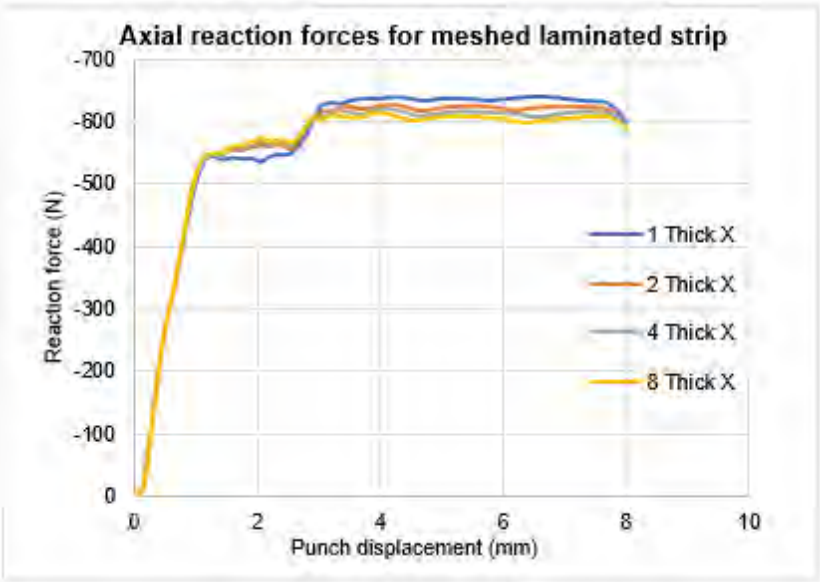

FIGURE 4.3: Axial reaction forces for PET and steel meshed simulations in dynamic explicit.

Elements across PET thickness	1	2	4	8
% Thickness reduction	31.2	32.8	33.63	33.95
% Elongation	26.7	27.89	28.52	28.87
Run time (hours:minutes)	00:27	00:43	01:56	04:45

TABLE 4.2: Comparison of geometry changes during ironing of different mesh densities in the polymer layer. This data is represented pictorally in figure 4.4.

The results clearly demonstrate that increasing mesh density through the polymer layer has minimal effect beyond a threshold. There is a noticeable difference between using 1 and 2 elements across the polymer thickness. The shape of the curves in Figure 4.3 change drastically between these two data sets and differ minimally beyond that, with error percentages not exceeding 5% between 2 and 4 elements through thickness. The data of the 1-thick study varies widely compared to the other three: under-reading and then over-reading force data throughout the process. There is some minor deviation in the force readings for

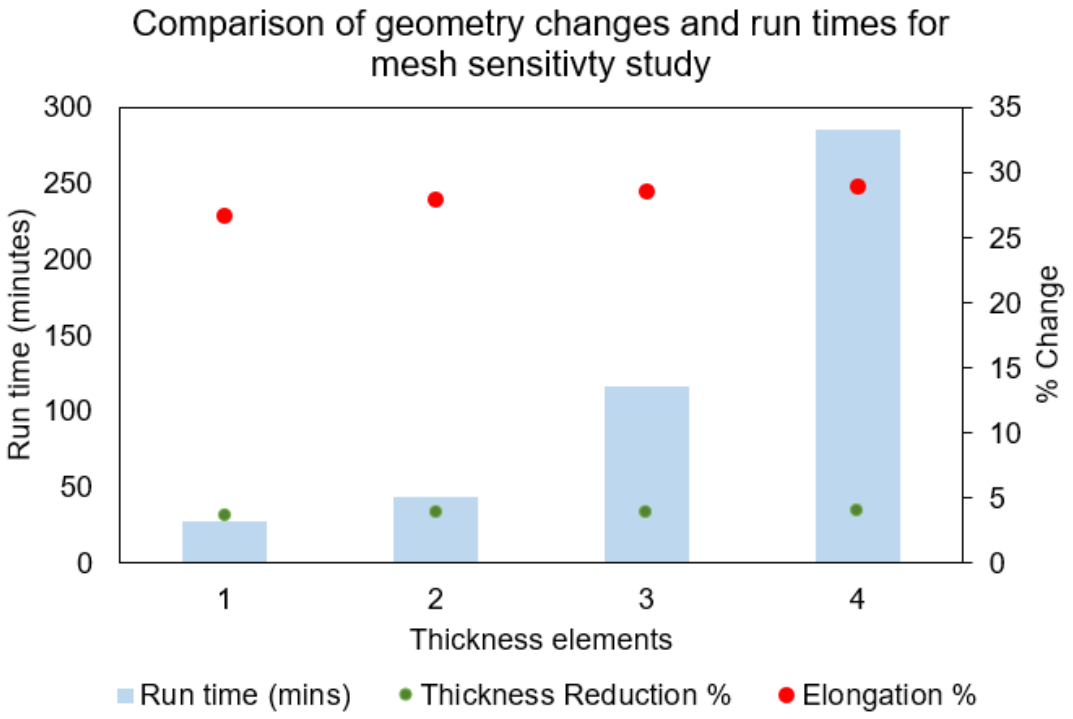

FIGURE 4.4: Graphical representation of the data seen in table 4.2.

the remaining three models after the force has peaked and plateaued, but this is likely to do with the difference in snagging as the rigid modelled surfaces slide freely over the varying node-density in each model. The 8-thick study shows the lowest force reading plateau, which is consistent with this concept, since a higher mesh density decreases snagging on the angled tooling.

Looking to Table 4.2 a trend can be identified: as elements across the thickness increase, so do both thickness reduction and elongation. This equates to a slightly longer ironing effect [83] and is likely caused by the differences in flaring of polymer elements at the final increment, seen in Figure 4.5. Since the effect of ironing was bound to the simulation setup these small differences are marked as anomalies involving the aspect ratios of the unrealistically-constrained elements at the top end of the blank. This issue highlights a need to ensure that metrology is not skewed by the pinching effect at the end of the specimen. The reaction forces should be included as a primary benchmark, as they are less affected by simulative differences such as these. It can be concluded that 2 elements through the PET thickness is optimal with regards to accuracy and computational time, so it is rational to use 2 elements when meshing PET is the only option. However, for the comparative study, 8 elements will be used as the benchmarked model is only ran once and thus an increased simulation time

is acceptable for any increase in accuracy.

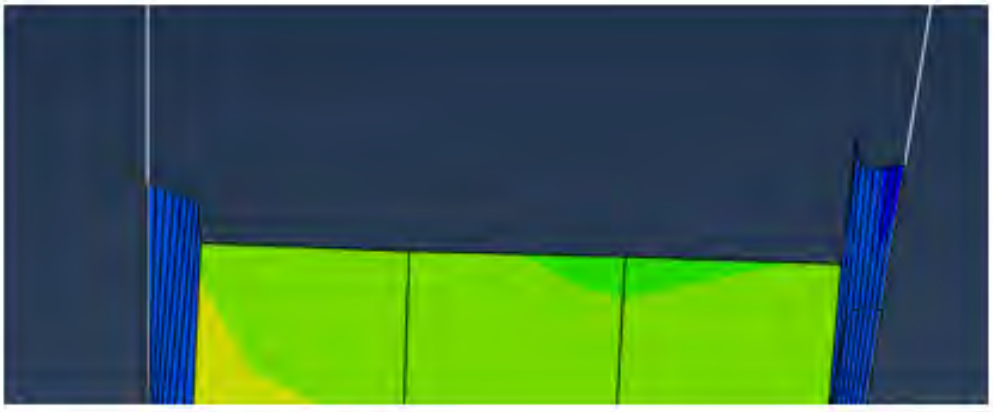

FIGURE 4.5: PET elements flaring at the end of an ironing simulation.

4.3.2 Modelling PET using a contact definition

The meshed simulations are computationally heavy as one would expect. Varying densities, yield strengths, youngs moduli, and element aspect ratios increases the processing load[84]. For this reason, any plans to run a DoE study on an entire can bodymaker tooling geometry highlight the need to simplify the models where suitable. After concluding the mesh density of the PET layer makes minimal difference to reaction forces, and noting the entirely homogenous behaviour of the stress distributions of the PET elements, the study progressed into investigating whether the PET layer be meshed at all. The pursuit turned towards simulating a PET [85] coating using a pressure/overclosure contact definition in Abaqus to impart upon the steel the same forces that a strip of PET would at the same proximity to the die. Reducing the mesh and materials in this way hoped to reduce run times, enabling more efficient optimisation whilst maintaining the results of a fully meshed model.

Obtaining a compression material model for PET

The first thing required for a properly calibrated contact definition was to create a simple force/displacement plot for the PET definition. This was done by constructing a small block of defined PET with a known size in Abaqus and compressing it in a 2D simulation between a moving and a fixed rigid surface. Sliding boundary conditions were fixated along the two exposed surfaces to ensure that the material was compressing and not simply displacing along the walls. A single CPE4R element was used to mesh the block and the contact

definition was defined using the same penalty contact/finite sliding method as before. This produced a plot of force and displacement, the force was then converted to a pressure and the displacement to strain using Equation 4.1 and Equation 4.2 [86].

$$P = \frac{F}{A} \tag{4.1}$$

$$e = \frac{\Delta l}{l} \tag{4.2}$$

Where:

- P is pressure derived.
- F is force applied.
- A is area onto which force F is applied
- e is strain
- Δl is the change-in-length of the PET block
- l is original length of the PET block

Figure 4.1 demonstrates the force/displacement data from the PET simulation and corresponds to the data entered for the PET material definition in a very limited manner. This is to be expected as the plastic definition is tabulated, but highlights an issue with the PET material data available. Following the line on Figure 4.1 would yield a linearly high force as thickness tends to zero, with no regard for interlocking or dislocation polymer chains [87], or any reasonable plastic behaviour.

Abaqus holds a material-evaluation function within the material model, which requires any known material data to be entered and subsequently computationally derived into a number of known material models. The tabulated PET data was entered in the material-evaluation module and the data set to hyper-elastic material models. Figure 4.7 demonstrates methods used and their results[88]: dotted lines represent the point at which the model was calculated as unstable and thus ineffective for the prediction of material behaviour. Various other

definitions were attempted but all not displayed failed before data could be produced. Instead the decision was made to use linearised polymer data available as the accuracy of the material definition itself is not important to the method of modelling which this chapter investigates.

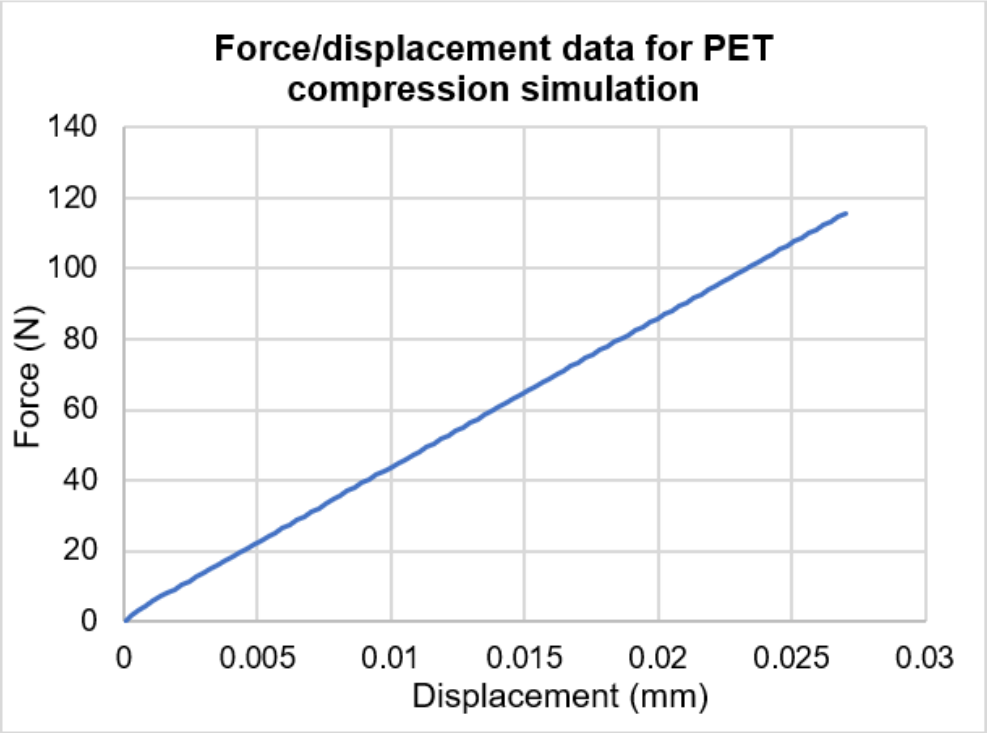

FIGURE 4.6: Force displacement graph of the compression simulation undertaken for a PET definition.

The conversion from displacement to strain was required to account for the differing thickness in PET layer either side of the steel. Displacement data was converted to strain using the same method as before (equation 4.2, and force data converted to pressure using equation 4.1. Two material definitions were created by proportionally shifting the values of pressure and strain until zero strain had been achieved at -30 microns and -20 microns respectively. In this sense the contact definition would apply no force until the die was close enough that a PET layer would have been displaced, were it being modelled with a mesh, for both of the differing layers of PET. Due to the unstable nature of the polymer compression curve derived from the simulation, it was decided that an exponential curve should be pursued, as it better matched known stress/strain curve patterns of PET in existing literature [89]. The adjusted simulation pressure/overclosure data was plotted and exponential definition using Equation 4.3 was tuned to approximately match the shape of the data.

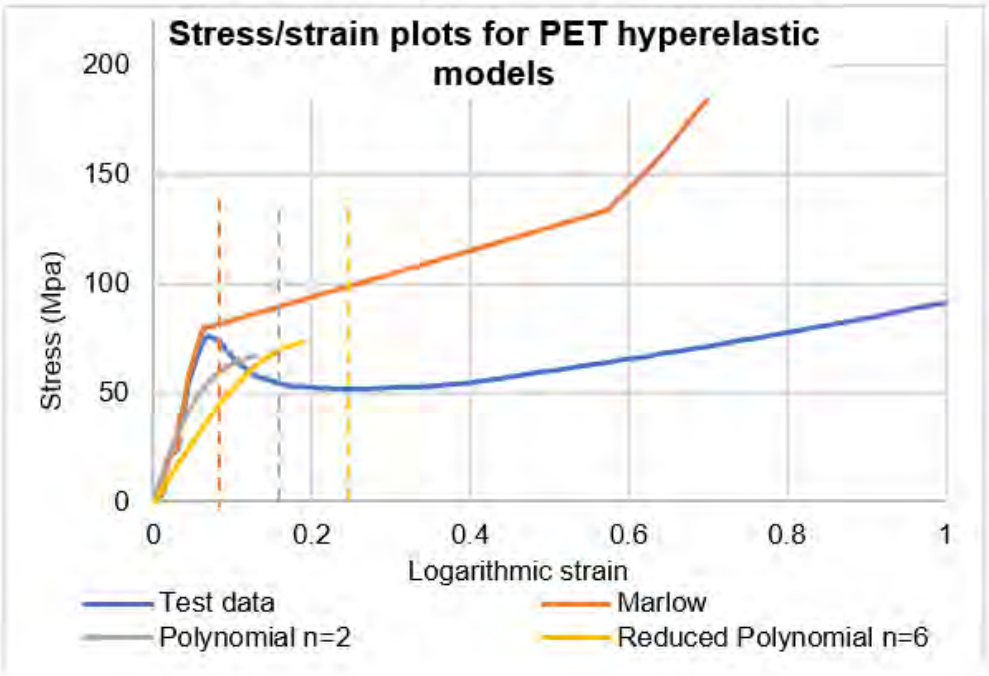

FIGURE 4.7: Stress strain plots for PET hyperelastic models derived in Abaqus.

$$P_z = Mn(x_z + x_0)^n \tag{4.3}$$

Where:

- P_n is the force data for a given data point z.
- M and n are coefficients for the exponential curve.
- x_z is the overclosure distance for given data point z.
- x_0 is the initial increment for the overclosure distance, which accounts for strain adjustment.

Using this equation, an initial exponential curve was set for both PET layer thicknesses, using the same coefficients but scaling with their width appropriately. This allowed a simple and direct transition of the data into an input file associated with the pressure/contact definition using the following input:

```
*parameter
n = value
M = value
Mn = M**n
```

```
**Layer 1 coefficients
PT1 = value
increment = value
**Layer 2 coefficients
PT2 = value
increment2 = value
x1 = value
x2 = x1+increment
P1 = (x1+PT1)**n*Mn
P2 = (x2+PT2)**n*Mn
```

These parameters would later be referred to in the surface interaction definition:

```
*Surface Interaction, name=Polymer1
*Friction
value,
*Surface Behavior, pressure-overclosure=TABULAR
<P1>, <x1>
<P2>, <x2>
```

This input of P and x is continued for as many values as is required until x = 0 in each of the two layers of polymer.

4.3.3 Optimising the contact definition in Isight

To best achieve matching behaviour between meshed and non-meshed PET models, an optimisation via commercially available data modelling software *Isight* was employed[90]. Using an iterative improvement approach via various optimisation routines, Isight can work towards a specific parameter-based objective. An Isight workspace was constructed using an optimisation loop containing an Abaqus module and a Data matching module. The Abaqus module was setup with the parameterised input file as the input, and the matching *.odb* file as the output after running a mock simulation with arbitrary parameter values. Parameters M and n were pulled into the workspace as input parameters and the axial reaction forces on the ironing die were used as output parameters. The Data matching module was included with axial reaction force data from the existing 8x100 fully-meshed PET-layered model used as the Target data. The contact-definition simultion axial reaction force was used

as the comparative simulation data, and a parameter created to measure the Y-squared-difference in the data lines. Finally, in the optimisation module settings the parameters M and n were set as variables, with arbitrary limits based on a trial-and-improvement approach. Minimising the Y-squared-difference parameter was set as an objective, and the Downhill-simplex [91] method configured to allow for an adequate number of simulations for convergence. A different non linear polynomial (NLPQLP) optimisation method was also employed to validate the optimisation and compare methods of convergence[92]. After an initial run, it became apparent that the optimiser was not necessarily completing the full ironing process, and instead comparing only a few increments before the simulation passed failure criteria. These small results sets were being converged upon by the optimiser, achieving minute error for only a handful of increments. A constraint was introduced such that the displacement of the moving die should always achieve maximum, which enabled the optimisers to converge towards a result which achieved the full amount of ironing consistently. The results to the optimisation studies and comparisons can be seen in Table 4.3, Figure 4.8, and Figure 4.9. Downhill-simplex and NLPQLP columns in said tables refer to the data obtained using a contact definition optimised with those respective methods. Assuming that the 8-PET-thickness-elements study is a reasonable benchmark with which to compare the efficacy of the optimisations, both of the optimisations have their advantages.

TABLE 4.3: Comparison of geometry changes during ironing of meshed and contact definition optimisations.

Study Description	8 PET elements	Downhill-simplex	NLPQLP
% Thickness reduction	33.95	41.23	38.35
% Deviation from meshed sim	0	21.41	13.00
% Elongation	28.87	34.90	31.66
% Deviation from meshed sim	0	20.89	31.66
Run time (hours:minutes)	4:45	00:16	00:16

Both optimiser solutions run reaction forces within 10% of the target curve. The Downhill-simplex solution runs slightly closer to the target than the NLPQLP solution, but does so at the expense of a more severe ironing effect characterised by the dramatic increase in elongation and thickness reduction visible in Table 2. Equally, the NLPQLP solution runs slightly further away as far as

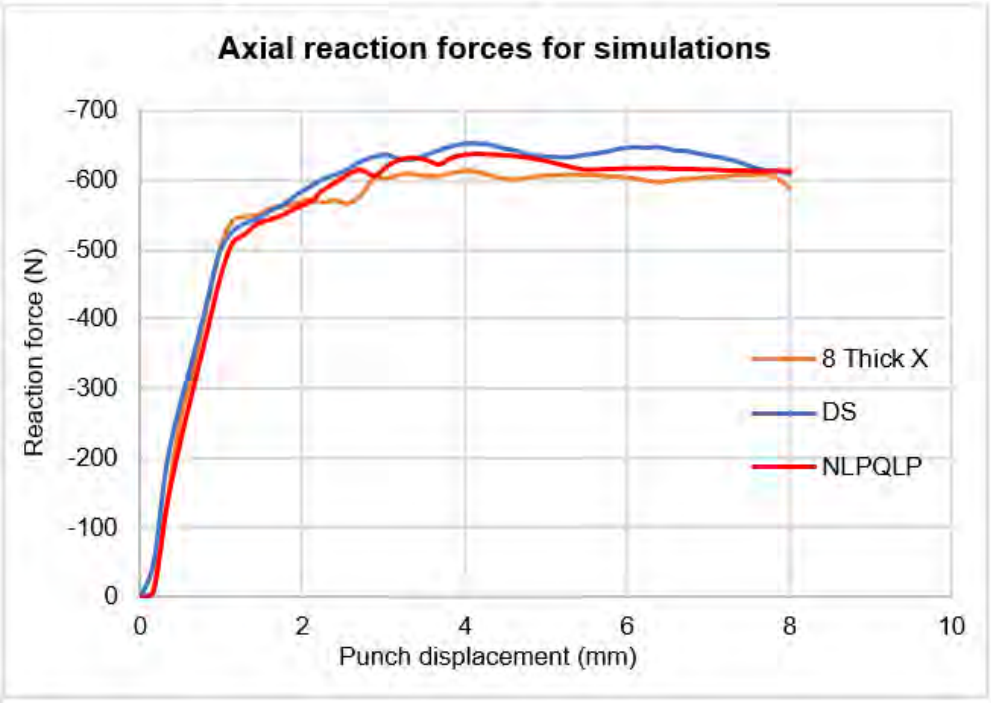

FIGURE 4.8: Graph comparing X axis reaction forces of meshed and contact definition simulations.

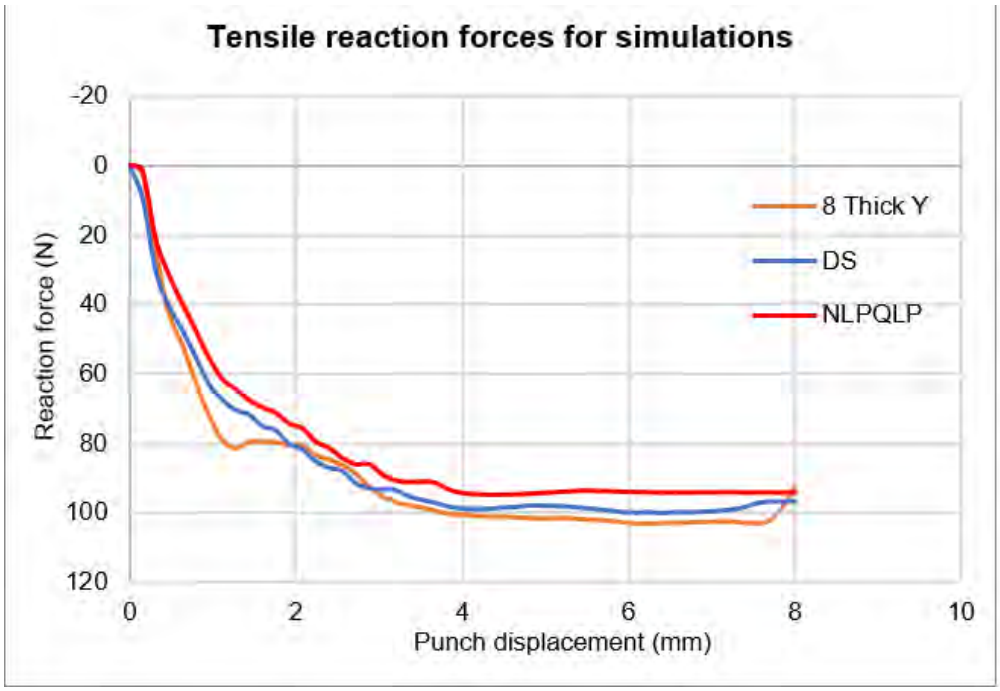

FIGURE 4.9: Graph comparing Y axis reaction forces of meshed and contact definition simulations.

reaction forces but achieves a closer ironing effect. It is noteworthy that both optimised contact-definition solutions essentially iron too much, though is difficult to tell which of the two optimisations is more suitable as the data is not

accurate enough to replace the meshed benchmark at this point.

The optimisations are promising, but dont yet effectively match the meshed simulations. Regarding the efficacy of the optimisation solutions the PET definition itself is not important, however for the progress of the project it becomes imperative to ensure that the basis of comparison is an effective and verified data set. To further progress the optimisation a more robust objective is necessary. Presently the data matching set only works on a single axial reaction force, and the similarity of other objectives like elongation are derived from the nature of the model but are not specifically being targeted. Introducing objectives for tensile reaction forces as well as elongation and thickness reduction would ensure that the final optimised solution satisfies every criterion available. For the time being it can be concluded that the Isight optimisation method is an effective approach to building the pressure/over-closure contact definition: which is itself a promising alternative to fully meshed laminated models.

4.3.4 Conclusions

The work undertaken in this chapter has sufficiently explored the major available methods for studying the polymer layer. The work has demonstrated the challenges involved in properly characterising coated materials with significantly varying properties, and highlighted the necessity for an alternative method. The contact definition method shows promising results: allowing an alternative approach when specific material characteristics remain unknown, and the coating itself is not considered a focus of study. This chapter has achieved its aims, and the contact definition will be used to model the polymer for the remainder of the project. Further study involving a physical experiment to validate the initial meshed ironing simulations will provide a better basis for comparison and optimisation in future optimisations. The necessity for further study was a key motivation behind the development of the ironing rig in chapter 5, which lays the foundations for a fully verified DWI model.

Chapter 5

Developing a rig to demonstrate the ironing process

5.1 Introduction

Having determined the preferred method to model the process, and characterised the polymer contact definition to the current capabilities of available model data, the next step was to devise a verifiable comparison between the contact-definition model and physical polymer-coated specimens. Instead of further attempting to characterise the film itself, it was decided to focus on creating a testing method capable of ironing polymer-coated material, in order to match force and deformation data in the model to physical results. This validation would prove vital to optimising the preliminary contact definition used in place of meshed polymer layers. Since no apparatus existed within reach, creating a prototype experimental rig was the best available solution. This chapter follows the design process, development and testing capabilities of such a rig. By the end of this chapter, a rig will have been designed and used to gather data for polymer-coated specimens, and the work aims to provide some physical basis of validation for the previous work on modelling the polymer-coated DWI process.

5.2 Developing a rig to demonstrate the ironing process

The nature of the cylindrical DWI process proves a challenge when attempting to measure or quantify engineering variables occurring within the tooling or

formable metals[93]. The DWI process occurs within a bodymaker, completely hidden from view and the annular geometry prevents any cross-sectional observation or metrology during forming [94]. Whilst theoretically possible to implement metrology devices in various places, the cost of doing so to an industrial bodymaker would be intense, and has historically been avoided [95]. Instead it is far more reasonable to imitate the process in a smaller scale where variables can be controlled and measured with greater ease. This section of the thesis details the design process and development of a bespoke Ironing Rig which can be utilised with a standard bench-top tensile testing apparatus, for use in FEA model validation.

Examples of bespoke rigs which attempt to imitate a forming process are spread evenly throughout the literature [96],[97][98][71], but none adequately demonstrate ironing with industry geometry. These previous rigs deal with much thicker material and loads, or model the contact die as a simple triangular construction and not the complex industrial die geometry seen in DWI. The most similar rig comparison (Van der Aa's work[71]) focuses on metrology of the polymer layers itself, the data presented does not provide a valid basis for validating simulations using the polymer-coated materials. Finally, since these previous studies were undertaken a number of decades ago, there is little to suggest that the material characteristics will be the same as the one used in can-making today. For all these reasons it becomes clear that the simplest solution is to create a bespoke ironing rig for use in the can-manufacturing project.

5.3 Designing the rig

When designing the apparatus two key factors were considered: the direction of punch movement with respect to the tensile test frame, and whether ironing would occur in one place (or on both sides of the punch). In addition to these key factors, several more requirements regarding user interface were specified:

- The rig needs to be light enough to move and install without lifting equipment[99].
- The rig must fit within or around a standard bench-top tensile testing machine.
- Some kind of metrology of the specimen must be possible during ironing.

- Severity of ironing should be easily adjusted without creating new die tooling each time.
- Deformation of tooling should be minimal in order to accurately measure ironing[100].
- The apparatus should be cost effective, using readily available materials and manufacturing methods.

Based on these considerations, three initial concept designs were developed.

5.3.1 Initial design concepts

The initial concepts for design began as simple sketches conveying the various geometric options of such an apparatus. These diagrams were used primarily to provoke discussion regarding design features, and identify any possible failure modes for the geometry early on in the process. The main three concepts are illustrated in figures 5.1 through 5.3, as well as a conceptual design for a complex punch in figure 5.4. The three designs differ, but all centre around the use of a tensile testing machine to force a thin sheet specimen between a punch and a die - reducing the thickness and increasing the length of the specimen as seen during production ironing. Since the tensile machine moves in a vertical vector, it is simplest that the rig concepts follow the same path of motion.

Design 1 uses compressive action to push the punch past the ironing dies. The original concept was to be machined from a single block of steel in order to satisfy the requirement for stiffness/rigidity and minimise deflection. Though expensive to produce[101], the excess material would ensure that deflection was minimised. However, the design would also increase the difficulty associated with calibrating and changing parts, since the entire rig would need to be disassembled to alter variables - and it the weight of the build would be difficult to keep down.

Design 2 is similar to *design 1* but instead uses extension to drag the punch through the apparatus. The intention of a dragging motion was to self-align the punch as it is pulled between the two die, in a way which open-ended pushing cannot achieve without an alignment sleeve (which adds friction)[102]. The disadvantages to this design revolve around the bulk of metal required for

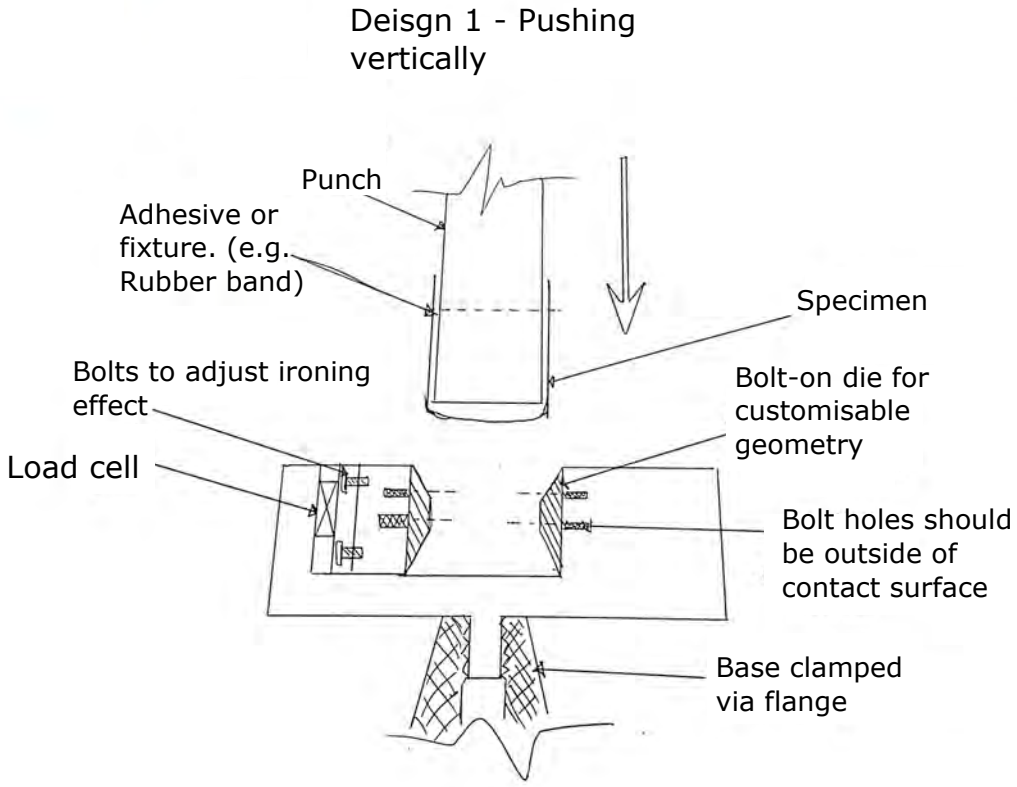

FIGURE 5.1: Ironing rig *design 1*: a vertical-loading open ended design using compression as the driving force.

the dragging motion to be possible. The long supporting structures would inevitably suffer greatly from the moments of forces generated; some extra reinforcement would be needed for success. With the drawn punch method, all force acts through a single bolt or hinge (a requirement for the self-alignment), which may prove a weak point during duty. Adding a bracer to the arm structures would increase the rigidity, but the extra metal required may offset the advantages to this design.

Design 3's defining feature is the single die construction. The intention was to reduce the forces generated during ironing, whilst halving the contact deformation and calibration time. Ideally this design would experience 50% less ironing forces than a two-die design which would prove advantageous for manufacturing, however the large flat contact surface between the alignment walls poses a different challenge. Even with highly polished surfaces, the friction generated on that interface may exceed any from the die. Subsequently, the forces which are generated during ironing may be lost in the noise of the friction forces[103]. One way to account for this would be to finely polish and te the sliding contact surfaces, perhaps including a rolling bearing. In this scenario the overall forces

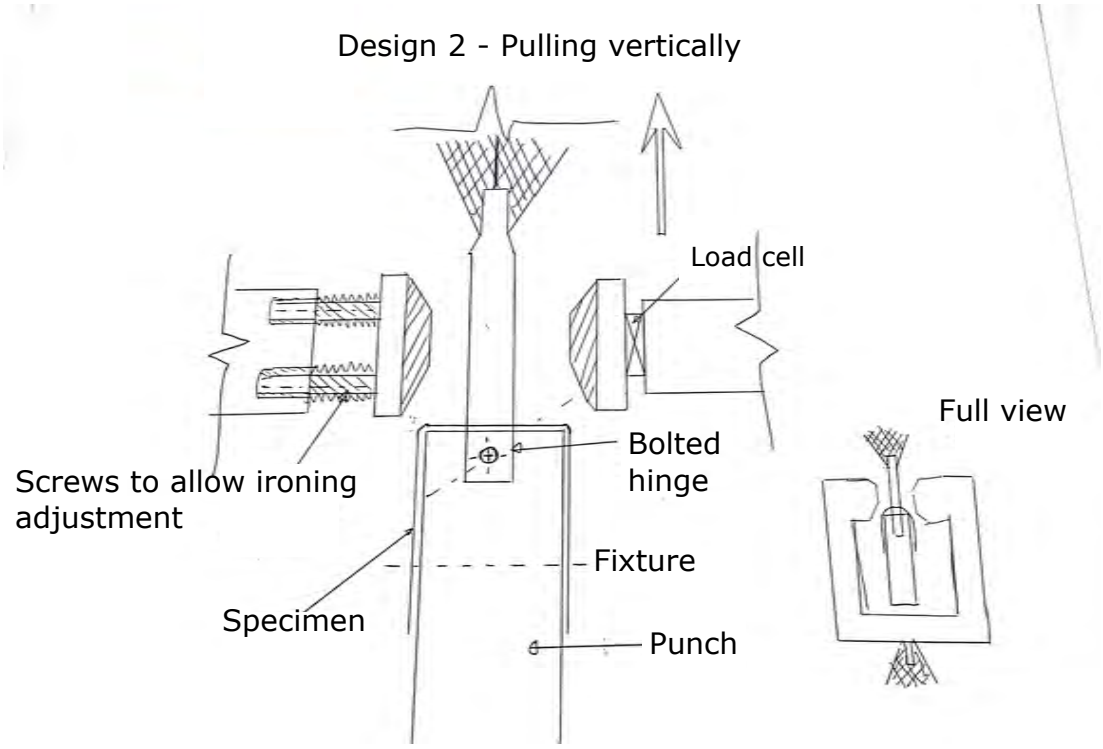

FIGURE 5.2: Ironing rig *design 2*: a vertical-loading open ended design using extension as the driving force.

would likely mimic that of a two-died rig, though the contact design holds the advantage of keeping alignment more effectively.

This *complex punch design* demonstrates the concept of a segmented punch, separated by load cells. The intention of this design was to allow for measurement of differing forces generated at different moments of ironing. As sections of the punch pass the contact zone and begin experiencing ironing forces, a variation in load would be measured by the various load cells; this would allow some quantitative analysis of ironing forces. Ultimately the decision was made not to pursue this design as the cost of manufacturing such a complex piece could not be justified as the force analysis was beyond the scope of the project.

Each design does not differ substantially in terms of overall geometry. The limitations of the ironing process and the machinery involved require certain characteristics from the rig. Table 5.1 summarises the initial design discussion in a pugh matrix; emphasis was placed on the consideration of rigidity and weight as any design would be unusable if deflection invalidated testing data, or the rig could not be installed.

Following the discussion demonstrated in the Pugh matrix, *design 1* was elected

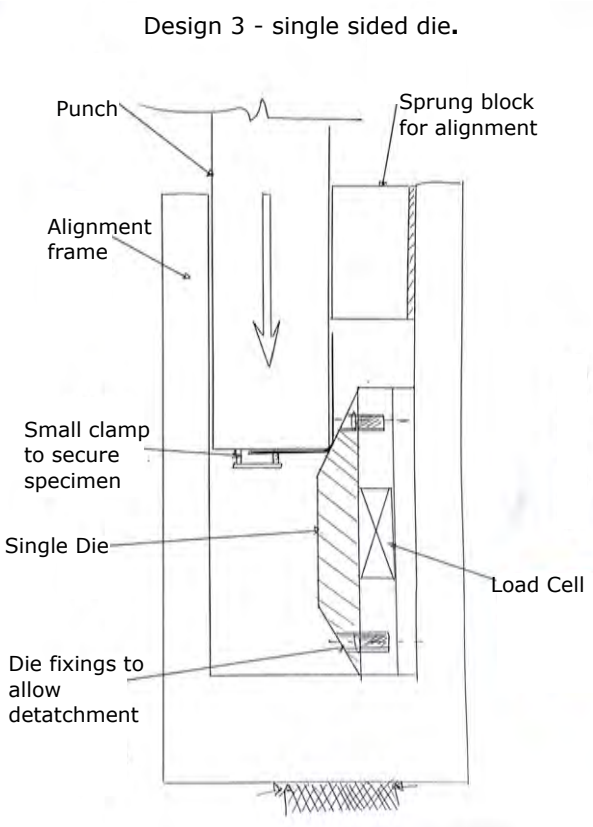

FIGURE 5.3: Ironing rig *design 3*: a vertical-loading open ended design using compression as the driving force.

TABLE 5.1: Pugh matrix summarising design discussion for three initial design concepts of an ironing rig.

Selection criteria	**Priority (% Importance)**	**Design concept score (3 high)** *design 1*	*design 2*	*design 3*
Weight	25	3	1	2
Manufacturability	20	3	1	2
Rigidity	30	3	1	2
Ease of setup	15	1	2	3
Cost	10	2	1	3
Overall total		12	6	12
Weighted total		**2.9**	**1.15**	**2.25**

as the concept to pursue. Rigidity and weight are the chosen priority factors for the build, and can be approximated using the physics equations 5.1 through 5.7. Rigidity is of primary importance, as a rigid build enables the rig to fully iron samples without deforming beyond forming tolerance. Since ironing relies on an interference between the specimen and forming tools. If the dies frame deforms substantially during ironing, this interference will relax and proper

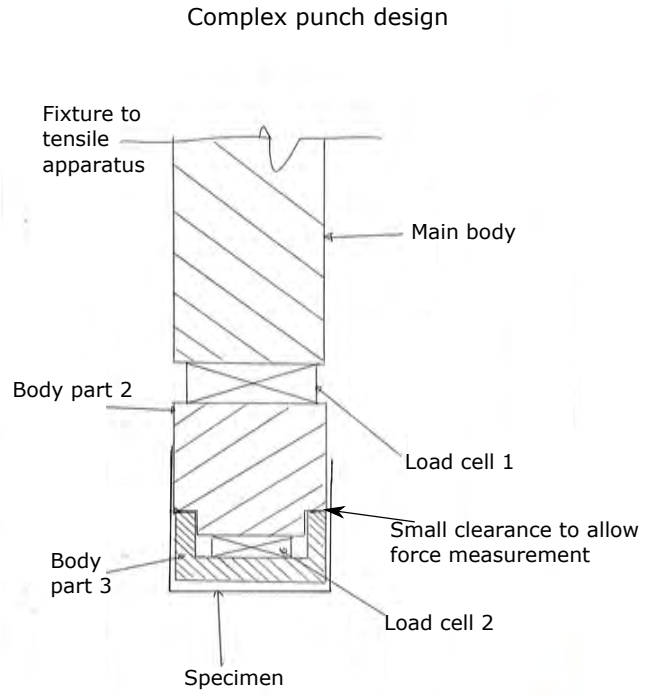

FIGURE 5.4: Design of a punch capable of measuring the differences in forces during different stages of ironing.

forming criteria will not be satisfied. Equally, the rig is intended to be operated solo with a bench top tensile machine, and must not exceed a reasonable weight limit (as mentioned previously).

For the equations 5.1 through 5.7:
k *= Stiffness*
A *= Cross-sectional area*
E *= Elastic/Youngs modulus*
L *= Length of element*
F *= Force applied on the body*
δ *= Displacement, assumed to be 'change in length' for simplicity*

$$k = \frac{AE}{L}(Hooke'sLaw) \tag{5.1}$$

$$k = \frac{F}{\delta} \tag{5.2}$$

$$\epsilon = \frac{\delta}{L} \tag{5.3}$$

$$\sigma = E\epsilon \tag{5.4}$$

$$\sigma = \frac{F}{A} \tag{5.5}$$

Substituting equation 5.1[104] into equation 5.2 gives the equation 5.6:

$$\frac{AE}{L} = \frac{F}{\delta} \tag{5.6}$$

Rearranging equation 5.6 to make deformation the focus gives equation 5.7 [105]:

$$\delta = \frac{FL}{AE} \tag{5.7}$$

The inversely proportional relationship between area and deformation demonstrates that minimising deflection requires the area through which force is exerted to be as large as possible [106],[107]. This relationship highlights a balance for the amount of metal used in the rig construction. A large cross-sectional area is the most immediate answer to deflection but will proportionally increase the weight of the build.

5.3.2 Developing the design into a simulation

The initial concept model for the ironing rig used a basic geometry from *design 1*, with the addition of some bracing bars at the point of the largest moment. This development can be seen in figure 5.5. Initial designs used a square geometry, the dimensions of which were derived using a 3D simulation, seen in figure 5.6. The simulation followed typical methods in this thesis using rigid surfaces for tooling, surface-to-surface/finite-sliding contact definitions, and a deformable mesh specimen with analytical rigid surfaces for tooling. The

stepped design exists to provide full support for the downward forces acting on the die. Ignoring this aspect of the design could see unreasonable bending moments[108] on the die holder as the punch makes contact.

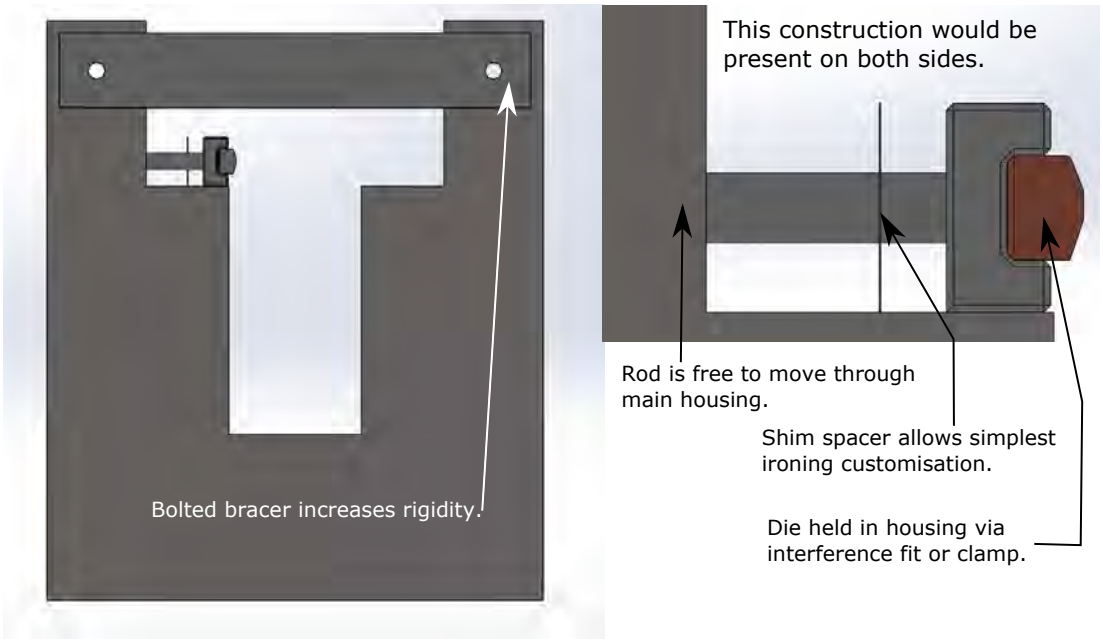

FIGURE 5.5: Diagram of the developed geometry design for the ironing rig. Both an overall structure and a close-up of the die area are featured.

This simulation used a specimen with a similar thickness to the ingoing sheet metal used by Crown, with a width of 15mm and an approximate ironing reduction of 20%. Figures 5.7 and 5.8 demonstrate the reaction forces upon the die during ironing, in X and Y respectively.

These results show typical reaction force behaviour for an ironing process[109]. The force ramps up after contact is made between the die and specimen, and continues to do so until full ironing is achieved. At this point the process becomes steady-state and the forces do not increase, accounting for the plateau visible in both graphs. The graphs are plotted from only seven data points, as they were intended primarily to observe the expected rise in force.

Using this setup the maximum X axis force on the die was approximately $15000N$. This gives a $1000Nm^{-1}$ force input. The Y axis force on the punch was approximately $2000N$. This equates to a force of approximately $133Nmm^{-1}$.

The next step was to mock up a simulation which reflected the desired geometry and forces to enable a more detailed analysis of stress concentrators and areas of waste. From this step area for the frame was calculaed arbitrarily using

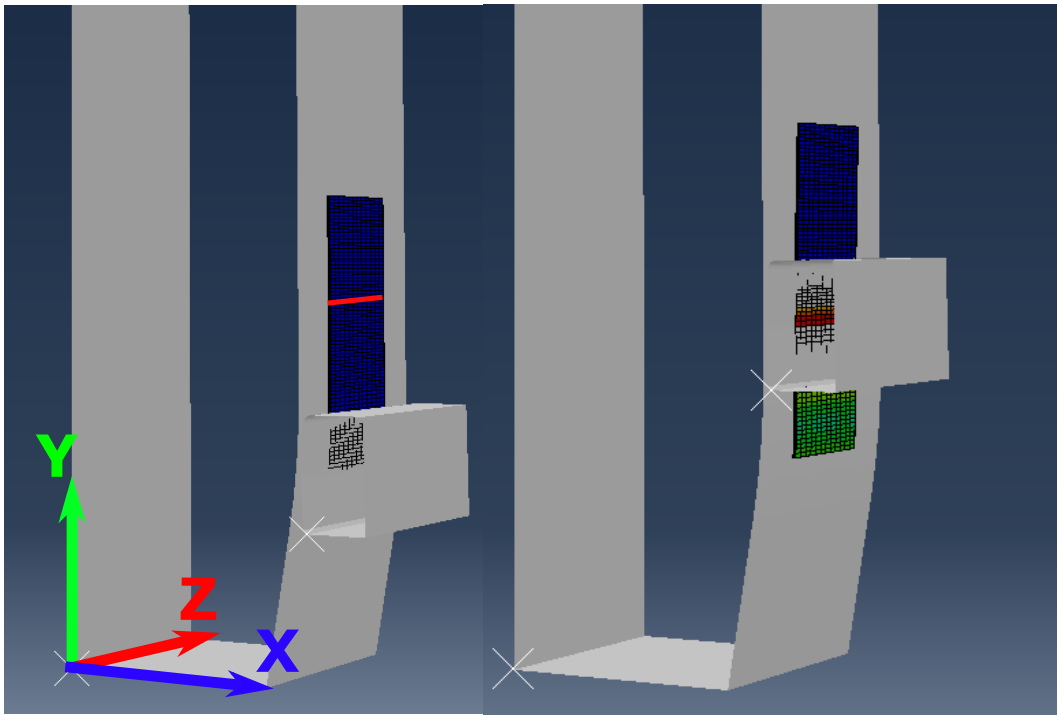

FIGURE 5.6: Diagram of the ironing simulation before and during ironing. The red line shows the Z axis, referred to throughout this thesis as *specimen width*. The global axis system can be seen bottom-left. Blue, Green, Red lines indicate the X, Y, Z axis respectively.

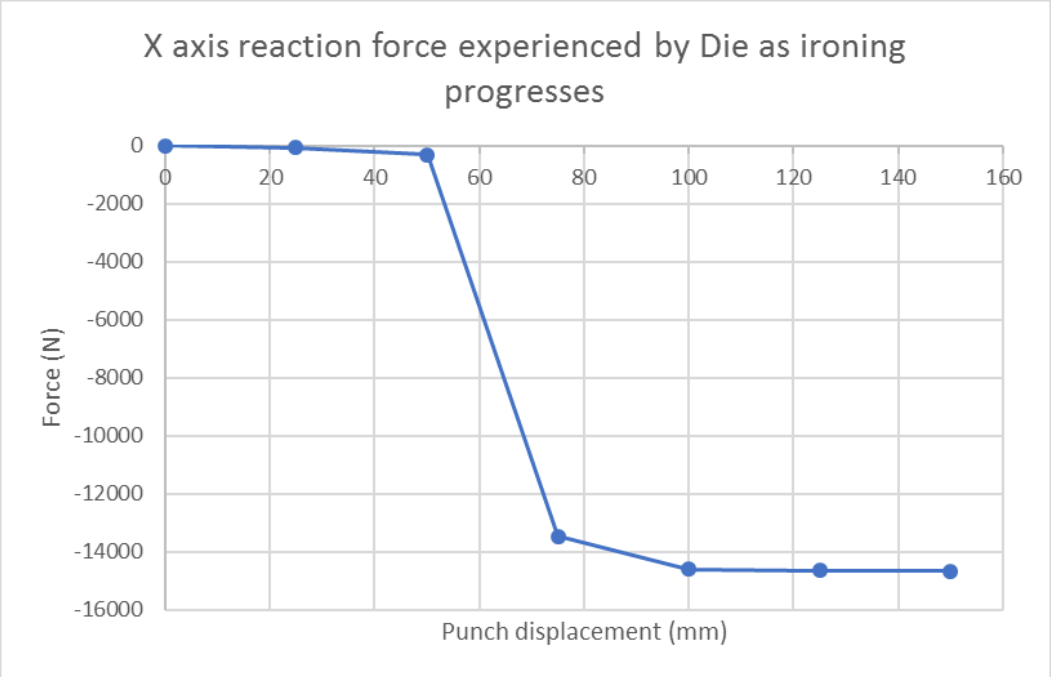

FIGURE 5.7: Graph showing the reaction force in X axis as punch displacement (and thus ironing done) increases. The punch makes contact with the specimen at approximately 50mm displacement.

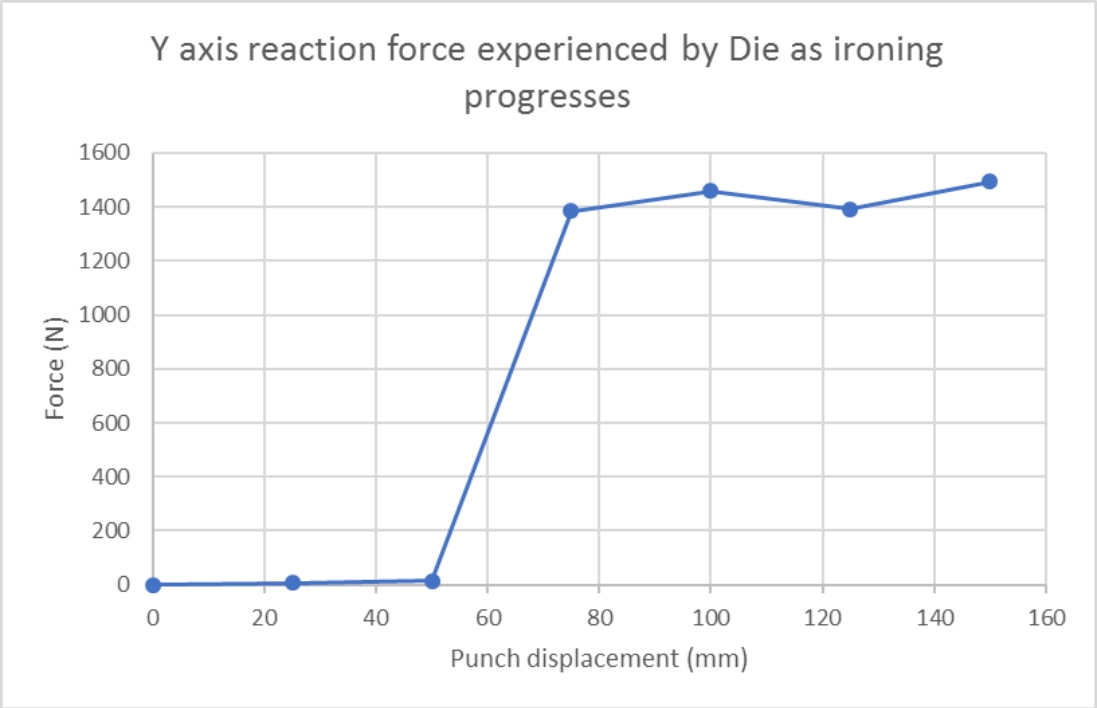

FIGURE 5.8: Graph showing the reaction force in Y axis as the punch displacement (and thus ironing done) increases. The punch makes contact with the specimen at approximately 50mm displacement.

the yield stress of mild carbon steel[110] and a safety factor of 20 to minimise max deformation. These calculations are broken down in equations 5.8 through 5.14. Due to the order of magnitude difference between the axial (pushing with the punch) and radial (pushing outward on the die) forces, axial forces were ignored for this step. For this step in the design progress, it was not important to start with dimensions close to the final goal, but instead understand the failure modes and stress concentrators in the initial design concepts.

Equations 5.8 through 5.14 are used to calculate the basic cross-sectional area needed for the supporting frame structure of the initial design. This dimension will then be used to inspire a basic simulation for FMEA. For simplicity the structure cross-section will be assumed square.

For the following equations:
Axial reaction force per mm = $F = 1000N$
Yield stress of mild carbon steel = $Y \approx 3.7E8N/m^2$
Safety factor = $S_F = 20$
Specimen Width = $W = 20$
Total force = WF_T
Effective yield stress = Y_E
Cross-sectional area required = A
Square edge dimension = x
stress = σ

$$F_T = F \times W \tag{5.8}$$

$$Y_E = \frac{Y}{S_F} \tag{5.9}$$

$$\sigma = \frac{F}{A} \tag{5.10}$$

From equation 5.10[111], equation 5.11 follows:

$$Y_E = \frac{F_T}{A} \tag{5.11}$$

By rearranging equation 5.11, equation 5.12 is derived:

$$A = \frac{F_T}{Y_E} \tag{5.12}$$

Compiling all of these equations together creates the following compound equation 5.13:

$$A = \frac{FWS_F}{Y} \tag{5.13}$$

Finally, to obtain the square side dimension, equation 5.14:

$$x = \sqrt{\frac{FWS_F}{Y}} = \sqrt{\frac{1000 \times 20 \times 20}{370000000}} = 0.03288m = 32.88mm \tag{5.14}$$

Ultimately a value of $32.88mm$ was derived for the square side dimension of the starting simulation model. An initial design concept was drawn up to resemble the geometry decided upon. The results of that model can be seen in figure 5.9. The arrows represent the forces which were applied and their locations in the simulation setup.

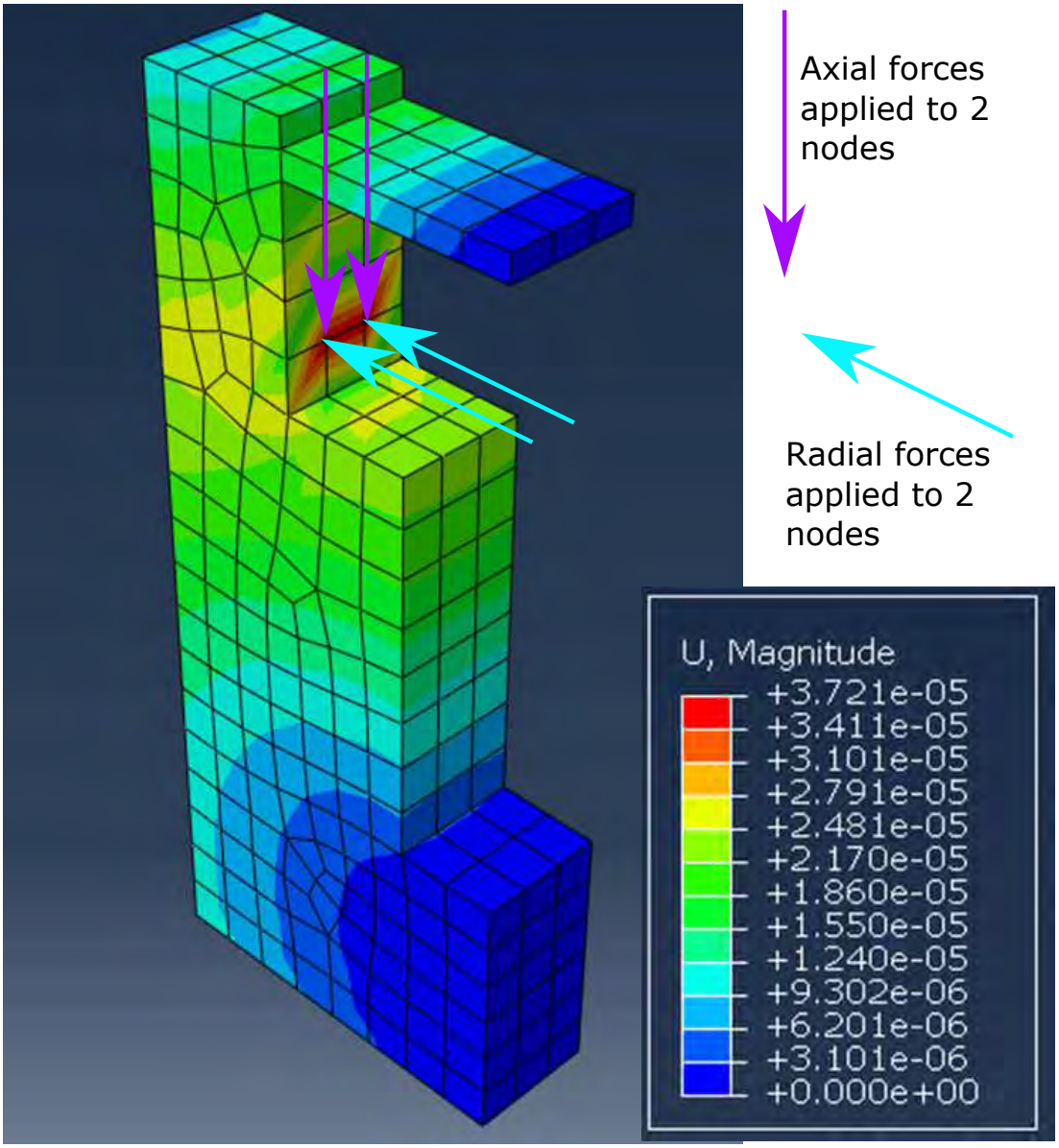

FIGURE 5.9: Deformation contour plot of initial ironing rig design. Geometry has been kept simple to produce initial directive results. This simulation has been modelled with a line of symmetry to reduce computational requirements.

Deformation magnitude has been plotted on the model, as this represents the rigidity distribution of the build[112]: the most important concept as per the pugh matrix. The large area of blue at the bottom and top should be considered carefully, as the fixtures were acting along those surfaces and subsequently a 0 deformation at fixtures is to be expected[113]. This aside, large incremental areas of lower stress can be identified around the bottom area of the build. It is expected that the majority of deformation will occur near the application of the force or stress concentrator [114]. This can be clearly identified in the small red shape near the force arrows - this red area represents a maximum deflection. The maximum deflection did not exceed $3.721e-5mm$: considering the specimen depth of 300 μm, an acceptable range of deformation would be $\approx 10\%$, around 30 μm. This design is excessively over-engineered and weighed 100kg, which is far beyond that designated in the earlier specification. Whilst the rigidity of this iteration would have proven suitable, the weight is far beyond what a single user could be expected to manipulate, and fine adjustment would have been difficult. This design concept existed primarily to certify whether small enough deformations would be possible in a bench-top build and thus the simulation gave useful indication of improvement vectors.

5.3.3 Width study

The next step was to determine the design progression based on the results of the first full simulation. a major focus was the width of the specimen. The planar geometry (exposing the ironing process to instruments of metrology such as a DIC system[115]) was a necessary part of the design, but provoked challenges not usually associated with the can ironing process. A primary concern was the concept of *edge effects* at the edge of the die interface. Based on the geometry two choices existed for a die-to-specimen ratio: either the die is smaller than the specimen (to which a kind of gouging effect would be expected at the edges of the die), or the die is bigger than the specimen (to which the edge of the specimen is pinched between die and punch). These two issues are not normally seen in can ironing as the cylindrical geometry and tooling naturally provides no edge [116]. Since any video capture metrology required a view of ironing from the side, the design progressed with a wider die than specimen.

To explore the effects of this pinching 'edge behaviour', a series of simulations were undertaken with varying specimen widths. The results of this simulation

sought to satisfy a handful of unanswered questions, including certifying the hypothesis about the relationship between width and reaction force. Primarily however, the simulations would demonstrate to what effect this pinching behaviour disturbed the distribution of stresses and strains normally seen during ironing, and if there was any proportional rate at which edges were affected compared to specimen width.

To properly demonstrate any edge effects the simulation needed to be undertaken in 3D[117]. Due to specimen symmetry, a sliding boundary condition was introduced to reduce computational time by modelling only half of the specimen. By reducing the model in this way, computational time is cut almost in half and allows a higher mesh density within the area which is simulated[118].

Simulations were setup in Abaqus standard using analytical rigid surfaces for tooling, and deformable 2D CPS4R mesh for the specimen. Contact between tooling and specimen was defined using a surface-to-surface definition, a friction value of 0.1 with the penalty contact (finite-sliding) method. Punch tooling was constrained using an *encastre* definition, and the moving die constrained in all but the Y axis; a specified displacement and smooth-step amplitude were used to move the die at a fixed speed. To further reduce computational load, vertical line of symmetry was simulated using a sliding boundary condition along one edge of the specimen. *Elastic* and *plastic* material data was specified for the steel, listed in table 5.2 and 5.3 below.

TABLE 5.2: Elastic material data for TH330 unstoved steel.

Density %	**Young's Modulus**	**Poisson's Ratio**
7800Kg/m^3	205GPa	0.3

TABLE 5.3: Plastic material data for TH330 unstoved steel (Johnson Cook model).[54]

YS	**n**	**K**
258.87MPa	0.35952	334.14MPa

Four widths were studied in this simulation analysis: 10, 20, 30, 40mm, which were simulated at half width using the line of symmetry. These four strips were ironed with a more aggressive 30% ironing-reduction and various variables were measured from the results to quantify the differences between widths. These results are reflected in figures 5.10 through 5.11. These simulations were undertaken using uncoated steel specimens, as the minimal polymer layer's

thickness and incomparable young's modulus deemed it a negligible inclusion to the results. Due to a lack of material definition, the polymer demonstrated homogeneous behaviour and identical movement to the steel (with proportionally lower stress values). At this point there was no reason to believe a polymer-coated specimen would behave fundamentally differently to an uncoated specimen, and so rig design was centred around uncoated specimens, with the expectation that a coated specimen would simply require different clearance in the final rig.

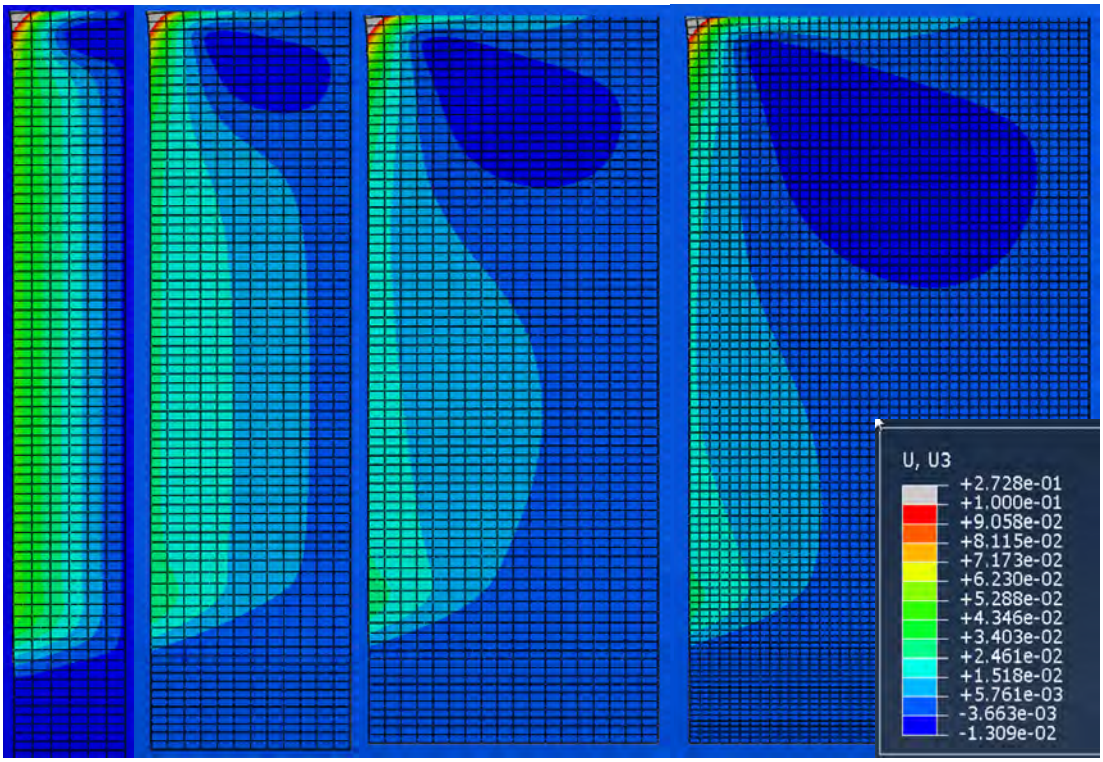

FIGURE 5.10: These diagrams illustrate the distribution of displacement in the Z axis for all four specimens (smallest to largest: left to right).

The images presented in figure 5.10 demonstrate the deformation during the flat planar ironing process. This displacement metric represents the amount of widening a specimen has undergone during the ironing process, and uses a max displacement scale of $0.1mm$ (grey areas are beyond the limit). The aforementioned concept of edge behaviour is indisputable, and there is also a clearly identifiable pinch occurring at the top-left corner of each specimen (grey area). The presence of this non-uniform deformation proves the necessity to carry out these such simulations before designing the ironing rig with any specimen width in mind.

The distinct cornering pinch which seems to be present in every simulation appears to be responsible for the large blue shape occurring at the top-left and spreading down through the specimen. The resulting dark-blue area demonstrates negative deformation (compression or narrowing) and appears to cover a higher proportion of the length of the wider strips, whilst covering approximately the same proportion of width. This may indicate that the pinching compression effect deformation has a more dramatic effect on a wider specimen, and wider specimens may need to be longer to compensate for this.

Similarly, the shades of green beginning from the left edge of all four specimens demonstrate widening, and a relative decrease in effected area as the specimen width increases. It appears the wider specimen suffers less from both widening and narrowing as a result of the lessened pinching effect. It is important to minimise these widening and compressive effects in the specimen, as a can cannot experience these behaviours in the cylindrical DWI process.

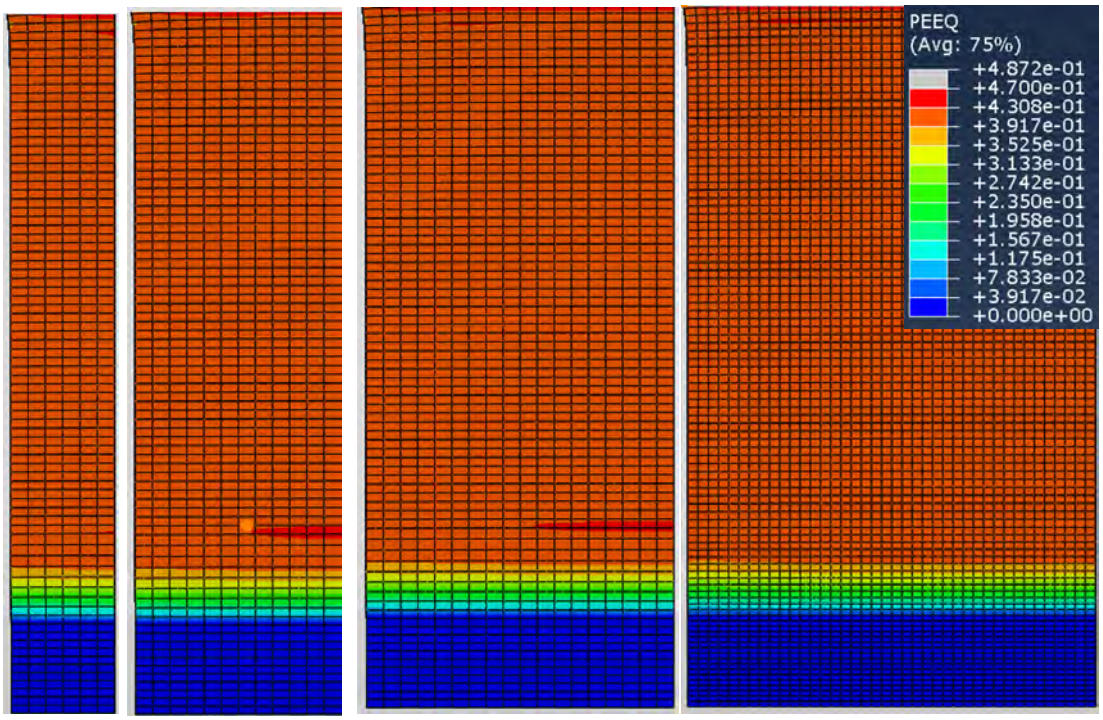

FIGURE 5.11: These diagrams illustrate the distribution of plastic equivalent strain for all four specimens (smallest to largest: left to right). Plastic equivalent strain distribution is a simple way to know which areas of the specimen have undergone permanent deformation and to what extent. All four specimens appear to have experienced approximately the same overall strain distribution here.

The plastic equivalent strain distribution in 5.11 displays the expected behaviour for strain in this sort of simulative Ironing study[119]. Since the setup does not change between width simulations, the plastic strain distribution is likely to

remain similar - specifically with little strain at the bottom (where the ironing clearance is greater than the material thickness) and maximum strain at the top (where the ironing and stretching has elongated the material the most)[120]. The red stripe inclusions are likely an element effect. One may expect the deformation and plastic strain distributions should be proportionally similar; and the compression/widening behaviour should be reflected in the plastic strain contour plot, however note the scale differences. The maximum width displacement of the $10mm$ specimen was less than 3 microns, (0.03%), whereas the specimens experienced a far greater degree of vertical deformation (27% minimum) and thus the plastic strain is two orders of magnitude larger in that direction. As a result the effect of the widening on plastic strain is minimal and difficult to demonstrate on the same scale.

Figures 5.10 through 5.11 provide valuable insight into what happens to the material during ironing, however some numerical quantification is needed to definitively decide which specimen width should be chosen for the ironing rig design. Figures 5.12 through 5.15 demonstrate this numerical data about the changes in geometry occurring during and after the ironing has completed.

Figure 5.12 demonstrates a behavioural change in width compared to the pre-simulation geometry inputs. There is a noticeable decay on both curves. Can-making is fully cylindrical and does not demonstrate width increase in the same way. Specimen width used in the ironing rig should try to minimise width increase during the process to minimise the flat pinching effect not seen in can-making. The graph shows a diminishing return when increasing width: a jump from 10 to 20mm can be clearly seen on both curves, however increasing width further yields progressively smaller changes.

Figure 5.13 similarly demonstrates geometry changes of the completed simulations. These geometric differences were measured by probing nodal coordinates from either end and either side of the specimen after forming simulation was complete. This graph depicts changes in specimen thickness and length. Similar behaviour to that seen in figure 5.12 can be identified here. The steep gradient change when moving between specimen widths is present in an identical manner. These curves demonstrate that the $10mm$ specimen is unsuitable for the ironing experiment, since the resultant behaviour is so different to the other specimen sizes. Note that whilst the $10mm$ result seems to demonstrate that a higher degree of ironing creates a shorter can, the planar geometry of

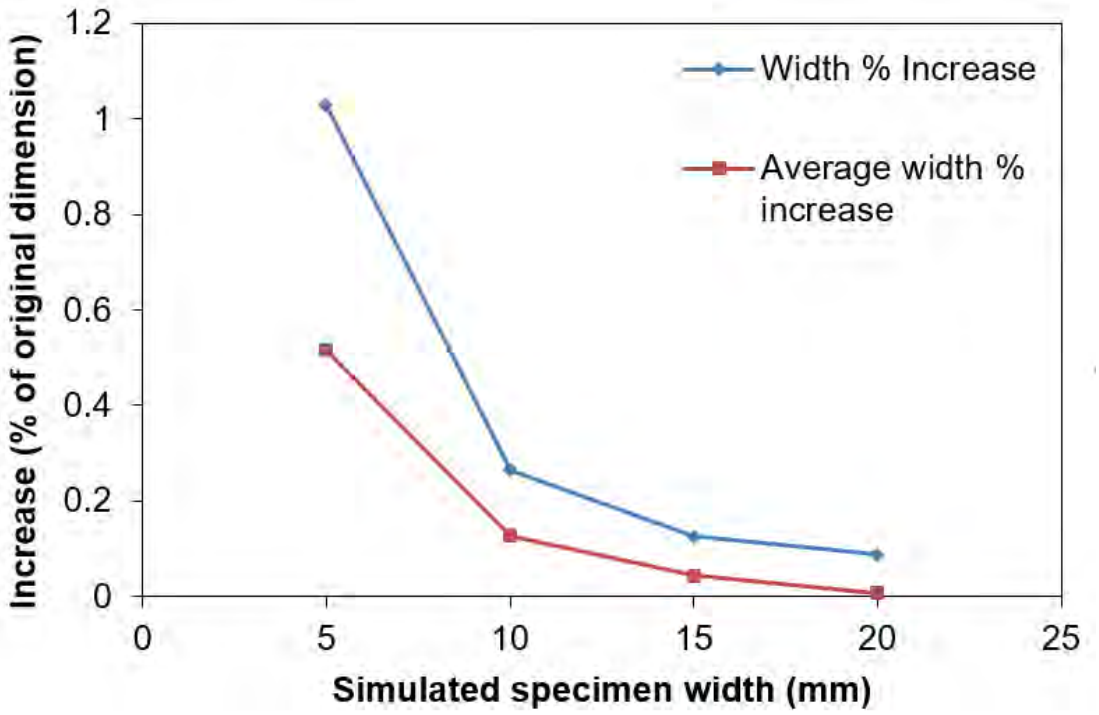

FIGURE 5.12: This graph depicts the relationship between the total increase of width after ironing, and the simulated specimen's original width. The blue line illustrates the increase in width for the total strip geometry, and the red line shows the average increase in width for all individual elements in the study. Both lines compare the final width as a percentage increase from the original width

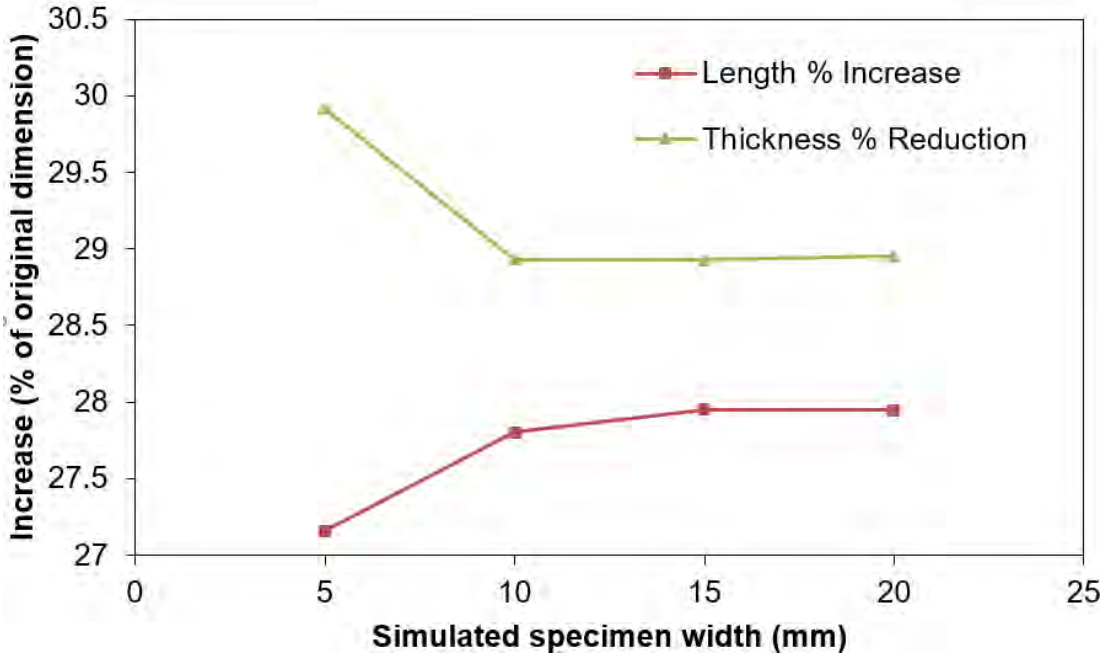

FIGURE 5.13: This graph illustrates the changes in thickness and length after ironing has completed, in terms of a percentage increase from the original measurements.

the strip allows widening where a cylindrical can does not. For this reason, the degree of material shift or general deformation is the same, but in this case material is instead moving out of the ironing area.

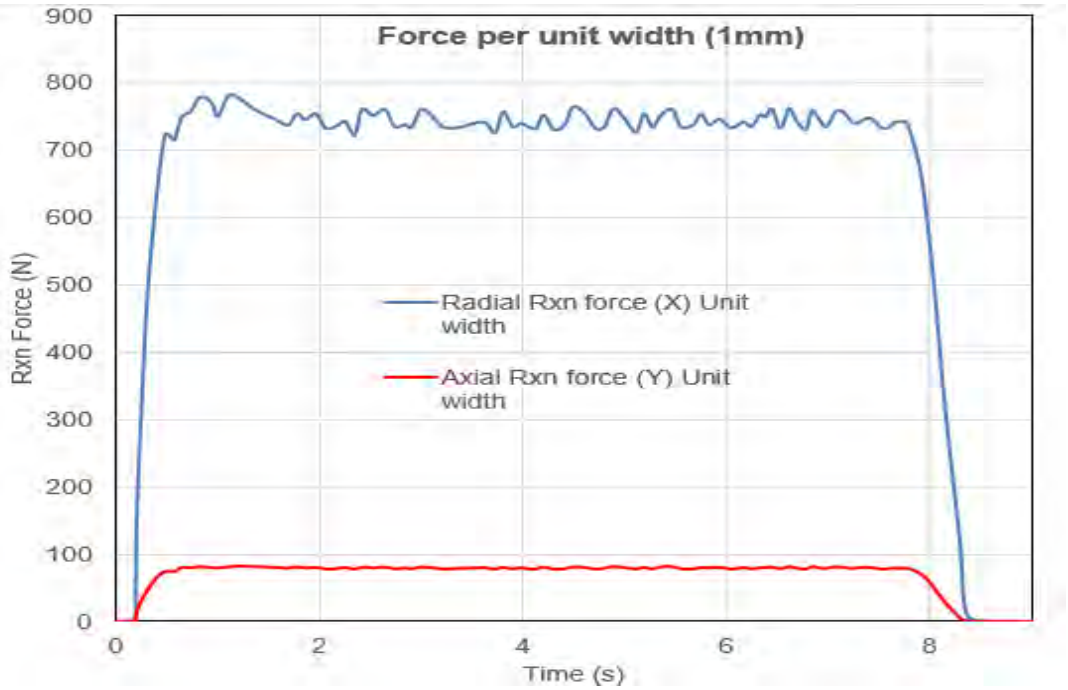

FIGURE 5.14: This chart shows the x and y forces per unit width (mm), acting on the punch during the design simulation.

Figure 5.14 confirms the hypothesis made earlier: the width increase linearly increases reaction forces. This validation provides two clear conclusions for the ironing rig's design. Firstly, the reaction forces in every case settle into a relatively straight line (barring noise) [121]. This further supports the concept that ironing should eventually reach a steady state situation where forces have balanced. The noise present within these straight lines is likely due to small snagging between elements and the subsequent discretisation of the surface of the blank [122][123]. The simulations were done using implicit time integration, which does not model inertia; for this reason it cannot be vibration or resonance.

A second conclusion to draw from the graph: there is no advantage in using a specimen wider than necessary. Following the earlier calculations of stiffness used to design the rig (equations 5.8 through 5.14), a higher reaction force will require more material to cope without deformation. This causes a heavier rig and issues with manual use. Since the rig needs to be as light and rigid as

possible whilst maintaining the best levels of process accuracy, the width chosen must find balance between the material accuracy, and the reaction forces generated as a result of the process.

Looking to figure 5.10, it becomes apparent that a specimen width between 20mm and 30mm is the most suitable for the rig design. This width seems to maintain the highest level of behavioural accuracy whilst keeping off the unnecessary addition to reaction forces seen in every step up width. The edge behaviour seen in the $U3$ distributions is not quite as good as 40mm , but far superior to the 10mm specimen. Equally the step change in width increase is almost negligible above 30mm, but the reaction forces added are a linear step for every 10mm, so the minimal advantages to using 40mm are outweighed by this subsequent increase in material required for the build.

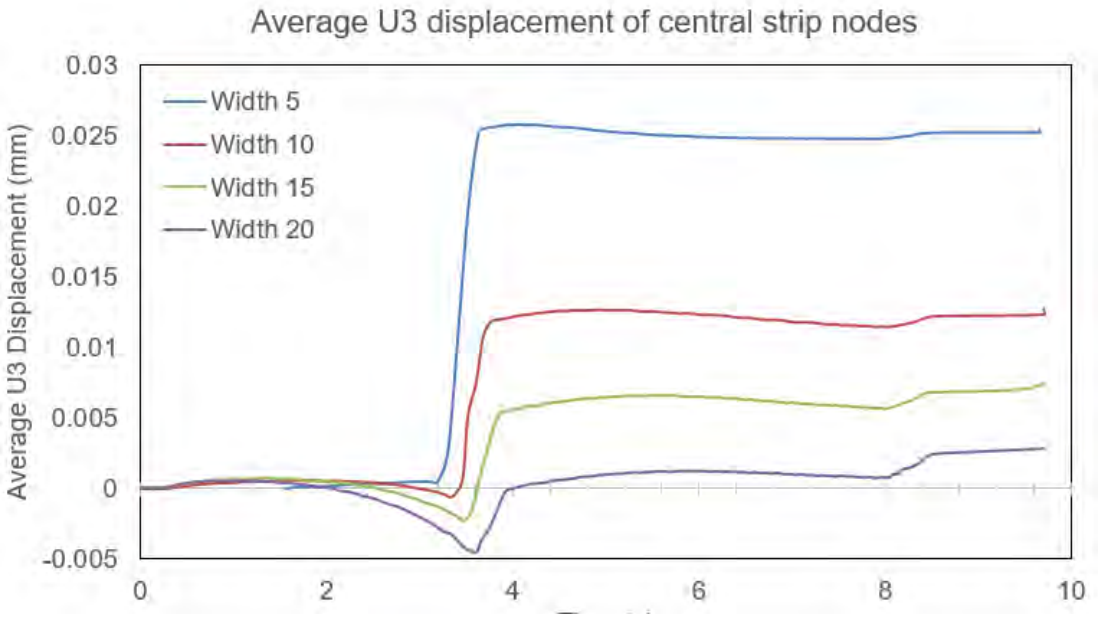

FIGURE 5.15: This graphic quantifies the width changes illustrated in figure 5.12. The lines represent average $U3$ (Z) displacement experienced by all nodes as the time increases.

Figure 5.15 demonstrates the U3 (Z displacement) of differing nodes along a central line within the ironed strip. In this case, a positive Z displacement refers to the outwards widening of the strip (increasing its shortest side measurement) as it is ironed. The average Z displacement of all nodes is displayed, and reinforces the hypothesis that a wider specimen is disturbed less in the Z axis. The lines on this graph follow a very similar shape: beginning with a dip in Z displacement and rapidly progressing to a peak before levelling out. This beginning dip can be attributed to the compression experienced during as

the ironing ring passes, as the process of ironing is effectively a combination of compression and stretching. After the punch has made contact and settled against the specimen, the following moment is purely compressive before the material yields and begins to shift against the die. The average Z displacement will thus become negative momentarily before it begins to rise - which can be seen clearly around ≈3.8 seconds.

5.3.4 Design Milestone

A simulation-driven approach was undertaken to improve the basic design concept, and the major design milestone can be seen in figure 5.16. Several features have been added to improve the rigidity of the structure, and minimise deformation. These features include tubular spacers to allow preload-tightening of the constructor bolts, as well as a thickened double-plate design for the main housing.

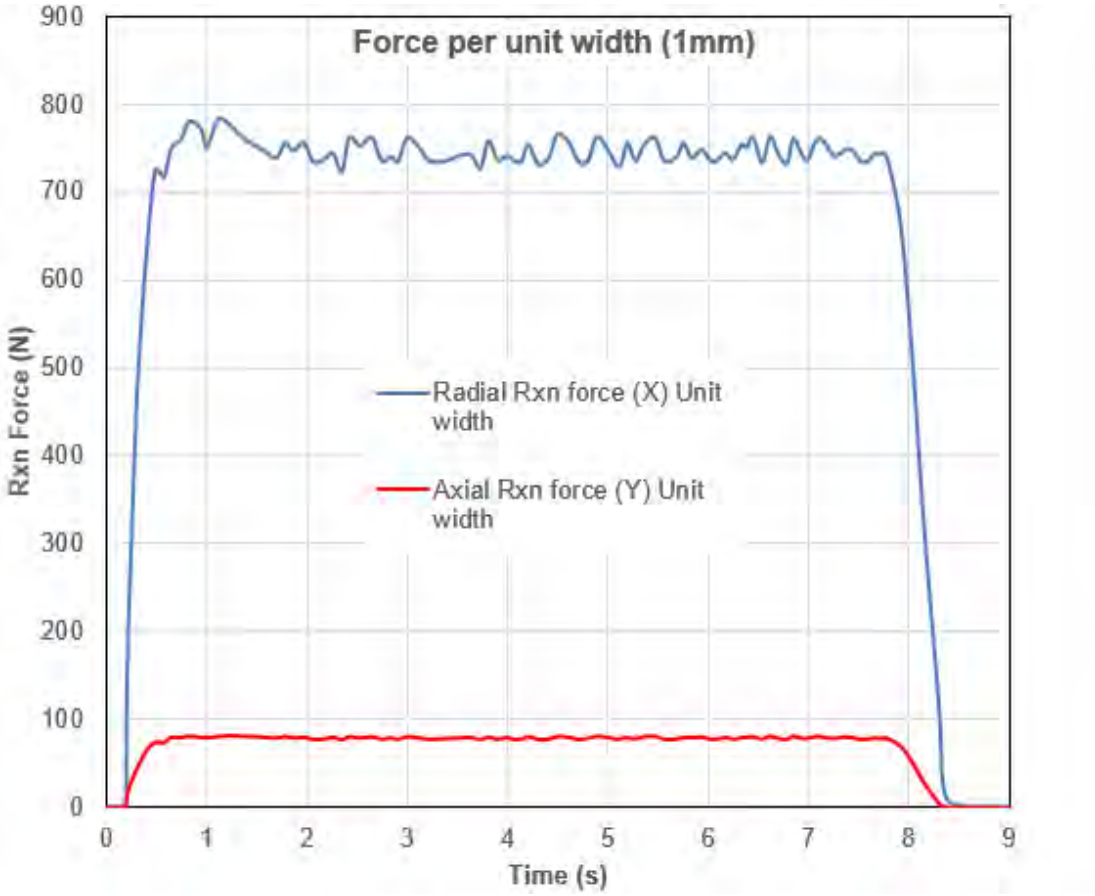

FIGURE 5.16: Figure showing a half-section view of the milestone design, with spacers and supports added for rigidity. Bolts were not included in this diagram.

Further simulation with accurate force loading was undertaken with the milestone design to identify any remaining major stress concentrators. The results are seen in figures 5.17 and 5.18.

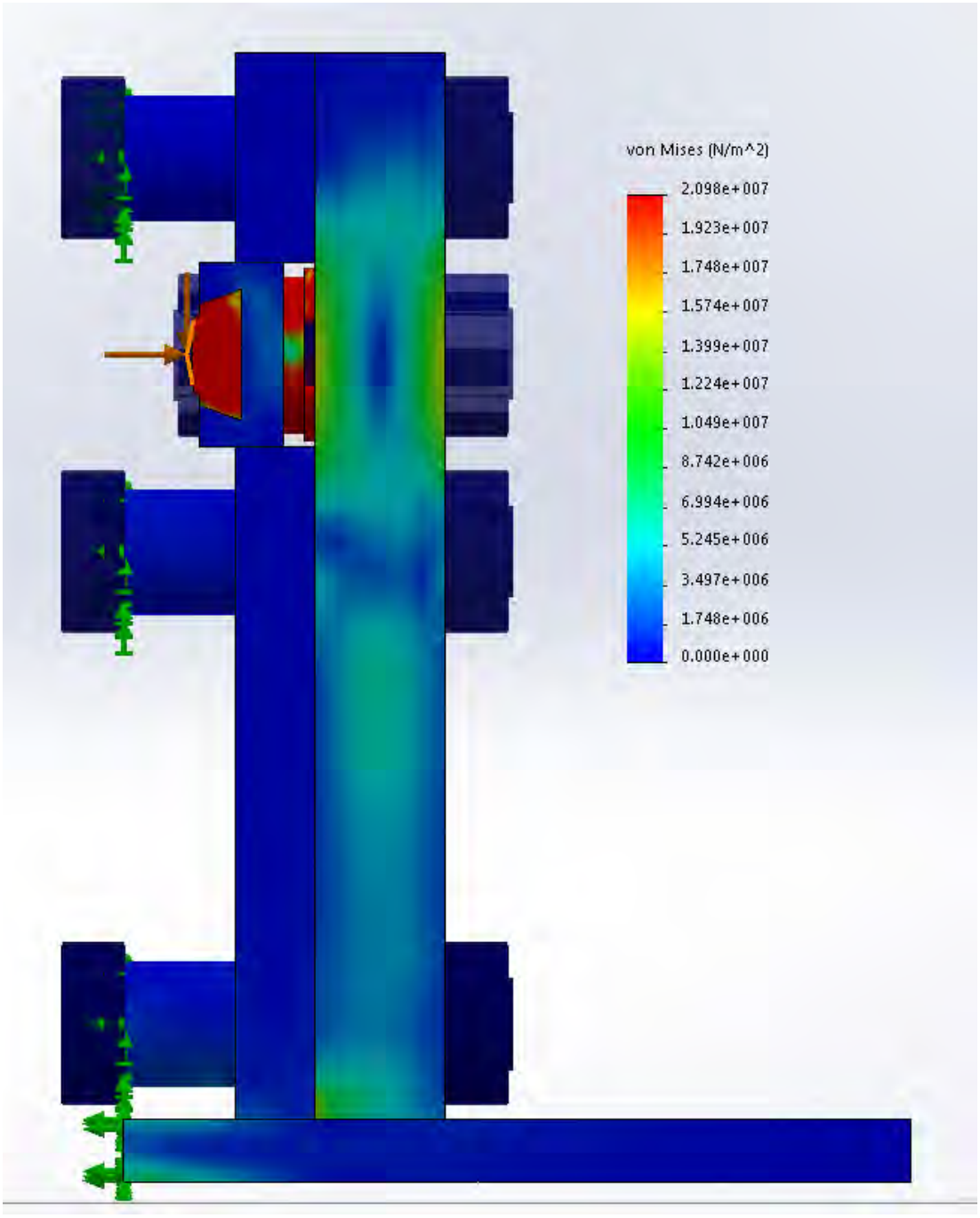

FIGURE 5.17: The stress distribution resulting from the design simulation undertaken on the second design milestone. For reference, the yield stress would be around $240MPa$.

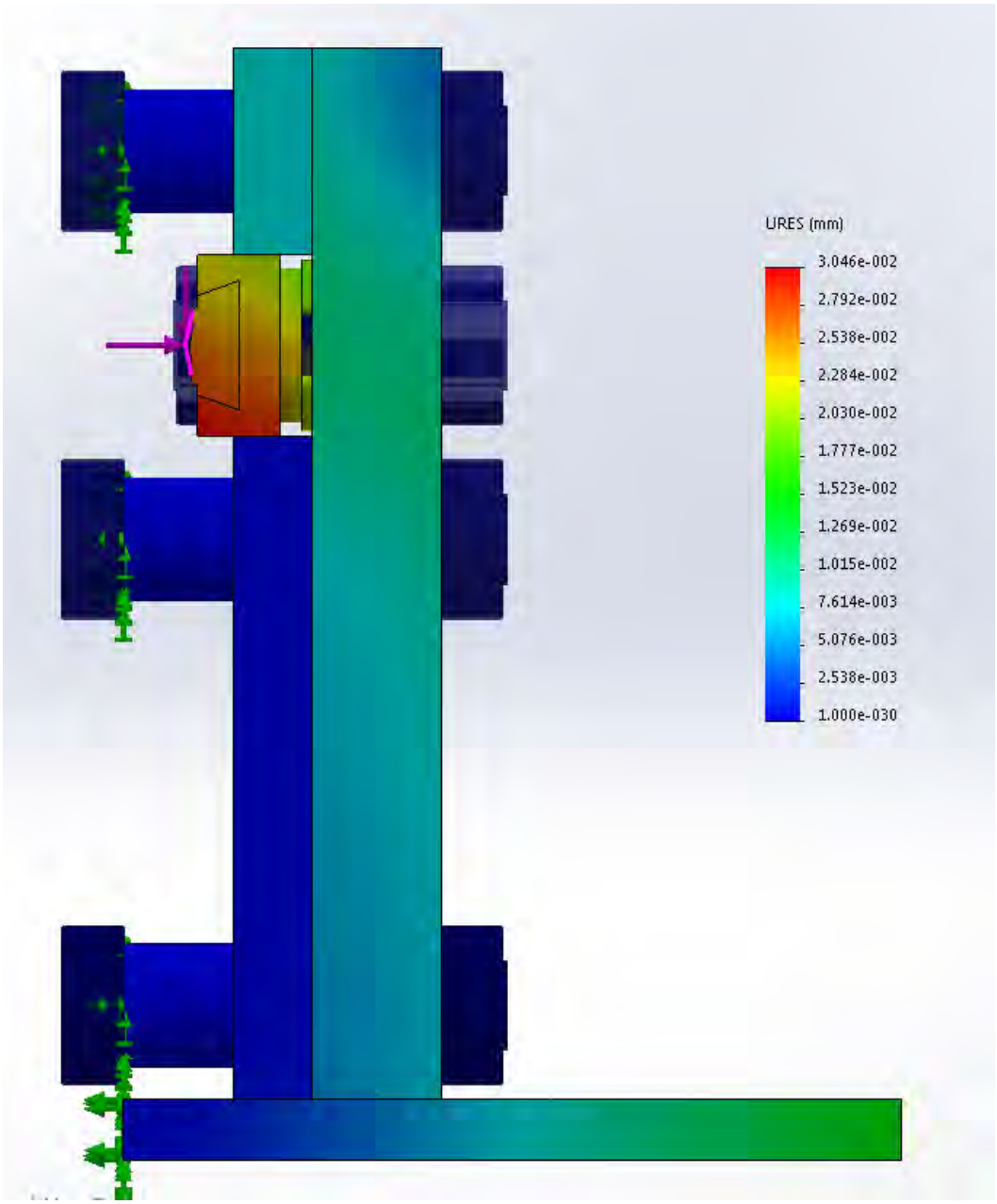

FIGURE 5.18: The displacement distribution resulting from the design simulation undertaken on the second design milestone. For reference, the maximum allowable displacement is 40 microns, and the maximum achieved displacement is 30.5 microns.

With a maximum stress of $\approx$ 20MPa, and a maximum deflection of $\approx$ 30 microns, the design directly succeeds in the rigidity criteria. The places experiencing most stress and displacement are all within the die, housing or spacers/load cells behind. This design holds major advantages regarding cost, build, and manufacturing, as fewer parts and fewer cuts exist compared to previous iterations.

The one primary concern was the complexity of fitting a transition fit die into

the holder-housing. Originally this concept was included to allow simple replacement of custom die shapes, but it was finally decided that a simpler design would see the die bolt directly to the housing. This, along with some other minor improvements gave way to the third and final major design milestone. The final design is illustrated in figures 5.19 and 5.20. The results from this final iteration gave a displacement decrease of around 2 microns in the thicker die. The final design had a weight of 20.01kg, which met the initial design specifications established earlier.

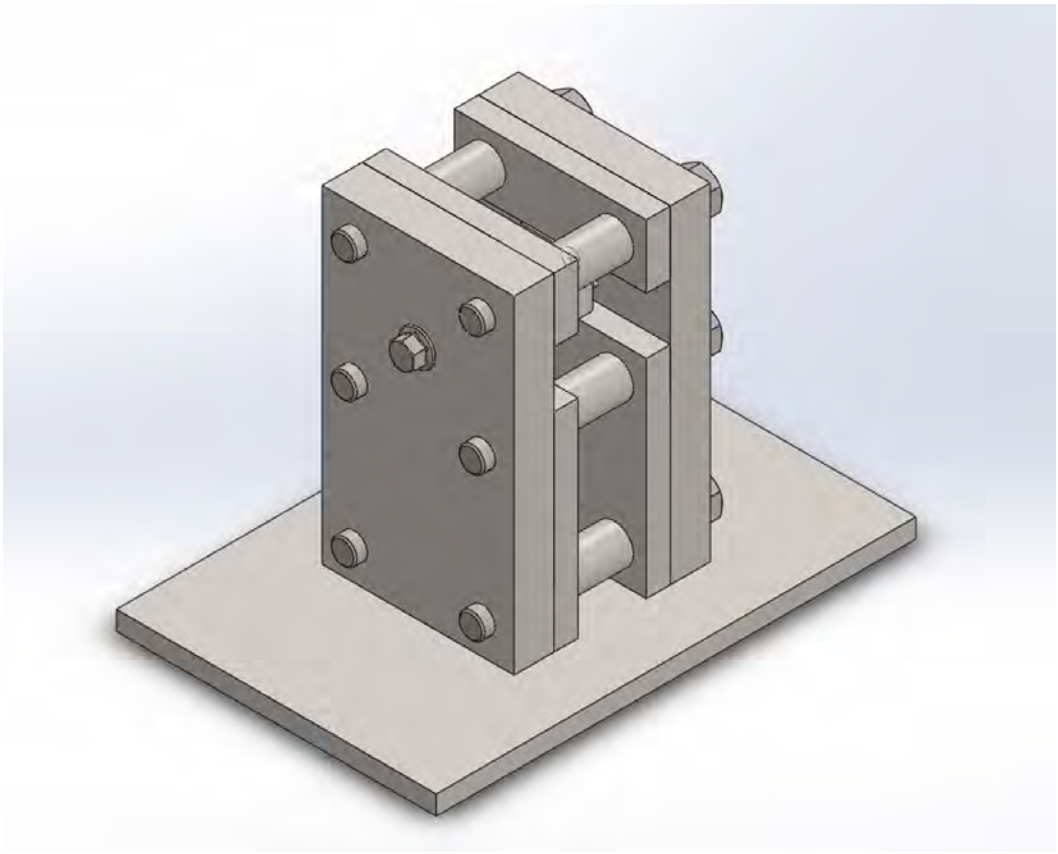

FIGURE 5.19: This figure demonstrates an isometric view of the final ironing rig design.

As required, the final design features larger (and subsequently stronger) dies which bolt directly to the structure. A washer-type force sensor can be threaded onto the bolt, spacers with a known thickness can slotted behind the die in order to customise the degree of ironing involved. This allows the rig a certain versatility without necessitating entirely new geometric dies between each experimental run. The spacer tubes allow fixing bolts to be pre-loaded which will prevent any undue deflection of parts whilst also decreasing the difficulty of parallel alignment when building the rig. The entire construction is a combination of mild steel housing and tool steel wearing-parts (namely the dies,

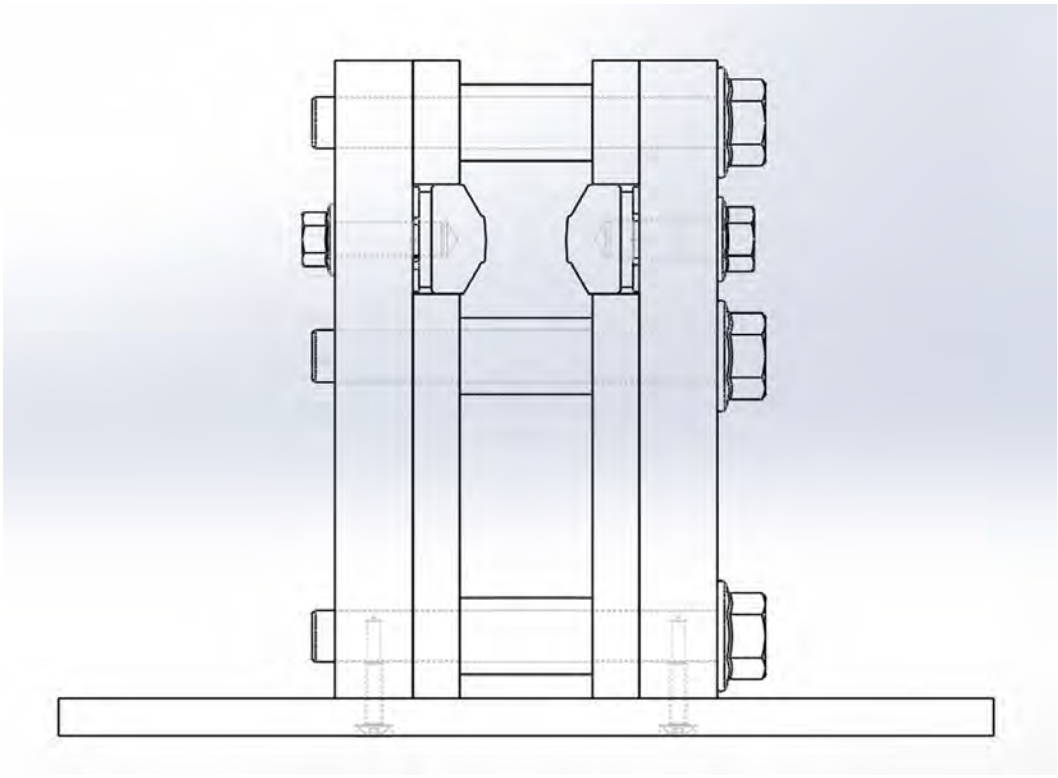

FIGURE 5.20: Figure showing a translucent side-view of the final rig design in order to demonstrate bolt and fixture locations

and a geometrically arbitrary punch which has not been featured). With proper calibration the ironing rig could be used for any manner of ironing-related experimentation.

5.3.5 Die geometry evaluation

The design intention of the ironing rig was to create an apparatus which could thoroughly simulate and observe ironing behaviour in an open format and experimentally validate numerical models. To understand the kinds of variables which cause changes in material behaviour and failure during ironing it is important to analyse the geometry featured in the dies.The die geometry consists of thee parts of interest: an inlet angle, a flat landing strip, and an outlet angle. The generic anatomy of the die geometry applies to many dies in the industry[124]. Figure 5.21 demonstrates the main contacting parts of the die.

Each of the five variables featured in figure 5.21 is a potential focus for study. The remaining geometry is simply for rigidity and positioning, and does not make contact with the specimen during ironing. Whilst the lengths of the inlet

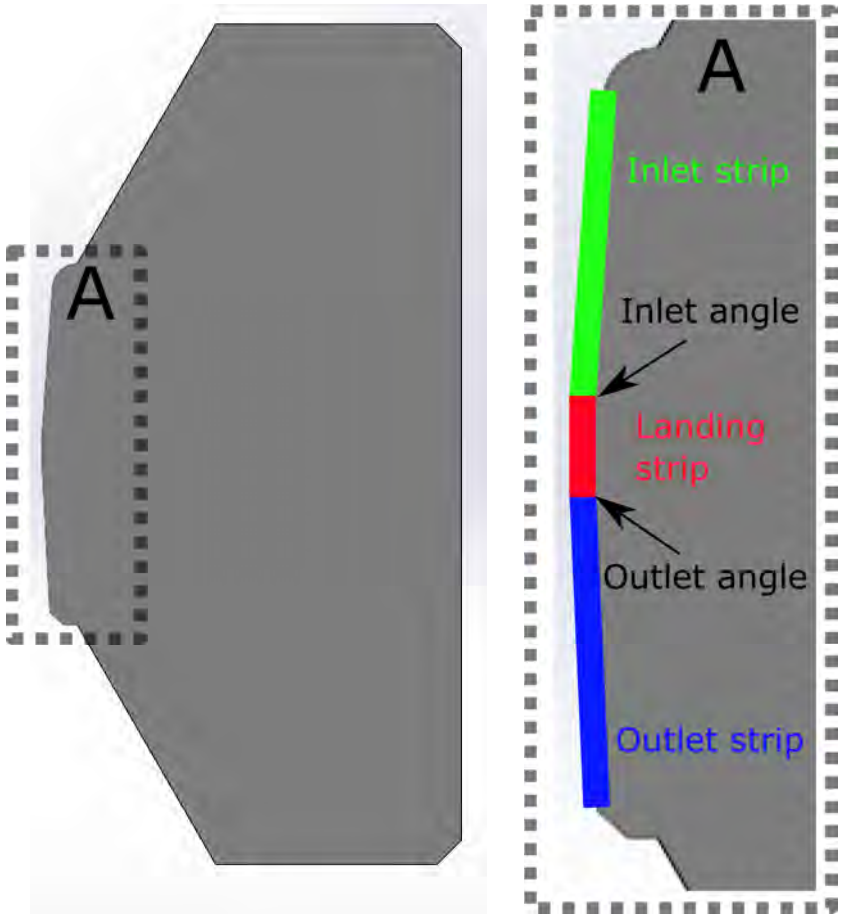

FIGURE 5.21: Break-down of three main contacting surfaces of an Ironing die, along with the conjoining angles.

and outlet strip only change as a result of a changing inlet/outlet angle, it is still important to highlight this geometry as an area of focus for modelling benefits.

By comparing rig data to similar simulation data, the numerical models can be tuned to accurately represent the ironing process. The physical behaviour observed during testing will allow adjustment and benchmarking for modelling behaviour moving forward, and when the more advanced full-process models are created - these benchmarks can be used to ensure that behavioural process accuracy remains in the model when physical experimentation cannot follow, such as the expensive creating new die tooling for each geometry change. A robust numerical approach allows the die parameters to be included in a DoE (Design of experiments) for numerical models later.

5.4 Validating results

5.4.1 Experimental method

The ironing rig functions with a temporary installation to a screw-driven tensile testing machine. Removing the bottom clamp allows the base of the rig to sit flush along the testing apparatus, and the punch is installed using the universal bolt-fitting present on the tensile testing machine, as shown in figure 5.22 .

FIGURE 5.22: The iron rig after basic installation into the tensile tester.

Due to the small dimensional tolerance involved in ironing, it is important to ensure precision is as high as possible. The simplistic wooden alignment block seen in figure 5.22 allows reliable repeatability between setups in the front/back spacing, however the left/right spacing proves somewhat harder to determine. Due to the customisation designed into the rig, the central path of compression shifts to the left or right depending on what shims are installed behind the dies.

To best align the centre of the punch to the centre of the unit, a measuring stick was affixed across the top of the apparatus. The unit moved left and right by hand, sliding along the wooden spacer until the centre of the measuring stick aligned with a centre mark on the punch. This hand-movement is responsible some error within measurement - but this error should be somewhat counteracted by the freedom of the punch along the two loosely bolted joints.

Once the apparatus was properly set up, the experimental procedure involved compressing the punch through the rig at a fixed speed, using the computer interface attached to the tensile tester. The experiment ran 2 sets of strips $30mm$ and $20mm$ wide of TH330 unstoved Steel (a heavily characterised material in the processing world [58]). The compression speed chosen was $250mm/$minute, which was the maximum compression speed of the apparatus. The compressive force measured by the punch was logged alongside punch displacement every 0.2 seconds, and the other metrics were measured manually before and after testing.

Thickness was measured before and after using double spherical-anvilled micrometer with an error of ± 1 micron, widths and lengths were measured with using a digital caliper with an error of ± 100 microns. The length measurements suffer an additional error of ± 500 microns due to the fineliner marking method used.

The method of setup and execution follows:

- A specimen is cut using a guillotine, from the stock coated metal, using a stopped to keep widths consistent.
- The punch is returned to the "zero" position using the machine control, and removed from the unit.
- If geometry change is necessary, the rig is removed from the tensile machine area and the holding bolts on each die removed. The desired combination of spacers is inserted onto the bolt behind the die, and the die reinstalled.
- The rig is then reintroduced to the apparatus.
- The ironing specimen is marked using fine permanent marker. Two lines on each side with three points on each line are used to measure average length and thickness on each side.
- The specimen is aligned by hand to the punch, and pre-bent over the punch to reduce movement during the test. An elastic band is used to fix the pre-bent specimen in place against the punch.
- The punch is reinstalled into the machine, and lowered until there is a small clearance before meeting the ironing dies.

- The measuring stick is affixed (tape was used for these experiments) to the top of the die, and the rig aligned central to both axes using the wooden alignment block.
- Once aligned, the maximum force load was set on the tensile machine at 20kN (dictated by the load cell used), and the compressive test executed.
- Once the punch was free of the dies and the specimen released, the machine was stopped.
- The tensile machine was powered down, and the specimen removed from the compression area, before powering the machine back on to zero the punch again.
- Each specimen was repeated 4 times

Geometric measurements and force results can be seen in tables 5.6. Each data entry listed represents the mean result of the 4 repetitions - the standard deviations of all measurements are listed in table 5.5. From this data, the experiment is clearly reasonably repeatable, and there is no significant different in deviations from one tooling setup to the next. The lengths vary more significantly than width or thickness, which is to be expected since the error for length measurement was two orders of magnitude higher thickness and several times higher than width. This deviation in length measurements compared to thickness and width highlights room for improvement, and the requirement for a more accurate metrology method in future work.

TABLE 5.4: Experimental results from ironing 0.27mm thickness, 31mm wide, TH330 steel, with the bench-top rig in a compression tester.

Tool ironing reduction %	**Elongation %**	**Thickness reduction %**	**Width change %**
12.22	8.03	11.76	-1.05
22.2	38.33	24.72	-0.49
34.44	47.5	38.99	-1.37
44.26	59.38	32.22	0.24

Now the experimental trials has succeeded, a simulation was created for better comparison to the final built model. This simulation was run in 2D using unity width CPE4R elements, a penalty-contact friction interaction of 0.1 magnitude, and displacement/rotation boundary conditions to move the die over the time step at the same speed (250mm/s) as the experiments. Simulations

TABLE 5.5: Standard deviation (STDEV) of the raw results measurements used to derive the metrics in table 5.4.

Tool ironing reduction %	**Length STDEV**	**Thickness STDEV**	**Width STDEV**
12.22	2.470	0.007	0.292
22.2	3.256	0.005	0.232
34.44	3.122	0.006	0.292
44.26	3.309	0.007	0.172

were undertaken at the same experimented ironing reductions, tested with and without a spring element behind the die to account for the compliance and deformation present during the experimental process. Force data was scaled up to match the widths of the experimental specimens. Results to the simulations are seen in table 5.4, and figure 5.23 and 5.24 demonstrate the Von Mises and plastic equivalent strain distributions respectively, during the ironing process. The behavioural difference between the engineering variables during various extents of ironing is clear.

TABLE 5.6: 2D Simulation results from ironing 0.27mm thickness TH330 steel in Abaqus

Tool ironing reduction %	**Elongation %**	**Thickness reduction %**
12.22	7.33	12.08
22.2	15.58	22.09
34.44	31.19	34.33
44.26	59.38	44.20

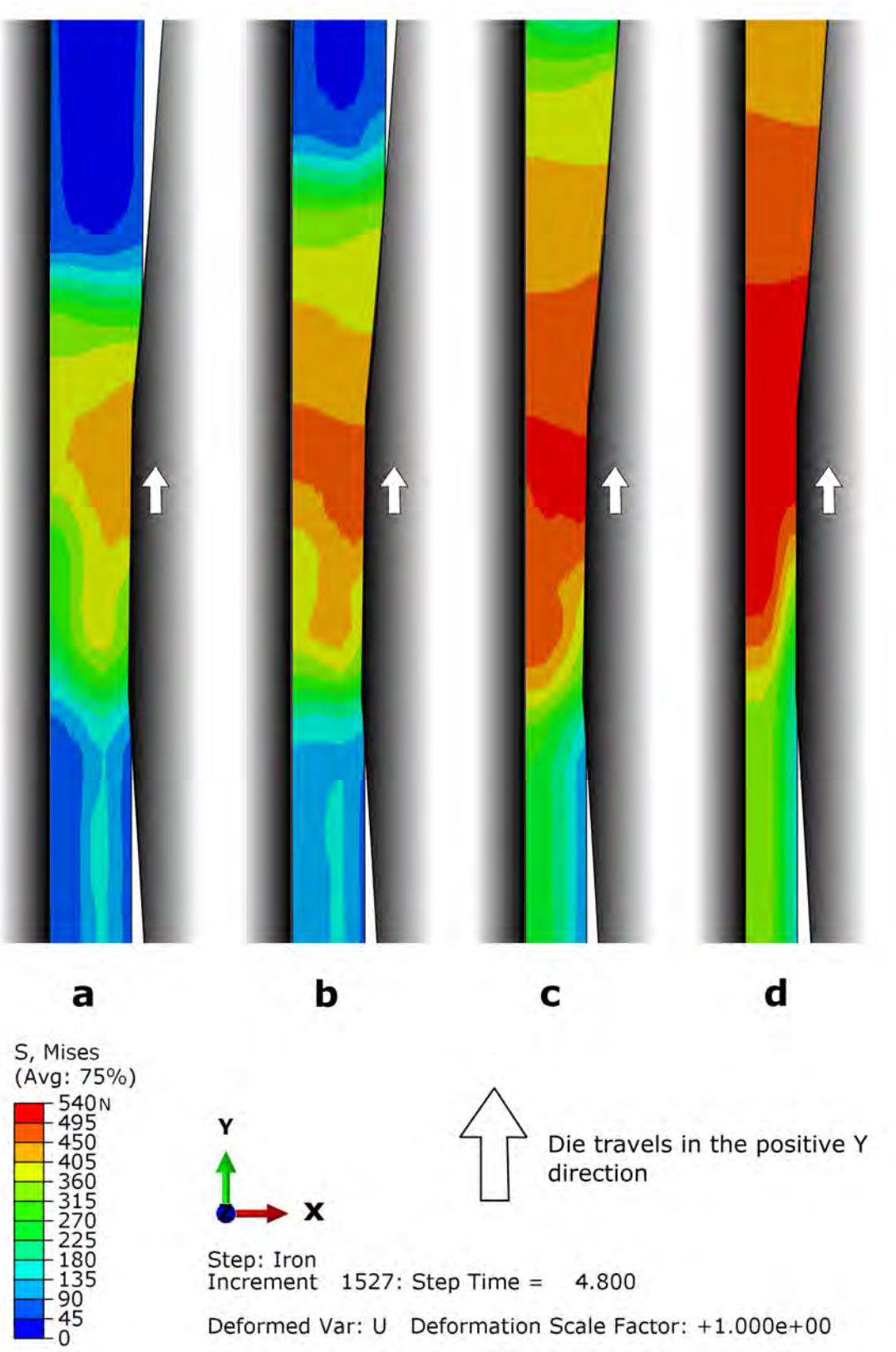

FIGURE 5.23: Illustration of the Von Mises stress distribution plots of the rigid simulations. A, B, C, D show 12, 22, 34 and 44% ironing respectively

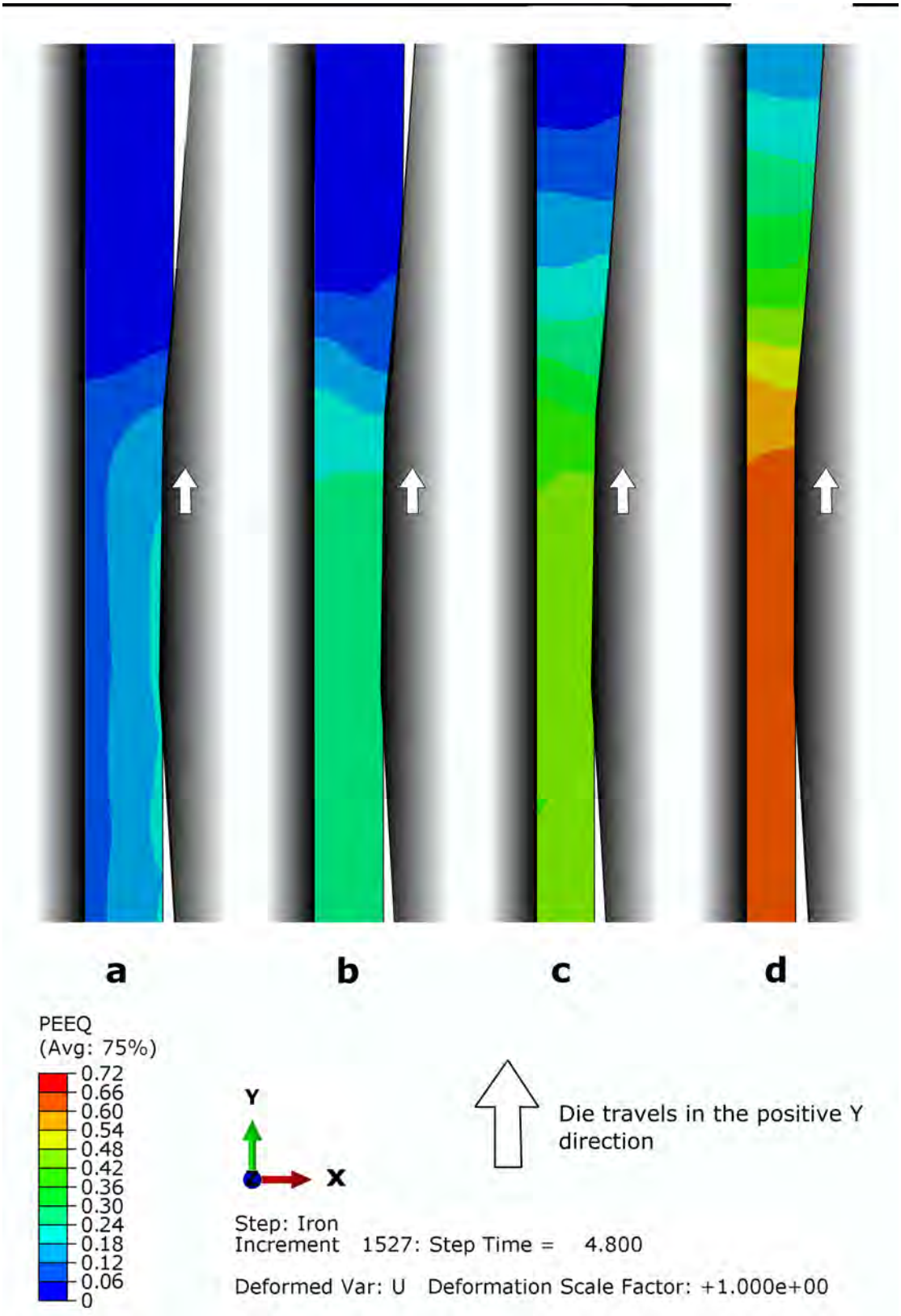

FIGURE 5.24: Illustration of the plastic equivalent strain distribution plots of the rigid simulations. A, B, C, D show 12, 22, 34 and 44% ironing respectively

The results demonstrate some interesting correlations. Looking at figure 5.25,

the closest matching experimental and simulation results are the *Rig 20mm* and *Sim rigid* data sets. The similarity between these geometric results is promising, however comparing this to the force results from figure 5.26, the relationship clearly does not follow suit. From what has been established about the ironing process, it is a reasonable assumption that similar ending geometry would result from similar ironing forces (given an identical setup), though this does not appear to be the case. This discrepancy should be investigated in future work, and is likely the result of other variables such as friction coefficients, compliance in the force sensor etc., which have been considered. Whilst this difference should not be ignored - the forces experienced by the equipment was not a focus of study, as all tooling in the ironing process is frequently replaced with use.

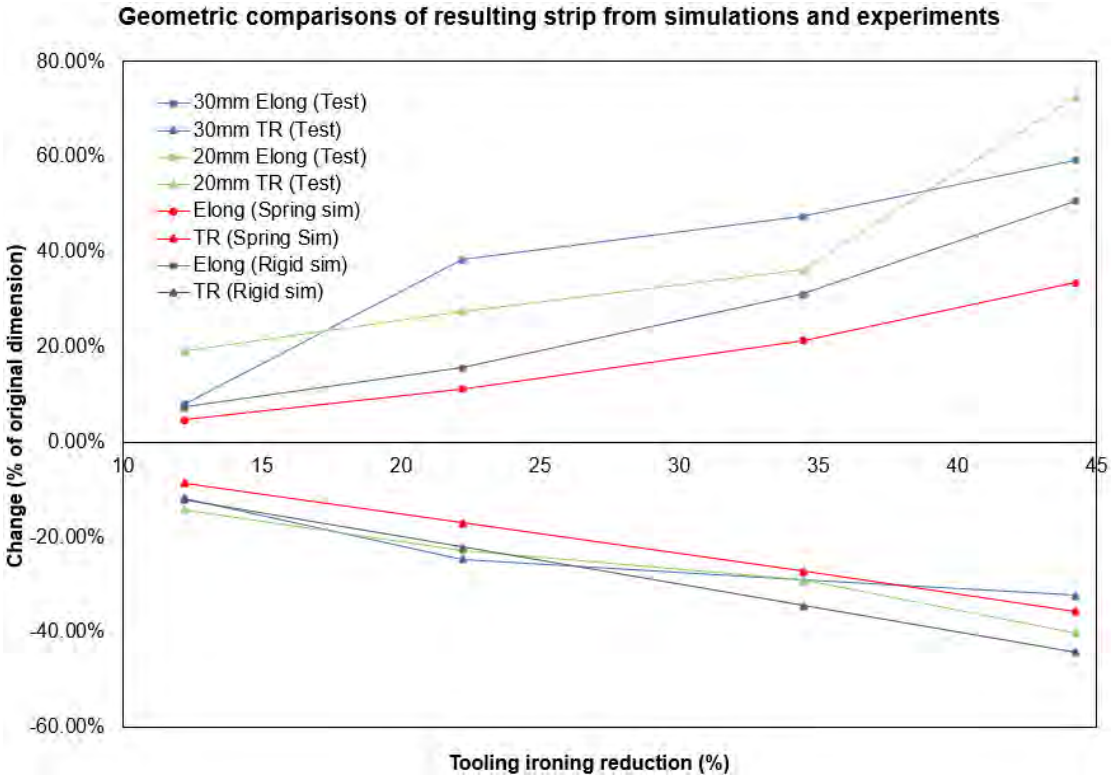

FIGURE 5.25: Graphical comparison of testing and simulation results on the final geometry of the strip. Changes in elongation (Elong) and thickness reduction (TR) are included.

Focusing on the curves for the spring-inclusive simulation and the 30mm specimen rig tests, it can be seen that the elongation measurements vary more significantly than the thickness reduction measurements. This difference is likely due to the decreased precision measuring rig specimen elongation using calipers,

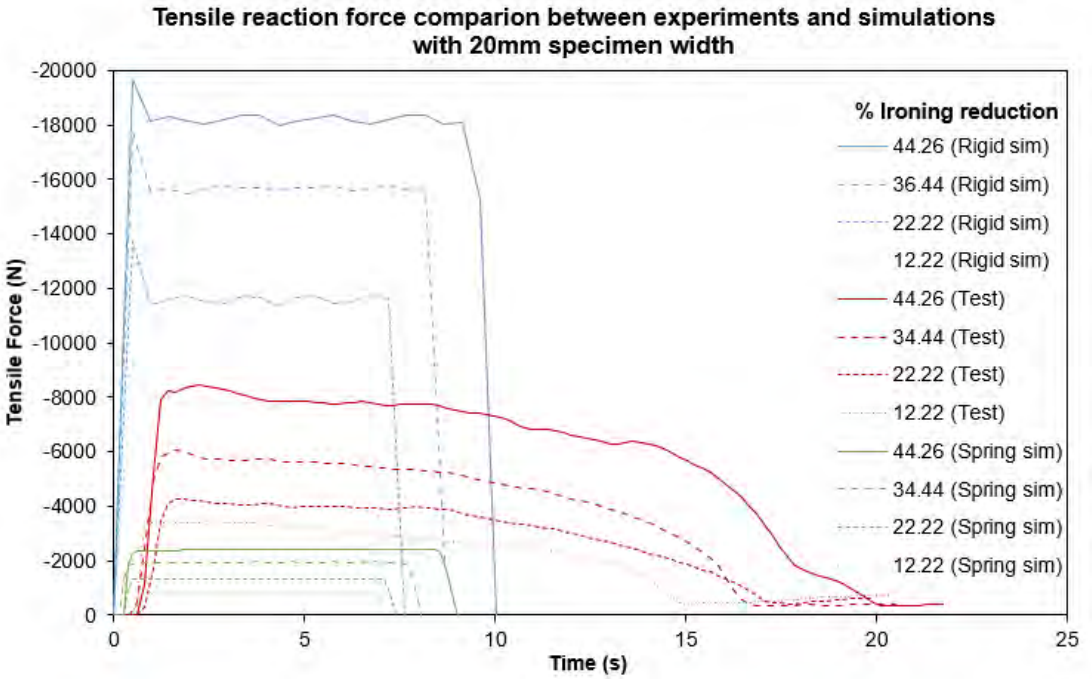

FIGURE 5.26: Graphical comparison of the reaction forces between rigid simulation, sprung simulation and rig test. Similar colours indicate the results groups. The lines within groups correspond simply as higher ironing creates higher forces.

compared to measuring thickness with the more precise spherical anvil micrometer. Metrology in simulations was all done using Abaqus CAE, where the distance calculations have minimal error. In order to better clarify what was happening during the rig process, a specimen was ironed partially at 34.44% tooling reduction, and the rig subsequently disassembled in order to remove the specimen without damage.

Figure 5.27 illustrates the moment mid-ironing, and demonstrates the process by which the steel specimen is ironed. It can be clearly seen that the lower length of specimen has a smaller thickness than the higher section above the landing interface - demonstrating clear thickness reduction during the process (as opposed to a stretching effect, where thickness reduction and necking is inconsistent throughout the piece). Using *ImageJ* image analysing software, a sample measurement was taken above and below the ironing point. The two samples measured at 24 and 19 (the units are related to the size of the image and have thus been omitted). This equates to an approximate reduction of 21%, which is not quite as high as the intended tooling reduction, but reinforces the presence of ironing in the specimen.

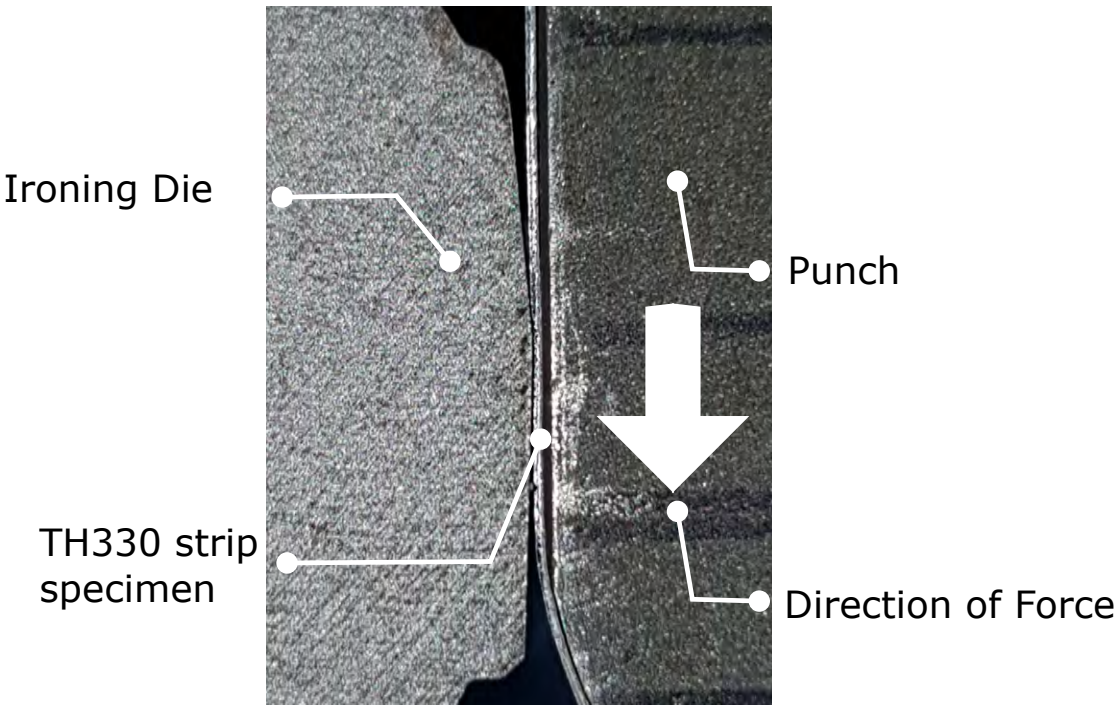

FIGURE 5.27: Closeup photograph of the Ironing rig. Labels indicate tooling and direction of driving force.

5.5 Optimising simulations to match rig output

The data seen in figure 5.25 clarifies the efficacy of using the spring element on the ironing die to replace the rig compliance effect in the model. Observing the differences in results, it is clear that the spring coefficient linearly changes the results (as is to be expected, since the level of ironing is effectively being reduced). When considering the geometric test data, the thickness reduction is a far more robust solution than the elongation. Since the apparatus for measuring thickness was much more accurate, there is very little error across the measurements compared to the drawn and hand-measured line grid used for elongation (seen in figure 5.28. The clear bend occurring in the specimen was a result of unequal ironing occurring across the dies - causing one side to be ironed (and elongating) faster than the other. The average of six measurements taken across the elongation marking lines were an attempt to minimise the significance of this, however the overall effect diminishes the accuracy of the elongation measurement, compared to the thickness.

With this discrepancy in mind, it is evidently a better idea to take all three metrics as a more robust solution for comparison (force, elongation, thickness reduction). Observing the rig-test thickness-reduction results, it appears the ideal

FIGURE 5.28: Photograph of an ironed specimen after testing. The black lines were used as before/after markers to measure elongation.

simulation solution runs between the perfectly rigid and the sprung ironing dies. The natural progression with this data was to run a study on the spring coefficient to see if a value could be reached that better matches the output data of a rig test.

The rig test data for the 22% ironed strip as well as the corresponding ironing simulation was imported into *Simulia Isight* using the Abaqus and Data-matching model, and in addition the calculator module was added. By specifying coordinate outputs for certain nodes, and manipulating these coordinates using said calculator module, parameters for thickness and elongation were able to be derived. Using these parameters an Isight optimisation was possible, targeting not only the data-matched force values but also the final elongation and thickness-reduction values from a rig test. However since only 1 parameter was in use, a *Parameter Study* was used instead - which maps the same design space with a predefined array for the chosen parameter. Figure 5.29 illustrates the optimiser evolution and demonstrates the general progression of the spring coefficient. Data from figure 5.26 for the 20mm Rig specimen was truncated and normalised to produce smoother data for a unity-width, steady-state specimen to enable a better comparison for the data matching. This data was then compared to the experimentally obtained data using a sum of squared difference method.

			PARAMETER_1_spring_stiffness_V...	Elongation	Sum of the Squared Difference	Thickness
✓	1	1	0	-2.481389578E-5	415299.4672	-1.644774851E-15
✓	1	2	20000	0.1726923077	69509.12455	-0.1455555556
✓	1	3	40000	0.2147022333	39333.25128	-0.1774074074
✓	1	4	60000	0.2349379653	29773.37077	-0.1914814815
✓	1	5	80000	0.2463027295	28455.90344	-0.1985185185
✓	1	6	100000	0.2533126551	24223.88133	-0.2037037037
✓	1	7	120000	0.2581885856	21214.70837	-0.2066666667
✓	1	8	140000	0.2617369727	21189.79287	-0.2088888889
✓	1	9	160000	-2.109181141E-4	6656.689483	1.151342396E-14
✓	1	10	180000	0.2665632754	21112.30504	-0.2118518519
✓	1	11	200000	0.2682754342	19874.84019	-0.212962963
✓	1	12	220000	0.2697146402	19181.33478	-0.2137037037
✓	1	13	240000	0.2708436725	18593.64057	-0.2140740741
✓	1	14	260000	0.2718858561	18409.70808	-0.2144444444
✓	1	15	280000	0.2727295285	17958.96781	-0.2144444444
✓	1	16	300000	0.2735235732	18005.7322	-0.2144444444
✓	1	17	320000	0.2741811414	18155.23881	-0.2144444444
✓	1	18	340000	0.2747766749	17857.84804	-0.2144444444
✓	1	19	360000	0.2753101737	17758.92583	-0.2144444444
✓	1	20	380000	0.2757940447	17533.46133	-0.2144444444
✓	1	21	400000	0.276191067	17418.85614	-0.2144444444
✓	1	22	420000	0.2765508685	16865.55641	-0.2144444444
✓	1	23	440000	0.27691067	17075.03984	-0.2140740741
✓	1	24	460000	0.2772208437	16598.37651	-0.2140740741
✓	1	25	480000	0.2775186104	16768.38533	-0.2140740741
✓	1	26	500000	0.2777791563	16682.01944	-0.2140740741

FIGURE 5.29: Illustration of the design process for the spring parameter study

The parameter study was stopped once changes to elongation and thickness reduction were no longer significant. Using Isight procured a reasonable match between the ideal rig-obtained results and the elongation and thickness-reduction geometry measured from the model. However whilst the geometric comparisons were favourable, the force matching was less than ideal during the optimised result. Figure 5.29 illustrates the comparison to the experimental result

set.

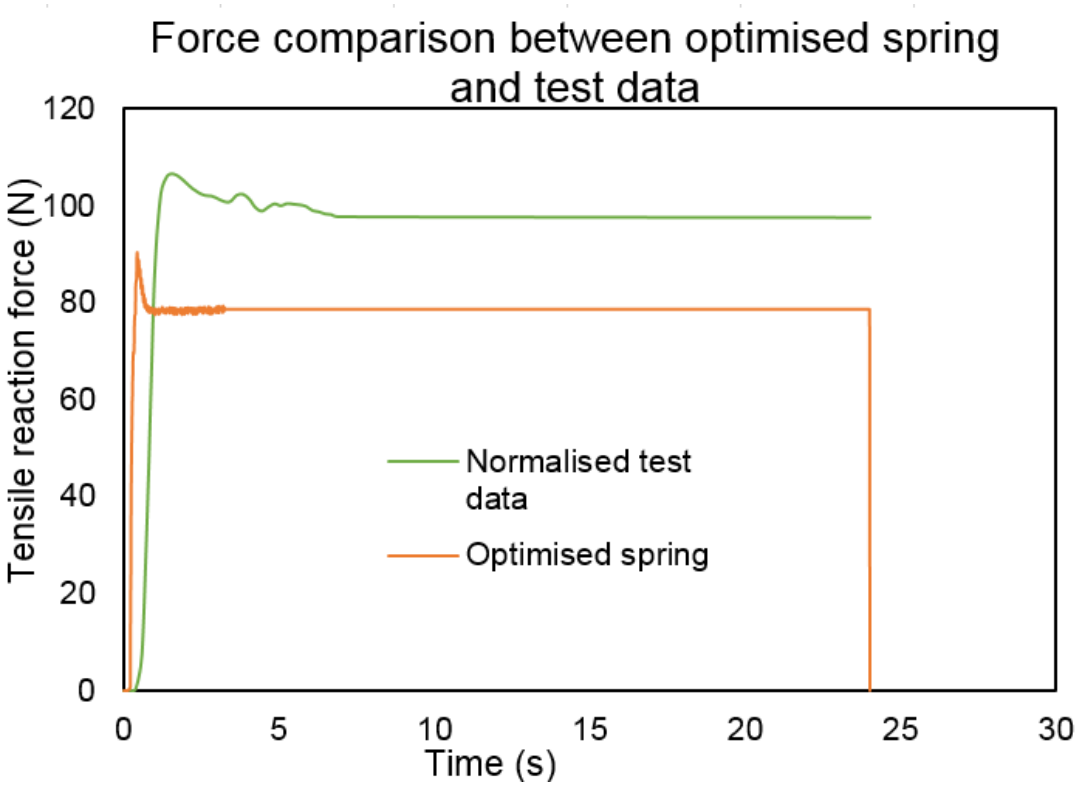

FIGURE 5.30: Graph showing the force comparison between the optimised spring coefficient simulation data, and the truncated and normalised force data previously seen in figure 5.26

It became apparent that there was an overlooked variable in the optimisation, and that optimising the spring coefficient alone was isolating the effect and not fully representing the rig behaviour. Given the relationship between friction and reaction force in *Amonton's first law of friction*[125], as well as *Coulomb's law of friction*[126] the coefficient of friction used in the model may be a defining factor in the forces generated - even if it does not alter geometric deformation as drastically. Equation 5.15 demonstrates Coulomb's approximation.

$$F_f \leq \mu F_n \tag{5.15}$$

A new optimisation was set up as before using a Downhill-simplex routine, once again targeting elongation and thickness-reduction, and minimising the squared difference between the force data. However this time, the friction parameter was entered as an input alongside spring stiffness, and the optimiser ran driven by the two.

TABLE 5.7: Tabulated data comparison of the measured geometry for the optimised models and original test data.

Results set	Elongation	Thickness reduction	SumYsqrdiff
Test data	26%	-21%	N/A
Spring pt.	27.8%	-21.4%	16682
Spring/friction opt.	25.6%	-20.5%	39.2

The results firmly proved the hypothesis that friction was the missing link in matching forces. Whilst the elongation and thickness reduction were affected, the force data was affected to a far greater extend. Figure 5.31 illustrates the initial optimisation data alongside the new friction/spring optimised solution. The difference in shape at the beginning of the curves is a result of the differences in starting conditions between the simulation and the rig. In the rig, the metal strip is bent to shape, but not perfectly formed to the die - whereas it is in the simulation. As a result, the reaction forces in the initial contact phase will be slightly different.

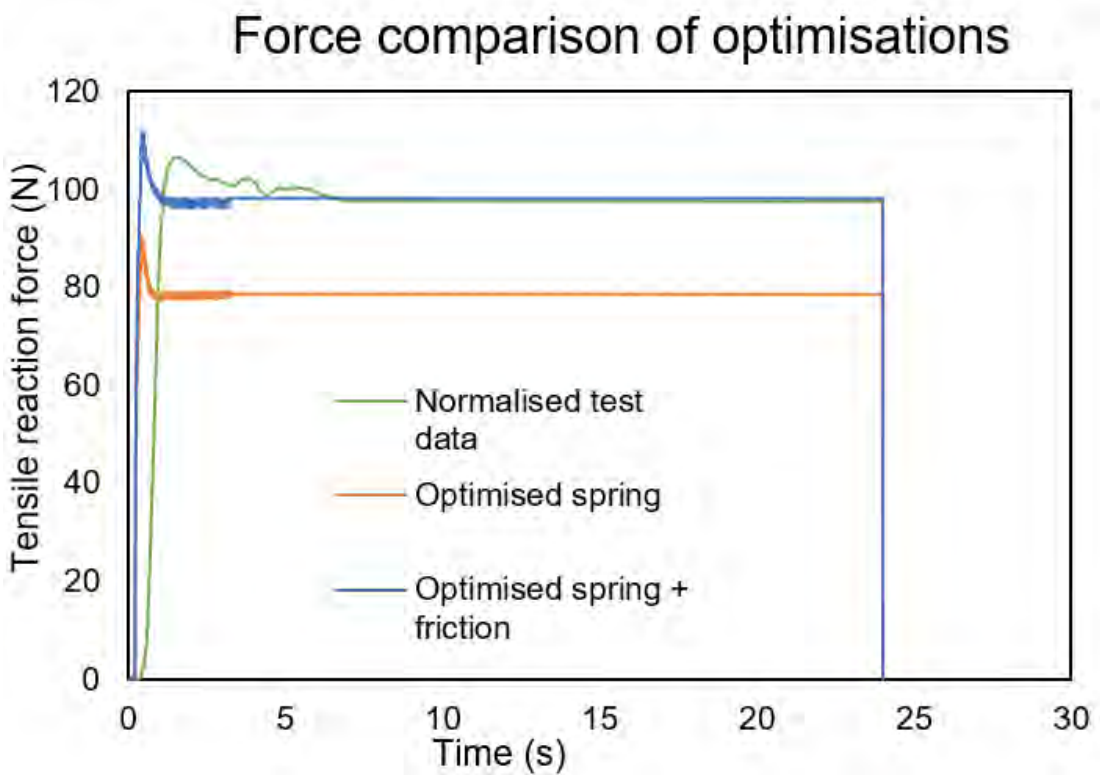

FIGURE 5.31: Graph showing the force comparison between the new friction/spring optimised spring coefficient simulation data (μ set to 0.146), and the truncated and normalised force data previously seen in figure 5.26. The spring optimised solution is also included for clarity.

The data for the friction/spring optimisation clearly matches the test data to a much better degree than simply using an optimised spring coefficient. Table 5.7 shows the results comparison between optimisations. Whilst the friction/spring optimisation isn't as close geometrically as other more rigid solutions displayed in figure 5.29, the data matching value of sum-squared difference is significantly better (improved from $16,600$ to 39.2). When compared with relative error, the friction/spring solution is only 1.5% out on elongation, and 2.5% out on thickness reduction. Ultimately this is not only a much better solution than the alternative spring-only optimisation, but also a generally robust match for the original test data.

With a suitable value of μ obtained, and the spring coefficient sufficiently emulating the compliance in the rig, there is finally a validated model which can accurately depict the behaviour of a specimen during ironing for TH330 unstoved steel.

5.6 Design points of interest and failure modes

During the use of the rig, it became increasingly apparent that variance of results was slowly increasing. With each pass of ironing the chances of a skewed specimen or failed test increased, and setups which originally provided clean ironing were beginning to give inconsistently successful results, and eventually complete failure. Figures 5.32 and 5.33 demonstrate the output difference between two identical tests, undertaken months apart (with hundreds of tests and calibrations between). It's possible that human error is to blame, but unlikely given the same operator and methods in both cases. After a few hundred tests and calibrations, every specimen was ironing inconsistently after only a few centimetres. A number of calibrations were re-adjusted including bolt pretension, as well as die height alignment (achieved by inserting shims of varying thickness beneath the die on either side).

Eventually the die were remeasured, and were flagged as the main issue. Depth measurements varied by as much as 50 microns throughout the width of the die, which were causing inconsistent ironing across the width of the specimen. Looking back to figure 5.33, these results are consistent with skewed ironing reductions. The curved side of the specimen has clearly been ironed more, which causes more elongation on one side - thus causing the skew. Since the *skew* is

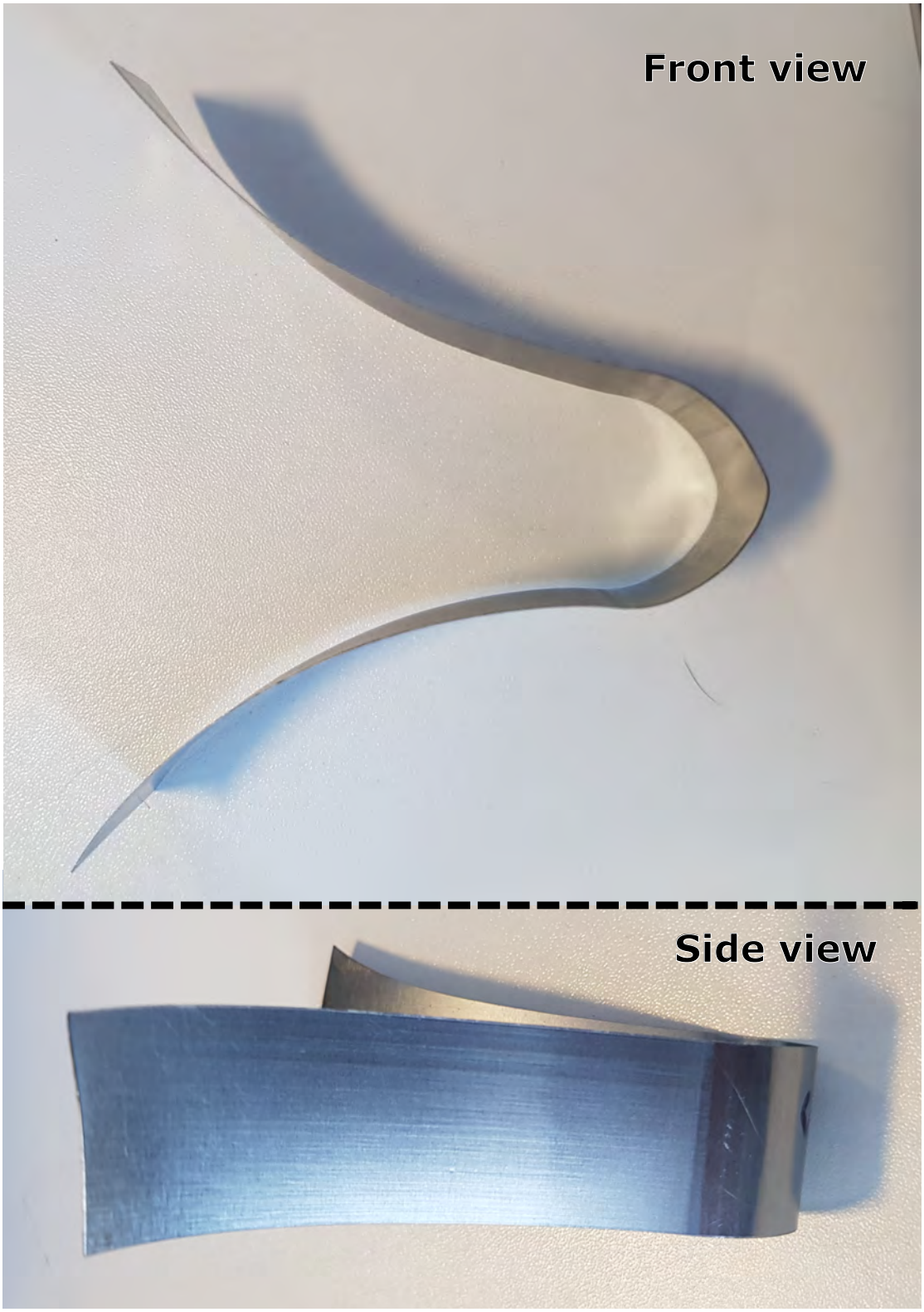

FIGURE 5.32: Photograph of a successfully ironed sample. The ironing on each side is approximately equivalent, and no skewing has occurered.

a result of greater elongation on one side: forcing material to the side of lesser ironing, the issue appears to be self-propagating, with specimens skewing more

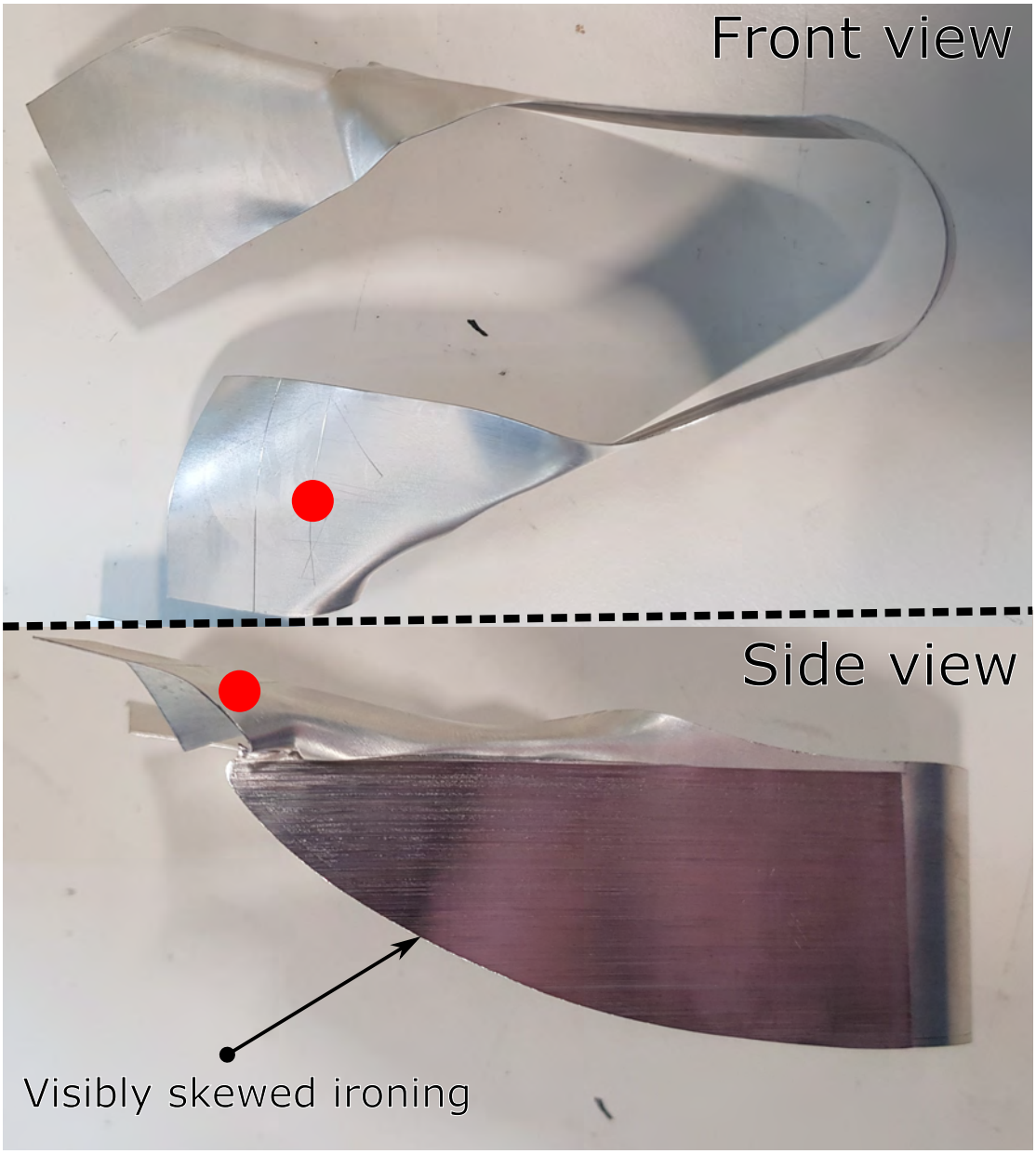

FIGURE 5.33: Photograph of a typical "skewed" specimen failure from front and side view. Red dot indicates the same area on both views.

dramatically the longer they are ironed. In this sense however, it is possible to get a moment of "good" ironing at the beginning of the test, before skewing is out of control - though it should still be noted that the specimen will still not be evenly ironed.

Clarifying this issue highlights a major point of design consideration. Inevitably, the uneven wear have a few major causes: alignment issues, uneven loading, and failures to name some. Alignment issues concern any test or calibration where the punch and specimen has not entered and passed the dies exactly

parallel in both planes. Even a slight angular entry causes uneven wear on one side or another (as ironing begins momentarily sooner on one side), and wears both the punch and dies unevenly. Uneven loading concerns situations where the specimen has not been perfectly centred during loading. Some tests were intentionally loaded to one side in order to gain access to photography of the process (one of the major interests when designing the rig). Unfortunately these non-centred specimens cause a specimen edge to be clamped between two dies - potentially causing a microscopic permanent deformation in the die during the process. Theoretically this happens every time a specimen is used which does not perfectly match the die width, but it was assumed that an equal indentation pattern would not dramatically affect the results. Uneven loading naturally causes a singular indentation as opposed to an equally spread pair of indentations, which is perhaps a larger issue. Finally, failures cause a combination of the aforementioned issues. Retrieving a specimen after failure is incredibly difficult and requires either forcible removal, or disassembly of the rig. Either way, uneven wear has occurred by the point of failure (assuming failure is asymmetrical, as has been the case).

Briefly, lubrication was investigated to solve the issue. In conceptual trials for polymer-coated cans, the PET layer itself reduces friction enough that lubricant isn't necessary (water is still used for cooling the tooling). An available machine oil was mixed with water in concentrations of 100%, 50%, 25%, but each lubricant trial failed to make any different to force readings, and appeared to be "scraped off" by the tooling, so lubrication was not pursued as a solution. Various coatings such a Titanium Nitride could be used in future iterations to reduce wear on the contact parts, but cost and specification of the prototype did yet not merit this change.

Generally speaking, these issues were all accounted for during design. The decision to heat-treat the dies was an attempt to manage the wear on the tooling, but a major issue with the planar alignment is the self-propagation of said issue. Even a slight difference in manufacturing of the aligning plates (which inevitably occurred, since the tolerance of the grinding machinery was around 100 microns) would theoretically cause slight uneven thickness reduction during the tests, and this uneven ironing would cause uneven wear. This uneven wear then causes more uneven ironing, in a cycle which continues until failure occurs at every test (a point now reached with the concept rig.)

This issue should not necessarily be attributed exclusively to the rig, however. Tool wear is an inevitable part of the ironing process, but ironing with cylindrical specimens potentially skews any data gathered for comparison with the strip-ironing rig. When a strip specimen is formed unevenly, a failure such as the one seen in figure 5.33 can be clearly observed. However if the same uneven wear occurred on a cylindrical can specimen the "skewing" cannot occur in the same way, and may instead be the cause of problems such as earring [127]. In this sense, the issues on the bespoke rig may be the exact same issues encountered during can-making - simply manifesting in a different way due to their differences in geometry. Unfortunately it is difficult to tell at this time, however investigating both defects may in future prove a relevant comparison.

A future design iteration would certainly use a harder material for the dies and punch. Tungsten carbide is generally used in the industry for such tooling (though at significant cost) so it's advisable to use that same compound to minimise wear. As mentioned, the alignment issues are inherent to planar ironing and changing to cylindrical design (whilst effectively minimising the alignment issues) defeats the purpose of the open-sided rig somewhat. Instead the focus should remain on tolerance during build, and even some further calibration for use during testing. Fitting a measuring system and a threaded adjuster would enable better calibration of the distances from front and back of the die during ironing. Wear is inevitable so taking steps to reduce and compensate would seem to be the main target in a future build.

5.7 Conclusions

The aims of this chapter have been fully achieved: the bespoke rig was capable of performing the ironing process with available testing equipment, and a combination of ready-characterised metal specimens and polymer-coated specimens allowed both the rig's compliance, and the polymer layers to be accounted for. Though the data gathered from the rig is not perfectly accurate, the work demonstrates a fundamental basis of validation for the modelling approach created in chapters 3 and 4. For the purpose of this project, the short-lived rig met its purpose and provides reasonable data for the final part of the thesis. The next branch of work in chapter 6 covers the final optimisation of the contact-definition modelling approach devised in chapter 4 using the data gathered from the ironing rig.

Chapter 6

Furthering the FEA models using optimisation.

6.1 Introduction

With the ironing rig complete and the corresponding simulations optimised to account for the correct compliance within the material deformation, an opportunity to further optimise the polymer contact definition arose. This chapter aims to cover the progression towards a substantially physically verified contact-definition method to model the polymer-coated steel in Abaqus. Once the contact definition is adequately characterised from real-world data, there is nothing prohibiting a final DoE study on the polymer-coated DWI process.

6.2 Revisiting the optimisation of the contact definition

The previous optimisation derived congruent spring and friction values for the specific setup in question: namely tempered tool-steel dies with TH330 unstoved specimens. The advantage of that optimisation is that the spring coefficient which represents the compliance within the entire ironing rig is going to be consistent regardless of which specimens are put in, and what levels of ironing reduction are undertaken. A further optimisation can be undertaken, revisiting the previously estimated PET coating pressure/over-closure definition which was only validated against existing PET material data. By transferring the derived spring coefficient into a new model but resetting the friction

Specimen ID	Elongation %	Thickness reduction %
PET-Steel 1	21.6	17.26
PET-Steel 2	22.0	17.08

TABLE 6.1: Comparison of the final geometry of two 30mm width PET-coated steel rig specimens, ironed at 250mm/minute with a tooling thickness reduction of 20%

coefficient, the exponential definition can be optimised alongside the PET friction coefficient to create a new contact definition which is validated against real-world ironing experiments on the PET-coated steel.

Though this new definition would appear to stem from more unknowns than the previous optimisation, it is important to revise that the PET pressure/overclosure definition is only intended to model the PET coating's contribution towards geometric change within the ironing process. The purpose of these models are not to demonstrate or predict coating failure, but instead to predict steel failure and resulting geometry (which the PET coating has no bearing on except to alter the thickness of the blank). For this reason any combination of friction and exponential coefficients which correctly emulate the PET coated steel specimen is acceptable substitution for modelling the coating itself.

The ironing rig experiments with PET-coated steel were undertaken with the exact same setup as the previous TH330 experiments at $250 mm/minute$, and geometry measured with marked lines and a spherical anvil micrometer. The only notable difference is that the percentages of ironing reduction necessarily change slightly to account for the difference in material thickness. Since the spacing washers are finite and their thicknesses unchangeable, the combinations are limited and experiments must settle with whichever combination provides an ironing reduction closest to that desired. The PET-coated specimens were undertaken towards the end of the ironing rig's useful duty; subsequently only two specimens were able to be properly measured before excessive skewing became an issue. The results of the two specimens are very similar and provide a confident basis of comparison to simulations. Results are shown in figure 6.1 and table 6.1.

For the comparative simulations, Isight was set up with a Downhill-simplex routine to optimise both the exponential definition (equation 4.3) and the friction coefficient (since friction for PET and steel was still unknown). The spring coefficient derived from the previous Isight optimisation was input as a fixed

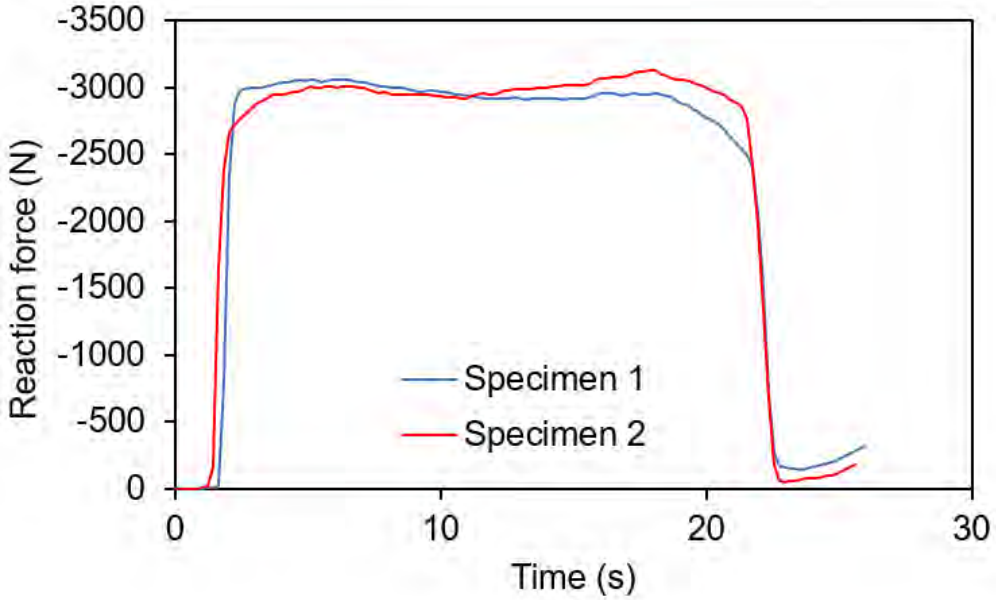

FIGURE 6.1: Punch reaction force of the two PET-coated steel rig specimens, graphed directly from the datalogger.

Specimen ID	Elongation %	Thickness reduction %
PET-steel sim optimised	23.04	17.68

TABLE 6.2: Geometric results of the friction/exponential definition optimised simulation for PET-coated steel strip.

value to account for the known compliance in the rig. The optimiser outputs used a target match for the elongation and thickness reductions obtained from the rig results in table 6.1, as well as a minimising Y-square-difference target for the normalised force data from figure 6.1. To normalise the force, the values were divided through by -30 to create a positive force value for 1mm of specimen (as the simulation models). No bounds were introduced for the independent variables as the design space was unknown.

The results demonstrate a positive match in both force results and geometric data. The difference in initial force curvature is be explained by the difference between simulation geometry and rig tests: the simulation begins with a pre-curved specimen whilst the experiment bends the specimen into place at first contact (this is why the force line gradient begins smaller for the experiment result). Ultimately, the contact model and friction coefficient derived from the Isight optimisation are suitable for further study, and the geometric differences

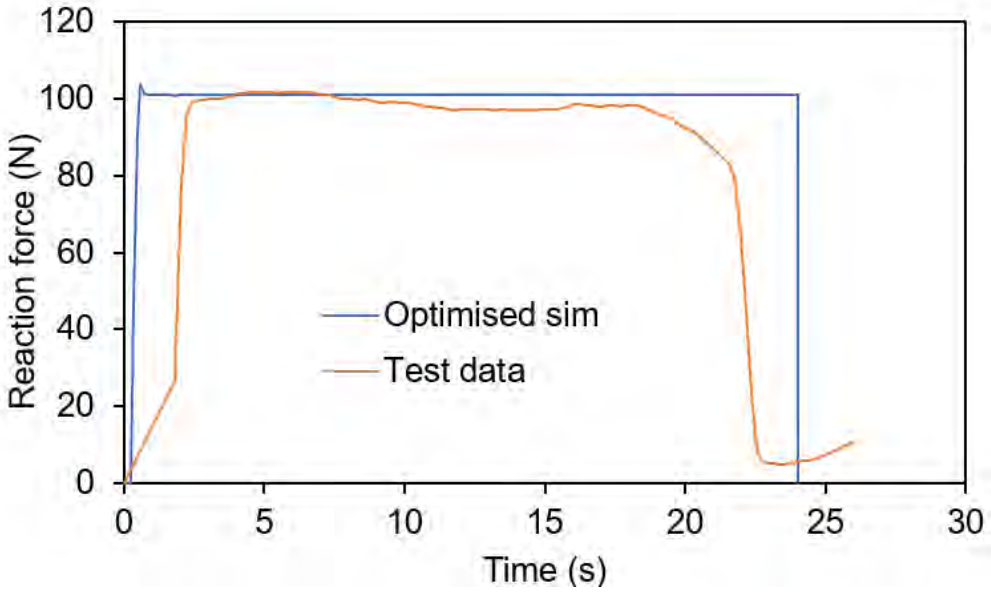

FIGURE 6.2: Comparison of the newly optimised contact definition simulation for PET-coated steel (including friction), and the truncated normalised data for a PET-coated steel specimen from the experimental ironing rig. The original contact definition has been included for clarify of comparison.

are acceptable for a project of this scale. The optimisation has therefore successfully reached a set of parameters which are suitable for modelling the PET-coated steel specimens in the ironing rig.

6.3 Conclusions

The aims of this chapter of work have been sufficiently achieved, and the contact-definition model is suitably matching real-world polymer-coated data from the previously developed ironing rig apparatus. Using the data from the work undertaken in chapter 5, the compliance of the apparatus was accounted for, and now using a combination of data, both the friction values and force-overclosure data have been calibrated such that the end result of the model adequately matches the end result of the experiments. Though this is not firm confirmation that the behaviours in the modelling process are identical to the experimental process, the work in this chapter supplies sufficiently matching end results which suit the scope of the project. The next and final chapter will combine the work undertaken throughout the project to perform a DoE study on changeable parameters in the polymer-coated DWI process, to better understand the significance of each, and their interactions.

Chapter 7

A Design of Experiments for a full DWI process.

7.1 Introduction

Having completed and verified each individual constituent of the FEA model in chapters 3 through 6, the natural progression was to assemble a full food can DWI process model and undertake a final DoE to demonstrate and explore tooling geometry. This DoE intends to explore the various unknowns concerning tooling geometry, and in some way quantify the relationship between those parameters and the final can geometry - as well as mapping the design space for interactions between said parameters. By the end of this chapter the DoE aims to grant a broader insight and understanding behind the effects of changing the various parameters of tooling geometry in the polymer-coated food can DWI process.

7.1.1 Initial full DoE using optimised contact definition

A run was assembled using *Simulia Isight* in a similar manner to previous DoEs in this thesis. The DoE design used an optimised *latin hypercube*[128] method, driven by the data matching algorithm created a design space exploring combinations of 4 tooling parameters at 33 levels recording two outputs. The inputs and outputs are listed in tables 7.1, and the formula for % reduction calculations found in equation 7.1. The blank thickness used for the FEA DoEs in this chapter was 0.285mm, with a 30μm and 20μm PET coating inside and outside (of the final can), respectively.

Independent variables (Inputs)	Dependent variables (Outputs)
Redraw radius Redraw reduction % Iron inlet angle (degrees) Iron reduction %	Mean wall thickness Mean Can Height

TABLE 7.1: Input and output parameters for the Design of Experiments studies.

$$Reduction(\%) = \frac{T_{blank} - \delta_{tool}}{T_{blank}} \times 100 \tag{7.1}$$

Where:
T_{blank} = *Initial thickness of the pre-cut blank.*
δ_{tool} = *Distance between the deformation tool (i.e. ring die) and the punch.*
$Reduction(\%)$ = *A positive measurement of over-closure interference.*

In equation 7.1, a reduction of 50% effectively designates the tooling interfering with the blank through 50% of the blanks thickness. Similarly, a negative 50% reduction demonstrates a gap between the edge of the blank and the tooling, which is 50% of the original blank thickness, and a 0% reduction means the blank touches both the punch and ring die with no clearance and no interference. The results from the DoE are tabulated in table 7.2 and 7.3.

Of the 33 runs, 5 failed during analysis (likely due to incompatible geometry generation)vs. Fitting an accurate, reliable response through this limited DoE proved challenging, as the error sample was only 6 of 28 successful runs. Both linear and quadratic polynomial responses yielded unreasonable error margins with coefficient of determination (r^2values) of less than 0.6 and 0.5 for height and thickness responses, respectively [129]. Whereas a cubic response provided very good r values, but the fitting curve did not adequately represent the data. These error predictions are derived in Isight by subtracting a sample of points and comparing the remaining DoE against them. By doing so, the overall DoE response sample is reduced, so ideally a DoE must have enough runs to subtract a reasonable error sample whilst keeping the design space density required.

The conclusion drawn was that the 33-run DoE had insufficient data to perform an accurate response surface and error sampling, and so the project opted for a larger DoE with the same parametric setup.

Run	Redraw Radius	Redraw reduction %	Iron inlet angle	Iron Reduction %	WT	Height
Baseline	0.508	0	4	30	0.189	90.916
1	0.495	8	5	29	0.000	0.000
2	0.419	4	4	32	0.000	0.000
3	0.591	-6	5	31	0.189	88.662
4	0.438	3	4	27	0.188	90.690
5	0.508	0	4	30	0.190	89.263
6	0.540	-2	5	29	0.189	88.848
7	0.457	5	3	28	0.181	91.117
8	0.413	-4	4	32	0.185	92.492
9	0.578	-7	4	32	0.184	90.012
10	0.502	-3	3	30	0.194	89.035
11	0.603	3	4	32	0.186	90.254
12	0.425	-1	5	29	0.000	0.000
13	0.584	6	3	31	0.000	0.000
14	0.597	7	5	29	0.189	88.991
15	0.432	9	4	30	0.000	0.000
16	0.514	-4	4	33	0.181	91.906
17	0.571	-9	4	28	0.188	88.449

TABLE 7.2: Input and results data from the 33 point FEA DoE. Zero-results for thickness and height indicate that the simulation failed to over-deformation, and the can would have torn. *WT = mean wall thickness*

Run	Redraw Radius	Redraw reduction %	Iron inlet angle	Iron Reduction %	WT	Height
18	0.56515	-9	3	29	0.19117	88.46760
19	0.4826	-10	4	30	0.19115	88.75490
20	0.4445	-6	3	33	0.18446	92.39560
21	0.5588	1	3	28	0.19007	88.84040
22	0.4699	-5	4	27	0.18977	89.34690
23	0.48895	-8	5	31	0.18974	88.91160
24	0.6096	-1	4	29	0.18981	88.59850
25	0.45085	6	5	32	0.00000	0.00000
26	0.52705	10	4	31	0.18664	90.98350
27	0.4064	-2	4	30	0.00000	0.00000
28	0.47625	8	3	31	0.00000	0.00000
29	0.5334	9	4	28	0.19097	90.90790
30	0.46355	-7	5	28	0.18928	89.06730
31	0.5207	2	3	33	0.18294	92.34400
32	0.55245	4	5	32	0.18593	90.57150
33	0.5461	1	4	27	0.18960	88.99150

TABLE 7.3: *Continued* input and results data from the FEA DoE. Zero-results for thickness and height indicate that the simulation failed to over-deformation, and the can would have torn. *WT = mean wall thickness*.

7.1.2 Second full DoE

A further DoE run was executed using a larger Optimised Latin Hypercube (OLH) method of 99 distributed points. For an OLH, each parameter is set to one of 99 levels simultaneously and independent to any other parameter. OLH is not the most robust method for a DoE as there are no repeating parameter levels, but it cuts down computational runs significantly and was necessary in this case. Parameters for the DoE were bound by logical geometry constraints: a minimum height and thickness output of 0, and an equal priority weighting for each. Setting boundaries in this way prevents the iterative solver from producing *technically favourable* results where thickness and height tend towards negative infinity and (positive) infinity, respectively. Similarly, reasonable limits of /pm 100% of the base values for each parameter were imposed (though these limits were never approached in the DoE). The resulting thickness was measured using a repeated point-distance calculation on the resulting mesh, at a certain height from the base. The height was measured from the base to the trailing edge of the can, in full. It should be noted that these methods of calculation are susceptible to anomalies, but ensure that specific geometry data is not lost through mean calculations.

11 runs failed entirely, leaving 78 successful result-yielding runs. These successful runs were used in a response surface method in Isight, where 15 were used for the error sampling using a random distribution, which was repeated with varying seeds until a fair distribution was found; this occurred repeatably at seed 55550. Linear, quadratic, and finally cubic polynomial responses were tested, but ultimately the cubic response provided the best fit for both dependent variables, compared to the error sample. which yielded r^2 of 0.790 and 0.925 for thickness and height, respectively, with root-mean-squared error values at 0.067 and 0.0979. The error plots can be seen in figures 7.1 and 7.2 and the formulaic relationships between independent and dependent variables are calculated and summarised using equation 7.2.

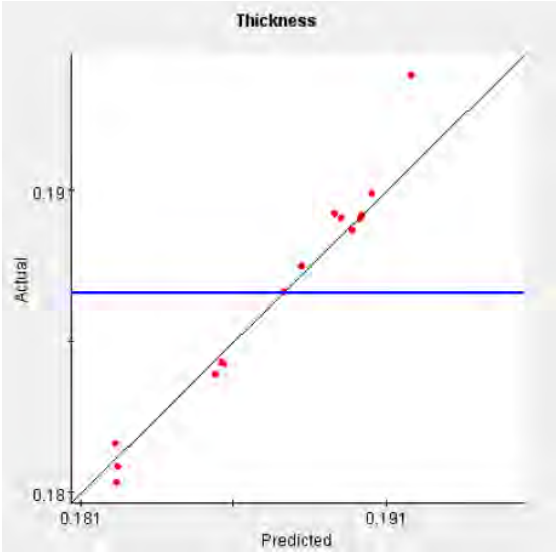

FIGURE 7.1: Response surface method error for thickness calculations in Isight. Actual data points from the DoE are graphed against the predicted behaviour derived from the error sample. For an ideal prediction, all points would lie on the black diagonal line. The blue line represents the median value of the "actual" data.

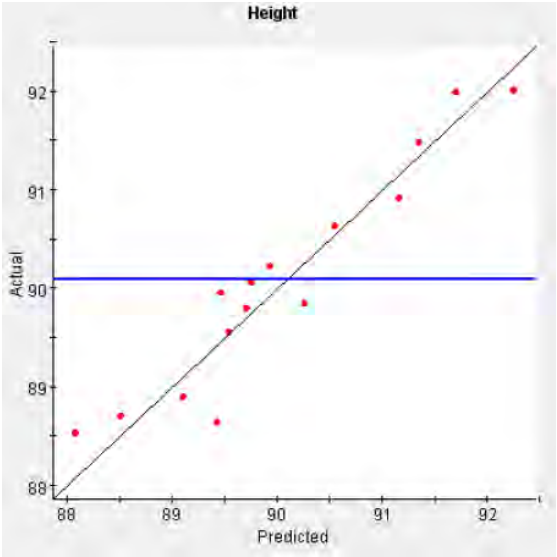

FIGURE 7.2: Response surface method error for height calculations in Isight. Actual data points from the DoE are graphed against the predicted behaviour derived from the error sample. For an ideal prediction, all points would lie on the black diagonal line. The blue line represents the median value of the "actual" data.

$$\begin{aligned}\textbf{Thickness} = &-4.20398040988642\times10^{-4}\,\mathbf{x_4^2} &&-2.35444466898959\times10^{-5}\,\mathbf{x_4x_3}\\ &+1.34296845859951\times10^{-5}\,\mathbf{x_4x_2} &&+3.09009195419495\times10^{-3}\,\mathbf{x_4x_1}\\ &+7.37664799812606\times10^{-5}\,\mathbf{x_3^2} &&+3.4274827808275\times10^{-5}\,\mathbf{x_3x_2}\\ &-2.15319062718833\times10^{-3}\,\mathbf{x_3x_1} &&-4.95216850097045\times10^{-6}\,\mathbf{x_2^2}\\ &+8.36048405233123\times10^{-4}\,\mathbf{x_2x_1} &&+0.100377627885726\,\mathbf{x_1^2}\\ &+2.25291241775414\times10^{-2}\,\mathbf{x_4} &&+1.25659099139762\times10^{-3}\,\mathbf{x_3}\\ &-1.0239606628168\times10^{-3}\,\mathbf{x_2} &&-0.18741729814435\,\mathbf{x_1}\\ &-8.49699533264436\times10^{-2}\end{aligned} \tag{7.2}$$

$$\begin{aligned}\textbf{Height} = &0.191151461537747\,\mathbf{x_4^2} &&-1.18651531035105\times10^{-2}\,\mathbf{x_4x_3}\\ &+1.34731622353091\times10^{-3}\,\mathbf{x_4x_2} &&-0.346132151614122\,\mathbf{x_4x_1}\\ &+3.78809695624122\times10^{-2}\,\mathbf{x_3^2} &&-1.47542069761466\times10^{-2}\,\mathbf{x_3x_2}\\ &+1.22454828674102\,\mathbf{x_3x_1} &&+4.12366422473839\times10^{-3}\,\mathbf{x_2^2}\\ &-0.788731732891031\,\mathbf{x_2x_1} &&+81.4013890859179\,\mathbf{x_1^2}\\ &-10.8199138253757\,\mathbf{x_4} &&-0.66065609296687\,\mathbf{x_3}\\ &+0.512881736149142\,\mathbf{x_2} &&-91.5390408868861\,\mathbf{x_1}\\ &+273.401598928401\end{aligned} \tag{7.3}$$

For equations 7.2 and 7.3:

Input Parameters:

x_1 = *Redraw radius*

x_2 = *Redraw percentage-reduction*

x_3 = *Ironing inlet angle*

x_4 = *Ironing percentage-reduction*

Output Parameters:

y_1 = *Mean thickness*

y_2 = *Mean height*

From equations 7.2 and 7.3, parametric contributions may be observed by analysing the magnitude of the coefficient belonging to each parameter (single x term) or parametric interaction (polynomial or multiplied x terms). Whilst every coefficient has a very small magnitude, certain patterns still appear observable. For example, x_1 (redraw radius) seems to provide a more significant impact on the height output compared to x_2 (redraw percentage-reduction). This significance diminishes far below both numerical values when the two parameters are interacting however - highlighting the unreliability in using the formula coefficients as the basis for accurate analysis. Equations 7.2 and 7.3 are displayed graphically in figures 7.3 to 7.14, which illustrate the interaction between two independent variables and the resulting dependent variable in the colour-band legend. All independent variables not displayed were kept to their base values in all following figures.

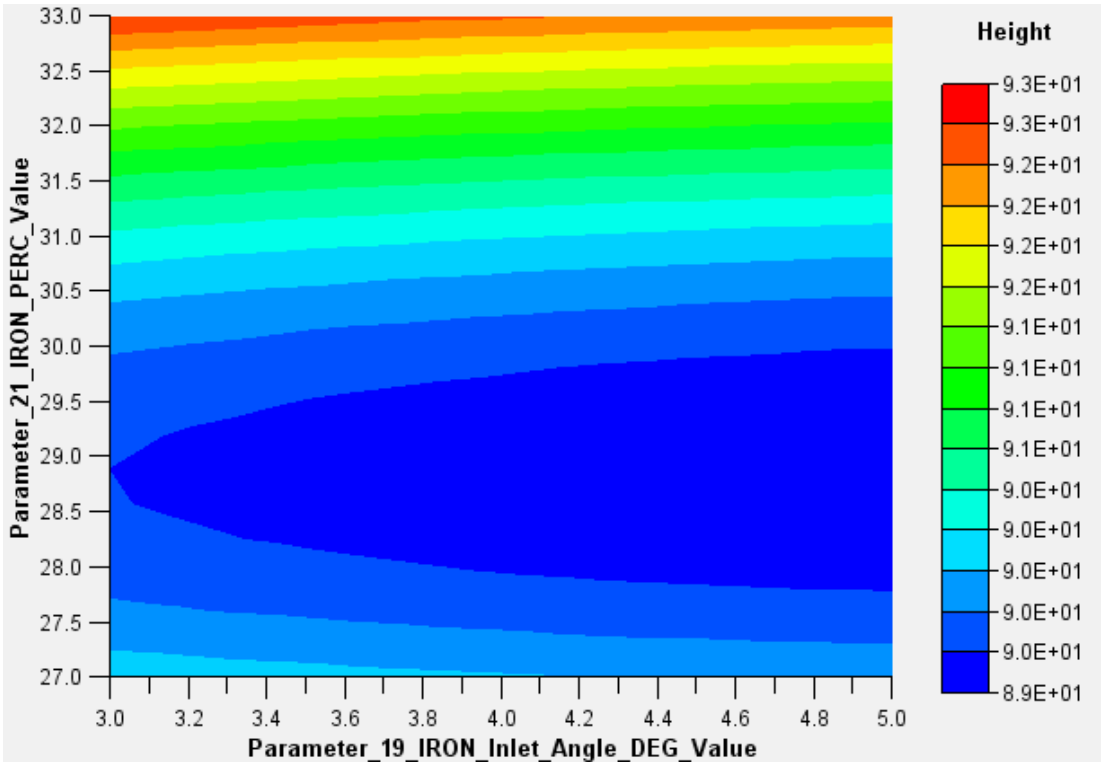

FIGURE 7.3: Contour plot illustrating resulting can height for changing *Ironing inlet angle* and *Ironing percentage-reduction* parameters during the DoE.

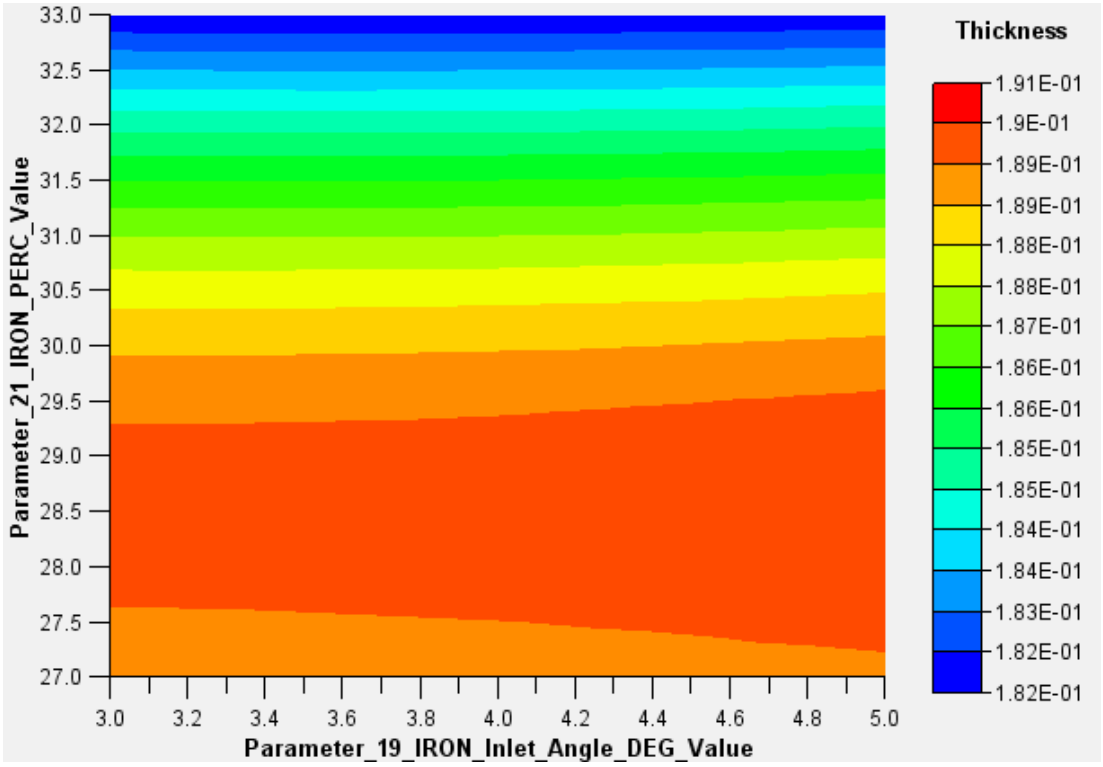

FIGURE 7.4: Contour plot illustrating resulting can wall thickness for changing *Ironing inlet angle* and *Ironing percentage-reduction* parameters during the DoE.

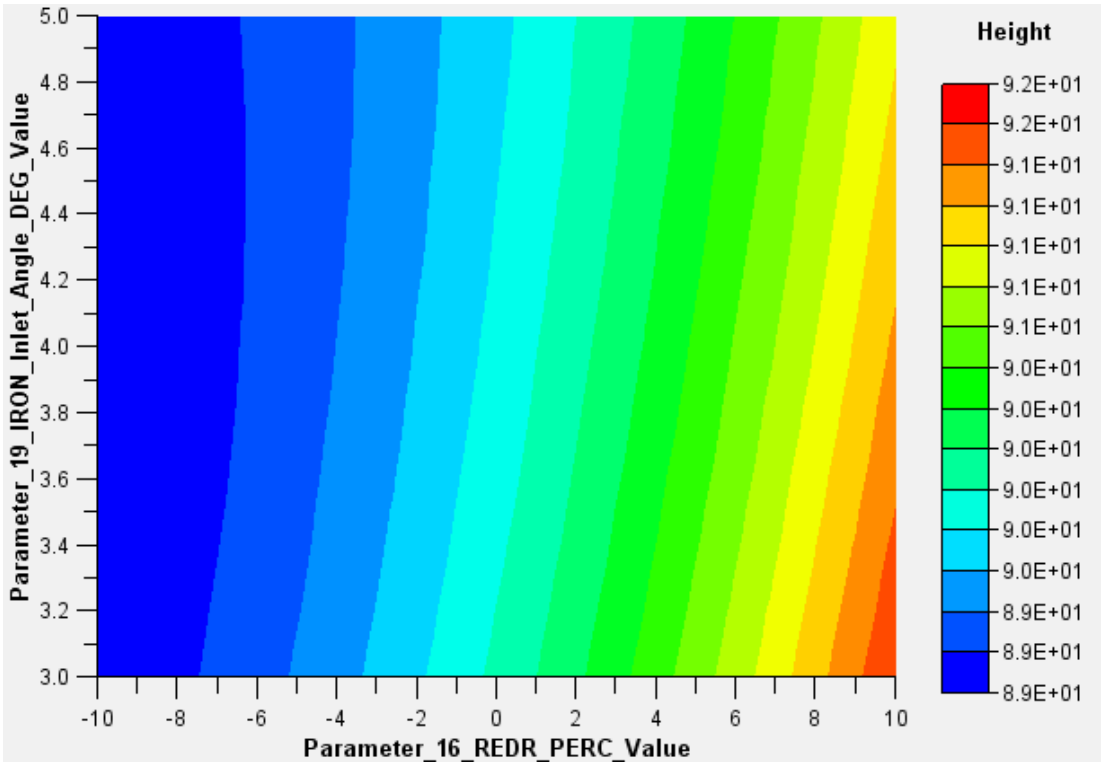

FIGURE 7.5: Contour plot illustrating resulting can height for changing *Redraw percentage-reduction* and *Ironing inlet angle* parameters during the DoE.

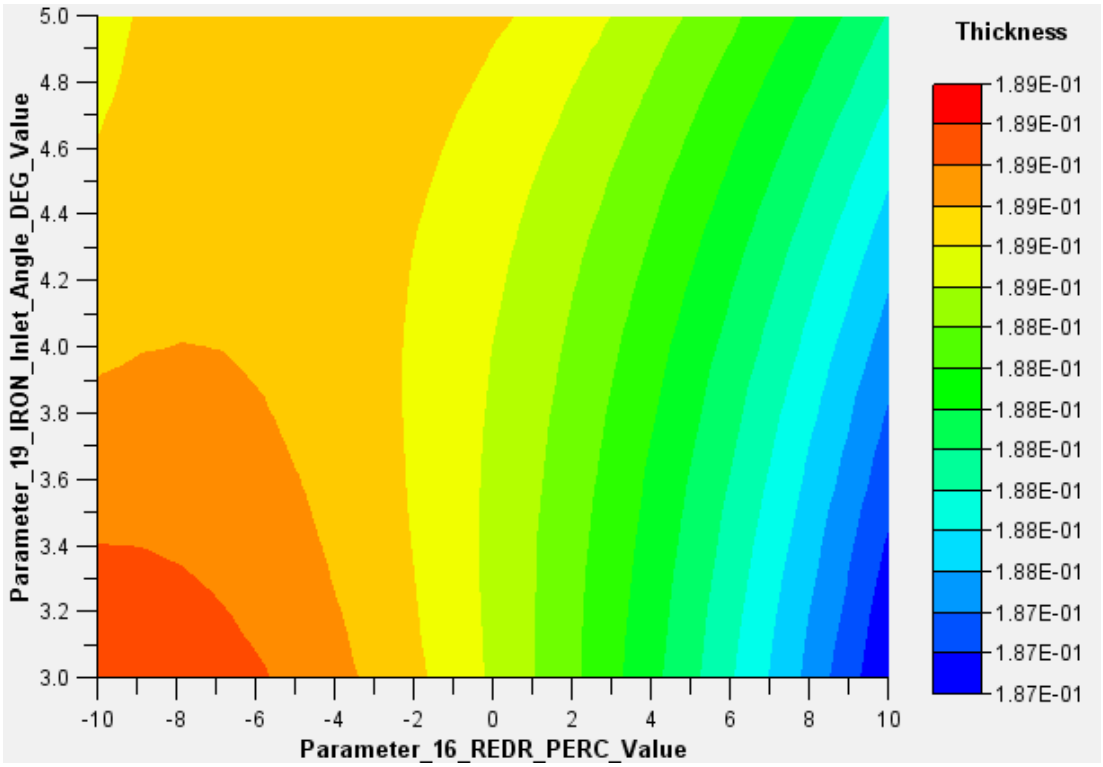

FIGURE 7.6: Contour plot illustrating resulting can wall thickness for changing *Redraw percentage-reduction* and *Ironing inlet angle* parameters during the DoE.

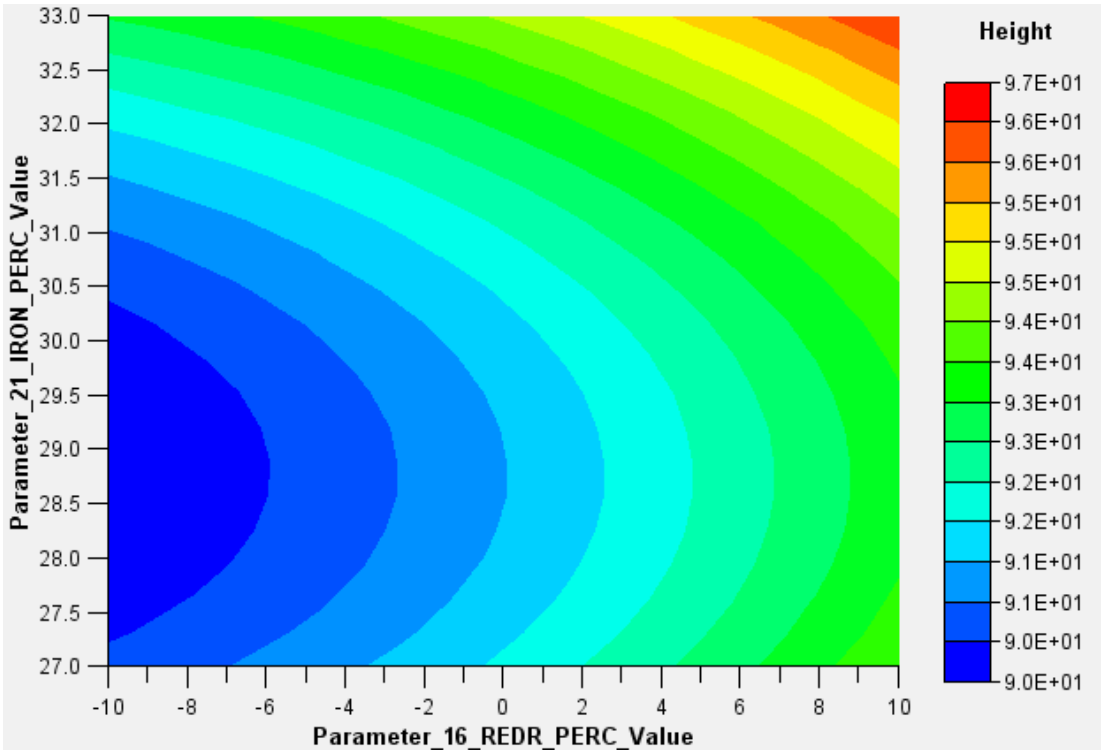

FIGURE 7.7: Contour plot illustrating resulting can height for changing *Redraw percentage-reduction* and *Ironing percentage-reduction* parameters during the DoE.

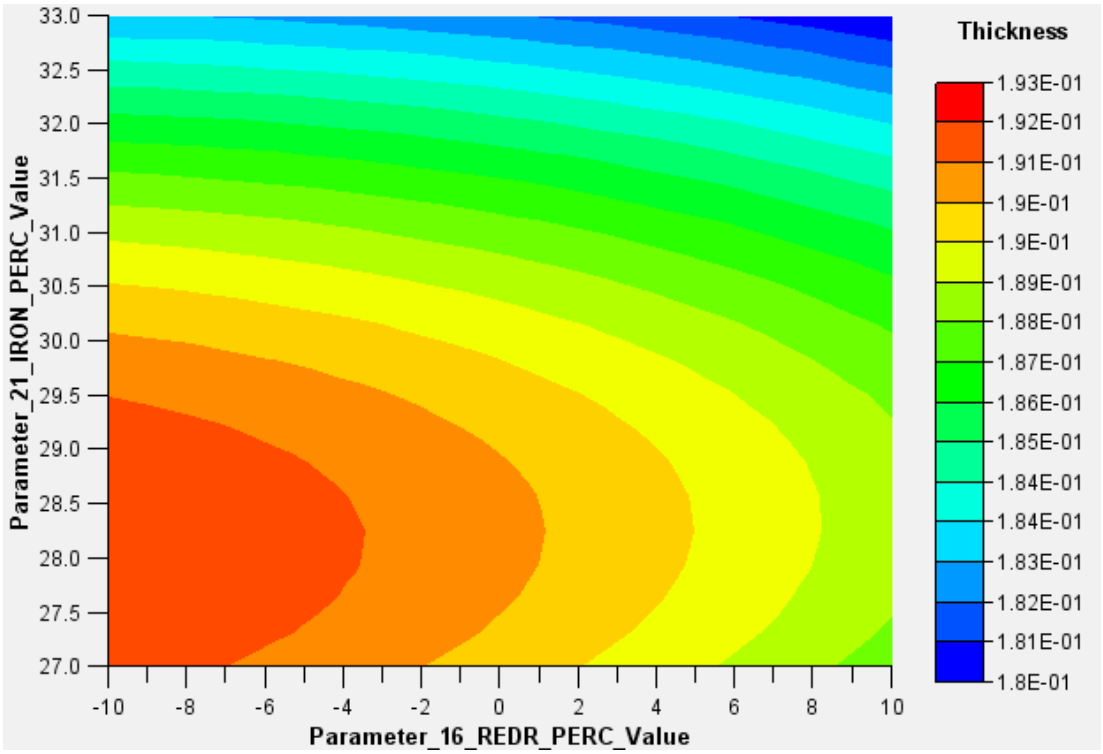

FIGURE 7.8: Contour plot illustrating resulting can wall thickness for changing *Redraw percentage-reduction* and *Ironing percentage-reduction* parameters during the DoE.

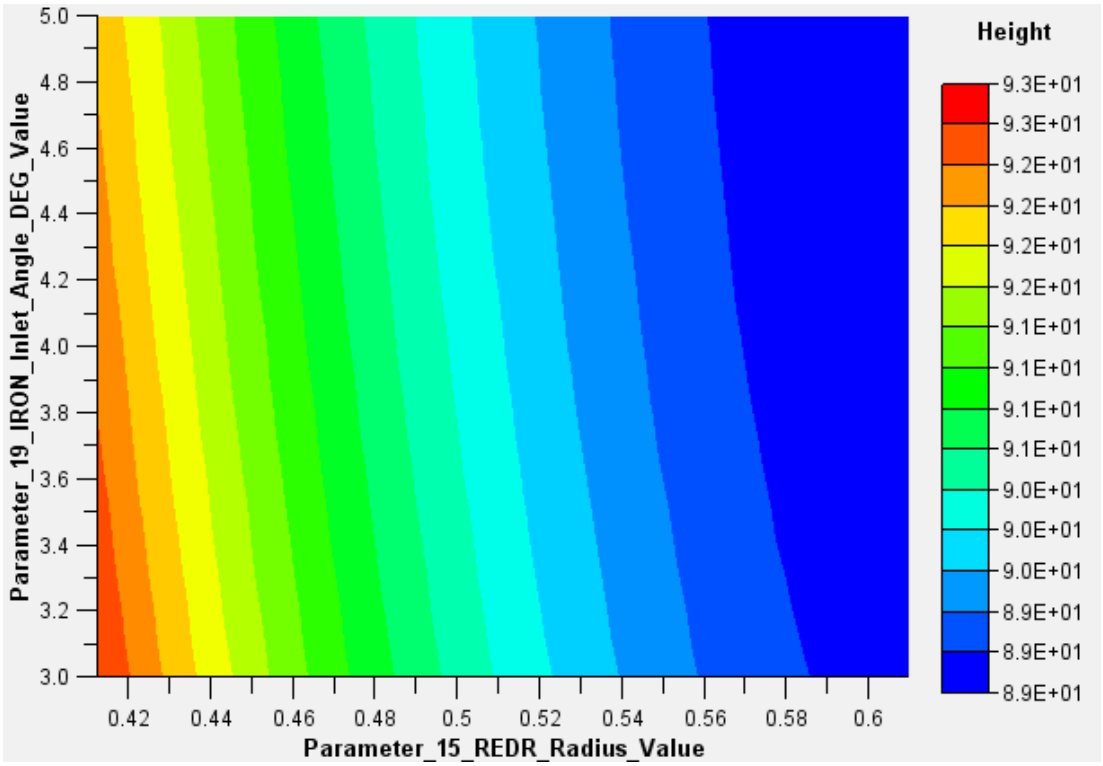

FIGURE 7.9: Contour plot illustrating resulting can height for changing *Redraw radius* and *Ironing inlet angle* parameters during the DoE.

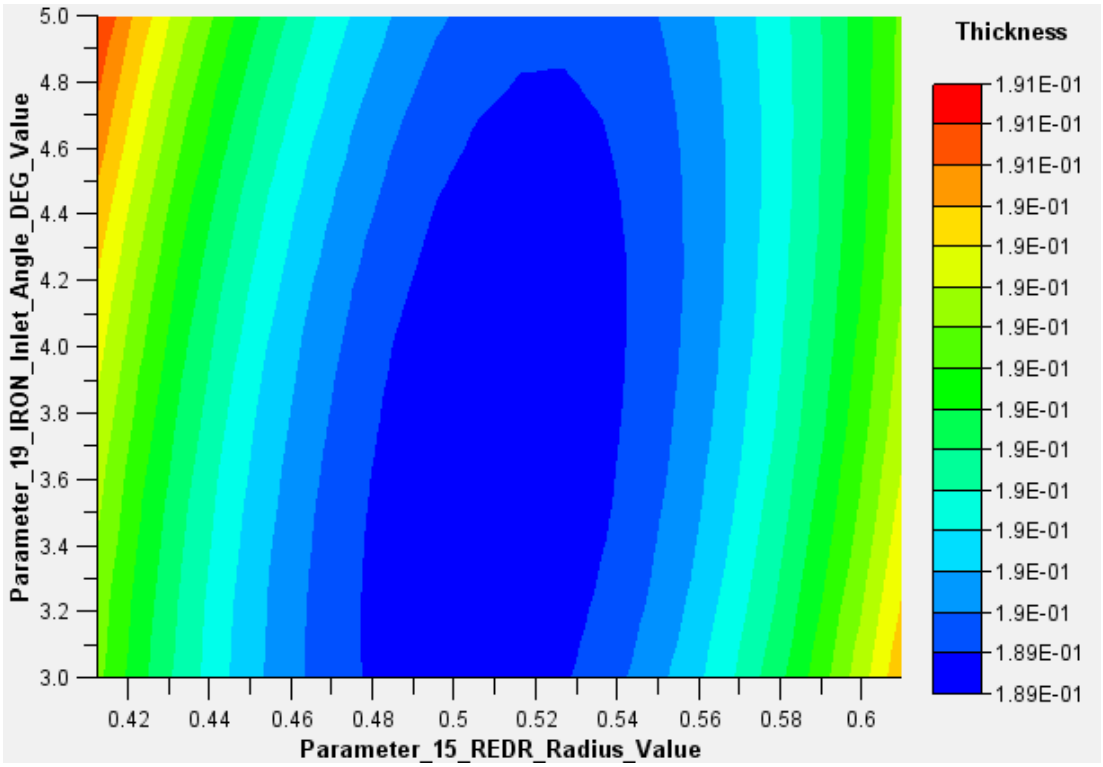

FIGURE 7.10: Contour plot illustrating resulting can wall thickness for changing *Redraw radius* and *Ironing inlet angle* parameters during the DoE.

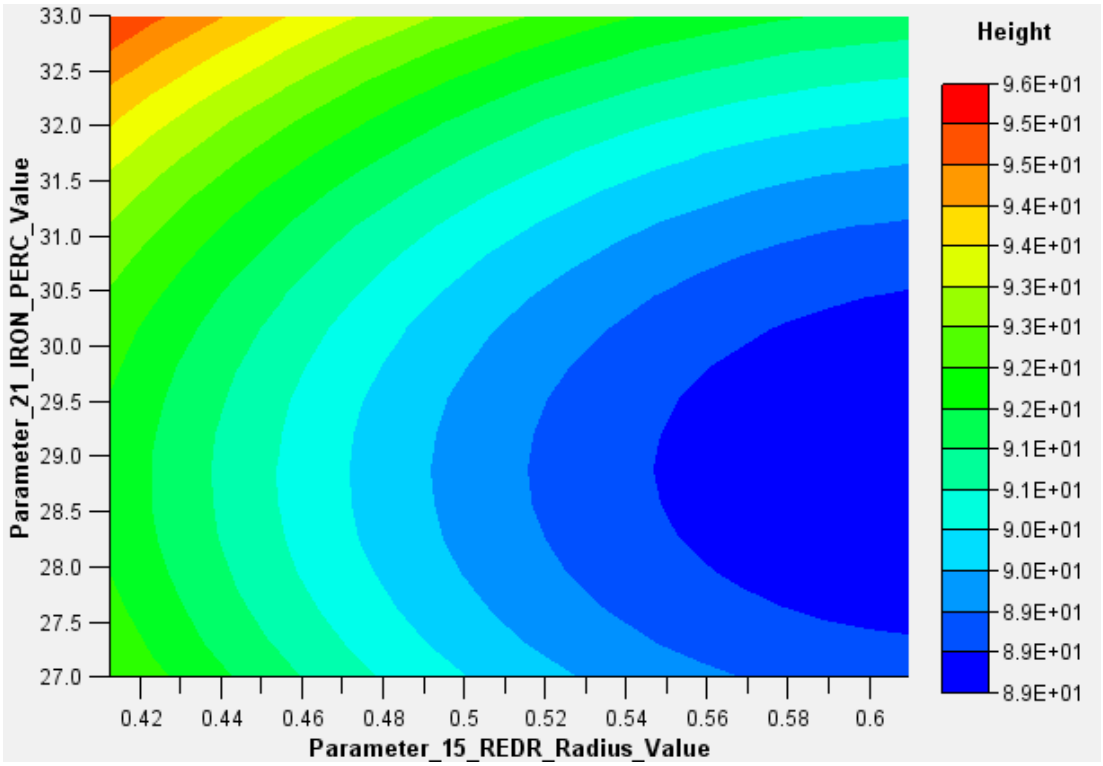

FIGURE 7.11: Contour plot illustrating resulting can height for changing *Redraw radius* and *Ironing percentage-reduction* parameters during the DoE.

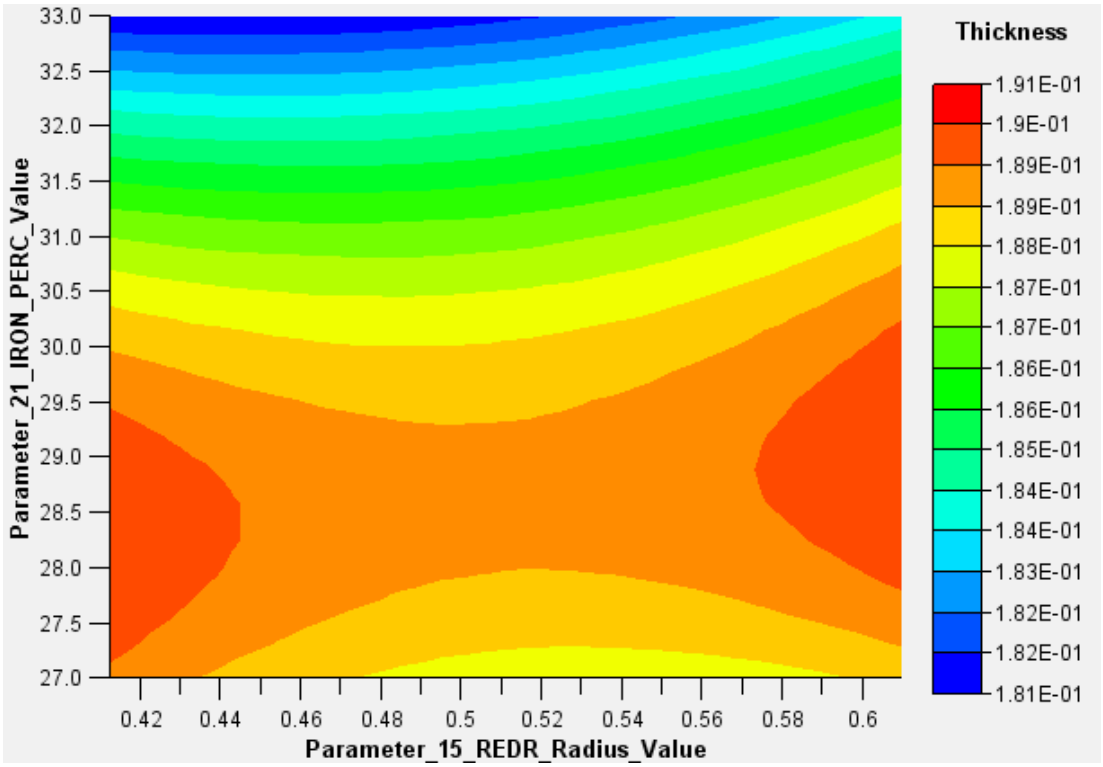

FIGURE 7.12: Contour plot illustrating resulting can wall thickness for changing *Redraw radius* and *Ironing percentage-reduction* parameters during the DoE.

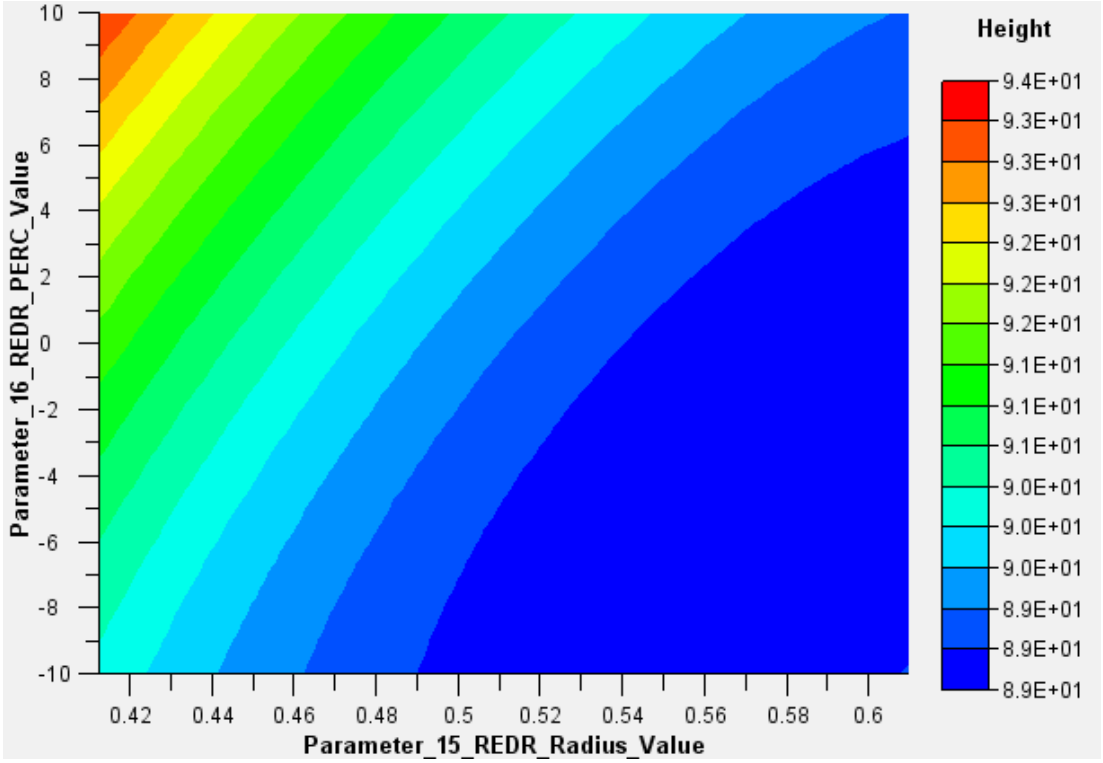

FIGURE 7.13: Contour plot illustrating resulting can height for changing *Redraw radius* and *Redraw percentage-reduction* parameters during the DoE.

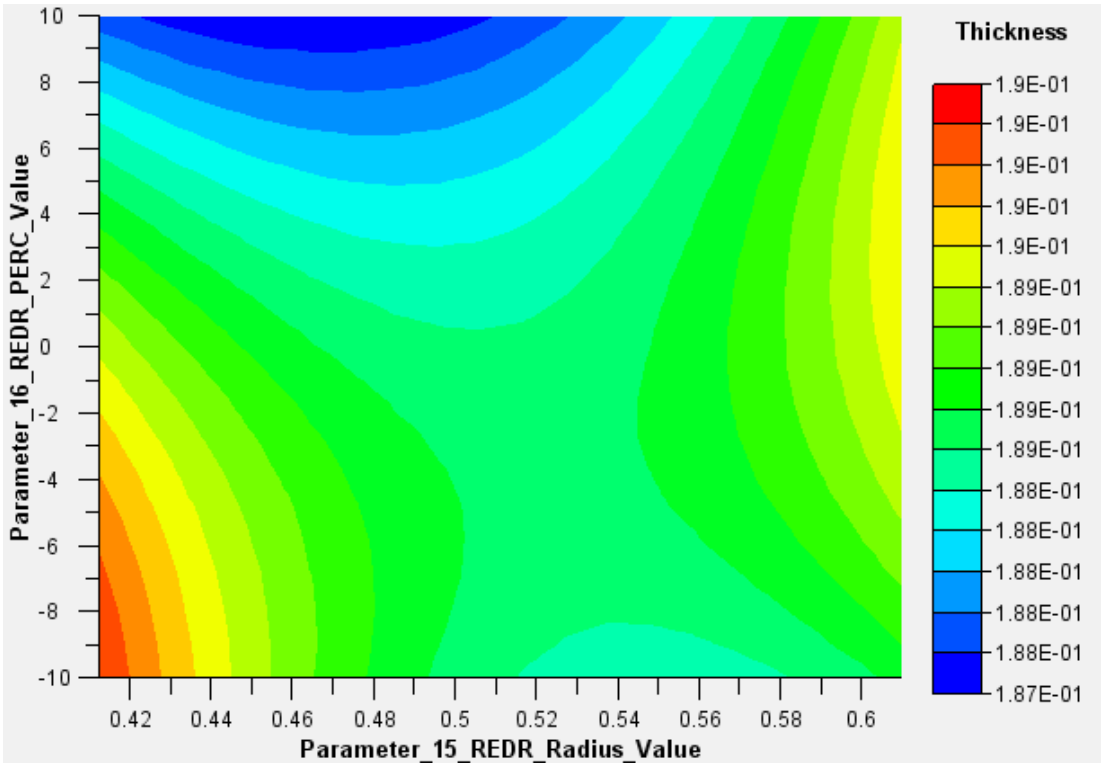

FIGURE 7.14: Contour plot illustrating resulting can wall thickness for changing *Redraw radius* and *Redraw percentage-reduction* parameters during the DoE.

The data from the larger DoE is better represented in figures 7.15 to 7.16, which combine the plots of both height and thickness for each combination of parameters. It is difficult to represent more than a single parametric interaction or output in a visual space, so the height plots are illustrated as 12 equally distributed contour bands throughout the output scale. The wall thickness is illustrated in the coloured contour plot, with the height illustrated as overlayed contour bands.

These 3D-style plots are capable of showing both single parametric implications, as well as parametric interactions between the X and Y axes. As one interprets these figures, it is important to understand that the DoE results (and plotted graphs) can only demonstrate parametric implications of interaction between the parameters on the X and Y axis. A relationship between two increasing parameters may not hold true as a different parameter increases or decreases, and further parameters may play a significant role in the interaction, unexplored by a DoE of this magnitude. Such is the difficulty in mapping the design space with a complex model [130].

Figure 7.15 clearly illustrates two parametric implications on both thickness and height outputs. The *Ironing percentage-reduction* (ironing reduction) parameter holds a strong correlation with height: both parametric input and output increase linearly together (and this relationship holds regardless of the redraw radius). Similarly, the thickness follows a linear decrease as the ironing reduction is increased. These kinds of behaviours are completely expected when dealing with the DWI process, as an reduction in clearance (and thus an increase in ironing) causes increased deformation - and the deformed metal manifests in a longer can with thinner wall-thickness, as explained earlier in this thesis. In this scenario, the implication of a decreasing can thickness is not always positive. It is currently unknown whether the minimum wall thickness for a polymer-coated can would be the same as the existing industry standard, so this may be an unforeseen limiting factor upon the adjustment of redraw and ironing radii.

The height bands increasing below the 29% mark are an area for concern, though this sort of unexpected behaviour can often be attributed to interpolation/extrapolation of the iterator as it attempts to map a full design space based only on an optimised hypercube of analyses. It is inevitable that certain areas of the design space will be more explored than others - more densely populated with

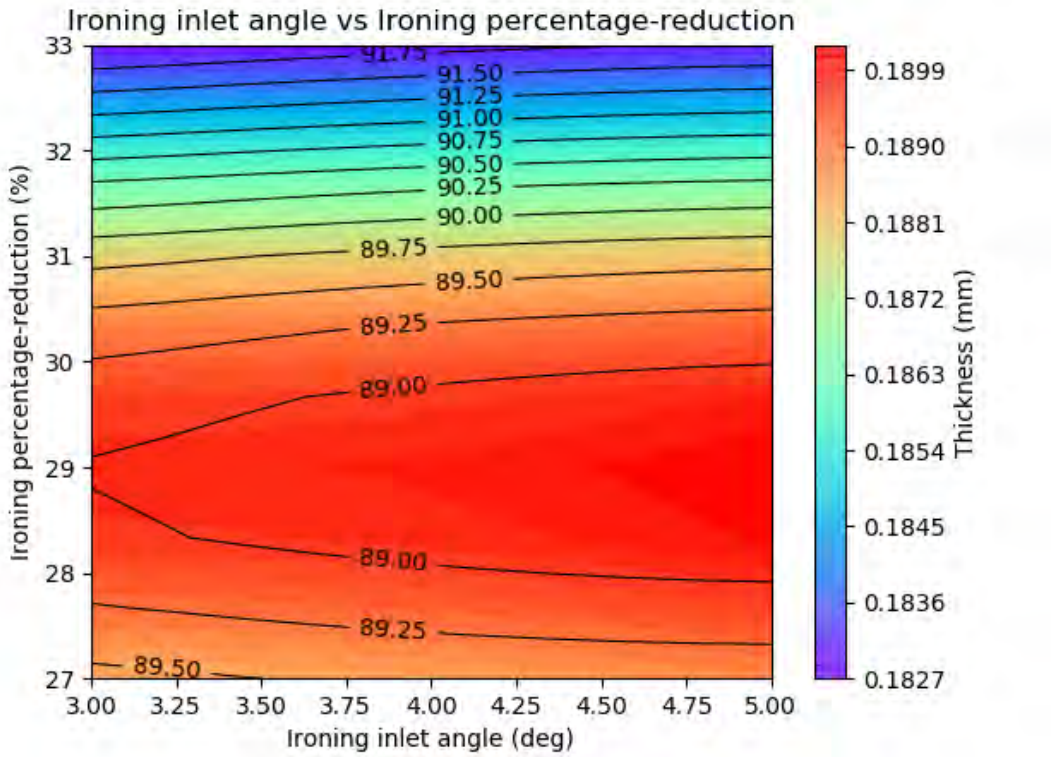

FIGURE 7.15: Contour plot illustrating resulting can wall thickness and height for changing *Ironing inlet angle* and *Ironing percentage-reduction* parameters during the DoE. The wall thickness is illustrated in the coloured contour plot, with the height illustrated as overlayed contour bands.

design points, and in the sparser areas the behaviour can be less reliable. It is not expected that reducing redraw reduction below a threshold point would increase can height, since this seems to defy conservation of volume.

Conversely, the *Ironing inlet angle* (inlet angle) seems to make little difference to both height and thickness outputs in this case. If the assumption can be made to ignore the height anomaly at 89.00, in fact inlet angle provides little impact whatsoever on the outputs, regardless of redraw reduction. Once again this is a heavily-expected outcome for that parameter, as Crown's inlet angles for ironing dies generally correspond to a desired surface finish, and not geometry.

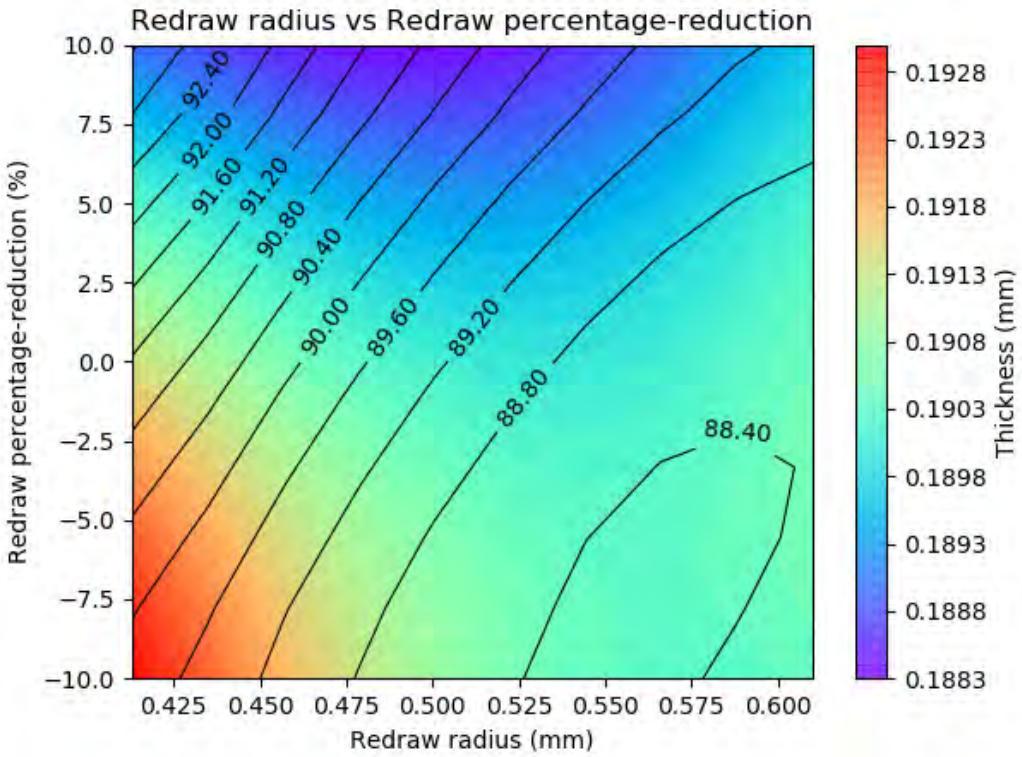

FIGURE 7.16: Contour plot illustrating resulting can wall thickness and height for changing *Redraw radius* and *Redraw percentage-reduction* parameters during the DoE.

Figure 7.16 demonstrates some interesting interactions between redraw radius and redraw reduction. An area of red in the bottom-left corner indicates an increased thickness during low redraw-reduction and low redraw radius, but increasing either parameter causes decreased thickness, which is not something expected of the redraw radius parameter (though it is expected of redraw reduction). Furthermore, the height bands demonstrate a similar behaviour, increasing in diagonal, near-parallel lines from bottom-right to top-left of the plot. However It should be noted that an increasing height should be partnered with a decreasing wall-thickness (red patterns bottom right with the lowest height band, blue patterns top-left with the maximum height), and this does not appear to be the case in this plot. This may be indicative of interpolative/extrapolative accuracy-loss during the formulation of the DoE output equation, or specific anomalies being conglomerated the response. Given the mechanics of drawing and wall-ironing, it would be expected that the graph would vertically graduate from red (bottom) to blue (top) as an increased iron reduction caused a decreased thickness. This is only true for low values of redraw radius - which perhaps further reinforces the idea of data inaccuracy for this plot.

Though the possibility of redraw radius creating a positive effect on reducing the severity of increased redraw reduction cannot be completely discounted without further study, if this were true one would not expect to see an increasing redraw radius both increase (at high redraw reduction)and decrease (at low redraw reduction) the resulting thickness.

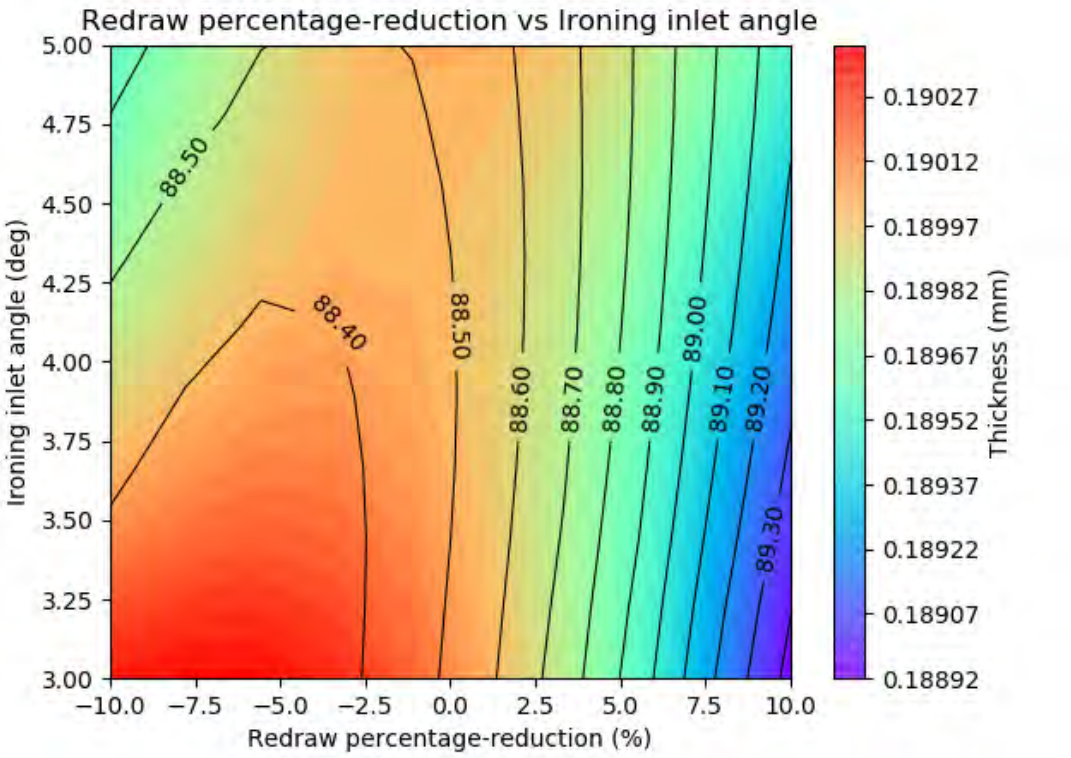

FIGURE 7.17: Contour plot illustrating resulting can wall thickness and height for changing *Redraw percentage-reduction* and *Ironing inlet angle* parameters during the DoE. The wall thickness is illustrated in the coloured contour plot, with the height illustrated as overlayed contour bands.

Figure 7.17 shows more strong implications that redraw reduction decreases wall thickness and increases height in a linear manner. Beyond a positive redraw reduction, the plot seems to indicate that ironing inlet angle has a limited effect on both outputs, though there is some skewing to both the thickness and height bands throughout, so the effect is certainly not negligible.

Below 0.0% redraw reduction (a positive clearance between tooling and specimen during redraw), some more interaction occurs between the two input parameters. It appears that a lot inlet angle with a low, negative redraw reduction causes increased can thickness and decreased can height, but this pattern is

lost above an inlet angle of approximately 4.10. Once again, this could be attributed to an extrapolation error, but with 80 valid data points it is unlikely that such resolution loss has occurred here, as to completely fabricate an area of high thickness output. Combined with the behaviours seen in figure 7.16, it is possible that an unexpected behaviour is surfacing when redraw reduction turns negative (and thus a clearance is introduced during redraw, instead of interference).

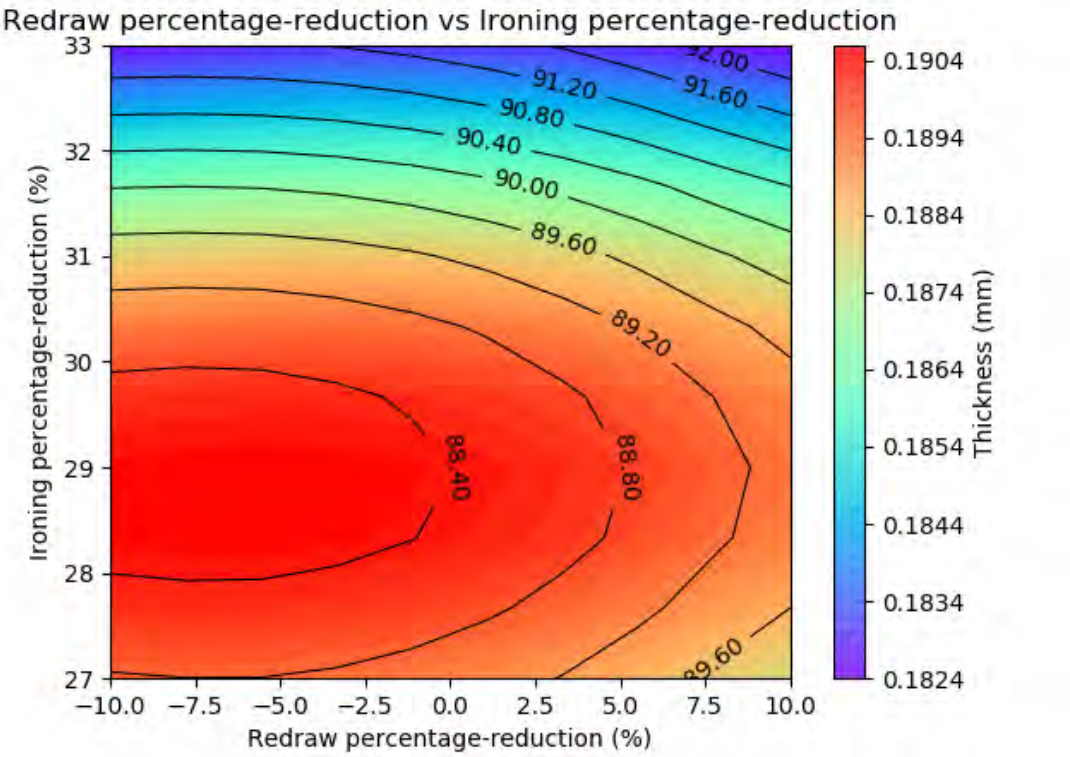

FIGURE 7.18: Contour plot illustrating resulting can wall thickness and height for changing *Redraw percentage-reduction* and *Ironing percentage-reduction* parameters during the DoE. The wall thickness is illustrated in the coloured contour plot, with the height illustrated as overlayed contour bands.

Figure 7.18 compares the two parameters which were hypothesised to have the largest impact on resulting geometry. When tested alone, the percentage-reductions of the tooling stages physically increase the interference during forming, providing longer, thinner cans. The interaction between the ironing and redraw reductions demonstrates a strong correlation between increasing either/both parameters, and decreasing the output thickness whilst increasing output height. Any increase in interference during the forming process is likely to result in these outputs, so these results seem unsurprising when reading through this thesis.

However, once again the unlikely distribution of reddening in the bottom-left corner indicates a threshold ironing reduction, before whilst a slightly increased height outcome, and slightly decreased thickness outcome occurs. This area of interest happens similarly to figure 7.17, below 0.0% redraw reduction. Since this is the only parameter which introduces positive clearance during the DoE, it appears increasingly likely that negative redraw reductions create an environment where the ordinary, expected parametric implications change. It should be noted however, that the *optimal latin hypercube* method used for the DoE creates a dataset where each parameter holds a unique value in each run. Effectively there are no two runs with the same ironing reduction, so it's possible that data has been lost or interpolated during the response surface fit.

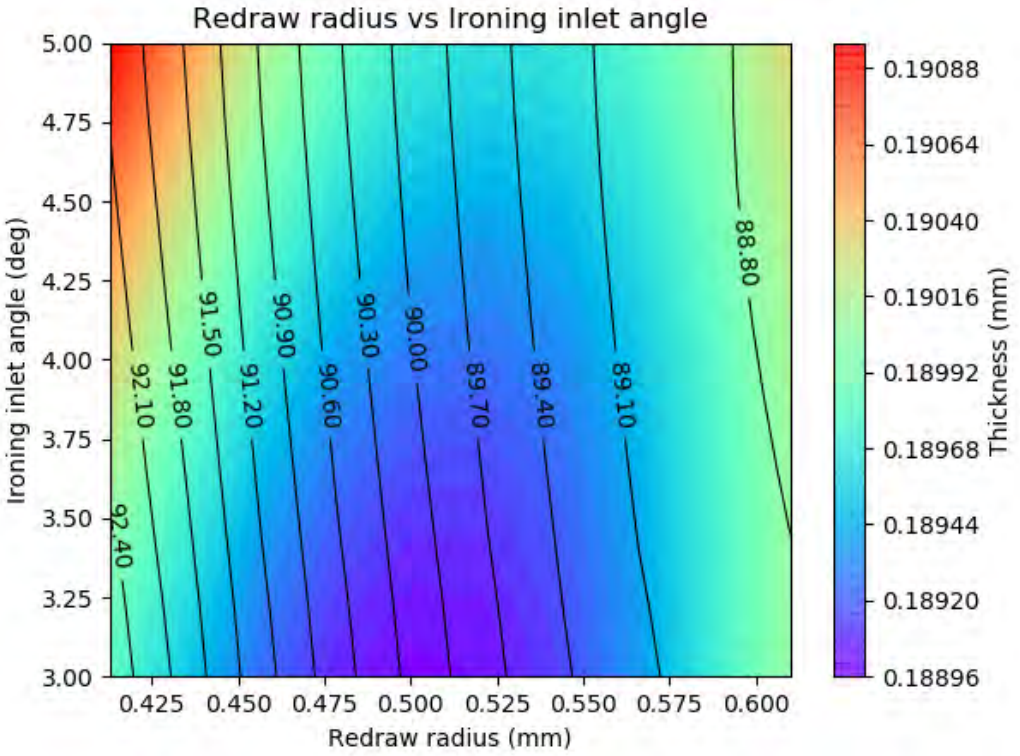

FIGURE 7.19: Contour plot illustrating resulting can wall thickness and height for changing *Redraw radius* and *Ironing inlet angle* parameters during the DoE. The wall thickness is illustrated in the coloured contour plot, with the height illustrated as overlayed contour bands.

Figure 7.19 demonstrates an important distinction in the interpretation of these plots. In other plots the ironing inlet angle has made minimal difference to the resulting geometries, whereas in this plot both parameters appear to cause significant change in the output parameters. In figure 7.19, the redraw radius

appears to have a dramatic, linear decreasing effect on the can height, as well as a threshold at which thickness is minimal.

These findings seem inconsistent with the results displayed in other plots: where both parameter inputs appeared to cause only minor geometric change. Demonstrating a hypercube in 2D space comes with certain limitations, and the inability to demonstrate all parametric interactions in one plot is highlighted here. For each of the 80 points used for this contour plot, every parameter was changing: not simply the two listed on the axes. This graph serves as a good reminder that these results plots cannot be considered in a vacuum, as there are more parameters contributing to the outputs than can be seen at any given moment. It is unlikely that ironing inlet angle suddenly finds significant contribution towards can thickness, and more likely that another parameter is changing simultaneously to cause this shift.

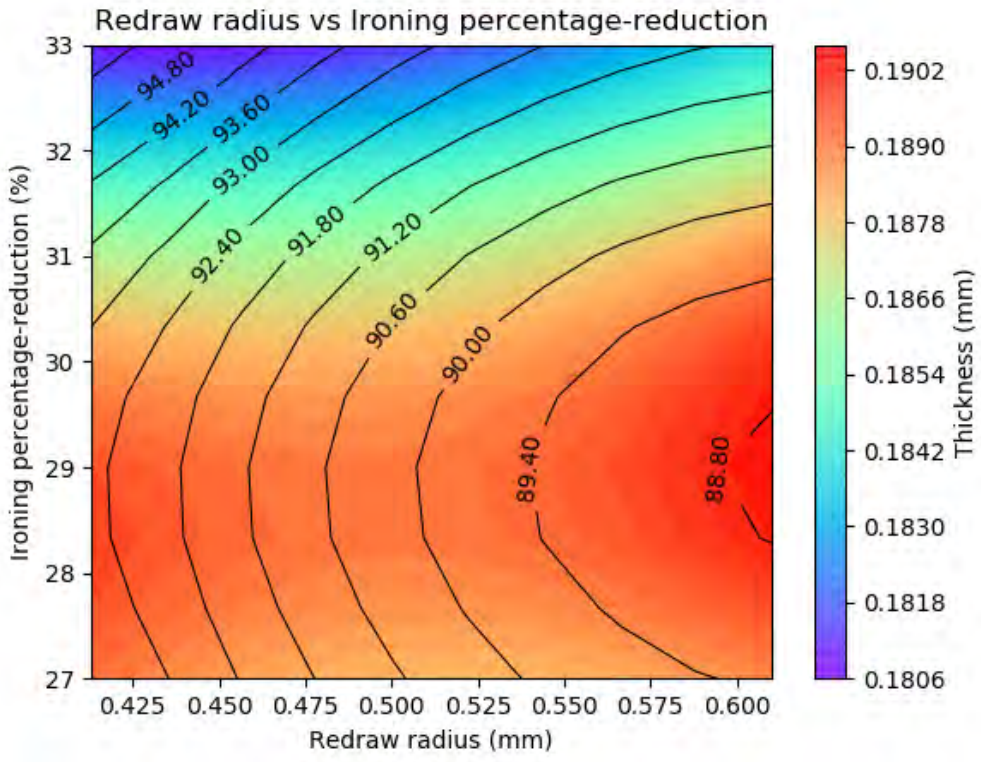

FIGURE 7.20: Contour plot illustrating resulting can wall thickness and height for changing *Redraw radius* and *Ironing percentage-reduction* parameters during the DoE. The wall thickness is illustrated in the coloured contour plot, with the height illustrated as overlayed contour bands.

Finally, figure 7.20 reinforces some of the previously marked relationships. Ironing reduction seems to strongly correlate with thickness and height, whilst redraw reduction shows a less significant (but still noticeable) change to both. Once again an area of interest exists at 29% ironing reduction and 0.600mm radius.

7.1.3 Physical trial verification

After the complete DoE of the DWI FEA model, an ideal verification would be to undergo physical trials of the same process, with the same setup (or a similar design space if an identical setup cannot be completed.). Due to availability, resulting cans from a previous DoE-style trial were documented with the same metrology used in the FEA DoE, to enable a comparison with the simulated design space.

The physical DoE was undertaken on Crown's physical trial pilot line. The machinery was allowed to heat to its equilibrium temperature on unmeasured cans between each change of tooling (the equipment heats up rapidly with friction), and then cans were formed using a water lubricant for cooling. All resulting cans were stored in the same conditions they were later measured in.

The output cans were measured at six points around circumference of the can using a plastic sleeve with measured locations for marking equidistant points (seen in figure 7.21. These six points allowed six strips to be considered down the height of the can, and those strips were used during the measurement of height and thickness. Figure 7.22 shows the method by which can height was measured: the can is rotated through the six points and the gauge is adjusted until the top of the can is met. Figure 7.23 demonstrates the method of measuring thickness: the can is inserted into the apparatus and a calibrated anvil is pushed up to clamp the can wall, digitally measuring the distance remaining. This process was done at $33mm$, $66mm$, and $100mm$ from the base of the can. Mean heights and thicknesses were conglomerated, and the resulting measurements can be seen in table 7.4.

FIGURE 7.21: Plastic sleeve with 6 equidistant locations marked, used for marking equidistant points onto an output can to enable accurate metrology at 6 different locations around the circumference.

FIGURE 7.22: Crown's can height gauge. The screw on top is slowly turned until the gauge touches the top of the can, at which point the measurement displayed is taken as can height.

FIGURE 7.23: Crown's thickness gauge. The can is inserted onto an inverted triangle and secured in place using the clamp (left). An calibrated anvil then meets the outside of the can wall, and the remaining distance (the can wall-thickness) is measured using the attached digital probe.

Batch letter	Run number	Redraw radius	% Redraw reduction	Iron inlet angle	% Iron reduction	% Burnish reduction	Mean WT	Mean height
A	1	0.508	0	4	-47.418		0.234	104.479
	2	0.508	0	4	-47.418	-48.309	0.179	108.838
	3	0.508	0	4	-47.418	-53.656	0.169	114.102
	4	0.508	0	4	-49.200		0.226	105.674
	5	0.508	0	4	-49.200	-53.656	0.166	113.823
	6	0.508	0	4	-47.418		0.223	105.304
	7	0.508	0	4	-47.418	-48.309	0.182	109.515
	8	0.508	0	4	-47.418	-53.656	0.167	114.644
B	1	0.4572	0	4	-47.418		0.233	104.623
	2	0.4572	0	4	-47.418	-48.309	0.179	108.928
	3	0.4572	0	4	-47.418	-53.656	0.168	114.234
	4	0.4572	0	4	-49.200		0.226	105.941
	5	0.4572	0	4	-49.200	-53.656	0.166	113.942
	6	0.4572	0	4	-47.418		0.219	105.681
	7	0.4572	0	4	-47.418	-48.309	0.178	109.475
	8	0.4572	0	4	-47.418	-53.656	0.169	115.106
C	1	0.4064	0	4	-47.418		0.231	104.848
	2	0.4064	0	4	-47.418	-48.309	0.180	109.101
	3	0.4064	0	4	-47.418	-53.656	0.168	113.885
	4	0.4064	0	4	-49.2		0.223	106.005
	5	0.4064	0	4	-49.2	-53.656	0.185	115.382
	6	0.4064	0	4	-47.418		0.217	113.971
	7	0.4064	0	4	-47.418	-48.309	0.549	109.693
	8	0.4064	0	4	-47.418	-53.656	0.168	114.929

TABLE 7.4: Geometry data for the PET-coated can trials at Crown. Blank burnish reduction indicates no burnishing die used for the run. WT = wall thickness. Results are the mean of 3 repetitions in each setup.

Letter ID	Redraw radius	Iron land	Burnish land
A	0.508	0.508	0.508
B	0.4572	0.508	0.508
C	0.4064	0.508	0.508

TABLE 7.5: Key for table 7.4, Burnish key only applies when burnishing die used.

Unfortunately, the design space available does not effectively match the simulated design space. The limits for all parameters exceed those used in the FEA DoE, and it was not possible to match the starting parameters of the blank. This DoE serves as a good example of the format, setup, and metrology of a verifying physical trial.

However, Since each constituent part of the FEA simulation was physically verified, the FEA DoE can still be used as a considerable opportunity to investigate the interactions and relationships displayed in the results, though future work would find great advantage in a full physical verification where possible.

7.1.4 DoE Evaluation

The experiments detailed in this chapter provide some clarity in mapping the design space of the full DWI process of the polymer-coated food can. It is evidenced that the DoE sensitivity to accuracy relies heavily on parameter and run count. No reliable metric can be derived solely from the work detailed, but it is clear that the 99-run DoE performs far better as an exploratory study compared to the 33-run DoE. The numerical outputs for thickness and height approximately match the magnitude and variation in results from the physical DoE (which operates on a slightly different base geometry), indicating that the polymer-coating contact model performs as an adequate substitution for modelling the physical polymer layer.

Though several of the conclusions drawn from the extended DoE were expected (percent-reduction parameters dramatically affecting the wall thickness and subsequent can heights), the observation of negative redraw-reduction affecting other parameters is a phenomenon new to the project. This implication, combined with the limitations of the physical trials as a comparative verification, highlights the area for future study.

7.2 Conclusions

Ultimately the FEA DoE featured in this chapter has been a successful exploration into the previously unmapped design space of polymer-coated food can bodymaking. The work serves as both an appropriate stepping stone for further study exploring the complex parametric interactions of the process, and equally a strong indicator that the novel technique of simulating a polymer-coating using force-overclosure contact modelling is highly effective when numerical metrology of the layer is not a priority. Whilst the DoE is not completely conclusive, the work fully satisfies the aims of gaining insights and broader understanding of the relationships between tooling geometry, and demonstrates a promising direction for future work.

Chapter 8

Reviewing the project

8.1 Overview of the aims and conclusions

The aims and goal of this project centre primarily around the investigation and exploration of a polymer-coated DWI process, as an alternative to currently implemented DWI processes. In this chapter, the work will be summarised and the major findings explained.

The aim of chapter 3 was to investigate the potential modelling directions for an FEA simulation of the DWI process in both aluminium beverage cans and steel food cans. This chapter primarily served to introduce the modelling methods and expand upon advantageous techniques of FEA for use in the project. The initial simulations undertaken in subsection 3.2.1 are simple and fundamental milestones of the work, and demonstrated the ability of Finite Element Analysis to effectively model the engineering variables such as stress and strain, as well as the geometric deformation undergone during the DWI process. Subsection 3.4 provided important utility for the basis of parametrising the larger models later in the work and helped demonstrate the efficacy of restarting simulations. Overall, the work in chapter 3 provided a valuable basis for understanding the most efficient and effective methods for modelling the can-making process.

The beginning of Chapter 4 proved significant value to the understanding of modelling the complex polymer-coated specimen. The material testing work undertaken in this chapter highlighted the challenges associated with proper material characterisation of polymer-coated specimens. A combination of increased friction and high aspect ratio differences for the materials layers created inaccuracy with all the traditional material tests available; in compression

tests it was accounted that the material data was being lost to machine compliance. Overall the difference between the 30μm thickness polymer coating and the 250μm thickness steel substrate, caused no valuable data for the polymer to be recorded in any test.

The work followed on by investigating the capability of Abaqus to model the polymer film with placeholder material data, comparing the traditional mesh-modelled format with the novel contact-definition method (introduced in this chapter). Using an Isight optimisation setup, various values for force and over-closure were iterated until an exponential equation returned with matched the available polymer data. Since this comparative data was gathered from a much thicker polymer specimen, the promising results highlighted the requirement for more relevant testing on the polymer-coated substrate. It was this requirement which led to the development of the ironing rig.

In chapter 5, a rig was developed and manufactured to demonstrate strip ironing at slow speed in lab conditions using the available bench-top tensile tester. Starting from drawn concepts analysed via a pugh matrix, the FEA methods and approaches from chapter 3 helped inspire the design of a rig which best represented the ironing process, whilst keeping manual handling limitations in specification. Basic calculations were used to get an approximation of the initial build, and more advanced FEA models were used to optimise and develop the rig design: minimising deformation during ironing and allowing for a specimen wide enough that the effects of pinching at the specimen edge did not heavily interfere with the overall deformation patterns. The rig settled on specimens between 20mm and 30mm wide - the smallest model specimens which did not demonstrate proportionally large edge behaviour. Specimens were kept on the smaller side as further increasing width proportionally increased the forces involved in ironing.

Once manufactured, the ironing rig proved effective at ironing steel strip specimens at speeds of up to 250$mm/minute$, and later provided valuable data for a small sample of polymer-coated specimens. Results from the experimental setup showed proportionally increasing elongation and decreased final thickness with increasing ironing reduction. These results matched expected outputs for the ironing process, demonstrating the rig's accuracy towards the can-making process. Rig tests for uncoated steel specimens were then compared to

a set of simulation results for identical tooling geometry, which gave clear indication that the stiffness and friction of the FEA models were too high. Models were then optimised with a spring and friction coefficient for the main tooling ring, which eventually yielded data to match the experiments within 1.5% error.

Using the results and optimised coefficients from the ironing rig experimental comparison, Chapter 6 focused on revisiting the force-overclosure contact definition method for modelling the polymer layers. Understanding that the friction coefficient would differ but the stiffness of tooling would not, FEA simulations were re-compared with results from the ironing rig experiments- optimising the force-overclosure and friction coefficient for the polymer contact model. This optimisation yielded a contact definition for the polymer layers which approximately matched the reaction force curve of an identically tooled rig experiment. This contact definition was decided sufficient for the final model.

Finally, chapter 7 covered a full Design of Experiments model for a fully tooled DWI process on a polymer-coated food can, using data and techniques from all previous chapters. The DoE ran with an OHL method, and yielded 78 successful result sets. These results were then matched to a cubic polynomial response surface model which minimised r^2 values of 0.790 and 0.925 for thickness and height respectively, when compared to an error sample of 15 data points. This response fit was used to calculate the formulae for deriving output thickness and height for a given set of input parameters, and this in turn was used to plot data for the unknown design space which matched expected behaviour for many of the tooling parameters. A physical DoE was attempted with available can data, but proved insufficient for validating the discoveries in the simulation. Ultimately chapter 7 provided a successful conglomeration of the work in the thesis, demonstrating the capability of the contact-definition FEA modelling approach as an effective alternative to meshing the polymer layer. The findings of this project would benefit further work with a larger DoE and matching physical experiments in order to fully validate the modelling technique, and provide more accurate and repeatable prediction as to the implications and interactions of the tooling parameters used in can-making, and their effect on the output polymer-coated can.

Overall, this project has thoroughly contributed to the packaging research field. The design, manufacture, and utilisation of the custom-made ironing rig provides novel research data behind the metrics of ironing strip metal, and offers a

varied scope of future usage: including microstructural study of material mid-ironing. In future design iterations, the rig could be adapted to deal with cylindrical geometry, tungsten carbide dies would offer increased resistance to wear and deformation, and the addition of a load cell behind the dies would allow a greater variety of force data to be captured.

The contact definition method of modelling polymer-coated metal demonstrates a suitable alternative to meshing the coating, at a considerably reduced computational cost. The methods undertaken in this thesis could be utilised to model any variety of coated materials where the behaviour of the coating is not the focus of study. A future optimisation with increased runs and parameters would be beneficial to match a higher number of metrics to physical tests, and produce a contact model with further increased accuracy.

8.2 Future work and study

The limitations of the doctoral project leave many areas of study relatively untouched or otherwise unexplored. This final section of the thesis provides a brief overview of each chapter, and the possibilities for future study either uncovered or encouraged by the work completed.

8.2.1 Chapter 3

The work on modelling the DWI process undertaken in this chapter left some questions answered regarding the oscillatory behaviour of the elements during contact with the tooling. Whilst a brief study was undertaken to investigate whether the difference between explicit and standard solvers offered an explanation, no certain verdict was reached. The primary work to follow from this section would be an investigative study of the vibration modelling during ironing process. The parameters to explore would be:

- *Mesh density.* Simulating with a wider variety of mesh densities, and quantifying the magnitude of the oscillations occurring would allow an understanding into whether or not snagging effects were responsible for the fluctuating force readings.

- *Punch speed modelled, as well as inertial effects.* It is possible that exploring a wider variety of speeds during simulation (and indeed varying mass properties of the material) would change the effect of the oscillations.
- Contact models. To fully explore the phenomenon, different kinds of contact methods should be used for the various models to determine is the penalty contact method is to blame.

8.2.2 Chapter 4

Whilst the characterisation of the contact definition is covered in chapter 6, the question of material characterisation for the polymer remains. This project did not have access to tooling sufficient to grip and test a polymer film in a tensile or compressive testing machine; however this is the natural progression for characterising the polymer. An apparatus with a much more sensitive force sensor, and a different kind of clamping or fixing system for the specimen would be required to fully test the mechanical properties of the thin polymer film. If the polymer layer is to be modelled fully in the future, some delamination properties must also be quantified to properly simulate the interface between metal and polymer. This could perhaps be achieved with a chisel-like apparatus attached to a force sensor, which could provide metrology behind the stripping of the polymer during ironing.

Once material characteristics were properly characterised, a more hollistic approach to modelling the polymer could be undertaken - focusing on meshing types and methods. Since delamination failure modes would require fully-meshed polymer layers, shell elements may provide a suitable middle-ground between the heavy computational load of continuum elements, and the much computationally cheaper (yet less data-yielding) contact method used in this thesis. Exploring and utilising suitable meshing methods for a fully characterised polymer would be an important feature of advanced work.

8.2.3 Chapter 5

As a prototype, the ironing rig leaves much room for improvement. If financial limitations were not a concern, the following amendments to the design are encouraged:

- *Tungsten Carbide (or otherwise carbide-coated metal) ironing dies.* Whilst the prototype performed it's function, the longevity of the tempered steel dies was less than desirable, and permanent deformation occurred in the order of ≈200 cycles. A harder die and punch material would allow more tests to be undertaken before deformation failure occurred.
- *Alignment.* Another major challenge with the prototype was the proper alignment of parts during calibration and specimen installation. Whilst contacting parts were intentionally kept to a minimum (to minimise excess contact forces), some guidance system installed onto the punch and the housing (like a laser pointer matching to a marked site), would enable more repeatable installation than the marking system previously used. This enhanced alignment would also reduce excess stress on a particular die, and reduce the chances of uneven ironing.
- *Specimen marking.* It is clear that the successful ironing tests suffered primarily from a lack of accuracy in the length measurements of the specimens. Difficulty adhering any king of paint or ink to the food-safe polymer layer left only manual markings as a possibility during the project, but an etched or printed grid system, combined with digital image correlation of the deformed grid, would serve far better for calculating deformation and strain in the specimen.
- *Tolerances.* Naturally, the tolerances of the build could be improved for better alignment and accuracy. Precision grinding the contacting and parallel parts would minimise risk of misalignment, and allow cleaner ironing to occur. The hand-guillotine cutting method also leaves room for improvement, as widths of specimens were subject to a higher degree of error than if they were machine cut.

8.2.4 Chapter 6

Since this chapter deals primarily in the combining of two previously explored constituent parts, the future work is mirrored from chapters 4 and 3.

8.2.5 Chapter 7

This final piece of work provides a promising basis for future study, but lacks more the depth of data involved in a more stochastic DoE. Some immediate

improvements to this facet of the work would involve:

- If time was not a limiting factor, rerunning the DoE study with further levels of parametric investigation. A full latin hypercube undertaken at 100 levels each would provide a better mapping of the parametric design space, and allow for more finely tuned study of the interaction between parameters. The geometric outputs of the can should be measured using multiple calculated averages at varying can heights (as opposed to the point-measurements taken in this thesis), to provide a higher degree of accuracy and account for uneven deformation.
- The physical DoE used in this work as a reference model was unfortunately undertaken long before the FEA study, and thus matching tooling parameters were not possible. Undertaking a new physical DoE with the geometric tooling setup mirroring the can geometry studied in this thesis, would provide a much more advantageous comparison between FEA and experimental results. Similar figures could be generated from the matching experimental study, and a data-matching algorithm could be used in Isight to determine the differences between the two outputs. Ultimately, a further optimisation loop could be utilised in Isight to properly refine the contact definition (or indeed all aspects of the FEA model) until results accurately mirrored the experimental output. This would provide an iron-clad confidence in the ability of the FEA model to accurately represent the DWI process for polymer-coated cans: which would allow full confidence simulating parametric combinations beyond experimental possibility.

8.3 Final Review

The aims set out at the start of this project have been achieved to a satisfactory extent. Throughout the project the task of exploring, modelling, refining, and even experimentally testing the polymer-coated DWI process has brought about many challenges.

Whilst there is always room for improvement in engineering, the work undertaken in this project has successfully created a firm basis of understanding behind the complexities and difficulties involved in working with polymer-coated metals in the DWI process. Equally, the project has given rise to both a novel method of FEA modelling for the polymer-coated metals (in the form of the

contact definition approach), and a prototype ironing rig capable of producing ironed and part-ironed polymer-coated specimens for analysis.

The DoE study undertaken, calibrated and optimised with the new experimental data from the rig, and new contact definition modelling approach, provides an interesting stepping stone into the full understanding of the DWI process, and how these tooling parameters affect the final can. Fundamentally, the thesis project has succeeded in fulfilling it's aims, and the encompassed work serves as newly explored ground in the area of polymer-coated processing.

Bibliography

[1] W. Soroka. *Fundamentals of packaging technology 4 edition*. institute of packaging professionals, 2010.

[2] CanCentral. *How cans are made*. [Online at `http://www.cancentral.com/can-stats/how-cans-are-made` Accessed 2016].

[3] MPMA. *3 Piece drinks can lores*. Online at `http://mpma.org.uk/pages/data/3piecedrinkscanlores.pdf` Accessed 2016].

[4] E Almeida et al. *Environmentally friendly coatings for tinplate cans in contact with synthetic food media*. JCT Research, 2004.

[5] P. King. *Wolverley Lower Mill and the beginnings of the tinplate industry*. Historical Metallurgy 22, 1988, pp. 104–113.

[6] John M. Jackson. *Fundamentals of canning technology*. AVI publishing company inc, 1979.

[7] R. Cawthray E Denison. *The big book of packaging prototypes*. Rotovision, 2010, pp. 4–22.

[8] T. Altan. *Cold and hot forging, fundamentals and applications*. Vol. 1. ASM international, 2005.

[9] K. Pöhlandt. *Materials testing for the metal forming industry*. Springer-Verlag, 2012, pp. 137–148.

[10] H. Fukumasu, T. Kuwabara, and H. Takizawa. "Influence of material modeling on earing prediction in cup drawing of AA3104 aluminum alloy sheet". In: *Journal of Physics: Conference Series* 734.3 (2016). ISSN: 17426596. DOI: 10.1088/1742-6596/734/3/032022.

[11] J. W. Yoon et al. "Influence of initial back stress on the earing prediction of drawn cups for planar anisotropic aluminum sheets". In: *Journal of Materials Processing Technology* 80-81.1998 (1998), pp. 433–437. ISSN: 09240136. DOI: 10.1016/S0924-0136(98)00148-4.

[12] A. M. Zaky, A. B. Nassr, and M. G. El-Sebaie. "Optimum blank shape of cylindrical cups in deep drawing of anisotropic sheet metals". In: *Journal of Materials Processing Technology* 76.1-3 (1998), pp. 203–211. ISSN: 09240136. DOI: 10.1016/S0924-0136(97)00349-X.

[13] R. Coles et al. *Food packaging technology*. Blackwell publishing, 2003, p. 124.

[14] Beverage Daily. [Online at `https://www.beveragedaily.com/Article/2011/07/20/Drink-size-guidelines-in-schools-present-market-opportunity-for-mini-can-says-Ball` Accessed 2016].

[15] Preparednessadvice.com. [Online at `http://preparednessadvice.com/wp-content/uploads/2015/04/can-welded.jpg` Accessed 2016].

[16] G. Totten et al. *Handbook of residual stress and deformation of steel*. ASM international, 2002.

[17] S. Natarajan et al. *Fundamentals of Packaging Technology*. 2nd ed. PHI Learning pvt Ltd, 2009.

[18] A.J. Mitchell. *Formulation and Production Carbonated Soft Drinks*. AVI, 1990, pp. 152–160.

[19] T. Turner. *Canmaking for Can Fillers*. Sheffield Academic Press ltd, 2001.

[20] A. Faizin. *A Review Paper on Product Surface Defect Detection of Ironing Processes*. Institut Teknologi Sepuluh Nopember, 2015.

[21] N.J. Rendler & I. Vigness. *Hole-drilling strain-gage (sic) method of measuring residual stresses*. Vol. 6. Springer, 1966, pp. 577–586.

[22] M. Helfrick. *An Investigation of 3D Digital Image Correlation for Structural Health Monitoring and Vibration Measurement*. University of Massachusetts, 2008.

[23] O.C. Zienkiewicz. *The Finite Element Method: Its Basis and Fundamentals*. Elsevier ltd, 2003.

[24] Simulia. *Abaqus documentation*. [Online: `https://www.sharcnet.ca/Software/Abaqus610/Documentation/docs/v6.10/books/gsk/default.htm` Accessed: 2016].

[25] G. Touzot G. Dhatt. *The Finite Element Method*. ISTE ltd, 2012.

[26] C. Teodosiu et al. "Modelling and simulation of the can-making process using solid finite elements". In: *Journal of Materials Processing Tech.* 50.1-4 (1995), pp. 133–143. ISSN: 09240136. DOI: `10.1016/0924-0136(94)01375-B`.

[27] S R MacEwen et al. *Understanding the forming and performance of aluminum beverage cans through finite element modelling*. 2000.

[28] D. M. Neto et al. "Numerical and experimental analysis of wrinkling during the cup drawing of an AA5042 aluminium alloy". In: *International Journal of Material Forming* 10.1 (2017), pp. 125–138. ISSN: 1960-6206. DOI: `10.1007/s12289-015-1265-4`. URL: `http://link.springer.com/10.1007/s12289-015-1265-4`.

[29] Jianguo Hu, Keisuke Ikeda, and Tadasu Murakami. "Effect of texture components on plastic anisotropy and formability of aluminium alloy sheets". In: *Journal of Materials Processing Technology* 73.1-3 (1998), pp. 49–56. ISSN: 09240136. DOI: `10.1016/S0924-0136(97)00211-2`.

[30] R. Vasanth Kumar et al. "Influence of hot rolling on microstructure and mechanical behaviour of Al6061-ZrB2 in-situ metal matrix composites". In: *Materials Science and Engineering A* 738.June (2018), pp. 344–352. ISSN: 09215093. DOI: `10.1016/j.msea.2018.09.104`.

[31] Yves Jean Respen Mario Economopoulos. *Producing rolled steel products*. US Patent 4016009 A. US Patent office, 1976.

[32] D.T. Llewellyn. *Work hardening effects in austenitic stainless steels*. Taylor & Francis, 2013, pp. 389–400.

[33] A Martnez-de Guerenu et al. "Recovery during annealing in a cold rolled low carbon steel. Part I: Kinetics and microstructural characterization". In: *Acta Materialia* (2004), pp. 3657–3664.

[34] M. Palanivendhan. *Mechanical working of metals*. [Online at `https://www.slideshare.net/palanivendhan/mechanical-working-of-metals-37308919` Accessed 2019].

[35] Guy M. Pound et al. *Kinetics of Crystalline Nucleus Formation in Supercooled Liquid Tin*. Carnegie institute of technology, 1952.

[36] J. Gruber et al. *Effect of Anisotropic Grain Boundary Properties on Grain Boundary Plane Distributions During Grain Growth*. Elsevier, 2004.

[37] A.E. Tekkaya et al. *Formability of Metallic Materials: Plastic Anisotropy, Formability Testing, Forming Limits*. Springer, 2000.

[38] E. Ahmad et al. *Effect of cold rolling and annealing on the grain refinement of low alloy steel*. Vol. 60. IOP Publishing ltd, 2013.

[39] J.L. Strudel A. Lassalmonie. *Review: Influence of grain size on the mechanical behaviour of some high strength materials*. Vol. 21. Kluwer academic publishers, 1986.

[40] T. Belytschko et al. *Hourglass control in linear and nonlinear problems*. Department of Civil and Mechanical/Nuclear Engineering at Northwestern University, 2003.

[41] G. Fix G. Strang. *An analysis of the finite element method*. Wellesley-Cambridge press, 2008.

[42] C.A. Felippa. *Introduction to Finite Element Methods*. Boulder, Colorado: University of Colorado, 2004.

[43] E. Wilson K. Bathe. *Numerical methods in finite element analysis*. Prentice Hall Inc, 1976.

[44] Encyclopedia of Mathematics. *Guass quadrature formula*. [Online: `http://www.encyclopediaofmath.org/index.php?title=Gauss_quadrature_formula&oldid=34105` Accessed: 2016].

[45] T. Hughes. *The Finite Element Method: Linear Static and Dynamic Finite Element Analysis*. Dover publications, 2000.

[46] Ajay Harish. *Implicit vs Explicit Finite Element Method (FEM): What Is the Difference?* [Online at `https://www.simscale.com/blog/2019/01/implicit-vs-explicit-fem/` Accessed 2020].

[47] U. Nackenhorst P. Wriggers. *Analysis and Simulation of Contact Problems*. Springer, 2006.

[48] *Contact formulation for Abaqus Explicit*. [Online at `https://classes.engineering.wustl.edu/2009/spring/mase5513/abaqus/docs/v6.5/books/usb/default.htm?startat=pt08ch21s04aus126.html` Accessed 2020].

[49] N. Sukumar. *An Abaqus implementation of the extended finite element method*. Elsevier, 2009.

[50] L. Lindkvist S. Dahlström. *Variation Simulation of Sheet Metal Assemblies Using the Method of Influence Coefficients With Contact Modeling*. Vol. 129. ASME, 2006.

[51] NDE-ed. *Metallic Structures*. [Online at `https://www.nde-ed.org/EducationResources/CommunityCollege/Materials/Structure/metallic_structures.htm` Accessed 2016].

[52] U. Liedl, S. Traint, and E.A. Werner. "An unexpected feature of the stressstrain diagram of dual-phase steel". In: *Computational Materials Science* 25.1-2 (2002), pp. 122–128. ISSN: 09270256. DOI: `10.1016/S0927-0256(02)00256-2`. URL: `https://linkinghub.elsevier.com/retrieve/pii/S0927025602002562`.

[53] *Steel phases*. [Online at https://www.lff-group.com/content/images/posts/carbon-steel-fundamentals-part-1/Carbon_Steel_Figs_1-5.jpg Accessed 2020].

[54] M. Watson et al. *Benchmark 1 Failure Prediction after Cup Drawing, Reverse Redrawing and Expansion*. 2016.

[55] S.L. Bazhenov et al. *The influence of preliminary rolling on the mechanical properties of polyethylene terephthalate*. Pleiades Publishing, 2015, pp. 210–241.

[56] *Polyethylene terephthalate chemical compound*. [Online at https://www.britannica.com/science/polyethylene-terephthalate Accessed 2020].

[57] Rebecca B. Dupaix and Mary C. Boyce. "Finite strain behavior of poly(ethylene terephthalate) (PET) and poly(ethylene terephthalate)-glycol (PETG)". In: *Polymer* 46.13 (2005), pp. 4827–4838. ISSN: 00323861. DOI: 10.1016/j.polymer.2005.03.083. URL: https://linkinghub.elsevier.com/retrieve/pii/S0032386105004118.

[58] Martin Watson et al. "Benchmark 1 - Failure Prediction after Cup Drawing, Reverse Redrawing and Expansion Part A: Benchmark Description". In: *Journal of Physics: Conference Series* 734.2 (2016). ISSN: 17426596. DOI: 10.1088/1742-6596/734/2/022001.

[59] N. Itoh K. Mine. *Method of ironing cylindrical workpiece of austenite stainless steel, with controlled thickness reduction*. US Patent 5333484 A. US Patent office, 1994.

[60] G.E. Totten et al. *Handbook of Metallurgical Process Design*. Marcel Dekker inc, 2004.

[61] S.S. Quek G.R. Liu. *The Finite Element Method, a practical course, 2nd edition*. Elsevier, 2014.

[62] V. Boljanovic. *Sheet Metal Forming Processes and Die Design*. industrial press New York, 2004.

[63] Underwood et al. *Fracture Mechanics*. Vol. 17. ASTM, 1984, p. 187.

[64] S.S. Rao. *The Finite Element Method in Engineering, Fifth edition*. Elsevier, 2011.

[65] J.E. Akin. *Finite Elements for analysis and Design*. Academic press, 1994, p. 65.

[66] U.S. Dixit R.G. Narayanan. *Advances in Material Forming and Joining*. Springer, 2014, p. 127.

[67] M.J. Bibby J. Neddoes. *Principles of Metal Manufacturing Processes*. Elsevier, 2003.

[68] J.E. Hatch. *Aluminum: properties and physical metallurgy*. ASM, 1984. Chap. 4.

[69] X-T. Yang et al. *Advanced Design and Manufacture to Gain a Competitive Edge: New Manufacturing Techniques and their Role in Improving Enterprise Performance*. Springer, 2008, p. 789.

[70] R. Pearce. *Sheet Metal Forming*. Adam Hilger, 1991.

[71] M.A.H. Van der Aa. *Wall Ironing of Polymer Coated Sheet Metal*. University Eindhoven, 1999.

[72] P.D. Harvey. *Engineering Properties of Steel*. American society for metals, 1982.

[73] W.F. Hosford. *Iron and Steel*. Cambridge University Press, 2012.

[74] K. Babski et al. *Evaluation of Residual Stresses in Ceramic and Polymer Matrix Composites Using Finite Element Method*. Warsaw University of Technology, 2006.

[75] R.V. Dukkipato J.S. Rao. *Mechanism and Machine Theory, second edition*. New age international(P) limited Publishers, 1992.

[76] P.E. Hugh F.J. Harewood. *Comparison of the implicit and explicit finite element methods using crystal plasticity*. Elsevier, 2006.

[77] C. King. *A Study of vibration problems of high speed rotating machines*. Cornell university, 1926.

[78] J.S. Sun et al. *Comparison of Implicit and Explicit finite element methods for dynamic problems*. Vol. 105. Elsevier, 2000, pp. 110–118.

[79] B. Szabó. *Finite Element Analysis*. 1st ed. Wiley-Interscience, 1991.

[80] Djordje Perić and D. R. J. Owen. "Computational model for 3-D contact problems with friction based on the penalty method". In: *International Journal for Numerical Methods in Engineering* 35.6 (1992), pp. 1289–1309. ISSN: 0029-5981. DOI: 10.1002/nme.1620350609. URL: http://doi.wiley.com/10.1002/nme.1620350609.

[81] Jianqiao Chen et al. "Reliability design optimization of composite structures based on PSO together with FEA". In: *Chinese Journal of Aeronautics* 26.2 (2013), pp. 343–349. ISSN: 10009361. DOI: 10.1016/j.cja.2013.02.011. URL: https://linkinghub.elsevier.com/retrieve/pii/S100093611300023X.

[82] J.C.H. Goh et al. "Development of an integrated CADFEA process for below-knee prosthetic sockets". In: *Clinical Biomechanics* 20.6 (2005), pp. 623–629. ISSN: 02680033. DOI: 10.1016/j.clinbiomech.2005.02.005. URL: https://linkinghub.elsevier.com/retrieve/pii/S026800330500029X.

[83] "Wall ironing of deep-drawn cups". In: *Mechanics of Sheet Metal Forming*. Elsevier, 2002, pp. 14–29. DOI: 10.1016/B978-075065300-8/50005-4. URL: https://linkinghub.elsevier.com/retrieve/pii/B9780750653008500054.

[84] F. Auricchio and R.L. Taylor. "Two material models for cyclic plasticity: Nonlinear kinematic hardening and generalized plasticity". In: *International Journal of Plasticity* 11.1 (1995), pp. 65–98. ISSN: 07496419. DOI: 10.1016/0749-6419(94)00039-5.

[85] Michiel A.H. Van der Aa. "Wall Ironing of Polymer Coated Sheet Metal". PhD thesis. Eindhoven: University Eindhoven, 1991.

[86] W.D. Callister and D.G. Rethwisch. *Fundamentals of Materials Science and Engineering: An Integrated Approach*. New York: John Wiley & Sons, Inc., 2001. ISBN: 1118061608, 9781118061602.

[87] R.A. Pethrick. *Polymer Structure Characterization: From Nano to Macro Organization in Small Molecules and Polymers*. RSC Publishing., 2014.

[88] Jörgen Bergström. "Hyperelastic Materials". In: *Mechanics of Solid Polymers*. Elsevier, 2015. ISBN: 9780323311502. DOI: 10.1016/C2013-0-15493-1. URL: https://linkinghub.elsevier.com/retrieve/pii/C20130154931.

[89] Elton L. G. Denardin, Shinichi Tokumoto, and Dimitrios Samios. "Stressstrain behaviour of poly(ethylene terephthalate) (PET) during large plastic deformation by plane strain compression: the relation between stressstrain curve and thermal history, temperature and strain rate". In: *Rheologica*

Acta 45.2 (2005), pp. 142–150. ISSN: 0035-4511. DOI: 10.1007/s00397-005-0004-z.

[90] Bo Yin et al. "Aerodynamic optimization of 3D wing based on iSIGHT". In: *Applied Mathematics and Mechanics* 29.5 (2008), pp. 603–610. ISSN: 0253-4827. DOI: 10.1007/s10483-008-0505-y. URL: http://link.springer.com/10.1007/s10483-008-0505-y.

[91] W.H. Press. *Numerical Recipes in Fortran 77*. 2nd ed. Press Syndicate, University of Cambridge, 1992.

[92] K. Schittkowski. "NLPQLP: A New Fortran Implementation of a Sequential Quadratic Programming Algorithm for Parallel Computing". In: *University of Bayreuth* ().

[93] M. M. Moshkar & A Hosseini Kalvarzi. *Ironing of Aluminum cups, Materials & manufacturing processes*. Taylor & Francis, 2002.

[94] A. Kumar et al. *Formability of Al-killed AISI 1040 Medium Carbon Steel for Cylindrical Cup Formation*. The Iron and Steel Institute of Japan, 2016.

[95] L. Folle et al. *Analysis of the manufacturing process of beverage cans using aluminum alloy*. Vol. 205. Elsevier, 2008.

[96] et al. Aleksandrovi. "Different ways of friction coefficient determination in stripe ironing test". In: *Tribology in Industry* 36.3 (2014), pp. 293–299. ISSN: 03548996.

[97] P. Deneuville and R. Lecot. "The study of friction in ironing process by physical and numerical modelling". In: *Journal of Materials Processing Technology* 45.1-4 (1994), pp. 625–630. ISSN: 09240136. DOI: 10.1016/0924-0136(94)90409-X.

[98] et al Stone E.R.H. "An exercise in cold ironing as the post-forging operation for net-shape manufacture". In: *Journal of Materials Processing Technology* 135.2-3 (2003), pp. 278–283. ISSN: 09240136. DOI: 10.1016/S0924-0136(02)00858-0.

[99] S.J. Allen & S.M. Mahdavian. *Manual handling operations regulations 1992*. Health and Safety Executive UK., 1992.

[100] S.J. Allen & S.M. Mahdavian. *The effect of lubrication of die expansion during the deep drawing of axisymmetrical steel cups*. Vol. 199. Elsevier, 2008.

[101] A. Iqbal et al. *Effects of tool life criterion on sustainability of milling*. Vol. 139. Elsevier, 2016.

[102] M. Phlipot. *SELF-ALIGNING TRIMMING PUNCH FOR REMOVING FINS OF CAST PARTS AND METHOD FOR REMOVING FINS*. Honda America MFG Patents, P2002035925 (A). US Patent office, 2002.

[103] H. Abdelounis et al. *An experimental study on roughness noise of dry rough flat surfaces*. Vol. 268. Elsevier, 2009.

[104] F. Baumgart. *Stiffness - an unknown world of mechanical science?* Vol. 31. Elsevier, 2000.

[105] D. Rees. *Basic Engineering Plasticity: An introduction with engineering and manufacturing applications, 1st edition*. Elsevier, 2012.

[106] J. Murin et al. *Calculation of stress in FGM beams*. Vol. 157. MATEC, 2018.

[107] W. Chen & D Han. *Plasticity for Structural Engineers*. J. Ross Publishing, 2007.

[108] P.P. Rossi. *Evaluation of the ultimate strength of R.C. rectangular columns subjected to axial force, bending moment and shear force*. Vol. 139. ASCE, 2013.

[109] H. Kim et al. *Evaluation of stamping lubricants in forming advanced high strength steels (AHSS) using deep drawing and ironing tests*. Vol. 209. Elsevier, 2009.

[110] S.R. Satish Kuma & A.R. Santha Kumar. *Design of Steel structures II*. Indian Institute of Technology Madras, 2017.

[111] F. Beer et al. *Mechanics of Materials 7th edition*. McGraw-Kill Professional, 2015.

[112] J.M. Gere & B.J. Goodno. *Mechanics of Materials, eighth edition*. CENGAGE Learning custom publishing, 2012.

[113] O. Wiippola. *Simplified modelling of Fixtures in FE Welding Simulation*. Springer, 1997.

[114] M.L. Williams. *The Bending Stress Distribution at the Base of a Stationary Crack*. ASME, 2011.

[115] N. McCormick & J. Lord. *Digital Image Correlation*. Vol. 13. Elsevier, 2010.

[116] S. Randelovic et al. *Deep drawing technology with wall ironing in mass packaging industry*. Vol. 15. University of Nis, 2017.

[117] L.C. Brezeanu. *Contact stresses between two cylindrical bodies: cylinder and cylindrical cavity with parallel axes - Part I: Theory and FEA 3D modelling*. Vol. 19. Elsevier, 2015, pp. 169–176.

[118] M. Batdorf et al. *A computational study of the effect of unstructured mesh quality on solution efficiency*. University of North Texas, 1997.

[119] Z.C. Zhang et al. *Formulation of Equivalent Plastic Strain Accumulated in Rotating Bending Process of Metal Tubes for Severe Plastic Deformation*. Vol. 5. Scientific.net, 2014, pp. 887–888.

[120] T. Shin et al. *Strain and hardness distributions in the cup wall drawn with ironing of 3004-H19 Aluminium alloy sheets*. Vol. 59. JISM, 2009.

[121] M.N. Ali Mukhtar et al. *Strain and hardness distributions in the cup wall drawn with ironing of 3004-H19 Aluminium alloy sheets*. Vol. 836. Scientific.net, 2016, pp. 197–202.

[122] K. Lee. *A simple node-to-segment contact technique of finite element models of elastic bodies to attain the node-to-node contact accuracy*. Vol. 228. SAGE, 2014.

[123] S. Jin et al. *Node-to-node scheme for three-dimensional contact mechanics using polyhedral type variable-node elements*. Vol. 304. Elsevier, 2016.

[124] K. Shimizu et al. *Simulation of Optimized Bolt Tightening Strategies for Gasketed Flanged Pipe Joints*. International Application No.: PCT/JP2000/003936. World Intellectual Properly Organisation, 2000.

[125] Jianping Gao et al. "Frictional Forces and Amontons' Law: From the Molecular to the Macroscopic Scale". In: *The Journal of Physical Chemistry B* 108.11 (2004), pp. 3410–3425. ISSN: 1520-6106. DOI: 10.1021/jp0363621. URL: https://pubs.acs.org/doi/10.1021/jp0363621.

[126] Harmon D. Nine. "The applicability of Coulomb's friction law to drawbeads in sheet metal forming". In: *Journal of Applied Metalworking* 2.3

(1982), pp. 200–210. ISSN: 0162-9700. DOI: 10.1007/BF02834038. URL: http://link.springer.com/10.1007/BF02834038.

[127] et al. I Tikhovskiy. *Simulation of earing during deep drawing of an Al3% Mg alloy (AA 5754) using a texture component crystal plasticity FEM*. Vol. 183. Elsevier, 2007, pp. 169–175.

[128] D. Novak, B. Teply, and Z. Kersner. "The role of Latin Hypercube Sampling method in reliability engineering". In: *Structural safety and reliability*. 1997, pp. 401–409.

[129] Raymond H. Myers, C. Douglas, and Christine M. Anderson-Cook. "Response surface methodology". In: *Response surface methodoloy*. John Wiley & Sons, Inc., 2016, pp. 1–13.

[130] Jiju. Antony. "Design of Experiments for Engineers and Scientists". In: *Design of Experiments for Engineers and Scientists*. 2nd ed. 2014, pp. 1–31.